

12th Australasian Biomechanics Conference (ABC12)

06 - 07 December 2021

Online Conference

Program



Online event platform by JT. Production Management 2021, Australia

12th Australasian Biomechanics Conference (ABC12)

06 - 07 December 2021

CONTENTS

WELCOME	3
OUR SPONSORS	4
COMMITTEE MEMBERS	5
SCIENTIFIC COMMITTEE	6
TRAVEL GRANT RECIPIENTS	7
KEYNOTE SPEAKERS	8
PROGRAM	10
ABSTRACTS	17
DAY 1	18
KEYNOTE 1 - Prof Silvia Blemker	18
PODIUM 1	20
PODIUM 2	27
PODIUM 3	34
PODIUM 4	41
PODIUM 5	48
DAY 2	56
Young Investigator Award Finalists	56
KEYNOTE 2 - Prof Steven Boyd	62
New Investigator Award Finalists	64
PODIUM 6	70
PODIUM 7	77
PODIUM 8	84
PODIUM 9	91
POSTERS DAY 1	94
POSTERS DAY 2	111
LIST OF REGISTERED DELEGATES	126

12th Australasian Biomechanics Conference (ABC12)

06 - 07 December 2021

In vivo, in vitro and in silico synergies in biomechanics

Welcome

Welcome to the 12th biennial Australasian Biomechanics Conference (ABC12). This is the first ABC meeting to be held completely online due to COVID restrictions, after last year's meeting meant to be held in Adelaide was postponed to this year.

Our warm welcome to our attendees from Australia, New Zealand and overseas, we look forward to engaging with you throughout the conference.

A special thanks to our sponsors for their support, thanks to them we are able to offer awards and to organise this great conference.

We received abstracts of the highest quality with topics from clinical biomechanics, physiology, computational biomechanics, imaging, orthopaedic biomechanics and sports biomechanics.

This makes a fantastic scientific program for ABC12 and highlights the multidisciplinary approach to complex problems in biomechanics within ANZSB. Thanks to all the authors and abstract reviewers that have helped shaping this program.

The program includes two great international keynote speakers from USA and Canada and two Award Finals sessions, one for the 'New Investigator award' and the other for the 'Young Investigator award'.

We will have also one award for the 'Best Podium' and 'Best Poster' presentation, with the award winners to be announced at the end of day two. Whereas we have dedicated judges and sessions for the first two awards, as of tradition, for the latter two awards we decided to give the opportunity to vote online to all the ABC12 registered delegates attending the conference; given this is an online conference, we feel this is also an excellent opportunity to engage with all of you.

We are looking forward to exciting days of biomechanics revealing synergies between in vivo, in vitro and in silico biomechanics. Please enjoy and engage with the great science presented over the next two days in our conference program.

The ABC12 organising committee

A/Prof Egon Perilli, A/Prof Dominic Thewlis, Prof Mark Taylor, A/Prof Saulo Martelli



Thanks to our sponsors:

Platinum Sponsor

LOGEMAS

Silver Sponsor



VICON

Bronze Sponsor



Awards Sponsor



**International Society
of Biomechanics**



**Joint Biomechanics
Training Centre**

12th Australasian Biomechanics Conference (ABC12)

06 - 07 December 2021

Organising Committee

A/Prof Egon Perilli	Associate Professor in Biomedical Engineering, The Medical Device Research Institute, College of Science and Engineering, Flinders University, Australia
A/Prof Dominic Thewlis	Associate Professor, Centre for Orthopaedic & Trauma Research, The University of Adelaide, Australia
Prof Mark Taylor	Professor, The Medical Device Research Institute, College of Science and Engineering, Flinders University, Australia
A/Prof Saulo Martelli	Associate Professor, School of Mechanical, Medical & Process Engineering, Queensland University of Technology, Australia

Online Platform

Online event platform by [JT. Production Management](#) 2021, Australia:

Heidi McKerrow

Opal McKenzie

Scientific Committee (alphabetical surname order)

Dr Rodrigo Bini	La Trobe University, Australia
Dr Carina Blaker	Kolling Institute, University of Sydney, Australia
Dr Bart Bolsterlee	NeuRA / UNSW / QUT, Australia
Dr Julie Choise	The University of Auckland, New Zealand
Mr Daniel Devaprakash	Griffith University, Australia
Dr Laura Diamond	Griffith University, Australia
Dr Taylor Dick	The University of Queensland, Australia
A/Prof Tim Doyle	Macquarie University, Australia
Dr Suzi Edwards	The University of Sydney, Australia
Dr Aaron Fox	Deakin University, Australia
Dr Michelle Hall	The University of Melbourne, Australia
Ms Meaghan Harris	University of Newcastle, Australia
Prof Rob Herbert	NeuRA, Australia
Dr Lauriane Juge	Neuroscience Research Australia, Australia
Dr Crystal Kean	Central Queensland University, Australia
Prof Glen Lichtwark	The University of Queensland, Australia
Dr Robert Lloyd	Neuroscience Research Australia, Australia
Dr Joe Lynch	Australian National University, Australia
A/Prof Saulo Martelli	Queensland University of Technology, Australia
Mr Fazle Rabbi	Griffith University, Australia
Dr Vijay Rajagopal	The University of Melbourne, Australia
Dr Elyse Passmore	Murdoch Children's Research Institute, Australia
A/Prof Egon Perilli	Flinders University, Australia
Dr Edmund Pickering	Queensland University of Technology, Australia
Dr Claudio Pizzolato	Griffith University, Australia
Dr David John Saxby	Griffith University, Australia
Prof Mark Taylor	Flinders University, Australia
A/Prof Dominic Thewlis	The University of Adelaide, Australia
Dr Oren Tirosh	Swinburne University of Technology, Australia
Dr Jodie Wills	Macquarie University, Australia

Travel Grant Recipients (alphabetical surname order)

ABC12 is proud to support its early career researchers. This year we have awarded 6 travel grants.

Mr Dylan Ashton	The University of Sydney, Australia
Mr Marco Branni	Queensland University of Technology, Australia
Mr Bradley Cornish	Griffith University, Australia
Mr Adam Kositsky	Griffith University, Australia
Mr Mukherjee Satanik	KU Leuven, Belgium
Mr Scott Starkey	The University of Melbourne, Australia

Keynote Speakers

Prof Silvia Blemker

Professor, Biomedical Engineering, Mechanical & Aerospace Engineering, Ophthalmology, and Orthopaedic Surgery, University of Virginia, USA

Silvia Salinas Blemker is a Professor of Biomedical Engineering, with joint appointments in Mechanical & Aerospace Engineering, Ophthalmology, and Orthopaedic Surgery, at the University of Virginia in Charlottesville, VA, USA. She obtained her B.S. and M.S. degrees in Biomedical Engineering from Northwestern University and her Ph.D. degree in Mechanical Engineering from Stanford University. At UVA, she leads the Multi-scale Muscle Mechanophysiology Lab ("M³ Lab"). The M³ lab group develops advanced multi-scale computational and experimental techniques to study skeletal muscle biomechanics and physiology, and they are currently applying these techniques to variety of areas, including speech disorders, movement disorders, vision impairments, muscle atrophy, aging, and muscular dystrophies. Dr. Blemker has multiple patents pending and is the co-founder of Springbok, Inc, a company focused on image-based muscle analytics for a variety of applications from sports medicine to neuromuscular disorders.



Keynote Speakers

Prof Steven Boyd

Professor, Department of Radiology, Cummings School of Medicine and Director of the McCaig Institute for Bone and Joint Health, University of Calgary, Canada

Dr. Steven Boyd, PhD, is a Professor, Department of Radiology in the Cumming School of Medicine at the University of Calgary and Director of the McCaig Institute for Bone and Joint Health since 2016. He is a Biomedical Engineer with joint appointments in the Schulich School of Engineering and Faculty of Kinesiology. His research program, at the Bone Imaging Laboratory that he established in 2004, focuses on applying novel high-resolution imaging techniques for the assessment of bone and joint disorders such as osteoporosis and acute knee ligament injuries. His work includes clinical trials on the effects of vitamin D on bone, using high-resolution peripheral quantitative computed tomography and finite element analysis for fragility fracture prediction, post-traumatic osteoarthritis of the knee, and studies of the effects of space-flight on bone in astronauts. He is a Fellow of the American Society of Bone and Mineral Research (2018) and holds two research chairs – the Bob and Nola Rintoul Chair in Bone and Joint Research and the McCaig Chair in Bone and Joint Health. He has published over 170 peer-reviewed manuscripts, 7 book chapters and has an H-index (Scopus) of 47 with over 10,000 citations. The goal of his research is to provide a basis to effectively treat bone and joint diseases to reduce the chances of fragility fracture and post-traumatic osteoarthritis.





PROGRAM

12th Australasian Biomechanics Conference (ABC12)

6 -7 December 2021 | Online Conference Program

<https://abc12.dryfta.com/>

Updated 30 Nov 2021, Subject to Change

Opening Session

8:15am-
9:15am
AEDT

Welcome **ABC12 Committee**, A/Prof Egon Perilli, A/Prof Dominic Thewlis, Prof Mark Taylor, A/Prof Saulo Martelli

Presidential Address **Prof Peter Pivonka**

Keynote 1 **Prof Silvia Blemker, University of Virginia, USA**
Pushing the boundaries of muscle modeling: examples in volumetric muscle loss injury

15 min

Break

Podium 1 | Chair: Dr Julie Choisne

Automatically identifying infants at high-risk of cerebral palsy from smart-phone videos | **Elyse Passmore**

Squatting biomechanics following treatment for femoroacetabular impingement syndrome: hip arthroscopy vs conservative care | **Tamara Grant**

Feasibility of personalised hip load modification using real-time biofeedback in hip osteoarthritis: a pilot study | **Laura Diamond**

Hip contact forces during sprinting in femoroacetabular impingement syndrome and asymptomatic cam morphology | **Basilio Goncalves**

Differences in impact and propulsion between military boots and sports shoes | **Rodrigo Bini**

Do clinicians want biomechanical solutions to help treat shoulder injury and pathology? A survey-based study | **Aaron Fox**

15 min

Break

Podium 2 | Chair: Dr Laura Diamond

Hip contact forces can be predicted in real-time using a long short-term memory neural network | **Bradley Cornish**

Task-specific device use in paediatric prosthesis users | **Maura Eveld**

Simulation and design for indirect sensing and mapping of deep muscle activity using electric field | **Massoud Alipour**

In-vivo kinematics during step-up and down in three total knee replacement designs: a randomised clinical trial | **Joe Lynch**

Femoral mechanics using in-vitro real-time replication of physiological loading cycles of normal walking | **Hoa Hoang**

Improving the control of a brain-computer interface using virtual reality training | **Malik Muhammad Naeem Mannan**

10:45am-
11:45am
AEDT

15 min

Break

Podium 3 | Chair: Dr Bart Bolsterlee

12:00pm-
1:00pm
AEDT

The impact of data arrangement and walking conditions on gait based person re-identification using force platforms | **Kayne Duncanson**

Real-time conversion of IMU data to ankle joint angles using artificial intelligence | **Dave Ackland**

Adaptive Bayesian model to predict ankle angle based on EMG signals | **Homayoon Zarshenas**

Textile electrodes for electromyography | **Nathan Lyons**

A neuromusculoskeletal model-based controller for functional electrical stimulation cycling | **Claudio Pizzolato**

Rapid and high accuracy reconstruction of the bony shoulder anatomy: a statistical shape modelling study | **Yichen Huang**

1:00pm--
2:10pm
AEDT

Lunch Break

Podium 4 | Chair: Dr David Saxby

2:10pm-
3:15pm
AEDT

Apparent mechanical properties of the entire human femur: indirect vs direct methods | **Marco Branni**

Muscle synergy driven modelling to predict knee joint contact forces in children with cerebral palsy | **Fazle Rabbi**

Deep-learning markerless tracking of infants general movements reveals similar trajectories to a marker-based approach | **Hamid Abbasi**

Fracture risk prediction of lumbar vertebra under dynamic compression | **Dale Robinson**

Variations in knee joint loading can be effectively modelled by exploring the uncertainty of muscle recruitment | **Kieran Bennett**

Multiscale modeling of knee joint pathophysiology: combined effect of mechanics and inflammation | **Satanik Mukherjee**

5 min

Break

Poster 1 | Chair: Dr Elyse Passmore

3:20pm-
3:44pm
AEDT

A flexible framework for real-time control of neuromechanical prostheses | **Ana Carolina Cardoso De Sousa**

Assessment of trabecular bone adaptation in adolescent idiopathic scoliosis due to altered joint loading | **Edmund Pickering**

Kneeling tasks with and without knee pads: repeatability and loading visualisation | **Simon Thwaites**

Effect of different treadmill-induced perturbations on agonist and antagonist muscle forces in compensatory step | **Tayebeh Namayeshi**

Validity of the calf raise application | **Kim Hébert-Losier**

Effect of incremental increases in load on lower-limb coordination variability during load carriage | **Brooke Hoolihan**

Changes to kinematics and kinetics of typically developing children using the pyCGM2 model | **Dan Anderson**

Poster 2 | Chair: Dr Elyse Passmore

3:45pm-
4:09pm
AEDT

- The effects of sex and age on human tendon biomechanics | **Dylan Ashton**
- Linking muscle mechanics to the metabolic cost of constrained hopping | **Luke Jessup**
- Probing muscle adaptation following localised and widespread damage using a mechanobiological model | **Stephanie Khuu**
- Design and evaluation of a novel expandable helmet for bicyclists | **KM Tse**
- Joint contact forces during posteriorly seated cycling | **Claire Crossley**
- Predicting the 3D ground reaction force of running using lstm based on kinematic parameters | **Ferryanto Ferryanto**
- Beyond muscle architecture: predicting ankle mechanics from 3D triceps surae muscle fascicle information | **Mousa Kazemi**

15 min

Break

Podium 5 | Chair: Prof Rob Herbert

4:25pm-
5:35pm
AEDT

- Passive ankle exoskeletons influence both ankle and more proximal joint responses to unexpected perturbations | **James Leigh Williamson**
- Feasibility of using ultrasound to track iliotibial band displacement during isolated contractions | **Laura Hutchinson**
- Free achilles tendon strain during landing, jumping, locomotor, and rehabilitation tasks | **Daniel Devaprakash**
- Tibial accelerations estimate instantaneous vertical loading rate and peak patellofemoral joint stress during running | **Eoin Doyle**
- Gluteal muscle forces during hip-focused strengthening and injury prevention exercises | **Tyler Collings**
- Biceps femoris long head neuromechanical behaviour during nordic hamstring exercise variations: preeliminary results | **Patricio A Pincheira**
- Do morphological changes explain knee flexor weakness after anterior cruciate ligament reconstruction? | **Adam Kositsky**

5:35pm-
5:40pm
AEDT

Day 1 Closing Remarks - Prof Rob Herbert

Day 2 Welcome

Young Investigator Award | Chair: Prof Thor Besier



International Society
of Biomechanics

8:10am-
9:15am
AEDT

Automating construction of subject-specific tongue models in patients with obstructive sleep apnoea | **Rob Lloyd**

Development of a safety-control trigger for functional electrical stimulation-induced cycling | **Ana Carolina Cardoso De Sousa**

Estimating facet joint apposition with specimen-specific computer models of subaxial cervical spine kinematics: the effect of axial compression and distraction during shear and bending motions | **Ryan Quarrington**

Effects of pubertal maturation on anterior cruciate ligament forces during a landing task in females | **Azadeh Nasseri**

Predicting rupture site in ascending aortic aneurysms using patient-specific finite element models | **Dermot O'Rourke**

9:15am-
9:45am
AEDT

Keynote 2 Prof Steven Boyd, University of Calgary, Canada

In Vivo Assessment of Human Knee Bone Microarchitecture and Mechanics

Chair A/Prof Egon Perilli

5 min

Break

Posters 3 | Chair: Dr Celeste Coltman

9:50am-
10:15am
AEDT

Exploring the relationship between size and shape of the human tarsal bones | **Paige Treherne**

The influence of spine cage position on the mechanical response of superior lumbar endplate-a finite element modelling study | **Yihang Yu**

Titanium press-fit tray implanted in human tibia: a zero-strain micro-CT and digital volume correlation analysis | **Lauren Wearne**

Biomechanical analysis of novel wrist implant | **Alastair Quinn**

Head excursion in high back booster seats is lower than in forward facing child seats with internal harness designed for children up to 8 years of age. | **Nicholas Kent**

Neck injury risk from head-first dives into trampoline dismount foam pits | **Tom Whyte**

Estimating cartilage contact mechanics and 3D joint space from radiographs informed by statistical shape models | **Mousa Kazemi**

Posters 4 | Chair: Dr Celeste Coltman

10:15am-
10:40am
AEDT

Effects of implant-bone contouring and screw configurations on stress distribution in temporomandibular implant | **Kwong Ming Tse**

The effect of speed on gait stability during load carriage | **L. Eduardo Cofré Lizama**

Determinants of throwing speed in elite male cricketers | **Alasdair Dempsey**

Sprint acceleration force-velocity profiles in track and field athletes with and without hamstring injury | **Lisa Wolski**

Objective assessment of fast bowling delivery intensity in amateur male cricketers | **Daniel Epifano**

Impact of foot-stretcher height on rowing performance: a nonlinear analysis | **Georgina Barratt**

The effect of different soccer shoe stud on traction ratio and running speed in turning movement | **Ferryanto Ferryanto**

15 min

Break

New Investigator Award | Chair: Prof Glen Lichtwark



Characterising the response of the human head during a simulated head-first impact | **Darcy Thompson-Bagshaw**

A new measurement and modelling approach to quantify occlusal loading across the dental arch | **Sarah Woodford**

The immediate effect of flat flexible vs stable supportive walking shoes on tibiofemoral joint contact force in people with varus-malaligned medial knee osteoarthritis | **Mr Scott Starkey**

Human passive neck stiffness and range of motion | **Mingyue Liu**

Relationships between tibial cartilage thickness and subchondral bone in osteoarthritis and controls | **Sophie Rapagna**

10 min

Break

PODIUM 6 | Chair: Dr Ryan Quarrington

Reconstruction of human subscapularis muscle architecture in vivo using diffusion tensor imaging | **Yilan Zhang**

Internal microstructural deformation of the tibial plateau under loading | **Kieran Bennett**

Deep learning methods for automated measurement of lower leg muscle volumes from MRI scans of children with and without cerebral palsy | **Bart Bolsterlee**

Shape differences in the semitendinosus following tendon harvesting for anterior cruciate ligament reconstruction | **William du Moulin**

Effect of upper airway fat on tongue inspiratory movement in awake people with obstructive sleep apnea | **Lauriane Juge**

Gluteal muscle atrophy in individuals with hip osteoarthritis and its effect on estimations of maximum isometric muscle forces | **Mohammad Mangi**

12:05pm - 1:06pm AEDT

1:06pm-2:20pm AEDT

Lunch + ANZSB AGM

all ANZSB members invited



PODIUM 7 | Chair: Dr Karen Mickle

Patient-reported outcomes and gait function in patients following primary and revision total hip arthroplasty: a 1-year follow-up study | **Harvey Chai**

Changes in post-operative lower limb biomechanics after femoral nailing of proximal femur fractures | **Arjun Sivakumar**

Accuracy and functional outcomes of virtual surgical planning and surgical guides for juvenile proximal femoral osteotomies | **Christopher Carty**

Differences of passive knee kinematics between males and females | **Francesca Bucci**

Finite element analysis of a 3D-printed scapholunate ligament under physiological conditions | **David John Saxby**

Simulating the effect of glenohumeral capsulorrhaphy on kinematics and muscle function | **Aaron Fox**

2:20pm-3:20pm AEDT

10 min Break

PODIUM 8 | Chair: Dr Taylor Dick

**3:30pm-
4:30pm
AEDT**

Plantar aponeurosis stiffness is related to more than just the shape of the medial longitudinal arch | **Robert Schuster**

Changes in lower limb bone measurements with growth including sex differences and measurement predictions | **Laura Carman**

In silico experiments identify the neuromechanical aetiology of idiopathic toe walking | **Kirsten Veerkamp**

Deep hip muscles can change the direction of hip loading | **Evy Meinders**

Statistical simulation of shoulder kinematics: a monte carlo approach | **Maxence Lavaill**

Understanding geometric variation of the human tibia: a public dataset of tibial surface meshes and statistical shape model | **Meghan Keast**

15 min Break

PODIUM 9 | Chair: A/Prof Saulo Martelli

**4:45pm-
5:25pm
AEDT**

Augmented respiratory mechanics during enhanced force production in trained martial arts practitioners | **Sherrilyn Walters**

Phase offset between arterial pulsations and subarachnoid space pressure fluctuations are unlikely to drive periarterial cerebrospinal fluid flow | **Adam Martinac**

A coupled biomechanical-sph model to investigate emptying of solid-liquid content from the stomach | **Shouryadiptha Ghosh**

Patient-specific radiocephalic arteriovenous fistula models for surgical training and flow visualisation | **Pujith Vijayaratham**

15 min Break

**5:40pm-
6:00pm
AEDT**

**President's Closing Address | Prof Peter Pivonka,
Award Announcement | Panel**



Should you have any questions regarding the program please contact abc12@jtproductionmanagement.com



ABSTRACTS



DAY 1

KEYNOTE 1 – Prof Silvia Blemker
University of Virginia, USA

PUSHING THE BOUNDARIES OF MUSCLE MODELING: EXAMPLES IN VOLUMETRIC MUSCLE LOSS INJURY

¹Blemker S.S.

**¹Biomedical Engineering, Mechanical & Aerospace Engineering, Ophthalmology, and
Orthopedic Surgery, University of Virginia**

Skeletal muscles are extraordinarily adapted motors that enable us to perform many important functions, from walking to sight to speech. The field of muscle modeling has benefited from several scientific discoveries related the fundamental mechanics of skeletal muscle; and therefore, muscle models are used in a wide variety of settings to understand muscle function in movement. However, current muscle modeling formulations are not capable of predicting several important behaviors of muscle, such as how muscle force is impacted by injury or how muscle regenerates from injury. The goal of the Multi-Scale Muscle Mechanophysiology (“M3”) Lab’s research is to develop and experimentally validate multi-scale computational modeling and experimental techniques of that allow us to relate structure, biology, and function of skeletal muscle across a range of scales, in order to push the boundaries of muscle modeling. We aim apply these models to answering questions related to the role of complex muscle biology and mechanics in a variety of clinical problems, including muscular dystrophy, speech disorders, vision impairments, and muscle injury. In this presentation, I will describe these approaches, present some recent examples of how computational models of muscle have led to new ideas and insights into volumetric muscle loss injury.



DAY 1

Podium 1

AUTOMATICALLY IDENTIFYING INFANTS AT HIGH-RISK OF CEREBRAL PALSY FROM SMART-PHONE VIDEOS

Passmore, E.; Kwong, A.; Greenstein, S.; Olsen, J.; Eeles, A.; Cheong, J.; Spittle, A.; Ball, G.
Murdoch Children's Research Institute, Parkville VIC, Australia; Royal Children's Hospital,
Parkville VIC, Australia; University of Melbourne, Parkville VIC, Australia; Royal
Women's Hospital, Parkville VIC, Australia.

INTRODUCTION

Cerebral palsy (CP) is the most common childhood disability, occurring at a rate of 2/1000 live births. Intervention in early life when the brain is highly plastic has the greatest effect on outcomes. In Australia, the average age of diagnosis is 19 months. Early diagnosis is essential to ensure targeted early intervention. The General Movements Assessment (GMA) is a good predictor of neurodevelopment. The assessment requires observation of the infant lying on their back and grading of movements by a trained assessor, performed at 3 months of age. However, access to trained GMA assessors is a limiting factor. Recent advances in deep learning image analysis have made video-based pose estimation feasible. Our aim was to determine if GMA ratings could be predicted from infant movement data obtained via automated video-based tracking.

METHOD

We analysed a dataset of 505 smart-phone videos from 327 unique infants acquired between 12 and 14 weeks corrected age through the Baby Moves app¹. The dataset consisted of 158 extremely premature infants (<28weeks) and 169 term controls (>37weeks).

We used the DeepLabCut toolbox² to train a deep learning model to label 18 key-points in video images of infants (Figure 1). The training set consisted of 100 videos where 5 frames were manually labelled. Model accuracy was evaluated by calculating the difference human labelling and computer model estimates of key-points. The computer model was then used to track movement across all frames in all videos. Twenty-one videos were excluded from further analysis as key-point labelling was less than 70% on average.

For the remaining 484 videos, key-point trajectories were processed to remove outliers, adjustment for camera movement and normalised by time and infant size for remaining 484 videos. Data dimensionality was reduced using principal component analysis (PCA). A classifier was built to predict the GMA (normal vs absent/abnormal). A series of timeseries features were extracted from a set of principal movement patterns

derived from the PCA. For each movement in each infant, this consisted of measures of frequency, variance and forecastability. These features served as inputs to a classifier using a regularised logistic regression model tuned using nested 5-fold cross-validation. Model performance was validated using a held-out, unseen dataset consisting of 33% of the data (161 videos). Due to the unbalanced ratio of normal and abnormal cases (n=426 vs 58), balanced accuracy is reported as a measure of classification accuracy.

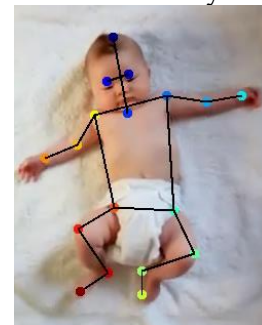


Figure 1. Infant with 18 key points labelled.

RESULTS

Human vs computer model labelling of key-points in the training dataset had an average difference of 1.7 (SD:2.5) pixels. During training, the classifier achieved a balanced accuracy of 59±9% (averaged over five cross-validation folds). When the classifier was trained on the entire training dataset (327 videos) the classifier achieved a balanced accuracy of 72% for the unseen validation dataset, identifying 14 out of 19 (74%) abnormal cases.

CONCLUSIONS

We demonstrate the ability of deep learning approaches to predict the General Movements Assessment using video data acquired outside a laboratory setting. This paves the way for automated approaches to screen for cerebral palsy at a population level.

REFERENCES

1. Spittle, A.J. et al., BMJ Open. 6(10), e013446, 2016.
2. Mathis, A. et al., Nat Neurosci. 21(9), 1281-1289, 2018.

Presented by Elyse Passmore

(elyse.passmore@rch.org.au).

SQUATTING BIOMECHANICS FOLLOWING TREATMENT FOR FEMOROACETABULAR IMPINGEMENT SYNDROME: HIP ARTHROSCOPY VS CONSERVATIVE CARE

Grant TM¹, Diamond LE¹, Pizzolato C¹, Savage TN^{1,2}, Lloyd DG¹, Hunter DJ², Bennell KL³, Hall M³, Saxby DJ¹

¹Griffith Centre of Biomedical and Rehabilitation Engineering (GCORE), Griffith University, Australia

²Kolling Institute of Medical Research, Institute of Bone and Joint Research, The University of Sydney, Australia

³Centre for Health, Exercise & Sports Medicine, Department of Physiotherapy, The University of Melbourne, Australia

INTRODUCTION

Femoroacetabular impingement syndrome (FAIS) is a hip disorder where asphericity of the femoral head/neck and/or acetabulum over-coverage lead to hip pain, which is exacerbated by repetitive or sustained hip flexion (e.g. squatting) [1]. FAIS is associated with hip osteoarthritis onset [2], and is commonly treated with hip arthroscopy, which addresses the osseous deformities, and physiotherapist-led conservative care, which targets neuromuscular deficits and activity modification. We compared trunk, pelvis, and hip angles, as well as hip moments, during a deep squat task before and 12-months following hip arthroscopy or physiotherapist care for FAIS.

METHOD

The Australian FASHIoN Trial recruited 140 participants from waiting lists for arthroscopic treatment of FAIS, and a subset (n=39) underwent biomechanical analysis. Participants were randomly assigned to hip arthroscopy (n=18) or 12 weeks of conservative care (Personalised Hip Therapy, PHT; n=21) [3]. Three-dimensional body motion and ground reaction forces were measured before treatment (baseline) and at 12-months (follow-up) during four deep squat trials. Inverse kinematics and dynamics were performed in OpenSim [4]. Trunk, pelvis, and hip angles (°), and external hip moments (Nm·kg/bodyweight·height[%]), were compared between baseline and follow-up and between treatment groups using a two-way repeated measures analysis of variance via statistical parametric mapping (p<0.05).

RESULTS

We observed no differences in treatment effects for any biomechanical variables during squatting. Compared to baseline, both hip arthroscopy and PHT groups increased squat depth (mean difference (MD): 26% leg length, [95% confidence interval (CI): 31.4, 20.6]%, p<0.001), and exhibited increased external rotation during squat descent (MD 8.7°, [95%CI 4.7,12.8]°, p<0.01) and ascent (MD 8.3°, [95%CI 4.5, 12.1]°, p<0.01) (Figure 1).

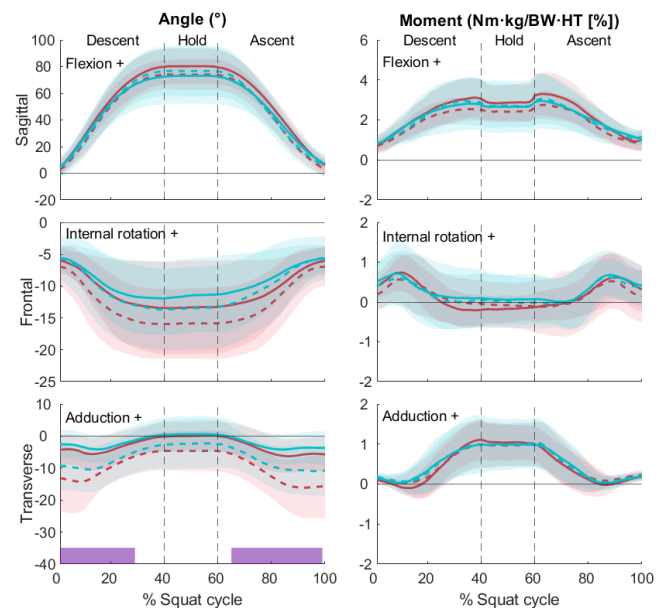


Figure 1. Ensemble average (± 1 standard deviation) hip angles (°) and moments (Nm·kg/BW·HT [%]) for hip arthroscopy (red) and Personalised Hip Therapy (blue) at baseline (solid) and follow-up (dashed). Purple bar: significant differences between baseline and follow-up for both treatment groups (p<0.05). Dashed lines: start/end hold. BW – bodyweight, HT – height.

CONCLUSIONS

Effects of hip arthroscopy and PHT on squatting biomechanics did not differ in participants with FAIS. However, participants in both groups squatted with increased external rotation and to a greater squat depth. Chondrolabral damage is often located anterosuperiorly in FAIS patients, and increased external rotation during squatting may reduce anterior hip loading [5], potentially altering local cartilage stresses at the hip. However, the effects of the observed kinematic changes on internal joint loading require further investigation.

REFERENCES

- [1] Griffin DR. BJSM, 50, 1169-1176, 2016.
- [2] Ganz R. Clin Orthop Relat Res, 112-120, 2003.
- [3] Murphy NJ. BMC Musculoskelet Disord, 406, 2017.
- [4] Delp, SL. IEEE Trans Biomed Eng, 1940-1950, 2007.
- [5] Tateuchi, H. J Sports Sci, 1-9, 2021.

Presented by Tamara Grant (tamara.grant@griffithuni.edu.au).

FEASIBILITY OF PERSONALISED HIP LOAD MODIFICATION USING REAL-TIME BIOFEEDBACK IN HIP OSTEOARTHRITIS: A PILOT STUDY

Laura Diamond^{1,2}, Daniel Devaprakash^{1,2}, Bradley Cornish², Melanie Plinsinga², Andrea Hams^{1,2}, Michelle Hall³, Rana Hinman³, Claudio Pizzolato^{1,2}, David Saxby^{1,2}

¹Griffith Centre of Biomedical and Rehabilitation Engineering (GCORE), Griffith University, QLD, Australia

²School of Health Sciences & Social Work, Griffith University, QLD, Australia

³Centre for Health, Exercise and Sports Medicine, University of Melbourne, VIC, Australia

INTRODUCTION

Conservative non-drug treatments are recommended for management of hip osteoarthritis (OA), though many patients report small-to-modest improvements in symptoms. These poor outcomes may exist because targets for treatment are not well defined, not personalised, and largely extrapolated from knee OA literature. Mechanical loading plays a fundamental role in OA worsening [1] and is potentially modifiable with movement retraining. Lower hip loads have been implicated in the pathogenesis of hip OA [2] and may have consequences for symptoms and cartilage health. This pilot study aimed to determine: 1) whether hip contact force could be increased by changing external biomechanical parameters with assistance from real-time visual biofeedback during walking; (2) associated changes in symptoms after 6-weeks of walking using a prescribed personalised load modification strategy.

METHODS

Eighteen participants with hip OA (age=60.8±6.3 yrs, BMI=30.0±4.1 kg.m⁻², 72% female) walked on an instrumented split-belt treadmill (Bertec, USA) while three-dimensional whole-body motion (Vicon, UK), ground reaction forces, and surface electromyography (EMG) (Cometa, ITA) of 12 lower limb muscles were synchronously recorded. Participants walked for 5-min at a self-selected speed (normal walk), then for 5-min under each of the following conditions: (i) neutral trunk lean (medial/lateral); (ii) neutral pelvic obliquity (rise/drop); and (iii) increased step length. The biomechanical parameter of interest and a corresponding target value were displayed via a bar chart in real-time. The personalised target was calculated from the normal walk condition and was set to increase peak hip contact force by ~5%. A decision tree, based on pain, confidence, and competence was used to assign one load modification strategy to each participant for integration into their walking routine over 6-weeks. Participants rated their hip pain during walking on a numerical rating scale (NRS, 0=none, 10=extreme) at baseline and 6-week follow-up. A calibrated EMG-assisted model [2] was used to estimate hip contact forces across 6 gait cycles per

condition. Peak hip contact force change scores (load modification condition minus normal walk) were calculated for subgroups based on their prescribed personalised load modification strategy.

RESULTS

Thirteen (72%) participants immediately increased peak hip contact force >5% when using a prescribed personalised load modification strategy. On average, the neutral pelvis and increased step length subgroups increased peak hip contact force >10% (Fig 1). After 6-weeks, 77% of participants reported a clinically important improvement in hip pain (>1.8 NRS units).

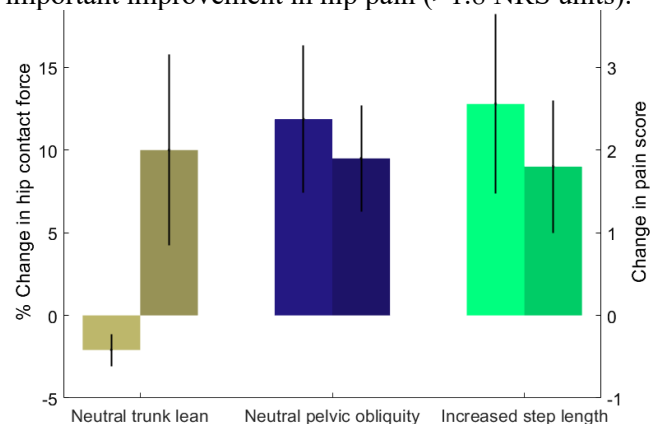


Fig 1. Immediate % change (±1 SE) in hip contact force relative to normal walk (left) and change (±1 SE) in hip pain after 6-weeks (right) for subgroups (neutral trunk n=3; neutral pelvis n=5; step length n=10).

CONCLUSIONS

Most participants with hip OA could immediately increase their hip load through personalised movement retraining by an amount expected to stimulate cartilage health and reported an improvement in hip pain after 6-weeks. The hip's load response to each modification was unique across participants, emphasising the need for personalised interventions to manage hip OA.

REFERENCES

1. Felson DT. OAC, 21:10, 2013.
2. Diamond LE et al. OAC, 28:921-931, 2020.

SPEAKER INFORMATION

Laura Diamond l.diamond@griffith.edu.au

HIP CONTACT FORCES DURING SPRINTING IN FEMOROACETABULAR IMPINGEMENT SYNDROME AND ASYMPTOMATIC CAM MORPHOLOGY

Basilio AM Goncalves¹, Evy Meinders¹, David J Saxby¹, Rod S Barrett¹, Laura E Diamond¹

¹Griffith Centre of Biomedical and Rehabilitation Engineering, Griffith University, Gold Coast, Australia

INTRODUCTION

Asphericity of the femoral head/neck junction, i.e. cam morphology, is a common imaging finding in active individuals [1]. During activities involving repetitive hip flexion and high impact loading, like sprinting, cam morphology can lead to hip pain and femoroacetabular impingement syndrome (FAIS) [1]. However, it is unclear why many athletes with cam morphology remain asymptomatic despite frequent participation in high impact activities [2]. This study aimed to compare the magnitude of hip contact force (HCF) during sprinting between individuals with FAIS, asymptomatic cam morphology (CAM), and healthy controls without symptoms or cam morphology (control).

METHODS

Participants (n=47) were divided into three groups (FAIS, n=14; CAM, n=15; control, n=17) based on hip symptoms, clinical presentation, and alpha angle (FAIS and CAM groups >55°; control group <55°). Three-dimensional motion capture, ground reaction forces, and electromyograms (EMG) from 12 lower limb muscles were recorded during two 10-metre overground sprints. Hip angles, hip moments, and moment arms from 40 muscle-tendon units (MTU) were estimated using linearly scaled musculoskeletal models in OpenSim [3]. A calibrated EMG-assisted neuromusculoskeletal model [4] was used to simulate musculotendon dynamics and estimate individual

MTU forces which were used to calculate HCF in OpenSim. The resultant and component HCF magnitudes (normalised to body weight, BW) were compared between groups using statistical parametric mapping. Peak HCF during stance and swing were compared between groups using a one-way analysis of variance ($p < 0.05$).

RESULTS

There were no between-group differences in running speed (5.6-5.8 m/s) or resultant HCF magnitude, but peak anterior HCF was lower during swing in FAIS compared to control (mean difference -1.34 [95%CI= -0.17 to -2.67] BW) (Figure 1). No other between-group differences in peak HCF were observed between any groups during either stance or swing.

CONCLUSIONS

Individuals with FAIS sprint with lower peak anterior HCF than individuals who are asymptomatic and have no cam morphology. This difference may represent a pain avoidance mechanism to minimise contact stresses characteristic of cam morphology [5].

REFERENCES

- [1] Frank Arthroscopy, 31, 1199-1204, 2015
- [2] van Klij Scand J Med Sci Sports, 30, 1221-31, 2020
- [3] Rajagopal IEEE Trans Biomed Eng 63,2068-79,2016
- [4] Pizzolato J Biomech 48, 3929-36, 2015
- [5] Ng, Clin Orthop Relat Res 477, 1053-63, 2019

Presented by Evy Meinders (evy.meinders@griffithuni.edu.au)

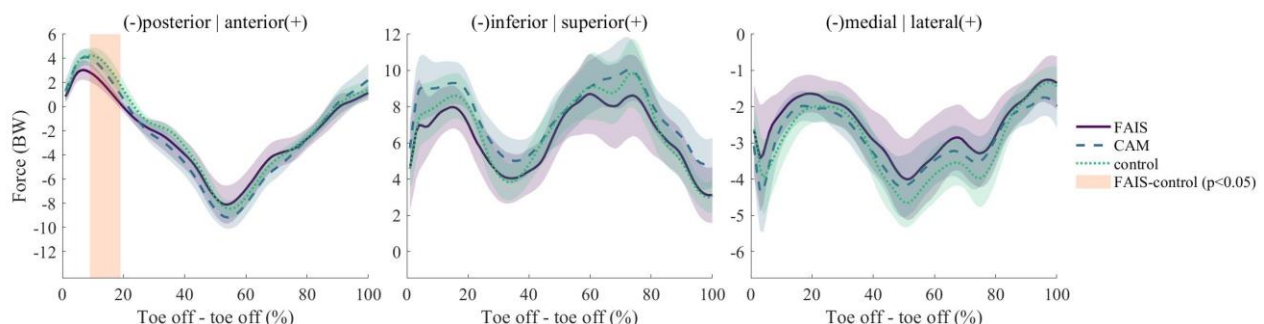


Figure 1. Ensemble averages ($\pm 95\%$ confidence intervals) of hip contact force components during a 10-metre sprint for individuals with femoroacetabular impingement syndrome (FAIS, solid), asymptomatic cam morphology (CAM, dashed), and asymptomatic individuals without cam morphology (control, dotted). Orange shade represents significant difference between FAIS and control ($p < 0.05$).

DIFFERENCES IN IMPACT AND PROPULSION BETWEEN MILITARY BOOTS AND SPORTS SHOES

Bini1, R.R.; Muniz2, A.

1 La Trobe Rural Health School, Bendigo, Australia; 2 School of Physical Education of the Brazilian Army, Rio de Janeiro, Brazil.

INTRODUCTION

Military boots have been designed with a stiff midsole and a long shaft to protect the foot and ankle from acute injuries (i.e. punctures, sprains, etc.). Moreover, stiffer midsoles apparently reduce impact during foot strike when walking compared to a softer midsole (Muniz and Bini 2017). However, the use of composite materials (mix of soft and stiff) has not been explored. In addition, implications of stiff midsole have not been assessed in terms of forces at toe-off, which can contribute to metatarsophalangeal pain and injuries (Knapik et al. 2015).

This study compared impact and propulsive outcomes from ground reaction force (GRF) during walking in military soldiers using combat boots and two types of sports shoes with different midsole structures. The comparison of boots and one sport shoe with the same midsole will provide clarity on implications from the long shaft in propulsive forces during gait.

METHOD

Ten army recruits walked over an 11-m wooden walkway with two force plates embedded (FP4060-10, Bertec Corporation, USA) at the centre of the walkway. They performed 10 trials at controlled velocity walking barefoot (used for data normalization), using combat boots (styrene-butadiene rubber; SBR midsole – 65 Shore A), wearing a military sport shoe (styrene-butadiene rubber; SBR midsole – 65 Shore A) and using a commercial sports shoe (Prorunner 17, Mizuno; 30% EVA – 45 Shore A), in random order. Study methods were approved by a local ethics committee and participants provided informed consent.

Loading rate, first and second peak forces and push-off rate of force were computed from vertical GRF and normalized by values obtained during the barefoot trials. Data were represented as a percentage of barefoot trials. One-way ANOVAs were utilized followed by post-hoc analyses to determine differences between footwear. Cohen's d were calculated to determine practically important differences, which were discussed when $p < 0.05$ and $d > 0.80$.

RESULTS

Reduced loading rate was observed for the running shoe compared to the combat boot ($p = 0.02$ and $d = 0.98$) and to the military sports shoe ($p = 0.04$ and $d = 0.92$). The running shoe elicited a smaller second peak force than the combat boot ($p < 0.01$ and $d = 0.83$). These results are illustrated in Table 1.

Table 2. mean (SD) gait speed, loading rate, first and second peak forces and push-off rate of force for walking trials with combat boot, military sports shoe and running shoes.

	Combat boot	Military shoe	Sport shoe
Loading rate (%) barefoot)	19 ±3	20 ±5	16 ±2* [#]
1 st peak force (%) barefoot)	106 ±3	105 ±3	105 ±3
2 nd peak force (%) barefoot)	104 ±1	101 ±2	101 ±1*
Push-off rate of force (%) barefoot)	90 ±12	83 ±11	86 ±10

* Indicates difference to combat boot and [#] Indicates difference to military sports shoe when $p < 0.05$ and $d > 0.80$.

CONCLUSIONS

Military shoes elicited larger force at foot strike than running shoes potentially because of the harder material used in midsole composition (i.e. SBR). Walking with combat boots required larger peak force at toe-off (i.e. 2nd peak) compared to shoes with same midsole potentially due to limited ankle range of motion. These results could lead to possible metatarsophalangeal pain and injuries while walking in combat boots with stiff midsole compared to traditional running shoes.

REFERENCES

- Muniz, A. Gait Post 58, 59-65, 2017.
- Knapik, J. Mil. Med. 180, 321-328, 2015.

Presented by Rodrigo Bini (r.bini@latrobe.edu.au).

DO CLINICIANS WANT BIOMECHANICAL SOLUTIONS TO HELP TREAT SHOULDER INJURY AND PATHOLOGY? A SURVEY-BASED STUDY

Fox, A.S.; Bonacci, J.; Gill, S.D.; Page, R.S.

Deakin University, Geelong, Australia; Barwon Health, Geelong, Australia.

INTRODUCTION

Biomechanical technologies allow assessment of human movement, muscle function and tissue loading – yet there are implementation challenges and lack of adoption in clinical practice (Smith et al. 2021). Perceived ease of use and usefulness are key factors that underpin acceptance (Davis et al. 1989). We assessed the perspectives of clinicians on biomechanical measures and technologies in evaluating patients with shoulder injury and pathology.

METHOD

We developed an online survey and invited clinicians currently treating individuals with shoulder injury, pain or disability to respond. Respondents provided demographic information and details on the conditions/patients they treat. Respondents were received descriptions of biomechanical measurements (i.e. joint kinematics; global arc of movement; muscle strength; range of motion; muscle activation and forces; tissue strain and stress; joint reaction forces) and technologies (i.e. inertial sensors; surface electromyography; video analysis; motion capture) in a randomised order and asked if they agreed (scale of strongly disagree; disagree; agree; strongly agree) it would be useful for evaluating shoulder function in their clinical setting. If they agreed they were asked to rate the priority of access to the measure/technology on a scale of 1 (low) to 10 (high). Respondents also estimated the set-up time and purchase cost they felt was appropriate for using such equipment. Responses

were included if they contained a response for at least one measure/technology. Descriptive statistics on each question were calculated across responses.

RESULTS

71 responses were obtained for analysis. Table 1 provides descriptive statistics on the rates of agreement for each measure and technology, alongside the priority rating from those who selected an agreeable response. Respondents ($n = 49$) indicated a set-up time of 7.41 minutes [5.52,9.30] and cost of 1,750AUD [1178,2323] for equipment use in the clinic (mean [$\pm 95\%$ CIs]).

CONCLUSIONS

Clinicians were most agreeable to more simplistic measures (i.e. muscle strength, range of motion) to assist with treating shoulder injury and pathology. There was mixed agreement on equipment use, but preferences for fast set-up (i.e. < 10 minutes) and low-cost (i.e. < 2,000AUD) solutions. Biomechanists should embrace these needs to promote clinical uptake. The outputs of more complex approaches may need to be simplified, and the benefits clearly articulated.

REFERENCES

- Davis, F.D. et al., Management Sci, 35: 982-1003, 1989.
Smith, H.L. et al., Clin Biomech, 83: 105292, 2021.

Presented by Aaron Fox (aaron.f@deakin.edu.au).

Table 1. Descriptive statistics for each measure and technology (ordered from highest to lowest priority).

	Strongly Disagree % (n)	Disagree % (n)	Agree % (n)	Strongly Agree % (n)	Priority Rating (/10) mean \pm 95%CI
Measure					
Range of Motion	1.7% (1)	1.7% (1)	28.3% (17)	68.3% (41)	8.63 \pm 0.41
Muscle Strength	0.0% (0)	1.6% (1)	39.3% (24)	59.0% (36)	7.98 \pm 0.51
Joint Kinematics	5.2% (3)	34.5% (20)	44.8% (26)	15.5% (9)	6.63 \pm 0.64
Muscle Act./Forces	5.0% (3)	26.7% (16)	56.7% (34)	11.7% (7)	6.15 \pm 0.56
Joint Reaction Forces	7.1% (4)	50.0% (28)	33.9% (19)	8.9% (5)	6.00 \pm 0.76
Tissue Stress/Strain	8.6% (5)	34.5% (20)	43.1% (25)	13.8% (8)	5.88 \pm 0.61
GAM	7.0% (4)	29.8% (17)	50.9% (29)	12.3% (7)	5.73 \pm 0.84
Technology					
Inertial Sensors	6.2% (3)	37.5% (18)	41.7% (20)	14.6% (7)	6.26 \pm 0.62
Video Analysis	0.0% (0)	27.1% (13)	54.2% (26)	18.8% (9)	5.54 \pm 0.78
Motion Capture	10.4% (5)	39.6% (19)	41.7% (20)	8.3% (4)	5.17 \pm 0.75
Electromyography	14.3% (7)	46.9% (23)	34.7% (17)	4.1% (2)	5.11 \pm 0.74

GAM – global arc of movement; Act. – activation; CI – confidence interval



DAY 1

Podium 2

HIP CONTACT FORCES CAN BE PREDICTED IN REAL-TIME USING A LONG SHORT-TERM MEMORY NEURAL NETWORK

Bradley Cornish¹, David John Saxby¹, Claudio Pizzolato¹, Daniel Devaprakash¹, Laura Diamond¹

¹Griffith Centre of Biomedical and Rehabilitation Engineering (GCORE), Griffith University, QLD, Australia

INTRODUCTION

Analysis of movement kinematics, kinetics, muscle forces, and joint contact forces is important for clinical and rehabilitation research. Such analyses have been largely confined to laboratories with state-of-the-art equipment and software. To improve treatment options for musculoskeletal and orthopaedic conditions, we must develop technologies that are simple to use, affordable, accessible, and robust in real-world environments [1]. The rise of wearable technologies such as inertial measurement units (IMU) has facilitated research outside the laboratory, and when combined with machine learning methods, can predict joint angles, moments, and ground reaction forces [2]. Gait retraining has been proposed as a management strategy to modify hip contact forces in individuals with hip osteoarthritis (OA) [3], but to be effective, it must happen in the real-world. To date, no studies have achieved real-time predictions of hip contact forces in the real-world. This study aimed to determine if a recurrent neural network could accurately predict hip contact forces, in real-time, from data obtainable from IMU and electromyography (EMG).

METHOD

Optical motion capture (Vicon, UK), ground reaction forces from a split-belt instrumented treadmill (Bertec Corporation, USA), and EMG from 12 lower-limb muscles (Cometa, ITA) were recorded from 18 participants with hip OA. For each participant, 99 ± 57 s of continuous self-paced walking was used. A calibrated EMG-assisted model (CEINMS) [4] was used to estimate hip contact forces of the affected hip and then to train and validate an artificial neural network. OpenSim body kinematics analysis tool was used to determine segment orientation, velocity, and acceleration for pelvis, thigh, and tibia at each frame. The EMG data were filtered (30-300 Hz band-pass, 6 Hz low-pass), down-sampled, and combined with segment kinematics, participant height and mass for neural network training (TensorFlow 2.3, python library). Data were segmented into 10-frame overlapping windows and used in a long short-term memory (LSTM) recurrent neural network. The network consisted of 1 bi-directional LSTM layer and 3 fully connected layers. Hyperparameters were tuned using hyperband optimisation. Leave-one-out cross-validation was used to assess prediction accuracy using coefficient

of determination (R^2) and root mean square error (RMSE). Bland-Altman analysis was used to evaluate agreement between CEINMS and LSTM peak hip contact force predictions.

PRELIMINARY RESULTS

The LSTM predicted hip contact forces had mean R^2 and RMSE of 0.84 (0.12) and 0.26 (0.10), respectively, for 51 stance phases of a single participant. Bland-Altman analysis showed minimal bias (0.02 BW) and agreement limits of -0.32 and 0.37 BW.

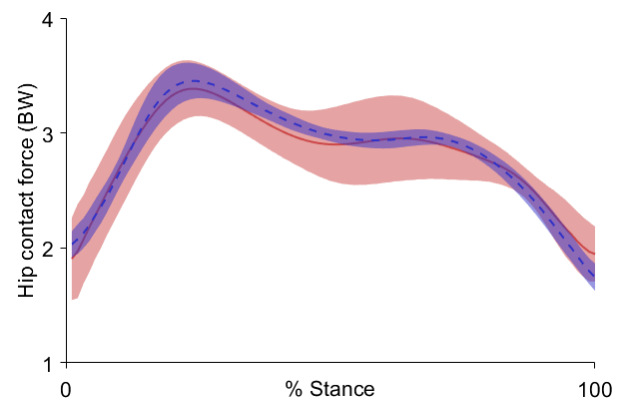


Figure 1. Hip contact force (± 1 standard deviation) predicted from EMG-assisted model (solid red line) and LSTM neural network (dashed blue line) for 51 stance phases from 1 participant.

CONCLUSIONS

A LSTM neural network can accurately predict hip contact forces during gait in real-time in people with hip OA, using segment kinematics and EMG. Future work will apply LSTM to remaining participants and validate this model using IMU and EMG embedded into wearable technology for management of hip OA.

REFERENCES

1. Saxby et al. Biomech Model Mechanobiol, <https://doi.org/10.1007/s10237-020-01367-8>, 2020
2. Gurchiek RD et al. Sensors, 10.3390/s19235227, 2019.
3. Diamond LE et al. OAC, 28:921-931, 2020.
4. Pizzolato C et al. JBiomech, 48(14):3929-3936, 2015

SPEAKER INFORMATION

Bradley Cornish (bradley.cornish@griffithuni.edu.au)

TASK-SPECIFIC DEVICE USE IN PAEDIATRIC PROSTHESIS USERS

Eveld, M.E.¹; Wolfe, A.E.¹; Cruz, J.P.¹; Sifuentes, N.J.¹; Ausec, B.N.¹; Zelik, K.E.¹; McDonald, K.A.^{1,2}

¹Vanderbilt University, TN, US; ²University of New South Wales, NSW, Australia

INTRODUCTION

Australian paediatric prosthesis users often have access to both a Daily-Use Prosthesis (DUP) and a Running-Specific Prosthesis (RSP). However, younger children engage in many spontaneous bouts of running throughout the day [1], and changing between a DUP and RSP is both time-consuming and physically demanding. Thus, children with lower limb loss are likely to select one device type and spend most of their day in it. It has been suggested that poor joint loading symmetry can lead to joint degeneration in adult prosthesis users [2], [3]; however, knowledge gaps pertaining to user experience and the musculoskeletal loading effects of non-task-specific device use remain unaddressed for the paediatric population. The objective of this work is to evaluate paediatric prosthesis user satisfaction and ground reaction force (GRF) symmetry for task-specific (e.g., DUP for walking, RSP for running) and non-task-specific (e.g., RSP for walking, DUP for running) device use.

METHOD

Children with varying degrees of unilateral and bilateral lower limb loss ($N=10$) aged between 7-18 years old participated in this study. Informed consent was provided by parents/guardians and their child. For this investigation, a subset of participants with unilateral, below-knee limb loss ($N=3$; 2M, 1F, age: 16, 11, 15 years) who wear the same RSP (Fillauer Blaze) were analysed to minimize effects of prosthesis type, age, and amputation level. First, participants were asked to rank their satisfaction when using their DUP for walking and running. This process was repeated for the RSP. A five-point scale with the options “very bad” (1) to “very good” (5) was used. Second, participants walked (1.0 m s^{-1}) and ran (2.6 m s^{-1}) on an instrumented, split-belt treadmill (Bertec) while GRF and synchronised 3D motion capture data (Vicon) were collected. Peak GRFs were extracted for ~20 strides per trial and averaged for each participant.

RESULTS

Each participant’s satisfaction rankings (top), and peak vertical GRF (prosthetic and intact limbs; bottom) during walking and running in both a DUP and RSP are shown in Figure 1. For brevity only vertical GRFs are presented. *Walking*: 2/3 participants were more

satisfied with a DUP for walking and walking in a DUP (task-specific device use) resulted in more symmetric GRFs for 3/3 participants. *Running*: 3/3 participants were more satisfied with an RSP for running, while running in an RSP (task-specific device use) resulted in less symmetric GRFs for 2/3 participants.

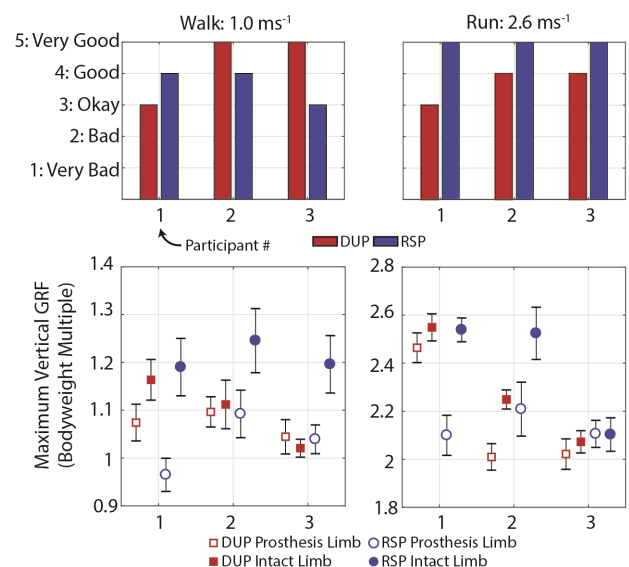


Figure 1. User preference and GRF outcomes.

CONCLUSIONS

Overall, task-specific prosthesis use resulted in improved user satisfaction but did not consistently improve peak vertical GRF symmetry. Walking in a task-specific prosthesis (DUP) resulted in better vertical GRF symmetry and user preference versus an RSP, suggesting that wearing an RSP may not be ideal for all-day use from a musculoskeletal health or user satisfaction standpoint. However, while running in an RSP was unanimously preferred over a DUP, limb loading symmetry decreased for 2/3 participants. Future work will investigate other biomechanical outcome metrics (e.g., joint work) to further investigate task-specific prosthesis use during running.

REFERENCES

- [1] Kerfeld, C. Pros. Orth. Int. 42, 437-45, 2018.
- [2] Gailey, R. J. Rehab. R&D. 45, 15-30, 2008.
- [3] Sepp, L. J. Biomech. 101, 109629, 2020.

Presented by Kirsty McDonald (kirsty.mcdonald@unsw.edu.au).

SIMULATION AND DESIGN FOR INDIRECT SENSING AND MAPPING OF DEEP MUSCLE ACTIVITY USING ELECTRIC FIELD

Alipour1, M.: Anand2, G.: Besier1, T.: Lowe2, A.

1Auckland Bioengineering Institute, the University of Auckland, New Zealand

2Institute of Biomedical Technologies, Auckland University of Technology, New Zealand

INTRODUCTION

Traditional surface EMG sensors use contact-based electrodes to record underlying action potentials as they propagate to the skin. Existing EMG systems suffer several limitations: obtaining quality signals requires shaving and cleaning of the skin; electrodes must be firmly attached using a conductive gel that loses its elasticity and adherence in less than 24hrs; and surface electrodes cannot measure the activity of deep muscles.

In this study, we simulate a novel active capacitive EMG sensor to measure muscle activity that can work for extended periods without skin preparation or electrode gel. This novel approach uses a varying electric field (E-field) applied to the muscle via non-contact, flexible capacitive sensors and generated using a high frequency converter. The generated E-field is disturbed with muscle activation and the E-field and sensor design can be optimised to record activity deep within the muscle.

METHOD

We simulated an electrical field passing through a simplified, cylindrical limb representing layers of bone, deep muscle, superficial muscle, fat, and skin (Figure 1-A). The length of the model was 200mm. Ansys Electromagnetics (Maxwell) [1] was used to simulate and observe the electrical field distribution when a 1V potential difference was applied between the muscle cross-section of the model. To mimic voltage measurement at the skin's surface, two points were chosen along which the electric field gradient was calculated through the Ansys solver. The two electrode points were separated by 15mm. The model was setup with the default Neumann boundary conditions for Electrostatics solver in Ansys Maxwell.

The model was split up into two halves. The top half is to simulate excitation of the muscle domains. The analysis involved: 1. Excitation of superficial or deep muscle and measure the voltage response; and 2. Changing electrode locations angularly at 15° steps with respect to excitation to optimise electrode placement and orientation.

RESULTS

The measured potential difference due to top muscle activation was found to vary from 140 mV to 180 mV as the electrode location was varied angularly. The least was observed when the electrodes were the

farthest (180 degrees) whereas the maximum was observed in the case of the closest position (0 and 360 degrees) (Figure 1-B).

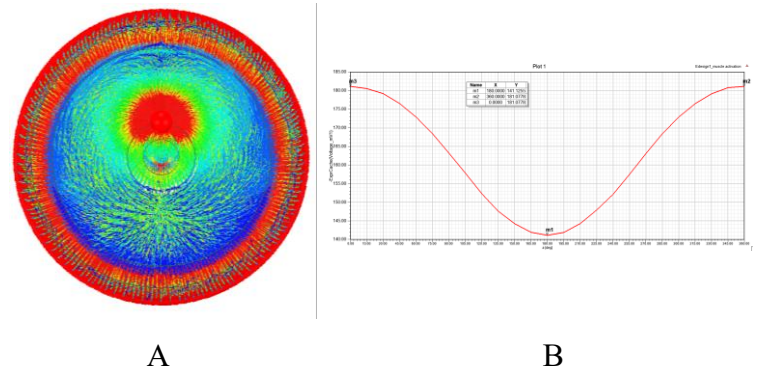


Figure 1-A: The output potential difference was measured along the line on the surface of the skin. Additionally, to mimic the varying location of the electrodes, the line was rotated along the surface of the skin with steps of 15 degrees.

Figure 1-B: Variation of surface voltage with changing angular position of electrodes.

CONCLUSIONS

This indicates that a muscle excitation of 1V resulted in the surface voltage measurement of 140 – 180 mV. While it remains to be verified using experimental design, this provides indication of the expected attenuation of the signal from the muscle as it is measured on the skin. Additionally, this is assuming no electrode-skin interfacial effects, which will come into play during capacitive sensing. To understand this, the next step will be phantom experimentation (initially with gel electrodes) to mimic the simulation setup and verify its response. Further iterations of phantom testing will involve employing capacitive electrodes in the same configuration as the gel electrodes to understand electrode-skin effects during non-contact sensing. Eventually, our simulation and phantom experimentation will lead to optimal design of electrodes for maximum sensitivity to deep muscle activity as well as measurement electronics to achieve a high SNR.

REFERENCES

[1] Martynov, A S., and Nikolay I. N. "ANSYS Maxwell Software for electromagnetic field calculations." (2014)

Presented by Massoud Alipour (m.alipour@auckland.ac.nz).

IN-VIVO KINEMATICS DURING STEP-UP AND DOWN IN THREE TOTAL KNEE REPLACEMENT DESIGNS: A RANDOMISED CLINICAL TRIAL

Lynch, JT¹; Perriman, DM¹; Scarvell, JM²; Pickering, MR³; Ripper, J¹; Galvin, CR¹; Smith, PN¹

¹Australian National University, Canberra

²University of Canberra, Canberra

³University of New South Wales at ADFA, Canberra.

INTRODUCTION

Modern total knee replacement prostheses are designed to reduce pain and restore kinematic function (1). However, randomised clinical trials are rarely conducted to control for bias in patient selection. Implant choice is guided by implant survival, surgeon preference and kinematic performance (2). However, the debate over which implant to use is still unresolved. Surgeons' choice of prosthesis typically does not have the benefit of the information from clinical trials. Therefore, this clinical trial aimed to prospectively compare outcomes, but also kinematics of three common designs: posterior-stabilised fixed-bearing (PS-FB), cruciate-retaining fixed-bearing (CR-FB) and cruciate-retaining rotating-platform (CR-RP) designs. Here we present kinematics of a step-up and step-down task.

METHOD

68 participants were randomised to receive either cruciate retaining (CR-FB), rotating platform (CR-RP) or posterior stabilised (PS-FB) knee prostheses. Image quality was sufficient for 49 of these patients to be included in the final analysis following a minimum 1-year follow-up. Patients completed a step-up and down task while being imaged using single-plane fluoroscopy. Femoral and tibial computer-aided design (CAD) models for each of the TKR designs were registered to the fluoroscopic images using bespoke software OrthoVis to generate six-degree-of-freedom kinematics. Differences in kinematics between design were compared as a function of flexion.

RESULTS

There were no differences in terminal extension or clinical outcomes (Oxford knee score, Pain or Satisfaction) between the groups. The CR-FB was further posterior and the CR-RP was more externally rotated at terminal extension compared to the other

designs (Table 1). Furthermore, the femoral component of CR-FB designs was more posteriorly positioned at each flexion angle compared to both CR-RP and PS-RB designs during both movements. Additionally, the CR-RP design had more external femoral rotation throughout flexion when compared with both fixed bearing designs. However, there were no differences in total rotation for either step-up. Visually, it appears there was substantial variability between participants in each group, indicating unique patient-specific movement patterns (Figure 1).

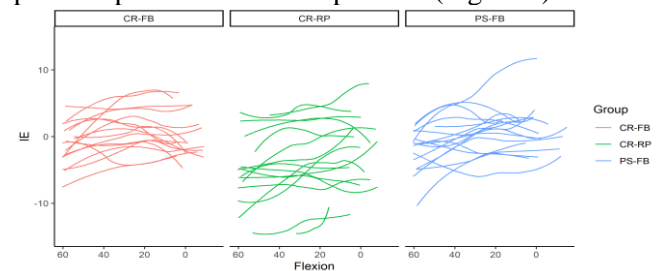


Figure 1. Individual kinematic curves for all three designs for internal- external rotation

CONCLUSIONS

This study found that CR-FB designs were more posterior across both movements compared the other designs, while CR-RP designs remained relatively more externally rotated than the fixed bearing designs. Although there were differences in step-up and down kinematics between designs, the inter-individual variation was high indicating that individual motor control factors are an important determinant of kinematic outcome.

REFERENCES

- [1] Lange T et al. J Arthroplasty 32(7):2093-2099. 2017
- [2] Vertullo CJ et al. J Arthroplasty 32:2980-2989. 2017

Presented by Joe Lynch (joseph.lynch@anu.edu.au).

Table 1: Kinematics at Terminal Extension

	Cruciate Retaining Fixed Bearing	Cruciate Retaining Rotating Platform	Posterior Stabilised Fixed Bearing
Anterior-Posterior(mm)	4.2 (2.6 to 5.8)	8.9 (7.3 to 10.5)#	8.6 (7.0 to 10.1) #
Abduction/Adduction (°)	0.9 (0.0 to 1.7)	1.1 (0.3 to 1.9)	0.2 (-0.6 to 1.0)
Internal External (°)	0.2 (-2.2 to 2.5)	-2.8 (-5.1 to -0.5) ¥	1.5 (-0.8 to 3.7)

FEMORAL MECHANICS USING IN-VITRO REAL-TIME REPLICATION OF PHYSIOLOGICAL LOADING CYCLES OF NORMAL WALKING

Hoang, H.X.¹; Martelli, S.^{1,2}

¹Queensland University of Technology, Brisbane, ²Australia, Flinders University, Adelaide, South Australia

INTRODUCTION

Understanding bone mechanical behaviour under real-world loading conditions is essential to prevent and treat bone fractures. In-vivo measurements of femur loading shows time-varying loads [1]. Bone is a complex composite material that exhibit rate dependent viscoelastic response [2]. Yet, current in-vitro femur mechanics studies evaluate the entire femora under quasi-static or impact loading [3]. The aim of this study was to measure in-vitro the dynamic force response of the human femur under the dynamic three-dimensional displacements experienced while walking using varying loading rates from quasi-static to real-time.

METHOD

Femurs from 8 healthy elderly white women were acquired from a body donation program (Science Care, Phoenix, USA). Each femur shaft was cut at 180mm from the proximal femoral head. Using dental cement, the femurs were placed 55mm deep in aluminium cups. Ten rosette strain gauges were attached at various locations on the femur to measure cortical strains. Strains were recorded at 2kHz using a data logger (National Instrument Corporation, Austin, TX, USA) and a 0.5V excitation of the strain gauge grid was used to prevent heating of the bone. A six-axis load cell (AMTI, Watertown, MA, USA) was used to measure the forces and moment at the femoral head centre. All tests were performed using a custom-built hexapod robot [4] which controlled the position of the top plate that the specimen was placed on. The average hip contact force profiles during walking were obtained from the Orthoload.com database [1] based off 25 measurements and 6 participants. The hip contact force profiles were scaled to 75% of each donor's body weight to prevent permanent damage to the femur. A load-control (LC) algorithm was used to apply the hip contact force profile for one gait cycle to each femur and the position of the top plate was recorded. The position of the top plate was then played back at increasing speeds to mimic stride duration of 12, 6, 2.4, and 1.2 sec (0.08, 0.16, 0.4 and 0.8 Hz). A trigger was used to synchronise the femur length (position of the top plate), force, and cortical strain.

RESULTS

The maximum change in femur length going from 0.08Hz to 0.8Hz was 0.019 ± 0.015 mm. The error of the hip contact force was 4.3 ± 15.1 N during LC. The average normalized force ranged from 1.01 to 1.15 going from 0.08 Hz to 0.8Hz (Figure 1.A). The increased in peak force had a linear relationship to the increase in speed with $R^2 = 0.89$ (Figure 1.B).

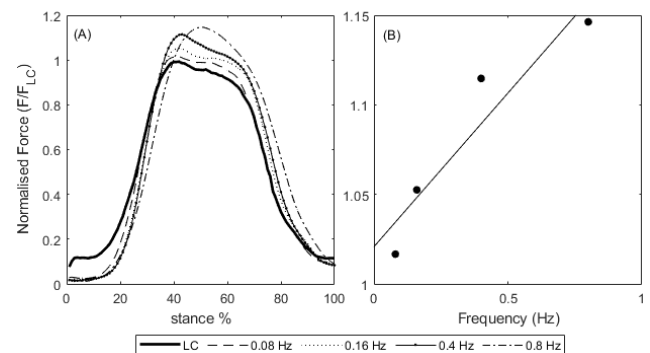


Figure 1. A) Ensemble average of the normalized hip force for the different loading rates during 1 gait cycle of walking; **B)** peak normalized force for the different load rates.

CONCLUSIONS

The protocol successfully reproduced three-dimensional hip forces during walking. Replicating real-time loading presents several difficulties due to the high dynamics of the system, which may require a lighter device and/or better control. The stiffness of the femur is load-rate dependent, and analysis of the cortical strain may provide more information on the relationship between femur stiffness and strain rate.

ACKNOWLEDGEMENTS

The authors would like to thank John Costi and Dhara Amin for the lab and driving the hexapod. Funding for this research was made possible by the Australian Research Council (DE140101530).

REFERENCES

- [1] G. Bergmann, et. al., PLOS ONE, 2016.
 - [2] N. Sasaki, et. al., J. Biomech., 1993.
 - [3] L. Cristofolini, et. al., Proc. Inst. Mech. Eng. [H], 2009.
 - [4] B. Ding, et. al., J. Dyn. Syst. Meas. Control, 2014.
- Presented by Hoa Hoang (hoa.hoang@qut.edu.au).

IMPROVING THE CONTROL OF A BRAIN-COMPUTER INTERFACE USING VIRTUAL REALITY TRAINING

Mannan, M.M.N.; Mulholland, K.; Lloyd, D.; Pizzolato, C.

Griffith Centre of Biomedical and Rehabilitation Engineering, Griffith University, Australia

INTRODUCTION

Brain-computer interfaces (BCIs) can be used in rehabilitation to supplement the lack of volitional motor control in neurologically impaired individuals. BCIs convert brain signals into commands to control external devices, like exoskeletons, without the participation of peripheral nerves and muscles [1]. As such, BCIs can be used to extend rehabilitation tools to all patients regardless of the severity of their injuries. BCIs commonly use electroencephalography (EEG) since it is non-invasive, portable, low cost, and has high temporal resolution, and because it is much less invasive and costly than electrode systems that are surgically implanted in the brain. Motor imagery (MI), the imagined movement of muscles without physical execution, can potentially produce appropriate BCI signals, but are seldom used outside of laboratories due to their unreliable performance and low classification accuracies. Indeed, using and controlling a BCI by efficiently modulating brain activity is a difficult skill to learn [2]. Combined MI-BCI and virtual reality (VR) experiments have recently shown improved engagement and motivation [3], but VR's impact of producing distinctly different MI and BCI control is still unknown. Therefore, this study investigated if a consumer-grade dry EEG system with a VR environment can be used to train naïve subjects (i.e., with no BCI experience) to improve their classification accuracies and BCI control with different MI.

METHOD

Three subjects (1 female) participated in 15 1-hour sessions of walking and relaxing MI-BCI to control ambulation of an avatar within a VR environment (Fig. 1). Each session began with a calibration phase, where participants underwent alternating periods of walking and relaxing MI with VR feedback while their EEG data were collected. In this they had first person view of their VR avatar walking during walking MI or no avatar walking during relaxing MI. Subsequently, a common spatial pattern algorithm was used to extract EEG features and train a linear discriminant analysis classifier. The training was followed by an online BCI evaluation, wherein subjects used walking and relaxing MI to control the avatar walking in the VR environment. All data collection and processing were implemented in the robot operating system and python.

Calibration comprised of 5 runs, with each run being 10 trials (10s each) for each MI task. Each trial had a fixation cross ($t = 0-2s$), audio and VR cues showing “relax” or “walk” to prompt the subject to perform the desired MI task ($t = 2-8s$), and rest ($t = 8-10s$). The BCI test session had 3 trials (60s each) for each MI task, with an audio cue to prompt the subject to perform the desired MI task for 60s, with VR feedback that matched the classified MI. Classification accuracies of each session were used to evaluate the BCI performance.

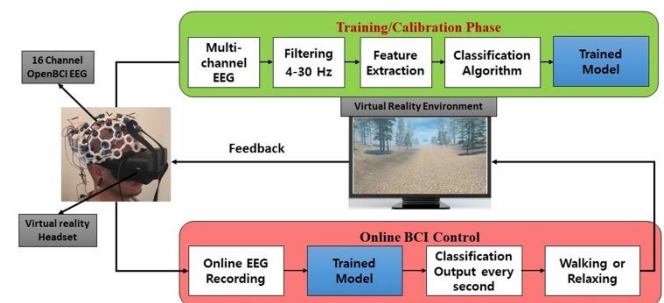


Figure 1: Experimental setup of the study.

RESULTS

Each subject's (different colours) classification accuracies increased with number of sessions undertaken (Fig. 2).

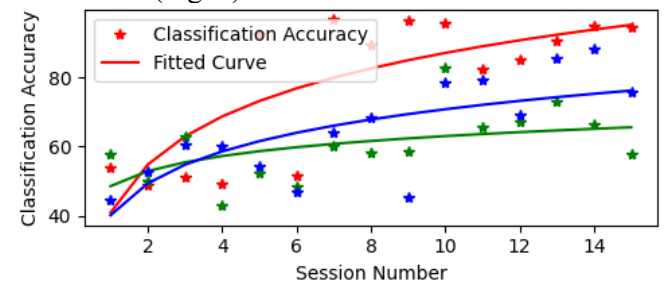


Figure 2: Classification accuracies (%) for online BCI.

CONCLUSIONS

To our best knowledge, this is the first study with a consumer-grade EEG system to train naïve subjects for lower-limb BCI in a VR environment. Results showed that VR+BCI training can improve the subjects' ability to master BCI control. Therefore, VR+BCI training may be used for improving neurorehabilitation interfaces and developing reliable low-cost BCIs.

REFERENCES

- [1] Wolpaw J.R., Clin. Neurophysiol. 113, 767-791, 2002.
 - [2] Jeunet C., J. Neural Eng. 13(3), 036024, 2016.
 - [3] de Castro-Cros M., Front. Neuro. 14, 882, 2020.
- Presented by Malik Muhammad Nacem Mannan (m.mannan@griffith.edu.au).



DAY 1

Podium 3

THE IMPACT OF DATA ARRANGEMENT AND WALKING CONDITIONS ON GAIT BASED PERSON RE-IDENTIFICATION USING FORCE PLATFORMS

Duncanson, K.¹; Hanly, G.²; Abbasnejad, E.³; Robertson, W.S.P.⁴; Thewlis, D.¹

¹Adelaide Medical School, University of Adelaide, Adelaide, AUS; ²Defence Science and Technology Group, Edinburgh, AUS; ³Australian Institute for Machine Learning, University of Adelaide, Adelaide, AUS; ⁴School of Mechanical Engineering, University of Adelaide, Adelaide, AUS

INTRODUCTION

Gait based person re-identification (re-ID) is the process of matching labelled gait samples to unlabeled gait samples to confirm identities. The impact of different walking conditions, input representations and deep learning architectures on the accuracy of force platform based re-ID systems remains largely unexplored [1]. We aimed to determine the most effective arrangement of kinetic data from two force platforms; compare the utility of a convolutional long-short term memory (LSTM) network to a convolutional transformer network for extracting kinetic features; and determine the impact of variations in footwear and walking speed on re-ID accuracy.

METHODS

The dataset used in this study was from a repeated measures experiment conducted on 193 healthy participants over two sessions (separated by 3-14 days). Participants wore their own clothing and footwear, and were instructed to walk approximately 10-m five times at three different speeds: slow, self-selected, and fast. Bilateral ground reaction forces, moments, and center of pressure coordinates were acquired from two force platforms at 2000 Hz. Six different deep neural network re-ID systems were tested on four different datasets. In each case, Fz, Fy and Cy were used as a three-channel input based on unpublished work from our laboratory identifying these as the most important parameters in re-ID. The datasets were same footwear and preferred walking speed (PWS) (C1); same footwear and all walking speeds (C2); all footwear and PWS (C3); finally, all footwear and all walking speeds (C4). Each system differed in terms of input data arrangement and network architecture. In the first arrangement ('split'), inputs from each stance side were processed separately and then the features pertaining to each side were summed to represent the entire gait cycle. In the second arrangement ('cat'), inputs from each force platform were concatenated lengthwise and processed together. In the final arrangement ('step'), inputs from each force platform were treated as separate samples such that each inference was made based on a single footstep. Each network featured 4-5 convolutional

layers (depending on the arrangement condition), either an LSTM layer or a transformer encoder layer, and then two fully connected layers. Network performance was inferred using a seven-fold cross-validation approach with different training and validation vs. testing splits (85:15% participant distribution).

RESULTS

Network architecture had negligible effect on re-ID accuracy as the convolutional transformer network was on average (\pm std) $0.88 \pm 1.55\%$ more accurate than the convolutional LSTM network regardless of data arrangement or walking condition. Figure 1 shows differences in test accuracy across each of the four dataset conditions using the convolutional transformer network.

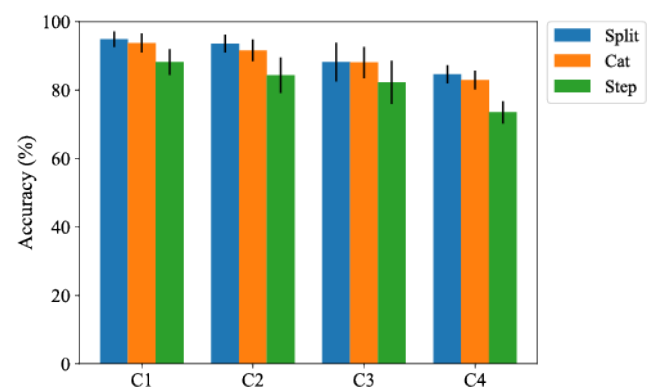


Figure 1. Mean (\pm std) test accuracy obtained using the convolutional transformer network grouped by dataset condition.

CONCLUSIONS

Re-ID inferences should be formulated based on kinetic data from the entire gait cycle rather than a single footstep. Changes to an individual's walking speed and footwear between measurement instances increases the difficulty of the re-ID task, with footwear exhibiting the greatest impact.

REFERENCES

1. Connor, P. CVIU. 167, 1-27, 2018.

Presented by Kayne Duncanson
(kayne.duncanson@adelaide.edu.au).

REAL-TIME CONVERSION OF IMU DATA TO ANKLE JOINT ANGLES USING ARTIFICIAL INTELLIGENCE

Senanayake, D.; Halgamuge, S.; Ackland, D.C
University of Melbourne, Parkville, Victoria, Australia

INTRODUCTION

Video motion capture systems such as Vicon and Optotrak are frequently considered the standard in non-invasive joint angle measurement using inverse kinematics (IK); however, these systems are costly, have a restricted capture volume, and are associated with significant setup time. Inertial Measurement Units (IMUs) are low-cost, wireless, and capable of data acquisition in and outside of the laboratory environment without limitation on capture volume; however, joint angle measurement depends on alignment of IMU sensors with body segments, or joint calibration (Lebleu et al. 2020), and accurate out-of-plane joint motion may be challenging to quantify. The aim of this study was to employ a new machine learning method based on deep neural networks to convert IMU data to ankle joint angles in real time such that the resultant angles data are indistinguishable from those derived from video motion capture.

METHOD

Nine healthy participants (age: 26.5 ± 6.2 years) were recruited and performed walking trials on a treadmill at three contrasting speeds each for one minute, specifically at 0.5m/s (slow), 1.0m/s (medium) and 1.5m/s (fast). Three-dimensional trajectories of retro-reflective markers attached to each subject's lower limbs using the Strathclyde cluster model were simultaneously acquired using a 12-camera video motion capture system (Vicon, Oxford Metrics, UK). Subjects also wore IMU sensors (Trigno, Delsys, USA) placed on the lateral mid-thigh, external mid-shank and lateral mid-foot of both lower limbs. IMU and video motion analysis data were acquired simultaneously and synchronised. Three-dimensional ankle joint kinematics were calculated using three approaches: (i) IK using the video motion analysis system (ii) IMUs, and (iii) deep neural network calculations derived from the IMU data. A generative adversarial network (GAN), a form of deep neural network, was employed to facilitate person-specific conversion of IMU data to ankle joint angles. When trained, the GAN 'simulated' joint angles derived from video motion analysis (i.e., IK) in real-time using only IMU data. To evaluate the GAN robustness, joint angle predictions were made for gait speeds not used in model training, and the results compared to IK.

RESULTS

There were significant differences between IK and IMU joint angle predictions for ankle eversion and internal rotation during walking at 0.5 m/s and 1.0 m/s ($p < 0.001$); however, no significant differences in joint angles were observed between the generative adversarial network and IK at any speed or plane of joint motion ($p < 0.05$) (Fig. 1). The RMS difference in ankle joint kinematics between the generative adversarial network and IK for walking at 1.0 m/s was 3.8° , 2.1° and 3.5° for dorsiflexion, inversion and axial rotation, respectively.

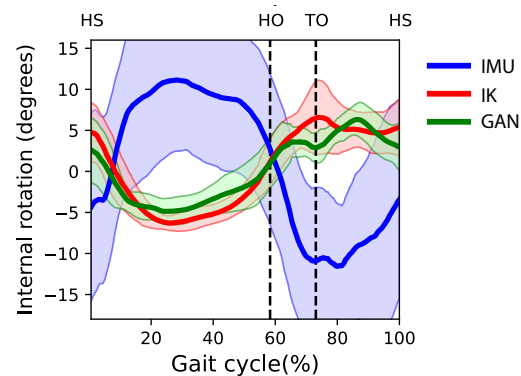


Figure 1. Ankle internal rotation angles for walking at 0.5 m/s as predicted by IMUs, IK derived from video motion analysis, and deep neural networks (GAN). The GAN model was trained using gait data at 1 m/s and 1.5 m/s and predicted kinematics at an arbitrary new speed

CONCLUSIONS

This study reported a novel machine learning approach to IMU-based joint angle calculation, with high ankle joint angle predictability demonstrated across a range of contrasting speeds and planes of joint motion. The deep neural network model, once trained using a reference dataset, produces accurate real-time joint-angle prediction for gait speeds not used in the initial model training. The modelling approach has application in gait classification, telemedicine, personal sports and exercise industries, and in defence.

REFERENCES

Lebleu, J et al. Sensors, 20, 1556-1565, 2020

Presented by Damith Senenayake (email address).

ADAPTIVE BAYESIAN MODEL TO PREDICT ANKLE ANGLE BASED ON EMG SIGNALS

Zarshenas, H.; Kempa-Liehr, A.W.; Ruddy, B.; Besier T.F.
The University of Auckland, Auckland, New Zealand

INTRODUCTION

Predicting motion intention is a necessary requirement to have safe and intuitive control of an assistive robot. Musculoskeletal models can estimate a current state, such as joint moment or angle, using EMG as input [1]. However, these models are complicated to calibrate to an individual and do not predict user intention ahead of the current state. Machine learning (ML) has also been used to estimate a current state based on EMG, but these models are limited to predicting motions that are part of a training set and are not capable of motion intention prediction for new movements. Here, we present an adaptive ML model, which predicts ankle joint kinematics 300ms ahead of the current time step. Performance was tested across four walking speeds and compared to a similar model without an updating feature.

METHOD

The Bayesian-based model was designed around a time-series feature extraction method called “tsfresh” [2]. The model takes EMG data from four muscles and the ankle angle at a current time step to predict ankle angles 300ms ahead of the current time step. The initial template of the predictive model was created by determining the coefficients of the Bayesian model during a training process based on data from one participant during walking on a treadmill at 1m/s. Instead of using input time series directly, a list of the most informative features was extracted and used for model training using the python tsfresh toolbox. Following the initial training, the model parameters were updated when an error term (predicted vs actual ankle angle) exceeded a predefined threshold. Continuous monitoring of the error term enabled ‘on the fly’ updating of the model. The model performance was evaluated on data collected from 9 participants, whose data were not used in the initial training. Participants walking on a treadmill at four speeds (1, 1.5, 2, and 2.5 m/s) for 2 mins. The adaptive model performance (“with updating”) was compared to the same time-series feature prediction model the new updating capability turned off (“without updating”). Mean RMSE and R^2 between predicted and actual values were determined.

RESULTS

The adaptive model predicted ankle angles to within 4° of measured angles, with an average R^2 above 0.9 (Fig 1a). The model achieved these results within 50 msec of being exposed to a new condition (Fig 1b). The performance of the model without updating was clearly worse, with errors up to 10° .

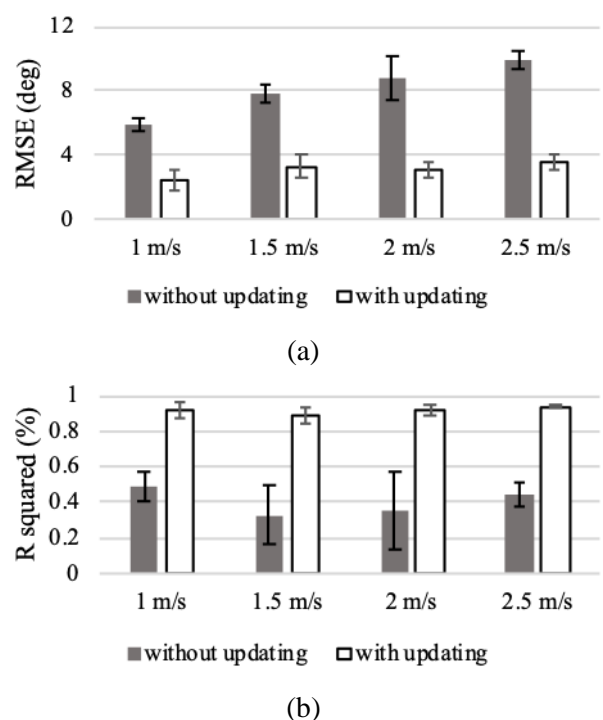


Figure 1. The average and standard deviation of RMSE (a) and R^2 (b) for the model were calculated for nine individuals.

CONCLUSIONS

In this study, an adaptive ankle angle prediction model was introduced. The embedded updating phase in the model structure improved the prediction accuracy across all speeds and values were predicted 300ms ahead of the current time step. Next, we will test the model performance on a broad range of activities to show its generalisability.

REFERENCES

1. Lloyd, J. Biomech 36, 765-776, 2003.
2. Christ, J. Neurocomputing 307, 72-77, 2018.

Presented by Homayoon Zarshenas
(hzar638@aucklanduni.ac.nz).

TEXTILE ELECTRODES FOR ELECTROMYOGRAPHY

Nathan Lyons^{1,2}, David Lloyd¹, David Thiel³, Sam Canning¹, Matthew Worsey^{1,3}, Daniel Devaprakash¹, Claudio Pizzolato¹,

¹Griffith Centre of Biomedical and Rehabilitation Engineering, Griffith University, Australia

²Queensland College of Art, Griffith University, QLD, Australia

³Griffith University Sports Technology, School of Engineering and Built Environment, Griffith University, Australia

INTRODUCTION

Acquiring high quality electromyograms (EMG) outside of controlled laboratory environments is challenging. Traditionally, EMG are acquired via single-use Ag/AgCl gel electrodes, which provide excellent results. However, there is great need to translate advanced biomechanical analyses to real-world applications in sport, rehabilitation, and defense. Garment-embedded EMG enables such in-field applications, but it is unclear which electrodes are best. Commercially available dry textile electrodes offer promising solutions for embedment in garments, but it is unclear which textile performs best for EMG, are easy to embed in clothing, and washable. In this study we manufactured dry textile electrodes from commercially available conductive fabrics and assessed the quality of EMG signals during a variety of motor tasks before and after washing and compared against gold standard Ag/AgCl gel electrodes.

METHOD

Seven commercially available conductive textiles of different material composition were purchased based on resistance values and physical characteristics. Electrodes were manufactured from each textile using laser cutting (Trotec: Speedy 300) and embedded into a garment for subsequent washing. This garment underwent 30 washing cycles of 30 minutes each using water temperature of 30°C and 15 grams of generic washing powder, with the garment placed in a laundry bag to protect the electrodes from mechanical stresses. Garments were let to dry after each washing cycle and photographs and resistance measurements were taken using a standard multimeter (Stanley). The textile that changed the least in electrical resistance and visual material degradation was used for further testing. EMG of the medial gastrocnemius were acquired at 1000Hz (Myon Aktos) using the washed and unwashed textile electrodes, and Ag/AgCl gel electrodes. Skin was prepared only when using the gel electrodes as per SENIAM recommendations. Participants performed a variety of motor tasks: isometric contractions, heel raises, walking, jogging and a bilateral counter-movement jump.

RESULTS

Electrode 7, a nickel/copper plated polyester with iron-on adhesive backing, was the most suitable electrode for embedding into a garment to measure EMG. It exhibited the least change in resistance throughout the washing process (pre wash: 0.9Ω , post wash: 1.4Ω) and showed little to no visual degradation. The EMG median frequency of the washed textile electrode resulted 111.5 ± 9.47 Hz vs the gold standard 51.44 ± 1.70 Hz. The coefficient of determination (R^2) of EMG envelopes between gold standard and washed dry electrode during gait (Figure 1) was >0.98 .

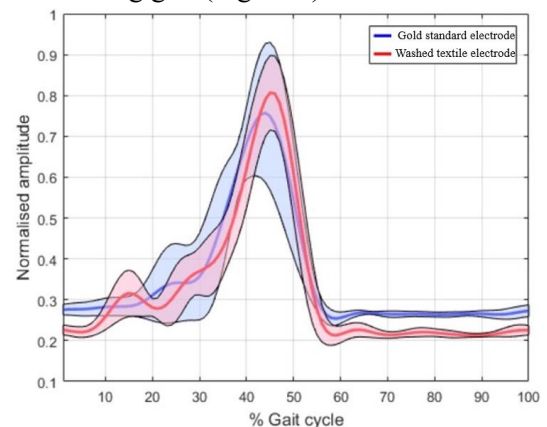


Figure 1. EMG envelopes (solid line: mean, shaded area: standard deviation) from 11 gait cycles using washed textile electrode 7 and gold standard gel electrodes.

CONCLUSIONS

Electrode 7 produced excellent results, enabling the future development of high-quality garment-embedded EMG sensors for applications in rehabilitation, training and diagnoses, outside of traditional laboratory settings.

REFERENCES

1. Trindade et al., Synthetic Metals, 210, 179-185, 2015.
2. Eskandarian et al., ACS Applied Electronics Materials, 2, 1554-1566, 2020.

Presented by Nathan Lyons n.lyons@griffith.edu.au

A NEUROMUSCULOSKELETAL MODEL-BASED CONTROLLER FOR FUNCTIONAL ELECTRICAL STIMULATION CYCLING

Pizzolato, C.¹, Sousa, A. C. C.¹; Crossley, C.¹, Quinn, A.¹; Mulholland, K.¹; Fornusek, C.², Lloyd, D. G.¹.

¹Griffith Centre of Biomedical and Rehabilitation Engineering, Griffith University, Australia

²Faculty of Medicine and Health, The University of Sydney, Australia

INTRODUCTION

Functional electrical stimulation (FES) involves artificially inducing a muscle contraction by delivering an electrical charge to motor neurons. FES is a popular rehabilitation tool to effectively reanimate limbs after paralysis, with cycling being one type of FES exercise available to individuals with spinal cord injury. Despite a long history of FES, orchestrating the stimulation of muscles across multiple joints and degrees of freedom to generate a target movement remains a challenge. Clinical approaches still involve complex manual tuning of stimulation patterns. Even research-based control system approaches require an *a-priori* selection of stimulation patterns. This protocol is not optimal as it hinders the rehabilitation process and delivers stimulation that is not consistent with the individual's neuromusculoskeletal (NMS) system [1].

We developed a closed-loop cadence control system for FES cycling using a real-time inverse NMS model. Our system automatically calculates appropriate stimulation patterns and is compatible with standard clinic-based equipment.

METHOD

The control system (Figure 1) was developed in OpenSim and CEINMS [2]. Specifically, a digital twin of a clinical cycling ergometer (RT300, Restorative Therapies, Baltimore, MD) was implemented in OpenSim and connected to a linearly scaled gait2392 model via weld constraints between feet and pedals. The neuromuscular dynamics was implemented in CEINMS, using 92 Hill-type actuators with elastic tendons. Muscles were assigned to 8 FES groups and one inactive group. Each FES group (i.e., quadriceps, hamstring, ankle plantarflexors, and ankle dorsiflexors for both legs) was associated to one FES channel, meaning that muscles belonging to the same group were assumed to be activated equally. Muscles in the inactive group contributed to the controller via passive force production. Within the controller, the ergometer's crank torque was estimated based on rigid-body dynamics. The estimated crank torque was then used as a constraint for a static optimization approach that minimized the activation squared of the

muscles within the 8 FES groups. Muscle activations were then used to control the delivered FES.

The developed controller was first tested *in silico* to debug and improve the computational efficiency of the controller. *In vivo* assessment on one individual with spinal cord injury was then performed using an 8-channel stimulator (Rehastim2, HASOMED, DE). We tested the ability of the controller to achieve and maintain the target speed in both *in silico* and *in vivo* experiments and qualitatively observed the predicted FES patterns.

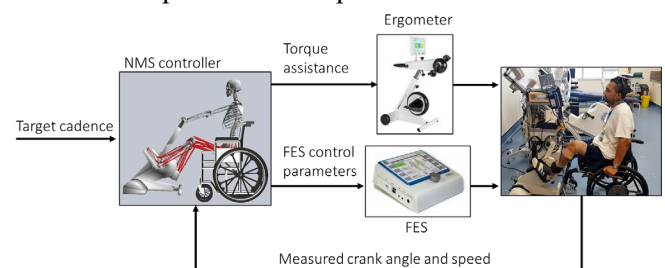


Figure 1. Simplified representation of the developed control system. NMS: neuromusculoskeletal, FES: functional electrical stimulation

RESULTS

The NMS controller functioned in real-time (<10ms per frame), enabling FES cycling and producing phasic muscle contractions compatible with expected biomechanical function. Further results will be presented at the conference.

CONCLUSIONS

We developed a NMS-based controller for FES cycling using only clinical equipment. Our approach removed the need of manually identifying muscle stimulation patterns for cycling and could be applied to other robotic rehabilitation modalities (e.g., exoskeletons) to generate optimal FES-induced movement.

REFERENCES

- [1] Pizzolato, C., Front. Neurorobot. 13, 97, 2019
- [2] Pizzolato, C. J. Biomech 14, 3929-36, 2015.

Presented by Claudio Pizzolato
(c.pizzolato@griffith.edu.au).

RAPID AND HIGH ACCURACY RECONSTRUCTION OF THE BONY SHOULDER ANATOMY: A STATISTICAL SHAPE MODELLING STUDY

¹Huang, Y; ¹Robinson, D.L.; ²Pitocchi, J; ¹Lee, P.V.S.; ¹Ackland, D.C.

¹University of Melbourne, Victoria 3010, AUSTRALIA; ²Materialise, Heverlee, Belgium.

INTRODUCTION

Reconstruction of subject-specific glenohumeral joint anatomy is used in computational model development, implant design and surgical planning; however, digitisation of medical images can be highly time-consuming. Statistical shape modelling (SSM) has been used to model the distribution of anatomical variation across a broad range of human bones and joints, but is rarely performed at the shoulder. The aims of this study were, firstly, to employ SSM to rapidly reconstruct subject-specific bony shoulder anatomy using only the locations of bony landmarks identified from Computed Tomography (CT) scans; and second, to validate the accuracy of this approach in reproducing complete anatomy of the scapula and humerus.

METHOD

Geometries of thirty right male scapulae (age 60.3 ± 10.0 years) and thirty female scapulae (age 58.1 ± 8.7 years) together with thirty right male humeri (age 61.0 ± 10.5 years) and thirty female humeri (age 58.6 ± 10.2 years) were digitally segmented from CT scans (Mimics, Materialise, Belgium). SSMs of the scapula and humerus were developed using non-rigid registration, rigid body alignment and principal component analysis.

Fifteen anatomical scapular landmarks and eight humeral landmarks of clinical relevance were manually identified on each surface mesh within a training set. All combinations of distances between the anatomical landmarks as well as the three-dimensional coordinates of each landmark were then assembled into a measurement data matrix. Complete scapula and humeral geometry were predicted using the landmark measurement matrix and SSMs via a Lasso regression. Bayesian information criterion (BIC) was used to control the Lasso regression and remove redundant measurements. The accuracy of the shape prediction was quantified using the closest-neighbor surface root-mean-squared (RMS) error calculated between the predicted mesh and the actual mesh using a leave-one-out strategy. Scapular and humeral shape predictions were evaluated using (i) all scapular and humeral morphometric measurements, and (ii) morphometric

measurements derived from the proximal humerus only.

RESULTS

The most representative prediction models achieved a mean surface RMS error of 1.8 mm, 1.6 mm, 1.6 mm and 1.4 mm for male scapulae, female scapulae, male humeri and female humeri, respectively (Figure 1). In addition, the glenoid and the proximal humerus were reconstructed with a mean RMS error of under 2 mm. Reconstruction of the entire humeral geometry using only proximal humerus morphometric measurements was achieved with a mean surface RMS error of 2.7 mm and 2.1 mm for male and female humeri, respectively. The proximal humerus was predicted with a mean RMS error of 3.0 mm and 2.5 mm for male and female proximal humeri, respectively. No more than seven morphometric measurements were required as model inputs in all cases.

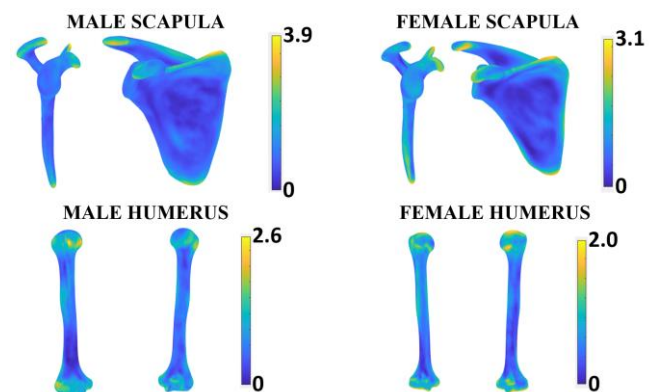


Figure 1. Error maps for male and female scapulae and humeri predicted using bony landmark data.

CONCLUSIONS

This study demonstrated that a small number of morphometric measurements (landmarks) can be used to reconstruct complete scapular and humeral geometries with high accuracy. The SSM-based technique presented in this study will facilitate rapid generation of subject-specific 3D anatomical models of the glenohumeral joint, which may be useful in patient-specific modelling and surgical planning.

Presented by Yichen Huang
(yichenh2@student.unimelb.edu.au).



DAY 1

Podium 4

APPARENT MECHANICAL PROPERTIES OF THE ENTIRE HUMAN FEMUR: INDIRECT VS DIRECT METHODS

Branni, M. (1); Perilli, E. (2); Taylor, M. (2); Martelli, S. (1)
1. Queensland University of Technology, Brisbane, QLD, Australia;
2. Flinders University, Adelaide, SA, Australia.

INTRODUCTION

Finite Element (FE) models have become common tools for investigating the mechanical behavior of the human femur. However, a lack of standardization in assigning bone mechanical properties leads variable accuracy across laboratories [1]. This study aims to compare apparent mechanical properties calculated using indirect fabric-based method against direct corresponding micro-FE calculations in entire proximal human femurs.

MATERIAL AND METHODS

Micro-CT images (29.81 $\mu\text{m}/\text{voxel}$) of four osteoporotic cadaveric femurs (76-81 years of age) were used [2]. Each image volume was subdivided into 5mm side-length contiguous trabecular cubes (Fig.1). A selection criterion based on morphometric parameters was implemented to guarantee bone homogeneity.

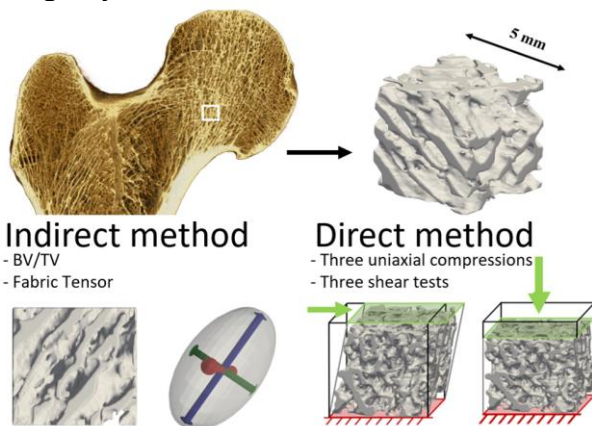


Figure 1. Anisotropic mechanical characterization.

Bone volume fraction (BV/TV), fabric tensor and degree of anisotropy (DA) were calculated using the Mean Intercept Length method (CT Analyser, Bruker, Belgium). Stiffness matrix was determined by using fabric-elasticity relationships [3]. Micro-FE models were developed by converting bone voxels into linear hexahedra elements. Bone tissue material properties were modelled as isotropic linear elastic material ($E = 5.33 \text{ GPa}$) with a Poisson's ratio equal to 0.3. The stiffness matrix was computed simulating in displacement control three uniaxial compression and three shear tests by homogenization procedure [4].

The stiffness matrix obtained by the direct and indirect methods were compared using linear regression.

RESULTS

The analysis was successfully completed for 1507 cubes from four femurs. The BV/TV and DA range were 8 – 47% and 1.08 – 2.05, respectively. The coefficient of determination was 0.85 and the slope was 1.25. The RMSE was lower than 7% of the maximum micro-FE predicted value (Fig.2).

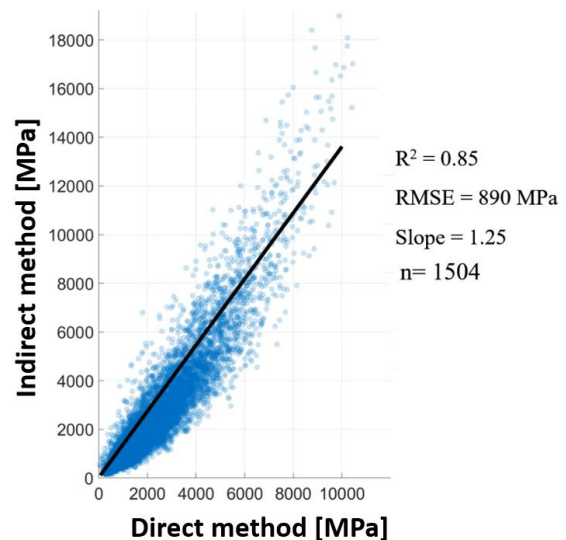


Figure 2. Linear regression analysis of stiffness matrix.

CONCLUSIONS

The procedure for determining the anisotropic stiffness matrix reveals a strong agreement between indirect and direct models. However, the indirect methods provided stiffer material properties than corresponding direct calculations. Further investigations are being performed to examine how these differences may influence stresses and strains continuum-FE models predictions.

REFERENCES

1. Klues et al, Comput Method Biom, 22.12:1020-1031, 2019
2. Martelli et Perilli, J Mech Behav Biome, 84:265-272, 2018
3. Zysset et al, J Biomech, 36:10:1469-1485, 2006
4. Van Rietbergen et al, J Biomech, 29.12:1653-1657, 1996

Presented by Marco Branni
(marco.branni@qut.edu.au).

MUSCLE SYNERGY DRIVEN MODELLING TO PREDICT KNEE JOINT CONTACT FORCES IN CHILDREN WITH CEREBRAL PALSY

Mohammad Rabbi¹, Laura Diamond¹, David Lloyd¹, Chris Carty¹, Giorgio Davico², Claudio Pizzolato¹

¹Griffith Centre of Biomedical and Rehabilitation Engineering, Griffith University, Australia

²Department of Industrial Engineering, Alma Mater Studiorum, University of Bologna, Italy

INTRODUCTION

Human movement is thought to be generated using coordinated control of synergistic muscle groups. Muscle synergies can be extracted from muscle electromyograms (EMG)s using mathematical approaches [1]. EMGs are also used to inform neuromusculoskeletal (NMS) models to understand the internal biomechanics of musculoskeletal tissues during movement, and applied to investigate joint contact forces in individuals with cerebral palsy (CP) [2]. However, the use of these models in clinical settings has been limited by practicalities, such as the inability to collect EMG data from a large number of muscles. Muscle synergy-driven (SD) NMS methods may solve this problem by enabling reconstruction of all muscle excitations from a reduced set of recordable EMGs. The reconstructed excitations could then be used as NMS models' inputs to estimate muscle and joint contact forces. Thus, we developed a SD-NMS modelling workflow where (i) excitations for all the NMS model's muscles were reconstructed from a small set of EMGs via muscle synergies, and (ii) then muscle and knee joint contact forces were estimated in children with CP during walking.

METHOD

Six children (age: 8.16 ± 1.8 years, height: 1.24 ± 0.1 m and mass: 23.85 ± 5.7 kg), including three children with CP (Gross Motor Function Classification System I) and three typically developing (TD) children, were recruited in this study. Motion capture and EMG data were recorded during 10 self-paced walking trials. Marker and ground reaction force data were filtered using 4th order 6 Hz low-pass Butterworth zero-lag filter. EMGs recorded from 13 lower limb muscles were band-pass filtered (30-400 Hz), full-wave rectified, low-pass filtered (6 Hz) and then normalised to each muscle's maximal excitation identified across walking. A custom 34-muscle, 5-DOF lower-extremity musculoskeletal model was used to run inverse kinematics, inverse dynamics and muscle analysis using OpenSim 3.3. NMS modelling was performed in CEINMS [3] using either EMG-assisted or EMG-driven modes to estimate muscle and knee joint contact forces.

The SD-NMS models had three stages. First, using the TD participants' 13 EMGs the EMG-assisted method was used to create excitations for 34 muscles as well as to estimate knee joint contact forces. Second, for each subject with CP, muscle synergies were identified from three muscles (SOL, SM, VL or MG, SM, VL) (Table 1) using non-negative factorisation and then used to reconstruct the remaining 31 muscle excitations via a synergy extrapolation method, leveraging the TD children's muscle excitations [4]. Third, 34 muscle excitations of children with CP were used as inputs to EMG-driven NMS models to estimate muscle and knee joint contact forces. These forces from SD-NMS and EMG-assisted simulations were compared using coefficient of determination (R^2) and root mean squared error (RMSE).

RESULTS

The SD-NMS compared with EMG-assisted approach well estimated knee joint contact forces ($R^2 > 0.91$, RMS < 0.33 body weight) for both TD and CP participants (Table 1).

Table 1. Knee joint contact force estimation vs EMG-assisted method

Muscles for EMG recording	CP		TD	
	R^2	RMSE	R^2	RMSE
SOL SM VL	$0.94(\pm 0.03)$	$0.29(\pm 0.16)$	$0.97(\pm 0.01)$	$0.13(0.01)$
MG SM VL	$0.91(\pm 0.01)$	$0.33(\pm 0.13)$	$0.97(\pm 0.01)$	$0.18(0.04)$

MG- medial gastrocnemius; SM- semimembranosus; SOL- soleus; VL- vastus lateralis

CONCLUSIONS

Our results suggest that muscle synergies extracted from the EMG of three muscles can be used to inform SD-NMS models and estimate muscle and knee joint contact forces both in CP and TD paediatric populations. This can reduce the amount of EMG data collected from participants with CP in clinical settings.

REFERENCES

- [1] Tresch MC. et al. J. Neurophysiol., 95, 2199-2112, 2006
- [2] Davico G. et al. Clinic. Biomech. 72, 141-149, 2020
- [3] Pizzolato C. et al. J. Biomech., 48, 3929-3936, 2015
- [4] Rabbi MF. et al. Sci. Rep. under review, 2021

Mohammad F. Rabbi, fazle.rabbi@griffithuni.edu.au.

DEEP-LEARNING MARKERLESS TRACKING OF INFANTS GENERAL MOVEMENTS PROVIDES SIMILAR TRAJECTORIES TO VICON MARKER-BASED APPROACH

Abbasi, H.¹; Lim, L.¹, Mollet, S.¹; Williams, S.²; Battin, M.³; Besier, T.¹; McMorland, A.^{1,4}
¹Auckland Bioengineering Institute, University of Auckland, Auckland, New Zealand; ²Liggins Institute, Auckland, New Zealand; ³Department of Newborn Services, Auckland City Hospital, Auckland, New Zealand; ⁴Department of Exercise Sciences, University of Auckland, New Zealand

Introduction

General Movements (GM) during 6-20 weeks of age provide prognostic information to whether an infant is at risk of developing neurodevelopmental disorders, such as cerebral palsy (CP) [1]. Early interventions improve neuromuscular outcomes. Clinical resources for manual GM scoring are limited and current automated strategies require using body-worn sensors in the lab environment [2]. Here we compare the tracking of infant motion by deep-learning markerless pose-estimation, using conventional 2D videos, against the gold-standard Vicon 3D motion capture system.

Method

Vicon tracking system [3] was initially used to record an infant's spontaneous GMs using body-attached retroreflective marker clusters. The infant was laid down on their back and moved naturally in the absence of external disturbance. The infant's GMs were also simultaneously filmed using a standard iPad. Twelve anatomical locations (3 per limb) were manually annotated on 200 random frames (total: 2,400 datapoints) of the video recordings using DeepLabCut environment (total 7412 frames, equal to 4'12"). A deep resnet-152 was then trained using the annotated dataset (train to test ratio: 19:1). The deep-net was then used to automatically track the "learned" body-parts in the entire 2D video, including 7212 unseen frames. The automatically labeled trajectories associated with each anatomical location in the markerless scheme were then plotted against the trajectories from the benchmark marker-based approach (Vicon). Equivalent segments of the trajectories from the automatic markerless tracking and the Vicon system were superimposed on each other. To illustrate, here we show arbitrary sections of the marker displacements in the left hand and left foot (Fig. 1). Correlations between these epochs were then evaluated to determine how closely the markerless pose-tracking resembled the Vicon's marker-based measurements.

Results

The deep-net's performance was evaluated to be more

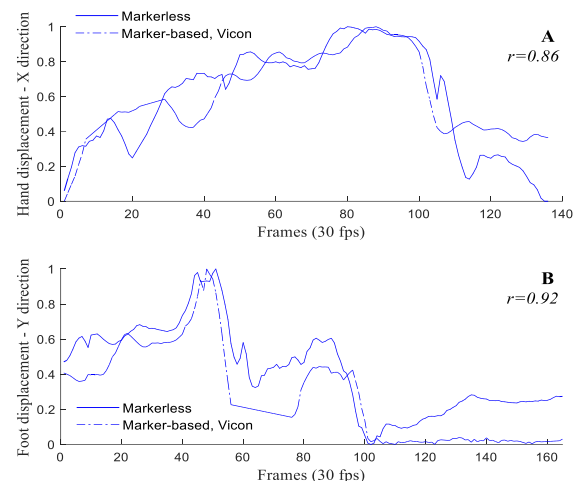


Figure 1. Markerless (solid lines) vs marker-based (dashed lines) trajectories of left hand (A) and left foot (B).

than 99% (SD: 0.25) accurate across all locations. We identified high correlations, namely $r=0.86$ and $r=0.92$, between the markerless and marker-based trajectories of the left hand and the left foot movements, respectively. The matching profiles in Fig.1 demonstrates that our markerless approach can perfectly track the exact same movements in a 2D video compared to the Vicon motion tracking system. Fig. 1A shows a hand's displacement's trajectory in the x-direction identified by the markerless approach (solid line) vs the same movement recorded by the Vicon's marker-based system at the same time (dashed line). A similar scenario for a foot movement is shown in Fig. 1B.

Conclusions

Results from this research highlight the reliability of markerless movement tracking using our proposed deep-learning markerless pose-estimation technology compared to the gold-standard marker-based scheme.

References

- [1] M. Hadders-Algra, *Developmental Medicine & Child Neurology*, vol. 60, (1), 39-46, 2018.
- [2] C. Marcroft, A. Khan. *Frontiers in Neurology*, 5, 284, 2015.
- [3] Vicon Motion Systems Ltd. <http://www.vicon.com>, 2020.

Presented by Hamid Abbasi (h.abbasi@auckland.ac.nz)

FRACTURE RISK PREDICTION OF LUMBAR VERTEBRA UNDER DYNAMIC COMPRESSION

Robinson, D.L.¹; Tse, K.M.²; Franklyn, M.³; Ackland, D.C.¹; Lee, P.V.S.¹

¹University of Melbourne, Melbourne, Australia;

²Swinburne University of Technology, Melbourne, Australia;

³Defence Science and Technology Group, Melbourne, Australia.

INTRODUCTION

In contemporary conflicts, underbody blast attacks on military vehicles have resulted in spinal fractures below the thorocolumbar junction at greater rates than those in civilian settings [1]. To design equipment that better protects against these injuries, injury probability curves are needed to evaluate spinal fracture risk based on the applied compressive force. Injury probability curves have been derived for fractures across the entire lumbar column [2], however, it is not known how this risk may vary within the lumbar spine, which is likely due to differences in morphology and stiffness between lumbar levels. The aim of this work was to develop injury probability curves describing fractures at each lumbar spine level under dynamic axial compression, and to establish how specimen- and level-specific properties influence fracture risk.

METHOD

Twenty sets of three-vertebra specimens were prepared from the lumbar spines of fifteen male cadavers (age: 61.5 ± 9.8 years). The outer vertebrae were potted and attached to a servohydraulic testing machine (Instron 8874) that applied compression at 1 m/s. Each specimen was repeatedly compressed for increasing peak displacements until a fracture was identified based on the signal of two acoustic emission sensors attached to the centre vertebral body. Fractures were confirmed by computed tomography (CT) imaging. Injury probability curves were created using a parametric survival analysis with a Weibull distribution. The peak compressive force of a fracture and non-fracture test for each specimen was treated as the survival variable. Variables such as age, lumbar level, volumetric bone mineral density (vBMD), vertebral body height (h_{VB}) and cross-sectional area (a_{VB}) were included as covariates in the survival model to assess their effect on fracture risk.

RESULTS

The injury probability curve derived for all lumbar levels with no covariates is shown in Figure 1. When considered independently, the lumbar level and vBMD covariates were found to have a significant effect on the fracture risk ($p=0.03$ and $p<0.001$, respectively),

while age, h_{VB} and a_{VB} were not significant ($p>0.05$). Interestingly, vBMD overrode the effect of lumbar level when these covariates were combined in the survival model ($p<0.001$ and $p=0.08$, respectively). The effect of vBMD is shown in Figure 1.

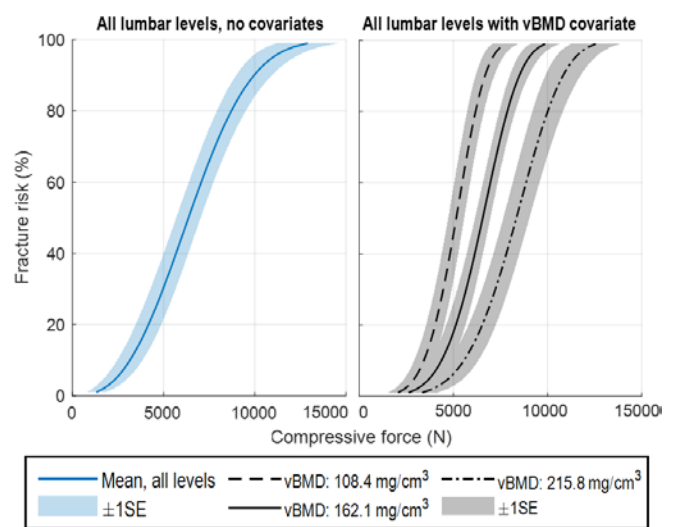


Figure 1. Injury probability curves with 1 standard error (1SE) for fracture risk across all lumbar levels, without covariates and with the vBMD covariate.

CONCLUSIONS

Injury risk prediction is a challenging area because subject-specific differences lead to large uncertainties in the analysis. For the lumbar spine, we found that vBMD had a significant effect on fracture risk and accounted for anatomical variations across all lumbar levels. Thus, the injury probability curves with the vBMD covariate established in this work allow fracture risk to be calculated with a greater degree of confidence compared to those previously established for the entire lumbar column [2]. These data allow for better evaluation of new underbody blast injury mitigation systems to be used in military applications.

REFERENCES

- Lehmann et al., Spine J 12, 784-790, 2012
- Yoganandan et al., J Mech Behav Biomed, 105, 103690, 2020.

Presented by Dale Robinson
(drobinson@unimelb.edu.au).

VARIATIONS IN KNEE JOINT LOADING CAN BE EFFECTIVELY MODELED BY EXPLORING THE UNCERTAINTY OF MUSCLE RECRUITMENT

Bennett, K.J.¹, Pizzolato, C.², Martelli, S.³, Bahl, J.S.¹, Sivakumar, A.¹, Atkins G.J.¹, Solomon, L.B.^{1,4}, Thewlis, D.^{1,4}.

¹The University of Adelaide, Adelaide 5000, Australia; ²Griffith University, Gold Coast 4215, Australia; ³Queensland University of Technology, Brisbane 4000, Australia; ⁴Royal Adelaide Hospital, Adelaide 5000, Australia.

INTRODUCTION

The internal forces acting on human joints are important in understanding the local mechanical environment. Musculoskeletal models are a powerful tool to estimate joint loads using human motion data. However, a major modelling challenge remains in estimating muscle activation patterns that are physiologically plausible, and that produce muscle forces that are consistent with external biomechanics, e.g. joint moments calculated via inverse dynamic approaches [1]. Different approaches to solve for muscle redundancy exist, but there is an increasing need to further validate these methods to understand the significance of model assumptions and uncertainties. The aim of this study was to compare knee joint loading using static optimisation (SO), with electromyogram (EMG)-informed, and stochastic approaches. Modelling results were compared to measured loads from instrumented knee implants.

METHOD

Data were obtained from the Grand Challenge Competition to Predict *in vivo* Knee Loads (challenges four, five, and six) [2]. Static and over ground gait trials were used. Marker trajectories, ground reaction forces, and EMG data for between 8-11 large superficial muscles of one leg were used as inputs to estimate knee joint loading in OpenSim 3.3 [3]. A generic full-body musculoskeletal model [3] was scaled using principal component analysis [4]. The inverse dynamics and SO toolboxes were used to estimate joint torques and muscle forces. The Calibrated EMG-informed Neuromusculoskeletal Toolbox (CEINMS) [1] was used to estimate muscle forces. These forces informed the inputs of the inverse EMG-informed stochastic method [5]. In CEINMS, four degrees of freedom were driven in EMG-assisted mode. In the stochastic method, one million solution samples were taken per frame, and muscle forces were constrained to within one standard deviation of the driven CEINMS solution or to half of their maximum possible force. The measured load from the prostheses was used as the ground truth for model validation.

RESULTS

Compared to the measured loads (Fig. 1), the SO solution had a root mean square error of 422 N, and the CEINMS solution 342 N. The stochastic method produced solution spaces encompassing the measured force for up to 98% of stance.

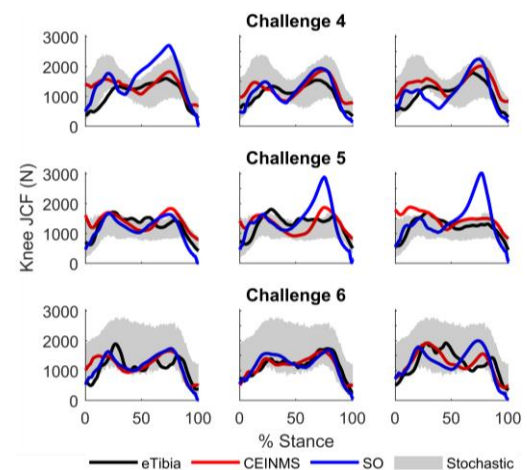


Figure 1. Measured knee joint contact forces JCFs (eTibia, black), overlaid with the estimates from CEINMS (red), SO (blue), and the stochastic method (gray) for individual over ground walking trials.

CONCLUSIONS

EMG-informed modelling showed, on average, better estimates of knee loading compared to SO. The results of the stochastic method show that, in general, the variation in knee loads can be modeled by investigating the uncertainty in muscle forces alone. Because the uncertainty in muscle forces can account for joint load, where possible, EMG measurements should be included to estimate knee joint loading.

REFERENCES

- [1] Pizzolato C. J. Biomech. 48: 3929-3936, 2015.
- [2] Fregly B.J. J Orthop Res. 4: 503-513, 2012.
- [3] Delp S. IEEE TBME. 54: 1940-1950, 2007.
- [4] Zhang J. ISMBS. 2014: 182-192, 2014.
- [5] Martelli S. Interface Focus. 5: 20140094, 2015.

Presented by Kieran James Bennett
(Kieran.bennett@adelaide.edu.au).

MULTISCALE MODELING OF KNEE JOINT PATHOPHYSIOLOGY: COMBINED EFFECT OF MECHANICS AND INFLAMMATION.

Mukherjee, S.^{1,2}; Lesage, R.^{1,2}; Geris, L.^{1,2,3}

¹Prometheus, Division of Skeletal tissue Engineering, KU Leuven, Belgium; ²Biomechanics Section, KU Leuven, Belgium; ³GIGA In silico medicine, University of Liège, Belgium.

INTRODUCTION

Chondrocytes, the primary cells in articular cartilage, require optimum mechanical signals to maintain homeostasis. Abnormal mechanical signals can lead to departure from the stable chondrocyte homeostasis and a switch to hypertrophy, as observed in osteoarthritis (OA). The objective of this paper is to develop a multiscale model of articular cartilage of the human knee joint to study the effect of physiological and pathological mechanical signals (post meniscectomy) on the fate of articular chondrocytes, in combination with pro-inflammatory cytokines.

METHOD

The multiscale modelling workflow incorporates in-silico models at 3 different length scales i.e. joint-level, cell-level and intracellular level as follows.

Finite Element (FE) modelling of the knee joint: FE model of the right knee of a 70 year old female weighing 77.1 kg was developed in FEBio (geometry obtained from the OpenKnee project [1]). Joint rotations, translations and joint reaction force for stance phase of the gait were used as input boundary conditions for the knee joint.

FE modelling of the chondrocyte: The chondrocyte and its microenvironment (containing the pericellular matrix (PCM) and extracellular matrix (ECM)) for the different zones of the cartilage (superficial zone (SZ), middle and deep zone (DZ)) were developed in Abaqus. The matrix was modelled as fibril reinforced poro-viscoelastic material whereas the cell was considered biphasic [2]. The maximum compressive and shear strains obtained at the different zones of articular cartilage from simulations of the knee joint were used as input boundary conditions for the cell-level model.

Regulatory networks for chondrocyte mechanotransduction: An additive model representing the intracellular gene/protein regulatory network involved in chondrocyte mechanotransduction and inflammation was developed based on literature studies and in-house microarray experiments. The forces acting on the integrins obtained from the cell-level model were used as input to trigger the intracellular pathways.

RESULTS

From the joint-level simulations, it was observed that meniscectomy lead to increased strains in the different zones of articular cartilage as compared to a healthy joint as seen in figure 1, resulting in higher forces sensed by the chondrocytes in the cell-level model. However, post-meniscectomy, in both the SZ and DZ, the chondrocytes initially remained in their stable state with high expression of stable chondrocyte biomarkers (SOX9, Coll-II, Proteoglycans). With subsequent build-up of pro-inflammatory cytokines with time due to abnormal loading, the SZ chondrocyte underwent a hypertrophic switch as was evident from the high activity of pro-hypertrophic biomarkers (RUNX2, CollX, MMP13, ADAMTS5). Due to this degenerative change in the SZ, the DZ chondrocytes were now subjected to higher strains, which when coupled with inflammatory cytokine build-up over time, led to their subsequent hypertrophic switch.

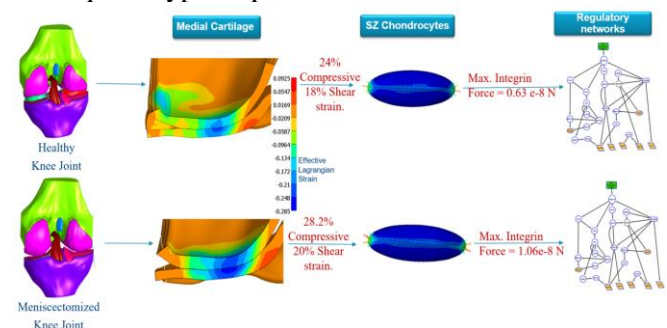


Figure 1: Workflow of multiscale modeling.

CONCLUSIONS

This study elucidates the ability of the developed multiscale model to predict the differential behavior of SZ and DZ chondrocytes to undergo hypertrophy at different stages of OA, which was due to the difference in mechanical signals sensed by the chondrocytes in the different zones. This model can be potentially used in future to predict the onset and gradual progression of OA in an iterative manner.

REFERENCES

1. Erdemir A. J. Med Device.7(4), 2013.
2. P.Julkunen et al., Med. Biol. Eng.Cmp.2009,47,1281.

Presented by Satanik Mukherjee
(satanik.mukherjee@kuleuven.be)



DAY 1

Podium 5

PASSIVE ANKLE EXOSKELETONS INFLUENCE BOTH ANKLE AND MORE PROXIMAL JOINT RESPONSES TO UNEXPECTED PERTURBATIONS

Williamson, J.L.¹; Lichtwark G.A.²; Dick T.J.M.¹

¹School of Biomedical Sciences, The University of Queensland, St Lucia, QLD, Australia

²School of Human Movement & Nutrition Sciences, The University of Queensland, St Lucia, QLD, Australia

INTRODUCTION

The behaviour with which lower limbs store and return energy during steady gait has inspired the design of passive wearable devices to assist walking [1], running [2] and hopping [3]. However, we still lack an understanding of how devices influence movement, and lower-limb joint biomechanics in real world environments (*i.e.* an unexpected drop or uneven terrain). This has limited our ability to design and implement wearable assistive technologies capable of augmenting movement in real world scenarios.

In this study we determined how bilateral passive ankle exoskeleton assistance affects the mechanics of lower limb joints (ankle, knee, hip) during unexpected vertical perturbations (*i.e.* a change in substrate height). We tested whether joint-level mechanical strategies varied with the size of the perturbation and with the amount of exoskeleton stiffness.

METHODS

Eleven participants (5M, 6F, 24±3y) completed an unexpected ‘falling-in-a-hole’ experimental paradigm. A vertical perturbation was elicited via the rapid removal of a ground platform (15 or 20cm) at an unknown time during hopping. Participants wore custom bilateral passive ankle exoskeletons (moment arm: 130mm; rotational stiffness (0,76 and 91Nm rad⁻¹). 3D motion capture (100Hz, OptiTrack, USA) and force plates (2048Hz, Bertec, USA) were used to measure joint motions and ground reaction forces, respectively. OpenSim was used to scale subject-specific models and then determine time-varying kinematics (inverse kinematics) and joint dynamics (inverse dynamics) [4]. Steady-state outcome measures were averaged over three hops prior to the perturbation. Linear-mixed effects models were used to determine the influence of condition (steady-state, perturbation), perturbation height (15, 20cm), and exoskeleton stiffness (0,76 and 91Nm rad⁻¹) on joint mechanics [5].

RESULTS

Duty Factor - During the perturbation, duty factor (proportion of hop cycle spent in contact with the ground) significantly decreased (steady-state: 0.54; perturbation: 0.46; $p<0.001$). Duty factor was not significantly different between spring conditions.

Joint Kinematics - During the perturbation, ankle angles were slightly more plantarflexed than in steady-state hopping ($p=0.039$). With exoskeleton assistance, a shift to a more plantarflexed ankle is observed during both

steady-state hopping ($p=0.001$) and at the perturbation ($p=0.021$). Knee and hip flexion both increased during the perturbation compared to steady-state hopping (both: $p<0.001$) but did not vary with exoskeleton assistance. Hip flexion increased with perturbation height ($p=0.020$), but ankle and knee kinematics remained similar across perturbation heights.

Joint Mechanics - Net ankle work did not vary between steady-state and the perturbation nor with exoskeleton assistance. There was a significant decrease in net knee work (*i.e.*, increased negative work) during the perturbation compared to steady-state ($p<0.001$). The effect of exoskeleton stiffness on net knee work was most pronounced at the 20cm hop height such that more negative work was done by the knee with increasing exoskeleton assistance (Fig. 1). Net hip work varied between the perturbation and steady-state ($p<0.001$), with an interaction between condition and perturbation height ($p=0.002$), and no effect of exoskeleton stiffness.

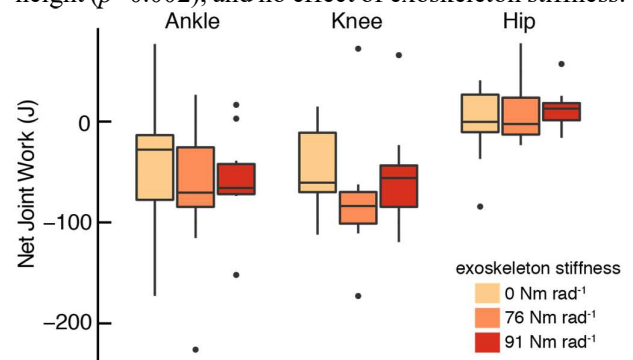


Figure 1. Net lower-limb joint work during the perturbation at a 20cm drop height. Boxplots show the median, 25th and 75th percentile. Outliers are represented as black dots.

CONCLUSIONS

Here we find that added stiffness at the ankle, via the use of passive exoskeletons, changed how the knee operated during unexpected perturbations, requiring greater negative work. We show a distal to proximal shift in energy dissipation, such that the knee takes on an increased energy absorbing role. This may aid with the dissipation of stored elastic exoskeleton energy.

REFERENCES

- [1] Collins S, et al. *Nature* **522**:212, 2015.
- [2] Nasiri, R, et al. *IEEE Syst. Rehab. Eng.* **26**:2026, 2018.
- [3] Farris D, et al. *J Appl. Physiol.* **115**:579, 2013.
- [4] Delp et al., *IEEE Trans. on Bio. Eng.*, **54**:1940, 2007.
- [5] Pinheiro et al., R package version **3.1**, 2013.

Presented by James Williamson

(james.williamson@uq.net.au).

FEASIBILITY OF USING ULTRASOUND TO TRACK ILIOTIBIAL BAND DISPLACEMENT DURING ISOLATED CONTRACTIONS

Hutchinson¹, L.A., Kelly¹, L.A., Lichtwark¹, G.A.
The University of Queensland, St. Lucia, QLD, Australia.

INTRODUCTION

The iliotibial band (ITB) is a unique anatomical structure in humans, believed to be important for bipedal locomotion. One curious feature of the band is that it transmits force across the lateral knee from two seemingly antagonist muscles; gluteus maximus (GM) and tensor fascia latae (TFL). We have been developing techniques to understand how these muscles transmit tension through the ITB using ultrasound imaging. Here we explore the feasibility of using a Kanade-Lucas-Tomasi (KLT)[1,2] algorithm to track ITB length changes during isolated contractions of GM and TFL.

METHOD

To validate our method, we moved the ultrasound transducer relative to the skin and compared the underlying ITB motion to the transducer motion. In six participants, a string potentiometer was attached between the transducer and the distal thigh (skin). Ultrasound RF-data was collected (Telemed, 110Hz) synchronously with string potentiometer displacement (Firstmark Controls, 5kHz) during a 5 second trial while the probe was manually moved proximally and distally a distance of less than 10mm. In Matlab, the RF data was filtered and up-sampled using conventional methods and displacement of the ITB tissue was tracked using point tracking functions (vision.PointTracker) across the entire trial. One hundred randomly selected frames of string potentiometer displacement and ultrasound displacement were selected and the average R^2 , slope, and intercept were found.

Two healthy males participated in the feasibility study (data collection and reliability measures ongoing) and provided informed consent. Participants were supine on an examination table, with their knees bent at 90° off the end of the table. A flat ultrasound transducer imaged the ITB in a similar location to described above, and joint movement was assessed by the string potentiometer attached between the transducer and Gerdy's tubercle. A constant current electrical stimulator (Digitimer) was programmed to deliver trains of electrical stimulation (60 rectangular pulses, 110 Hz) via two fine wires inserted into the TFL and GM muscles via ultrasound guidance. A "high" current condition was determined as the maximum tolerable response to the stimulus train (where a near maximum recruitment occurred) and the "low" condition was 50%

of this current. Participants received 3 stimulation trains in each muscle (separated by 6 seconds) at both the high and low stimulation levels, repeated after the ultrasound probe and potentiometer were removed and replaced and the protocol was repeated. Ultrasound and string potentiometer data were recorded and analyzed in the same manner as the validation protocol. Displacement data was plotted to compare high and low stimulation levels with and between sessions within each muscle (TFL and GM).

RESULTS

The ultrasound and string potentiometer displacements had an average R^2 of 0.91, slope of 0.77, and intercept of -0.16. In TFL, within sessions we consistently measured lower ITB displacement during low stimulations than in high stimulation trials. However, between sessions, absolute displacement varied, though difference in displacement between high and low stimulations is repeatable between sessions. In GM, the magnitude of ITB displacement was considerably lower than TFL when measured with the ultrasound probe in the same location.

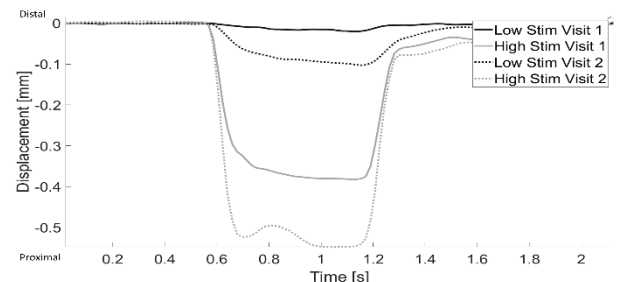


Figure 1. Within and between session ultrasound tissue displacement for low and high stimulation levels.

CONCLUSIONS

Point tracking KLT algorithm shows promising results for validity and feasibility in tracking and comparing isolated muscular contractions to displace the ITB. We hypothesize that a more posterior ultrasound probe placement will capture increased ITB displacement during GM stimulation due to GM's more posterior location.

REFERENCES

- [1] B. Lucas and T. Kanade, *IJCAI 81*.
- [2] C. Tomasi and T. Kanade, 1991.

Presented by LAH (laura.hutchinson@uq.edu.au).

FREE ACHILLES TENDON STRAIN DURING LANDING, JUMPING, LOCOMOTOR, AND REHABILITATION TASKS

Daniel Devaprakash¹, David F. Graham², Rod S. Barrett¹, David G. Lloyd¹, Steven J. Obst³, Ben Kennedy¹, Claudio Pizzolato¹

¹Griffith Centre of Biomedical and Rehabilitation Engineering, Griffith University, Australia

²Department of Health and Human Development, Montana State University, MT, USA

³School of Health, Medical, and Applied Sciences, Central Queensland University, Australia

INTRODUCTION

Ex vivo studies have shown that pathological rabbit Achilles tendons (AT) subjected to ~6% strain at 0.25 Hz, can restore and maintain tissue strength [1]. Similarly, *in vivo* studies have shown that AT-aponeurosis subjected to ~4.7% strain at 0.17 Hz resulted in tissue adaptation and increased mechanical stiffness [2]. Combined with additional evidence from literature, these results suggest that the existence of a strain magnitude “sweet spot” for training and rehabilitating tendons is plausible. However, the strains experienced by the AT during commonly prescribed rehabilitation and locomotor tasks are poorly known. The purpose of this study was to describe the free AT strains across a range of tasks using neuromusculoskeletal models informed by 3D imaging and surface electromyography (EMG).

METHODS

Sixteen trained runners (run > 80 km/wk) (10 male, 6 female, age: 25.2±5 yrs, BMI: 20.9±1.8 kg.m⁻²) with no prior history of AT injury completed the following tasks: 1) single leg heel rise with and without added mass, 2) walking (1.3 m/s), 3) countermovement jump, 4) squat hop landing, 5) maximal hop landing, and 6) running (3 m/s, 5 m/s). Marker trajectories (n=42), ground reaction forces, and surface EMG data (n=16) were synchronously recorded during all tasks. A calibrated EMG-informed neuromusculoskeletal [3] model with personalised AT properties [4] was used to estimate triceps surae muscle forces and free AT strain. Differences in average and peak free AT strain across all tasks were assessed using ANOVA and planned contrast tests were used to compare AT strain during heel rise against other tasks. Our model estimates of free AT force were also compared with *in vivo* experimental data reported in the literature.

RESULTS

Average free AT strain during unloaded heel rise was significantly higher when compared to walking and bilateral countermovement jump, and lower when compared to other tasks (Figure 1). Peak free AT strain during unloaded heel rise was significantly higher when compared to walking, and lower when compared

to other tasks (Figure 1). Our model estimates of AT forces agree well with experimental measures of AT force measured during walking (R^2 : 0.94), countermovement jump (R^2 : 0.86), and running (R^2 : 0.92).

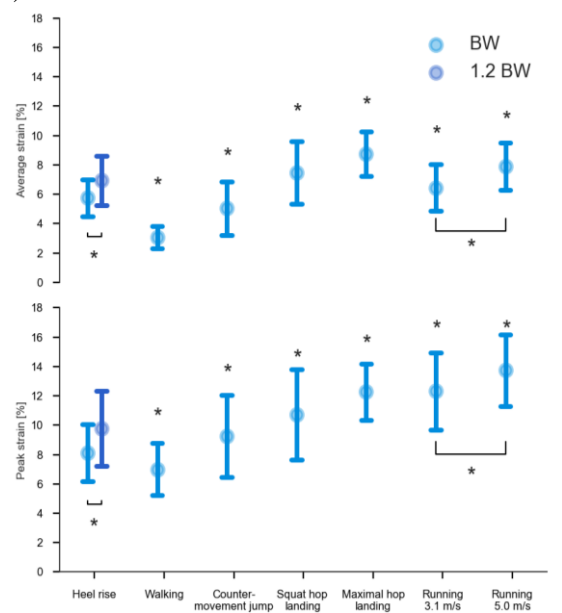


Figure 1. Average and peak free AT strain during rehabilitation, landing, jumping, and locomotor tasks. *indicates significant difference in AT strain between unloaded heel rise and the given task.

CONCLUSIONS

Our results strongly aligned with *in vivo* literature data, demonstrating the plausibility of our proposed methodology. These results could inform AT training programs to optimize exercise prescription for rehabilitation.

REFERENCES

1. Wang T et al. J Orthop. Res., 33:1888-1896, 2015.
2. Arampatzis A et al. J. Biomech., 43:3073-3079, 2010.
3. Pizzolato C et al. Front. Bioeng. Biotechnol., 8:878, 2020.
4. Devaprakash D et al. Front. Physiol., 11, 2020.

SPEAKER INFORMATION

Daniel Devaprakash d.devaprakash@griffith.edu.au

TIBIAL ACCELERATIONS ESTIMATE INSTANTANEOUS VERTICAL LOADING RATE AND PEAK PATELLOFEMORAL JOINT STRESS DURING RUNNING

Doyle, E.¹; Doyle, T.L.A.¹; Bonacci, J.²; Fuller, J.T.¹

¹Macquarie University, Sydney, Australia; ²Deakin University, Sydney, Australia

INTRODUCTION

Patellofemoral pain (PFP) is a commonly reported running-related injury. Runners with PFP demonstrate greater peak patellofemoral joint stress (PFJS) during running than pain-free individuals,¹ which may be associated with injury development. Inertial measurement units (IMU) allow estimation of site-specific stress and vertical loading rates² in field settings by directly measuring acceleration at anatomical landmarks. These estimations could provide a method for field-based load monitoring and running gait retraining that may assist with PFP prevention and management. However, the relationship between IMUs and knee specific kinetics, such as PFJS, is currently unknown. This study investigated the relationship between IMU acceleration measured at different lower limb locations and PFJS and instantaneous vertical loading rate (IVLR) in healthy runners.

METHOD

Thirteen healthy runners (11M / 2F, mean age (years \pm SD) = 35.8 \pm 7.5) were fitted with three IMUs at the distal tibia, proximal tibia, and distal thigh on the right limb. Participants performed 3-minute running intervals on a force-instrumented treadmill at 9, 11, 13, 15 and 17 km/h. Simultaneous kinematic data were collected using an 8-camera 3D motion capture system. Peak vertical (relative to segment) and resultant accelerations were extracted from each IMU and compared to PFJS and IVLR. Relationships between dependent (PFJS and IVLR) and independent variables (IMU acceleration) were explored using linear mixed models that included speed and IMU acceleration as fixed effects and participant as a random effect. The magnitude of differences (effect sizes) was calculated using Cohen's f^2 with values of 0.02, 0.15 and 0.35, representing a small, medium, and large effect size, respectively.

RESULTS

There was a significant relationship between PFJS and peak resultant (coefficient [b] = 0.021, p = 0.041, f^2 = 0.05) (Figure 1A) and peak vertical acceleration (b = 0.019, p = 0.43, f^2 = 0.04) at the proximal tibia regardless of speed. There were no significant relationships between PFJS and acceleration measured at other locations. There was a significant relationship

between IVLR and peak vertical acceleration at the distal tibia (b = 0.644, p < 0.001, f^2 = 0.36), proximal tibia (b = 0.174, p < 0.001, f^2 = 0.22) and thigh (b = 0.584, p = 0.036, f^2 = 0.21) regardless of speed (Figure 1B).

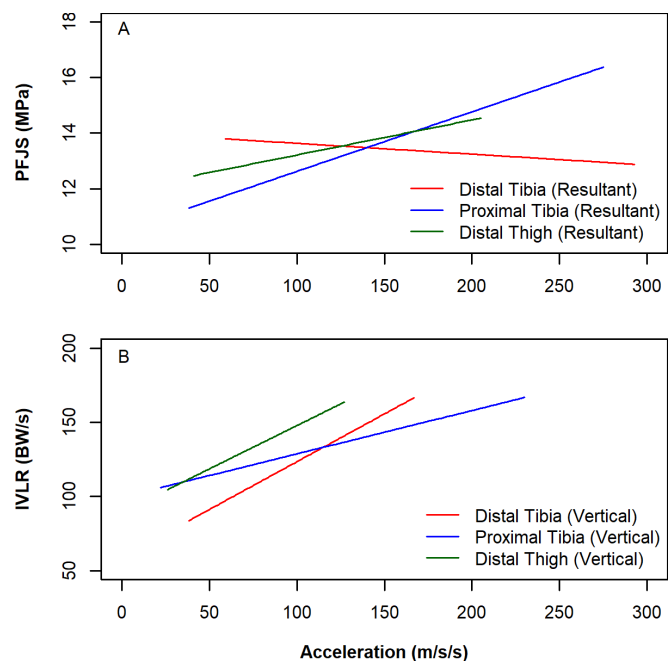


Figure 1. Relationship between peak acceleration for each IMU and PFJS (A) and IVLR (B) at 13 km/h.

CONCLUSIONS

Peak resultant and vertical acceleration values from an IMU attached to the proximal tibia are positively related to PFJS, but the relationships are unlikely to be practically meaningful. Consistent with previous research, peak vertical acceleration values from IMUs attached to the lower limb are positively related to peak IVLR in runners. The strongest relationship to IVLR was observed with peak vertical acceleration measured at the distal tibia. This relationship could form the basis of running gait retraining and monitoring for injury prevention and management.

REFERENCES

- ¹ Liao, T. C. J Appl Biomech. 34(4):298-305, 2018.
- ² Tenforde, A.S. PM&R. 12(7):679-684, 2020.

Presented by Eoin Doyle (eoin.doyle@mq.edu.au).

GLUTEAL MUSCLE FORCES DURING HIP-FOCUSED STRENGTHENING AND INJURY PREVENTION EXERCISES

Collings, T.C.^{1,2}; Bourne, M.N.^{1,2}; Barrett, R.S.^{1,2}; Meinders, E.^{1,2}; Diamond, L.E.^{1,2}
 School of Health Sciences and Social Work, Griffith University, Gold Coast, Australia
 Griffith Centre of Biomedical and Rehabilitation Engineering (GCORE), Menzies Health
 Institute Queensland

INTRODUCTION

Weakness of the hip abductors and extensors are associated with greater dynamic knee valgus in females during single-leg landings (Dix et al., 2017), which may predispose players to knee ligament and patellofemoral injuries. As such, strengthening the gluteal muscles is a core component of knee injury prevention training. However, the optimal exercises to target specific muscles remain unclear. An improved understanding of gluteal muscle forces during common strengthening exercises will enable practitioners to make more informed decisions regarding exercise selection in injury prevention programs. The aim of this study was to compare and rank gluteal muscle forces between hip-focused exercises when performed with and without external weights.

METHOD

This cross-sectional study analysed eight hip-focused exercises commonly used to target the hip abductors and extensors (Moore et al., 2020). Exercises included: banded side-step, hip hike, lunge, side-lying leg raise, side-plank, single-leg hip thrust, single-leg Romanian deadlift (RDL), single-leg squat. Data were collected from five female footballers who regularly performed lower body strength training. Participants reported no history of lower body surgery, and had not sustained any time-loss injuries in the previous 12 months. Participants attended two sessions. In the first, participants were familiarised with the exercises and underwent an assessment of their 12-repetition maximum (12RM) weight for each exercise. All exercises were performed using the preferred balancing leg only. In the second session, three-dimensional whole-body motion (Vicon, UK) and ground reaction forces (AMTI, US) were synchronously recorded while participants performed two sets of five repetitions of each exercise with body weight only, followed by two sets of five repetitions with their 12RM weight. Exercise order was randomised. Data were processed in OpenSim. A generic full body musculoskeletal model (Rajagopal et al., 2016) was linearly scaled to each participant's standing posture. Joint angles were calculated using inverse kinematics. Muscle forces were determined

using static optimization, by minimising muscle activations and constraining force-length-velocity properties. Muscle forces from segments of gluteus maximus (3) and medius (3) were summed, respectively, and peak force (N) was extracted.

RESULTS

The RDL produced the largest magnitude of gluteus maximus muscle force, both with and without external weight. The body weight side plank and hip hike with external weight produced the largest magnitude of gluteus medius muscle force with and without external weight, respectively (Figure 1).

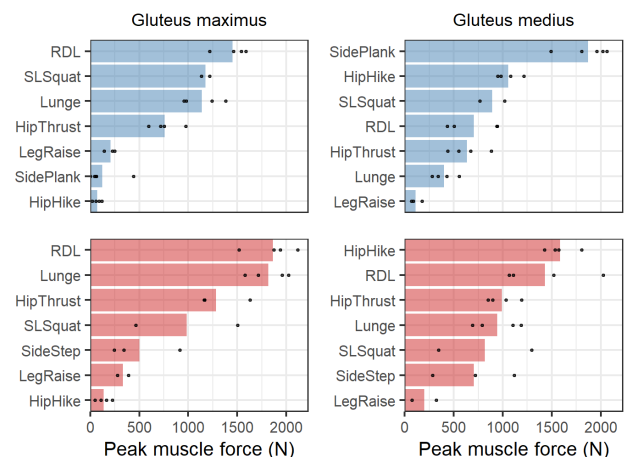


Figure 1. Mean (bars) and individual (dots) peak gluteal muscle forces for body weight only (blue) and 12RM external weight (red) by exercise. RDL, Romanian deadlift; SL, single-leg.

CONCLUSIONS

Peak gluteal muscle forces vary with exercise and external load applied. These preliminary results will be confirmed with a larger sample, and may inform exercise selection for injury prevention and rehabilitation training.

REFERENCES

- Dix, J. Phys Ther Spor 37, 197-209, 2017.
- Moore, D. Int J Sports Phys Ther 15, 856-881, 2020.
- Rajagopal, A. IEEE Trans Biomed Eng 63, 2068-2079, 2016.

Presented by Tyler Collings
 (tyler.collings@griffithuni.edu.au)

BICEPS FEMORIS LONG HEAD NEUROMECHANICAL BEHAVIOUR DURING NORDIC HAMSTRING EXERCISE VARIATIONS: PREELIMINARY RESULTS

Pincheira, P.; Riveros-Matthey, C.; Lichtwark G.

The University of Queensland, School of Human Movement and Nutrition Sciences, Brisbane (4072), Australia.

INTRODUCTION

One exercise that is commonly used to confer protection against hamstrings injury is the Nordic hamstring exercise (NHE) [1]. While the mechanism(s) underlying NHE's preventive benefits are not fully understood, it has been suggested that muscle lengthening induces changes in muscle fascicle lengths so that the muscle is not overstretched in following exercise bouts [1]. Surprisingly, however, the amount of stretch that the muscle suffers during the NHE and his variations is still unknown, largely due to a lack of studies assessing hamstrings' fascicle behaviour during the lengthening phase of the exercise. The aim of this study was to assess and compare biceps femoris long head (BFlh) neuromechanical behaviour during NHE variations. This information may help to reveal the stimuli behind the protective adaptations seen after NHE exercise.

METHOD

Data from six participants is included in these preliminary results (age: 22 ± 2 years; mass: 76 ± 3 kg; height: 176 ± 5 cm), however a full data set of 12 participants has been collected. Participants were asked to perform two NHE variations starting from a kneeling position: the Nordic curl, where the body slowly descends forward with the hips in a fixed position; and the Razor curl, where the participants simultaneously extend at both the hip and knee while extending forward. This variation was chosen to favour stretch in the proximal part of the hamstring muscles. After warming up, participants performed three repetitions of each variation, resisting gravity at a constant speed to the greatest achievable depth. From the dominant leg, BFlh fascicle length (FL) behaviour was recorded using B-mode ultrasound with a dual probe configuration (12 cm field of view). Hip and knee joint displacement was estimated using a motion capture system. An Opensim biomechanical model was then used to estimate BFlh muscle tendon unit (MTU) length. Eccentric knee flexion torque was calculated using a custom-made board with load cells attached to the participant's ankles. BFlh EMG activity was recorded from the contralateral leg. Differences between NHE variations during the eccentric phase (from movement onset to peak of eccentric torque)

were estimated for the dependent variables using Statistical Parametric Mapping ($p < 0.05$).

RESULTS

BFlh MTU operates at a longer length during the Razor, between 22–38 % of the eccentric phase of the exercise (shaded blue area in Figure 1). Absolute MTU stretch was 5.4 cm for the Nordic and 4.1 cm for the Razor (15 and 11% of stretch respectively). FL was similar between exercises (Figure 1), with absolute stretch being 1.28 cm for the Nordic and 0.84 cm for the Razor (12 and 8% of stretch respectively). BFlh activity was higher during the Nordic at 65–77% of the eccentric exercise. No differences were found when comparing eccentric knee torque between NHE variations.

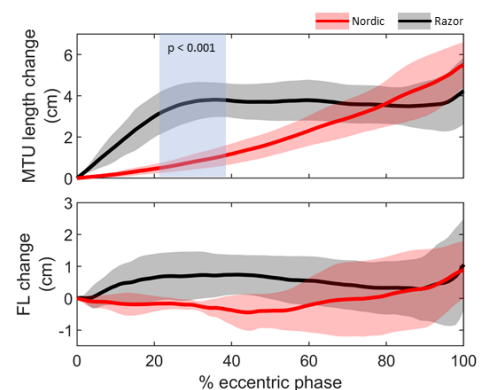


Figure 1. MTU and FL mean (line) and SD (shade) changes during NHE variations.

CONCLUSIONS

Little fascicle stretch occurs during NHE variations in comparison to the MTU. BFlh presents a rather isometric fascicle behaviour during much of the exercise. Hip flexion seems to favour MTU stretch rather than fascicle stretch during the early phase of the Razor. Decoupling between fascicle and MTU length during the NHE suggests that stretch of the elastic tissue of the MTU has an important role in absorbing energy during eccentric contractions. This may be important when considering adaptations to BFlh muscle and connective tissues that might occur from NHE training.

REFERENCES

Bourne, M. J. Br J Sports Med 51, 469-477, 2017.

Presented by Patricio Pincheira (uqppinch@uq.edu.au)

DO MORPHOLOGICAL CHANGES EXPLAIN KNEE FLEXOR WEAKNESS AFTER ANTERIOR CRUCIATE LIGAMENT RECONSTRUCTION?

Adam Kositsky, Rod S. Barrett, Laura E. Diamond, David J. Saxby
Griffith Centre of Biomedical and Rehabilitation Engineering (GCORE), Menzies Health
Institute Queensland, Griffith University, Gold Coast, Queensland, Australia

INTRODUCTION

The semitendinosus (ST) tendon is commonly harvested for anterior cruciate ligament reconstruction (ACLR). Although peak isokinetic knee flexion torque can be recovered following ACLR, weakness at deeper knee flexion angles is consistently reported [1]. As ST is a major contributor to knee flexor torque at high knee flexion angles [2], determining the mechanism(s) behind this deep flexion strength loss is important for successful rehabilitation. Here, we conducted a simulation study investigating the effects of muscle morphology changes post-ACLR with an ST graft on knee flexor strength.

METHOD

Preliminary data from five individuals (29 ± 7 years) that underwent ACLR with an ST-only graft (13 ± 4 months post-surgery) and had confirmed tendon regeneration were included. Participants were positioned prone (hip neutral) and performed maximal voluntary isometric contractions on an isokinetic dynamometer (System 4 Pro, Biodex) at four knee angles (15° , 45° , 60° , 90° ; 0° = full extension), with the order of joint angle and tested limb randomized. T_1 Dixon magnetic resonance images (MRI) were acquired on a 3T unit (Philips) from the iliac crest to mid-shank. The ST muscle was segmented (Mimics v20, Materialise) and muscle volume and length were measured.

Simulations using the mean group data were performed using a Thelen muscle model [3] implemented in a musculoskeletal model [4] (OpenSim 4.1). Adjustments to muscle parameters were made to match MRI measures of muscle morphology. Simulations were performed following adjustments to muscle volume and/or length. For volume, simulations were performed with the maximal isometric muscle force altered by ± 1 standard deviation of the between-leg ST volume deficit. Length-based simulations were performed based on the ± 1 standard deviation change in muscle length; the optimal fiber length was adjusted based on a change in either the number or length of sarcomeres in the anatomical position using a standard equation [5]. Baseline sarcomere data were obtained from previously published cadaveric data [5]. Activation for all involved agonist muscles was set at 1.

RESULTS

ST muscle morphology in the ACLR leg was substantially altered (volume: $-25 \pm 3\%$; length: $-9 \pm 4\%$). Experimental isometric strength was recovered at lower flexion angles (15° : $-1 \pm 11\%$; 45° : $-3 \pm 13\%$) but not in more flexed positions (60° : $-20 \pm 10\%$; 90° : $-33 \pm 8\%$). Simulations demonstrate that muscle morphological changes do not explain strength loss at 90° (Figure 1).

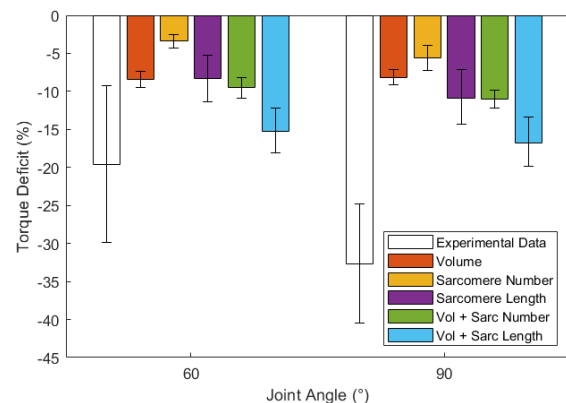


Figure 1. Experimental and simulated torque deficits at 60° and 90° of knee flexion.

CONCLUSIONS

Adjustments to the muscle parameters of ST based on MRI data did not simulate the reduction in flexion torque seen experimentally at 90° . Thus, it appears that factor(s) which were not accounted for in this model (e.g., muscle quality, neural inhibition, etc.) must play a role in strength deficits at 90° . As 90° may preferentially assess ST function given ST's large moment arm at this joint angle [2], determining the mechanism(s) of torque loss may guide and enhance rehabilitation protocols post-ACLR.

REFERENCES

- [1] Ardern, C. *Orthop. Rev.* 1, e12, 2009.
- [2] Herzog, W. *J. Anat.* 182, 213-230, 1993.
- [3] Thelen, D. J. *Biomech. Eng.* 125, 70-77, 2003.
- [4] Lai, A. *Ann. Biomed. Eng.* 45, 2762-2774, 2017.
- [5] Ward, S. *Clin. Orthop. Relat. Res.* 467, 1074-1082, 2009.

Presented by Adam Kositsky adam.kositsky@griffith.edu.au



DAY 2

Young Investigator Award

Award Sponsor:



AUTOMATING CONSTRUCTION OF SUBJECT-SPECIFIC TONGUE MODELS IN PATIENTS WITH OBSTRUCTIVE SLEEP APNOEA

Lloyd, R.A.; Bilston, L.E.

NeuRA, Randwick, NSW, Australia; UNSW, Kensington, NSW, Australia.

INTRODUCTION

Obstructive sleep apnoea (OSA) is a respiratory disorder, characterised by the repetitive partial, or complete closure of the upper airway, reducing air flow during sleep. Coordinated anterior motion of the tongue is needed to maintain airway patency during inspiration¹, and the magnitude of the displacement required depends on individual anatomy¹, and the position of the head².

Subject-specific models can help improve the current understanding of sleep apnoea, as they can isolate the effect of different factors within the population such as variation in anatomy or neural activation. However, producing subject-specific models is too slow and labour-intensive for clinical use. In this work, we aim to produce a pipeline to automate the production of subject-specific models.

METHOD

To automate the segmentation of the oral cavity, the nnU-net framework was used³. For training data, 9 (2 control: 7 OSA) sets of head mDIXON images (1mm isotropic voxels), previously acquired in a 3T MRI, were manually segmented. 7 of these (1 control: 6 OSA) were used to train the 2D Unet segmentation model, 2 were withheld from the model and used for validation. DICE similarity scores were used to assess the accuracy of the segmentation.

Muscle fibre orientations of the tongue are derived from diffusion weighted images (DWI). Constrained spherical deconvolution was used to capture intersecting fibres within the tongue. To reduce the effect of noise on individual fibre paths, an atlas was produced, which was then fitted to each subject's data. DWI were acquired for 6 participants (2 control: 4 OSA) in a 3T MRI (voxel size=3mm isotropic; b-value=700s/mm² in 32 direction). DWI were corrected for eddy current distortion, the fibre orientation distributions (FOD) calculated in MRtrix3, and registered to produce a population average of the FOD. Diffeomorphic registration⁴ was used to align the fibre atlas with the individual FODs.

RESULTS

Figure 1A,B show segmentation of withheld data. Dice

scores were: mandible=0.95, hard palate=0.88, tongue=0.95, geniohyoid=0.89, and hyoid bone=0.75. Figure 1C,D show an example of the fibre atlas fitted to a subject's FOD image. The fitted tracts in the tongue agree with the expected anatomy.

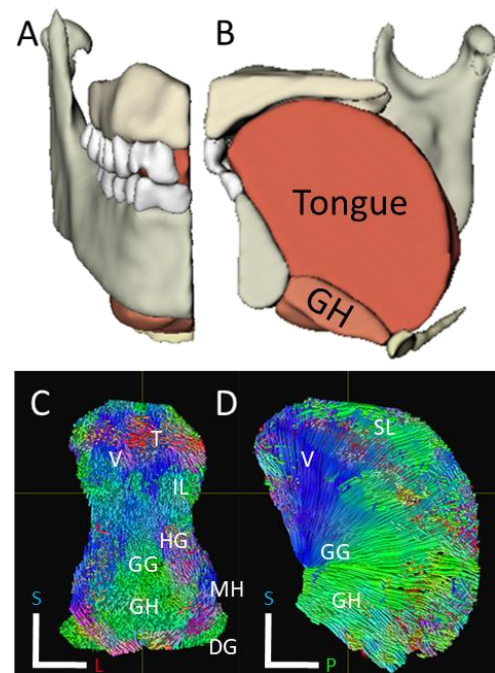


Figure 1. Top: Section view of unsupervised segmentation shown from frontal (A) & midsagittal (B) views. Bottom: Coronal (C) and sagittal (D) slices showing fibre tracts produced from fitting the fibre atlas to this subject. GG: genioglossus, GH: geniohyoid, MH: mylohyoid, HG: hyoglossus, SL: superior longitudinal, IL: inferior longitudinal, DG: digastric, V: vertical, and T: transverse. Where the anatomical directions are coloured as shown by the axes.

CONCLUSIONS

The trained Unet model accurately segments the oral cavity, making subject-specific modelling of a large cohort feasible. Fitting the fibre atlas to subject data, reduces noise and provides an improved estimate of the muscle architecture. Further work is undergoing to combine the geometry and fibre structure into statistical shape models to fully automate the setup of finite element models of the tongue.

REFERENCES

1. Cheng, S. J. *Physiol.* 592, 4763-4774, 2014.
2. Cai, M.. *J.Appl. Physiol.* 188, 362-369, 2016.
3. Isensee, F. *Nat. Methods.* 18, 203-211, 2021.
4. Raffelt, D. *Neuroimage.* 56, 1171-1180, 2011.

Presented by Rob Lloyd (r.lloyd@neuara.edu.au).

DEVELOPMENT OF A SAFETY-CONTROL TRIGGER FOR FUNCTIONAL ELECTRICAL STIMULATION-INDUCED CYCLING

Sousa, A.; Quinn, A.; Mulholland, K; Lloyd, D.; Pizzolato, C.
Griffith Centre of Biomedical and Rehabilitation Engineering (GCORE), Griffith University,
Gold Coast, Australia

INTRODUCTION

Functional electrical stimulation (FES) cycling is considered a safe exercise for individuals with spinal cord injury (SCI). However, there is a recorded risk of bone fractures during the use of FES [1]. Fractures ultimately emerge from excessive forces to the bone, but determining the exact chain of events leading to FES-induced fracture remains challenging. The most plausible cause of injury appears to be a combination of high-intensity FES, spasticity, clonus, low bone density, and additional external forces (e.g., ergometer's motor). The impaired sensory system of individuals with SCI also prevents clinicians from immediately identifying if injuries occurred, possibly contributing to the under-reporting of the issue in the literature [2].

Some closed-loop control strategies attempted to reduce the likelihood of injuries by automatically adapting to biomechanical perturbations [3]. However, control approaches cannot account for all unforeseen conditions (e.g., clonus and spasms). Moreover, automatic control responses may be insufficient or take too long to react. Therefore, we developed a safety-control trigger that continuously monitors cycling torque data, detects harmful activities, and addresses shortcomings. Our system only uses a commercial rehabilitation ergometer without additional sensor inputs while gracefully shutting down the system when events are detected.

METHOD

We developed our solution on a commercial ergometer commonly used for FES cycling in outpatient clinics (RT300, Restorative Therapies, Baltimore, MD, USA). Ergometer torque data were continuously monitored at 50Hz through a framework based on Robot Operating System. Figure 1 illustrates the FES-cycling system with the safety-control trigger. For *clonus detection*, we constantly check if motor torques hold on their maximum value, indicating that muscles are co-activating but not generating movement. We also filter (2nd order Butterworth high-pass filter with a 4Hz cutoff frequency and State-space low-pass filter with a 10Hz cutoff frequency) and differentiate torque for *spasm detection*. The safety-control triggers shutdown if the result is higher than a pre-determined threshold. We tested the entire system with one person without

neurological disorders, instructing them to simulate spasticity and clonus three times each.

RESULTS

The system correctly detected the perturbation in all trials and triggered the stimulator to shut down in less than 12ms and the ergometer in less than 66 ms. Furthermore, the trigger works on a flexible software design. Therefore, it runs with any control setup in the same environment.

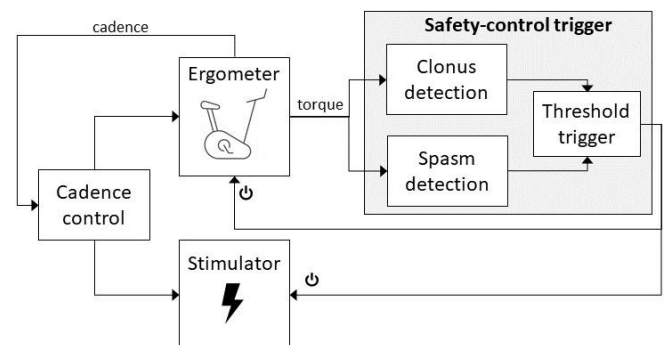


Figure 1. Diagram for the FES-cycling system. *Cadence control* controls the *stimulator* and *ergometer*. The *ergometer* generates assistance torque to adjust speed, while the *stimulator* generates stimulation to muscles. The *safety-control trigger* processes the torque response, and if it detects abrupt movements, it shuts down the *stimulator* and *ergometer* to avoid injuries.

CONCLUSIONS

The presented solution uses the ergometer torque feedback data to detect clonus and spasm automatically. When the safety-control trigger responds, it interrupts the training session by shutting down the hardware. This response decreases the chances of injury by responding faster than current controllers and may contribute to broader use of this therapy. Future work will use electromyography and personalized models to improve torque predictions and voluntary movements.

REFERENCES

- [1] Guimarães et al., E. J. Trans. Myology, 27, 4, 2017
- [2] Young, Neurology, 44, 11, 9, 1994
- [3] Bo et al., IEEE R.&A, 24, 4, 2017

Presented by Ana de Sousa (a.cardosodesousa@griffith.edu.au).

ESTIMATING FACET JOINT APPPOSITION WITH SPECIMEN-SPECIFIC COMPUTER MODELS OF SUBAXIAL CERVICAL SPINE KINEMATICS: THE EFFECT OF AXIAL COMPRESSION AND DISTRACTION DURING SHEAR AND BENDING MOTIONS

Quarrington R.D., Thompson-Bagshaw D.W., Jones C.F.

Spinal Research Group, Centre for Orthopaedic and Trauma Research, Adelaide Medical School, University of Adelaide, Australia

INTRODUCTION

Facet fracture occurs in up to 77% of traumatic cervical facet dislocations (CFD) but is rarely observed in experiments with cadaver tissue [1]. Muscle activation may superimpose an intervertebral compression load on traumatic intervertebral motions, increasing facet joint contact and thereby increasing the probability of fracture with dislocation. Computational models of experimental data can provide a non-invasive method to estimate joint biomechanics during spinal trauma and resulting from surgery. Existing models typically consider each vertebra as one rigid-body (vertebral body + posterior elements) and assume a uniform cartilage depth for each facet. However, facet deflection occurs during intervertebral motion [2], and cervical facet cartilage depth is not uniform [3].

The aim of this project was to use specimen-specific, multi rigid-body C6/C7 computational models with specimen-specific cartilage profiles to investigate the change in facet joint cartilage apposition when intervertebral axial distraction or compression is superimposed on intervertebral flexion (10°), anterior shear (1 mm), axial rotation (4°) and lateral bending (5°) motions.

METHOD

Twelve C6/C7 motion segments (70±13 yr, nine male) underwent high-resolution CT scanning. Specimens were subjected to non-destructive quasi-static anterior shear (AS; 1 mm), right axial rotation (AR; 4°), flexion (F; 10°), and left lateral bending (LB; 5°) motions using a six degree-of-freedom materials testing machine. Each motion was superimposed with: 1) neutral (50 N compression); 2) neck muscle contraction (300 N compression); and, 3) inertial intervertebral separation (2.5 mm distraction). Intervertebral kinematics and facet deflections were measured with motion-capture markers on the vertebral bodies, and the bilateral inferior facets of C6, respectively. The motion-capture data was applied to specimen-specific computer models, and facet cartilage apposition area (CAA) was calculated. For

each test direction, linear mixed-effects models were used to compare CAA at peak motion between axial conditions.

RESULTS

For all motions, CAA was significantly larger for the compressed condition, compared to the neutral and distracted conditions, and for neutral vs distracted ($p<0.001$ for all). CAA was significantly larger for the 'loaded' left facet during axial rotation and lateral bending for all axial conditions ($p<0.001$ for both).

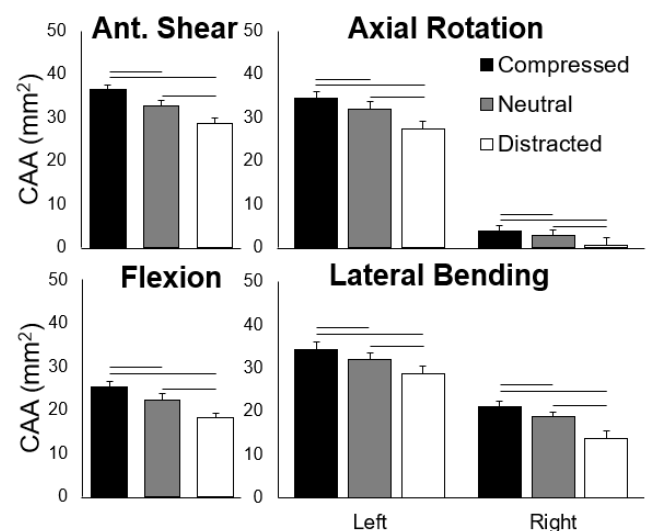


Figure 1. Cartilage apposition area (CAA) results for each motion/axial condition combination. Horizontal lines indicate statistical significance ($\alpha=0.05$).

CONCLUSIONS

Simulated compressive neck muscle activation increased C6/C7 facet contact, compared to distraction, when superimposed on intervertebral shear and bending motions. This suggests that intervertebral compression forces may play a role in facet fracture associated with CFD.

REFERENCES

- [1] Foster, B. IRCOB 2912. [2] Quarrington, R. J. Biomech. 72, 116-124, 2018. [3] Womack, W. Ost. Cartilage 16, 1018-1023.

Presented by Ryan Quarrington

(ryan.quarrington@adelaide.edu.au).

EFFECTS OF PUBERTAL MATURATION ON ANTERIOR CRUCIATE LIGAMENT FORCES DURING A LANDING TASK IN FEMALES

Nasseri, A.; Lloyd, D.G.; Minahan, C.; Sayer, T.A.; Paterson, K.; Vertullo, C.J.; Bryant, A.L.; Saxby, D.J.

Griffith University, Southport 4222, Australia; The University of Melbourne, Parkville 3010, Australia.

INTRODUCTION

Anterior cruciate ligament (ACL) rupture is a common knee injury resulting in substantial health care costs (i.e., surgical care and physical therapy) and elevated risk of early onset knee osteoarthritis. Rates of ACL rupture in young people have increased dramatically over past decades [1], with the resultant burden of early knee osteoarthritis falling on young people with the history of ACL injury. Sex- and age-specific differences in rates of ACL rupture have been observed [1]. There is a two to four times greater risk of sustaining ACL injury in female athletes compared to male athletes. Compared to pre-pubertal girls, late- to post-pubertal young women are at greater risk of ACL injury [2]. However, conclusive causal mechanism(s) for this increased risk of ACL injury in young females have yet to be presented. The purpose of this study was to determine the effects of pubertal maturation in females on ACL force during a dynamic motor task.

METHOD

Based on Tanner's classification system, 19 pre-pubertal, 19 early/mid-pubertal, 24 late/post-pubertal females performed standardized drop-land-lateral jump while three-dimensional body motion, ground reaction forces, and surface electromyography were acquired. These data were used to model external biomechanics, lower limb muscle forces, and knee contact forces, which were subsequently used in a validated computational model [3, 4] to estimate the ACL loading. Statistical parametric mapping analysis of variance was used to compare ACL force, and its causal contributors, between the three pubertal maturation groups during stance phase of the task.

RESULTS

Compared to pre- and early/mid-pubertal females, late/post-pubertal females had significantly higher ACL force (mean differences 482 N and 355 N during 3%-30% and 55%-89% of stance; and 381 N and 296 N during 3%-25% and 62%-85% of stance, respectively). At the peak point of ACL force, contributions from the sagittal, and transverse plane loading mechanisms to ACL force were higher in

late/post pubertal group compared to pre and early/mid pubertal groups (medium effect sizes ranging from 0.44 to 0.77). No differences were found between pre- and early/mid-pubertal groups in ACL force or its contributors (Figure 1).

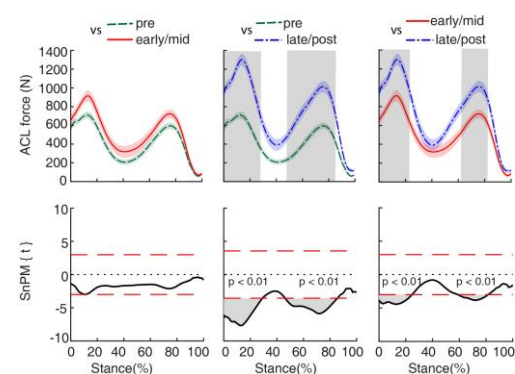


Figure 1. Comparisons of the ACL force during the stance phase of the task between pre-, early/mid-, and late/post-pubertal females performed with statistical non-parametric mapping (SnPM).

CONCLUSIONS

During a standardized drop-land-lateral jump, late/post-pubertal females generated higher ACL forces compared to less mature females across a large percentage of stance, including the instances of peak forces. The sagittal plane was the primary contributor to ACL force in all maturation groups but made relatively lower contribution in the late/post-pubertal group compared to less mature females. Results indicate ACL forces increased across pubertal maturation, and, given the cessation of ACL growth at ~10 years of age in females, may explain the dramatic rise in ACL rupture sustained by females 15-19 years of age. Quantifying ACL force can advance our understanding of the ACL loading mechanism thereby providing insight into better approaches to injury prevention.

REFERENCES

1. Zbrojkiewicz, D. Med J Aust, 208(8), 354-358, 2018.
2. Shea, K.G. J Pediatr Orthop. 24(6), 623-628, 2004.
3. Nasseri, A. Med Sci Sports Exerc, 53(6), 1235-1244.
4. Nasseri, A. Comput Methods Programs Biomed, 184, 105098.

Presenter: Azadeh Nasseri (a.nasseri@griffith.edu.au).

PREDICTING RUPTURE SITE IN ASCENDING AORTIC ANEURYSMS USING PATIENT-SPECIFIC FINITE ELEMENT MODELS

O'Rourke, D; Surman, T; Abrahams, J; Edwards, J, Reynolds, K

College of Science and Engineering, Flinders University, Australia.

D'Arcy Sutherland Cardiothoracic Surgical Unit, Royal Adelaide Hospital, Australia.

INTRODUCTION

Ascending aortic aneurysms are a localised dilation that present a significant clinical risk if untreated. Surgical repair to prevent rupture is recommended for patients with a diameter > 5.5 cm. However, aorta size alone has limited ability in predicting rupture [1]. Finite element (FE) models improve rupture risk prediction by providing an estimation of strength [2]. However, the accuracy in predicting rupture location ascending aorta FE models remains unclear. The aim of this study was to investigate CT-based FE models in predicting regions in the ascending aorta likely to rupture.

METHOD

Pre-rupture and post-rupture CT scans were obtained for 7 patients (5 males) who underwent emergency repair following an ascending aortic rupture. All geometries were retrieved using segmentation and applying a surface mesh. Visible contrast extravasation on the post-rupture image was considered a rupture site. Pre-rupture FE models were characterised with a hyperelastic constitutive model [3] and assigned a 2 mm wall thickness [4]. The equivalent strain from the continuum tissue damage theory was calculated using the backward displacement method [5]. The post-rupture model was registered to the pre-rupture model with a rigid iterative closest point algorithm. The rupture site was projected onto the FE model (Fig. 1). Rupture was predicted if the peak equivalent strain value within the rupture site was greater than the 99th percentile.

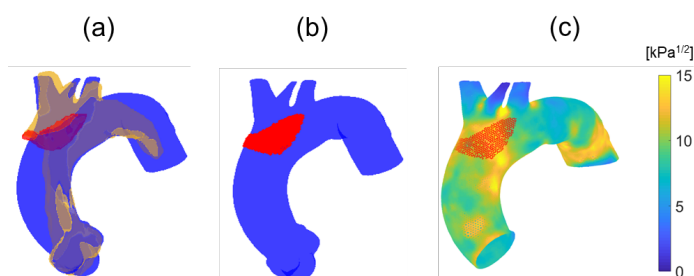


Figure 1. Registering the post-rupture (yellow) and rupture site (red) onto the pre-rupture model (blue) (a) Rigid registration, (b) projecting the rupture site, (c) equivalent strain distribution with rupture site overlaid.

RESULTS

The peak equivalent strain within the rupture sites across the patients was 7.81 – 14.96 kPa^{1/2}. Registration failed in 1 patient due to misalignment of the models. The models predicted rupture in 4/7 remaining patients (Table 1).

Table 1: Peak equivalent strain within rupture site and 99th percentile strain across the aorta for each patient.

Patient	Rupture Site Peak (kPa ^{1/2})	99 th Percentile (kPa ^{1/2})	Rupture	Time between scans (Months)
1	19.7	17.0	Y	0.7
2	14.66	11.67	Y	1
3	7.81	11.25	N	7
4	14.96	14.15	Y	22
5	10.47	19.81	N	46
6	8.58	12.89	N	48
7	Registration failed			59
8	11.85	11.00	Y	64

CONCLUSIONS

The results indicated that the FE models predicted high equivalent strain in regions that coincided with locations of rupture. A limitation was the rigid registration gave only an approximate alignment of the models and failed in one instance. Current preliminary work is investigating the accuracy of patient-specific FE models to aid surgical guidelines for preventing ascending aortic rupture.

REFERENCES

1. Elefteriades et al. J Am Coll Cardiol, 2010
2. Polzer et al., J Vasc Surg, 2020.
3. Gasser et al. J R Soc Interface, 2006
4. Martin et al. Am J Physiol Heart Circ Physiol, 2015
5. Liang et al. Biomech Model Mechan, 2017.

Presented by Dermot O'Rourke
(dermot.orourke@flinders.edu.au)



DAY 2

KEYNOTE 1 – Prof Steven Boyd
University of Calgary, Canada

IN VIVO ASSESSMENT OF HUMAN KNEE BONE MICROARCHITECTURE AND MECHANICS

Boyd, S.K.; Kroker, A.; Besler, B.A.; Bhatla, J.; Shtil, M.; Neeteson, N.; de Bakker, C.; Knowles, N.; Salat, P.; Mohtadi, N.; Manske, S.L.; Walker, R.E.A.
McCaig Institute for Bone and Joint Health, University of Calgary, Canada

INTRODUCTION

Anterior cruciate ligament (ACL) tears are a common knee injury and are associated with an elevated risk of developing osteoarthritis (OA). Bone plays an important role in OA development, and bone mass has been shown in animal models and human studies to decrease immediately following ACL injury before partially recovering. ACL transection models have confirmed this bone loss is driven by trabecular structure degradation, however, this has not been confirmed in humans due to limited *in vivo* image resolution.

The objective of this presentation is to describe the detailed bone microarchitectural changes in the human knee following a unilateral acute ACL tear, using high-resolution peripheral quantitative computed tomography (HR-pQCT), complementary imaging technologies, and numerical methods such as the finite element method.

METHOD

We will focus on a recent study of participants with unilateral ACL tears ($n=15$, 22-44 years of age, 10 female and 5 male) that were followed with HR-pQCT with up to four time points (baseline, +2 months, +4 months, +8 months). The baseline measurement occurred within 6 weeks of injury. Both the ACL deficient and uninjured contralateral knees were imaged at $61\mu\text{m}$ isotropic voxel size (XtremeCT II, Scanco Medical). Bone microarchitecture was assessed up to 7.5 mm below the weight-bearing surfaces of the medial and lateral tibia and femur. The subchondral bone plate (density, thickness), and trabecular bone (density, thickness, number, separation) were quantified. Longitudinal bone changes within each knee were assessed using quadratic temporal mixed effects models.

Complementary imaging modalities such as dual-energy computed tomography (DECT) and magnetic resonance imaging (MRI) provided assessment of the knee joint, specifically applying this multi-modal assessment to the detection and monitoring of bone marrow lesions. Isolating the regions where bone marrow lesions are present, high-resolution image data

was used as input to finite element analysis so that non-invasive assessment of joint mechanics could be determined, and to explore whether these were sites of accelerated changes.

RESULTS

An *in vivo* protocol for knee images was developed using HR-pQCT (Figure 1). We measured bone loss that occurred throughout the injured knee (-4.6% to -15.8%). That loss occurred in a non-linear manner, with loss occurring within the first 7 to 8 months post-injury before a recovery phase was initiated. The subchondral bone plate of the lateral femur significantly decreased in thickness. The contralateral knee was mostly unaffected. Using DECT and MRI images in combination with HR-pQCT, we showed that loss was accelerated where bone marrow lesions were present, although these lesions were transient following the acute injury.



Figure 1. *In vivo* assessment of knee microarchitecture by high-resolution peripheral quantitative CT.

CONCLUSIONS

New techniques for *in vivo* assessment of the human knee will help understand the trajectory of joint changes that may lead to OA, and provide a basis to develop strategies to alter the disease etiology and avoid joint degeneration.

Presented by Steven Boyd (skboyd@ucalgary.ca).



DAY 2

New Investigator Award

Award Sponsor:



CHARACTERISING THE RESPONSE OF HUMAN HEADS DURING A SIMULATED HEAD-FIRST IMPACT

Thompson-Bagshaw, D.W.^{1,2}; Quarrington, R.D.²; Jones, C.F.^{1,2}

(1) School of Mechanical Engineering, The University of Adelaide, South Australia, Australia

(2) Spinal Research Group, Centre for Orthopaedics and Trauma Research, Adelaide Medical School, The University of Adelaide, South Australia, Australia

INTRODUCTION

Tetraplegia can result from spinal trauma during head-first impacts, which are common in automotive rollovers and falls [1]. To understand the mechanisms of such spinal trauma and thereby develop injury prevention tools, biomechanical experiments are performed using cadaver material. Recent head-first impact cadaver models investigating neck trauma have omitted the head (e.g. [1]). However, the impact response of the head is likely important for biofidelic loading of the spine and should be considered in neck-only experiments. The response of the head to a vertex impact has not been characterised. The aim of this study is to assess the effect of vertex impact velocity on the stiffness and absorbed energy of the human head.

METHOD

Twelve fresh-frozen human heads (76±13 yrs; 7 male) were disarticulated from the neck at the occipital condyles, and the mandible was removed. Density-calibrated pre-test computed tomography (CT) scans were obtained to screen specimens for existing trauma. Mean vertex (apex of the sagittal suture) bone mineral density (BMD) and bone thickness were measured from computer segmented models developed from the CT scans, using MIMICS (Materialise NV, Leuven, Belgium). Specimens were fixed to a load cell (20 kN, K6D110, ME, Germany) at the base of a drop tower via a custom support mount that simulated the articular surfaces of the atlas and aligned the head with a horizontal Frankfort plane. Dental acrylic was used to ensure congruency between the mount and occipital condyles. A 17 kg carriage (50th percentile male upper torso mass), with a steel platen (400 cm²), was raised to predetermined heights and dropped via a frictionless rail to impact the specimen at 1 or 3 m/s (the latter is the minimum velocity thought to cause cervical trauma [1]). A linear encoder (10µm resolution, LM15, Rotary and Linear Motion Sensors, Slovenia) fixed to the carriage, was used to measure impact velocity and head deformation.

Stiffness was defined as the slope of the most-linear region of each force-displacement curve. Absorbed energy was defined as the area under the curve to the point of failure, where failure was identified by a sudden reduction in force and verified against time-synchronised high-speed footage. Separate ANCOVA models were used to assess the effect of impact velocity on stiffness and absorbed energy; models were adjusted by gender, age, scalp thickness, vertex bone thickness, and vertex BMD. Fracture type was assessed from post-test CT scans.

RESULTS

Stiffness and absorbed energy were significantly greater ($p < 0.05$) for 3 m/s impacts (4.48 kN/mm; 12 J), than for 1 m/s impacts (2.18 kN/mm; 7.2 J; Figure 1). None of the adjustment factors were significantly associated with the outcome measures. For 1 m/s impacts there was no evidence of cranial vault failure, but basilar fractures consistently occurred at 3 m/s.

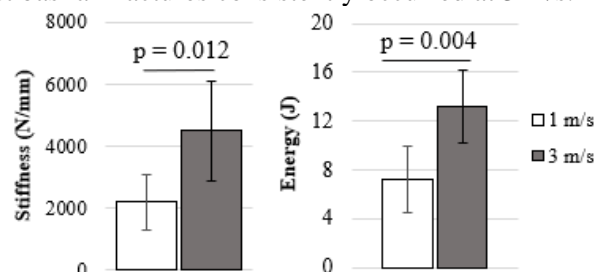


Figure 1: Mean stiffness and absorbed energy, at each impact velocity.

CONCLUSIONS

The stiffness and absorbed energy of cadaveric heads increased from 1 to 3 m/s during a vertex impact with anatomically relevant support conditions. Future head-first impact neck injury models could use this data to select materials to simulate the impact response of the head at the relevant loading rate, to ensure accurate transmission of loads to the cervical spine.

REFERENCES

[1] Saari A, J. Biomech Eng. **135**(11): 111003, 2013

Presented by Darcy Thompson-Bagshaw
(darcy.thompson-bagshaw@adelaide.edu.au).

A NEW MEASUREMENT AND MODELLING APPROACH TO QUANTIFY OCCLUSAL LOADING ACROSS THE DENTAL ARCH

Woodford, S.C.¹; Robinson, D.L.¹; Edelmann, C.²; Mehl, A.²; Röhrle, O.³; Lee, P.V.S.¹ & Ackland, D.C.¹

¹University of Melbourne, Parkville, Australia. ²University of Zurich, Zurich, Switzerland.

³University of Stuttgart, Stuttgart, Germany.

INTRODUCTION

Dynamic, three-dimensional occlusal loading during mastication is clinically relevant in the design and functional assessment of dental restorations and implants, and temporomandibular joint (TMJ) replacements. Unfortunately, dynamic bite force magnitude and direction cannot be measured directly with conventional instrumentation. The aim of this study was to employ low-profile magnetic field sensors, together with intra-oral scanning, to produce accurate measurements of occlusal kinematics during biting and chewing; and secondly, to use this strategy to estimate subject-specific occlusal loading over the entire dental arch using computational modelling.

METHOD

Motion experiments were performed on one male participant (age: 39 yrs, weight: 82 kg) with healthy dentition. Two low-profile magnetic sensors were fixed to the participant's teeth using dental adhesive. The surfaces of both the maxillary and mandibular dental arches, including the magnetic sensors (DMD, Igident), were digitized using an intra-oral scanner. The participant held a soft polyurethane rubber sample between their second molars and ten continuous chewing cycles were undertaken at the participant's preferred bite force. The participant then performed maximal compression (clenching) of the rubber sample. This process was repeated at the first molars, premolars of both the left and right sides, and central incisors. Jaw motion was simultaneously recorded from the two magnetic sensors.

A 3D surface model of the subject's dental arches was reconstructed from the intra-oral scans and imported into a commercial finite element modelling package (Abaqus, Dassault Systems). The rubber sample was digitally reconstructed, meshed and assigned visco-hyperelastic material properties, which were determined from mechanical testing experiments. The measured mandibular motion data was applied to the virtual mandibular teeth to kinematically drive the finite element model for the chewing and biting cycles (Figure 1). Bite force and occlusal loading for each condition were quantified across the entire dental arch.

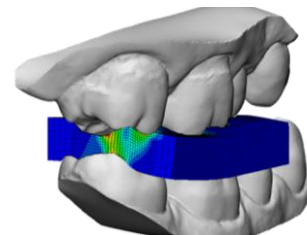


Figure 1: Finite element model of the right first molars compressing the polyurethane rubber sample

RESULTS

The first molars generated the largest bite forces of all teeth, a finding consistent for both chewing (left: 309 N, right: 311 N) and maximum-force biting (left: 496 N, right: 495 N). The incisors generated the smallest bite forces during chewing (75 N) and maximum-force biting (114 N) (Figure 2). The highest bite forces on the mandibular teeth were directed anteriorly.

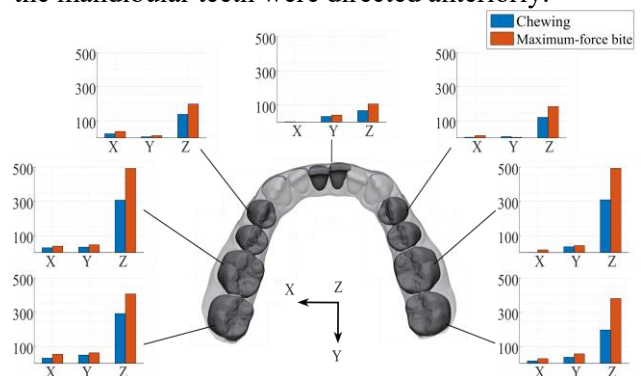


Figure 2: Tooth-specific mandibular bite forces for mean chewing and maximum-force bite tests.

CONCLUSIONS

This study presents a new method of measuring jaw kinematics and provides the modelling methodology to allow the study of dynamic, three-dimensional occlusal loading. These techniques have the potential to facilitate far greater understanding of jaw biomechanics, including investigating the limitations to pain free biting, and the effects of non-axial loading on jaw biomechanics, dental and joint prosthesis design.

Presented by Sarah Woodford
(swood1@student.unimelb.edu.au).

THE IMMEDIATE EFFECT OF FLAT FLEXIBLE VS STABLE SUPPORTIVE WALKING SHOES ON TIBIOFEMORAL JOINT CONTACT FORCE IN PEOPLE WITH VARUS-MALALIGNED MEDIAL KNEE OSTEOARTHRITIS

Starkey, S.C.¹; Hinman, R.S.¹; Paterson K.L.¹; Saxby, D.J.²; Knox G.¹; Hall, M.¹.

¹Centre for Health, Exercise and Sports Medicine, University of Melbourne, Australia

²Griffith Centre of Biomedical and Rehabilitation Engineering, Griffith University, Australia

INTRODUCTION

Pathogenesis of medial knee osteoarthritis (OA) may be due in part to abnormal joint loading. As knee loads are sensitive to foot mechanics, shoe interventions are an attractive self-management strategy for people with knee OA. Clinical guidelines for knee OA recommend stable supportive shoes, and a recent clinical trial by our team showed that stable supportive shoes reduced knee pain compared to flat flexible shoes¹. In contrast, previous biomechanical research has found a lower peak knee adduction moment (KAM) during walking in flat flexible shoes compared to stable supportive shoes². However, the peak external KAM provides limited insight into internal knee mechanics and ignores other features of the medial tibiofemoral contact force (MTCF) waveform, including loading rate.

The aim of this study was to use electromyogram (EMG)-informed neuromusculoskeletal modelling to compare the effects of flat flexible and stable supportive shoes on MTCF waveforms and discrete measures of MTCF and MTCF loading rate in people with medial knee OA and varus malalignment.

METHOD

A randomised cross-over study including 28 participants aged ≥ 50 years with medial knee OA and varus malalignment was conducted. Three-dimensional lower-body motion, ground reaction forces and surface EMG from 12 lower-limb muscles were acquired during six speed-matched walking trials for flat flexible (Vivobarefoot Primus Lite) and stable supportive (ASICS Kayano) shoes, tested in random order. An EMG-informed neuromusculoskeletal model with magnetic resonance imaging informed geometry was used to estimate MTCF (bodyweight, BW). The MTCF waveforms across stance phase of gait were analysed using statistical parametric mapping (SPM) with a repeated measures analysis of variance model (ANOVA). Peak MTCF, MTCF impulse and MTCF loading rates (discrete outcomes) were evaluated using a repeated measures multivariate ANOVA model.

RESULTS

The SPM ANOVA revealed a significant effect ($p=0.001$) (Figure 1), and post-hoc tests showed lower MTCF in stable supportive shoes compared to flat flexible shoes during 5-18% of stance. Peak MTCF and MTCF impulse were not different between the shoe styles. However, mean differences [95% confidence intervals] in loading impulse (-0.02 BW·s [-0.02 , -0.01], $p<0.001$), average loading rate (-1.42 BW·s⁻¹ [-2.39 , -0.45], $p=0.01$), and max loading rate (-3.26 BW·s⁻¹ [-5.94 , -0.59], $p=0.02$) indicated lower measures of loading in stable supportive shoes compared to flat flexible shoes.

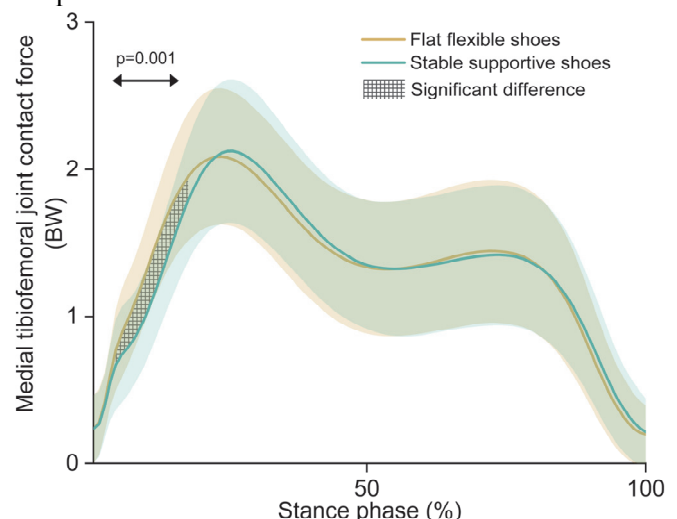


Figure 1. Ensemble average (\pm standard deviation) and region (grey) where MTCF is significantly different between stable supportive shoes (blue) and flat flexible shoes (yellow).

CONCLUSIONS

Stable supportive shoes reduced MTCF during the loading phase of stance and reduced loading impulse and loading rate compared to flat flexible shoes. Stable supportive shoes may therefore be more suitable in people with medial knee OA and varus malalignment.

REFERENCES

1. Paterson, K.L. Ann. Intern. Med. 174, 462-471, 2021
2. Paterson, K.L. Osteoarthr. Cartil. 25, 234-241. 2017.

Presented by Scott Starkey SSSTA@unimelb.edu.au

HUMAN PASSIVE NECK STIFFNESS AND RANGE OF MOTION

Liu, M.^{1,2}; Quarrington, R.D.¹; Robertson, W.S.P.²; Jones, C.F.^{1,2}

(1) Spinal Research Group, Centre for Orthopaedic and Trauma Research, Adelaide Medical School, The University of Adelaide, South Australia, Australia;

(2) School of Mechanical Engineering, The University of Adelaide, South Australia, Australia.

INTRODUCTION

Traumatic cervical spine injuries often have devastating consequences such as long-term disability or even death, and they can be exacerbated by improper neck immobilisation prior to hospital care [1]. Management of these injuries might be improved through better paramedic training via patient simulator mannequins (PSMs). However, a lack of human neck kinematics data restricts the improvement of PSM neck biofidelity. Therefore, the aim of this study is to determine human passive neck stiffness and range of motion (ROM) in flexion/extension, lateral bending and axial rotation.

METHOD

Two custom testing apparatus were used for the bending (flexion/extension and lateral bending) and axial rotation tests. Participants were strapped to each apparatus in the prone or lateral position, and their head was slowly rotated by the researcher to their maximum ROM. The flexion/extension/lateral bending moment was calculated by multiplying the tangential pulling force (9327C, Kistler, SUI; 2 kHz) by its instantaneous moment arm. The axial rotation moment was recorded by a 6-axis load cell (MC3A, AMTI, USA; 2 kHz). Reflective markers were placed on the participants' head, neck, and upper torso to provide the instantaneous moment arm and head/neck kinematic data, via a 13-camera motion capture system (Vantage, Vicon, UK; 100 Hz). An electromyography system (Trigno, Delsys, USA; 2 kHz) with real-time audio feedback was used to alert participants if they exceeded a "passive" muscle activation threshold. Moment-angle plots were generated for each test direction, and neck rotational stiffness was determined from the slope during the final 10 degrees. Paired t-tests were conducted to compare stiffness and ROM between different motion directions (SPSS, IBM, USA).

RESULTS

To date, passive neck stiffness and ROM associated with the six rotational motions have been determined for 5 healthy males (age: 22.8 ± 2.2 years). The final cohort will include males and females from 20 to 80 years of age. Axial rotation had the largest ROM

(Figure 1), followed by flexion and extension. Necks were least mobile in lateral bending. Necks were stiffer in lateral bending (left: 0.138 ± 0.089 Nm/degrees; right: 0.160 ± 0.093 Nm/degrees) than in axial rotation (left: 0.048 ± 0.020 Nm/degrees, $p = 0.035$; right: 0.043 ± 0.010 Nm/degrees, $p = 0.043$). Neck stiffness in flexion (0.053 ± 0.013 Nm/degrees) and extension (0.051 ± 0.040 Nm/degrees) was similar ($p = 0.957$); they were larger than in axial rotation ($p = 0.022$) yet smaller than in lateral bending ($p = 0.004$).

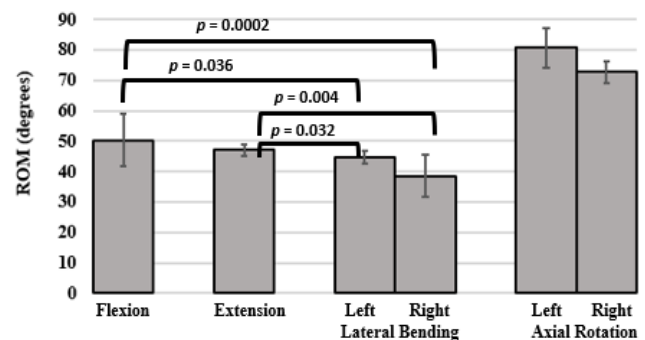


Figure 1. Mean (\pm S.D.) ROM for each neck motion.

CONCLUSIONS

In this study, human necks had the greatest ROM and lowest stiffness in axial rotation, followed by flexion and extension; they were stiffest in lateral bending. Our ROM results were similar to those described in the literature [2, 3], but stiffness values were lower; this may be due to the passive neck muscle condition in our test. Further testing with male and female adult participants in a wide age range will allow us to determine age- and gender-specific reference limits for passive neck stiffness and ROM. This information will inform the design of a biofidelic PSM neck for training and evaluating neck immobilisation techniques.

REFERENCES

- [1] Prasad, V. Spinal Cord 37, 560-568, 1999.
- [2] McGill, S. Clin Biomech 9, 193-198, 1994.
- [3] Dugailly, P. Clin Biomech 53, 65-71, 2018.

Presented by Mingyue Liu
(mingyue.liu@adelaide.edu.au).

RELATIONSHIPS BETWEEN TIBIAL CARTILAGE THICKNESS AND SUBCHONDRAL BONE IN OSTEOARTHRITIS AND CONTROLS

¹Rapagna, S.; ^{1,2}Roberts, B.C.; ^{3,4}Solomon, L.B.; ¹Reynolds, K.J.; ^{3,4}Thewlis, D.; ¹Perilli, E.

¹Medical Device Research Institute, Flinders University, Adelaide, Australia

²Insigneo Institute for in silico Medicine, University of Sheffield, United Kingdom

³Centre for Orthopaedic & Trauma Research, The University of Adelaide, Australia

⁴Department of Orthopaedics and Trauma, Royal Adelaide Hospital, Adelaide, Australia

INTRODUCTION

Tibial cartilage and bone act as a functional unit, responding to daily stimuli together [1]. Nevertheless, relationships between the cartilage thickness and underlying bone microarchitecture, and whether they differ between osteoarthritic (OA) and healthy joints, has not yet been fully investigated.

Aim: to perform, in micro-CT scans of human tibial plateaus from people with end-stage OA and in controls: 1) a systematic spatial mapping (22 regions) of the cartilage and underlying bone morphology; and examine 2) region-specific relationships in these parameters.

METHOD

Participants: Tibial plateaus were retrieved during total knee arthroplasty surgery from 26 people with end-stage knee OA (68±7 years, mass 90±18 kg; varus-aligned (varus-OA; n=16), non-varus-aligned (non-varus-OA; n=10) and from 15 cadavers (62±13 years, mass 83±16 kg; controls) free of musculoskeletal disease in the examined joint. Joint alignment was measured from mechanical axis (pre-operative radiographs).

Micro-CT: The entire plateaus were micro-CT scanned (17 µm/voxel, model 1076, Skyscan-Bruker). Cartilage thickness (Cart.Th), subchondral bone plate thickness (SBPl.Th), porosity (SBPl.Po), and subchondral trabecular bone volume fraction (BV/TV) were analyzed in 22 sub-regions across the tibial condyles (square ROIs, 5 mm width, 3-5 mm length).

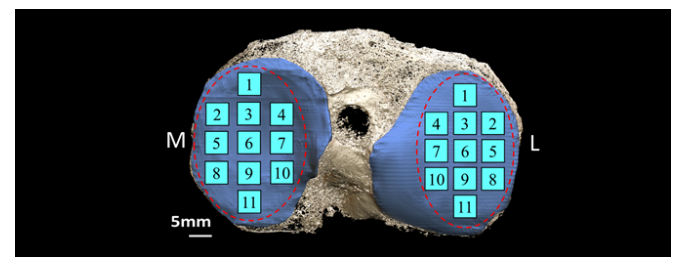
Statistics: For each tissue, within- and between condyle regional differences were evaluated in each group (paired t-tests with Bonferroni adjustment for multiple comparisons). Region-specific relationships between cartilage thickness and subchondral bone parameters were investigated (Pearson's correlations). Statistical significance, p<0.05.

RESULTS

In controls, Cart.Th, SBPl.Th and BV/TV were lowest in the external condylar ROIs and highest in the central and anterior ROIs. In varus-OA the cartilage was thinnest anteriorly in the medial condyle, with high SBPl.Th and BV/TV. In non-varus-OA, the

cartilage distribution was similar to controls, but with higher SBPl.Th and BV/TV.

In controls, there were no relationships between cartilage thickness and the subchondral bone. In OA, however, several significant negative correlations were found (Cart.Th vs SBPl.Th, $r = -0.40$ to -0.72 ; Cart.Th vs. BV/TV, $r = -0.41$ to -0.78 , Fig 1). In both controls and OA, strong positive correlations existed between SBPl.Th and BV/TV ($r = 0.49$ to 0.89) and negative between SBPl.Th and SBPl.Po ($r = -0.40$ to -0.77).



CONTROLS						OSTEOARTHRITIS					
Cart.Th vs. BV/TV						Cart.Th vs. BV/TV					
Medial			Lateral			Medial			Lateral		
-0.01			-0.36			-0.49			-0.39		
0.36	-0.06	0.37	0.15	0.00	-0.28	-0.66	-0.37	-0.29	-0.41	-0.43	-0.32
0.40	0.13	0.01	0.12	-0.09	-0.05	-0.67	-0.51	-0.20	-0.31	-0.42	-0.34
0.35	0.21	0.16	-0.23	-0.14	-0.13	-0.78	-0.51	-0.39	-0.22	-0.48	-0.34
	0.19			0.03			-0.48			-0.48	
Avg 0.23			Avg -0.23			Avg -0.61			Avg -0.45		

Figure 1. Top: 3D representation of a right tibial plateau with the 22 cubic ROIs. Bottom: r-values of region-specific correlations "Cart.Th vs. BV/TV" for control and OA group. Bold values indicate p<0.05.

CONCLUSIONS

This mapping revealed region-specific differences in cartilage thickness and subchondral bone microarchitecture, and relationships among them, depending on the group. Our findings may suggest a cartilage and bone response to habitual loading in OA, which might be altered compared to controls. This systematic approach to tissue mapping of the tibial plateau reveals patterns and region-specific relationships, which may be important in monitoring the progression of OA.

REFERENCES

Imhof H. Invest Radiol 35(10):581-8, 2000.

Presented by: Sophie Rapagna (sophie.rapagna@flinders.edu.au)



DAY 2

Podium 6

RECONSTRUCTION OF HUMAN SUBSCAPULARIS MUSCLE ARCHITECTURE *IN VIVO* USING DIFFUSION TENSOR IMAGING

Zhang, Y.^{1,2}; Herbert, R.D.^{1,2}; Bolsterlee, B.^{1,2,3}

1) University of New South Wales, Randwick NSW, Australia; 2) NeuRA, Randwick NSW, Australia; 3) Queensland University of Technology, Brisbane QLD, Australia.

INTRODUCTION

In vivo quantification of skeletal muscle architecture is usually carried out using ultrasound imaging. However, the human subscapularis muscle cannot be imaged with ultrasound since ultrasound waves are unable to penetrate the scapula. Consequently, measurement of subscapularis architecture has been limited to cadaveric measurements. In this study, we investigated the feasibility of using diffusion tensor imaging (DTI) to reconstruct and quantify the three-dimensional (3D) architecture of the human subscapularis muscle *in vivo*.

METHOD

The study was performed on five healthy adult subjects (three males, two females; age 37 ± 8 years; height 170.0 ± 5.4 cm; weight 67.0 ± 5.1 kg). mDixon anatomical scans and DTI scans were acquired from the right shoulder of each participant using a 3T MRI scanner (Philips Ingenia CX). The subscapularis muscle was manually outlined on mDixon scans to create a 3D surface model (Figure 1A), from which muscle volume was calculated. Anatomically constrained DTI tractography [1] was used to reconstruct the path of muscle fascicles and quantify 3D muscle architecture (Figure 1B). Physiological cross-sectional area (PCSA) was calculated by dividing muscle volume by the mean fascicle length.

RESULTS

The orientation of reconstructed fascicles showed convincing visual correspondence with the known anatomy of the subscapularis muscle (Figure 1C).

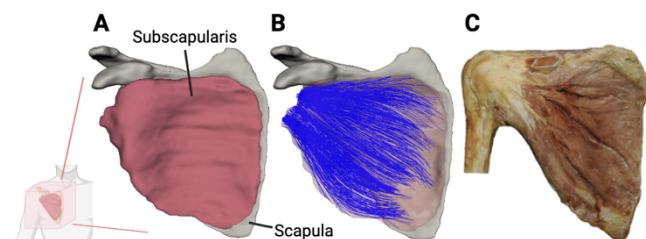


Figure 1. Anterior view of (A) 3D surface models of the scapula and subscapularis; (B) fascicle reconstruction of the subscapularis; and (C) subscapularis of a cadaver [2].

Table 1 compares the muscle architectural parameters from this study and previously published data obtained by cadaveric dissection. Overall, the DTI measurements are in good accordance with

measurements reported in cadaver studies. The mean muscle volume and fascicle length measured in this study are, respectively, 41% and 20% larger than those reported by Ward et al. [2], and 11% and 13% larger than those reported by Mathewson et al. [3]. Age differences could account for differences between our data and the cadaveric data.

Table 1. Age and muscle architectural properties from this study and two previously published cadaver studies. Values are mean \pm standard deviation across participants.

Studies	Age (years)	Muscle volume (cm ³)	Fascicle length (cm)	PCSA (cm ²)
This study (n = 5)	37 \pm 8	129 \pm 32	7.2 \pm 0.2	18 \pm 4
[2] (n = 10)	89 \pm 12	92 \pm 33	6.0 \pm 1.5	16 \pm 4
[3] (n = 12)	62 \pm 14	117 \pm 42	6.4 \pm 1.3	19 \pm 7

CONCLUSIONS

This study demonstrates the feasibility of reconstructing, visualizing and quantifying the complex 3D architecture of the human subscapularis muscle *in vivo* using DTI and anatomically constrained tractography. This technology provides an opportunity to noninvasively study muscle structure-function relationships in living humans, develop anatomically realistic computational models of the human shoulder, and help evaluate (patho)physiological adaptation of rotator cuff muscles.

REFERENCES

- [1] Bolsterlee et al., PeerJ 6, e4610, 2018.
- [2] Ward et al., Clin. Orthop 449, 157-163, 2006.
- [3] Mathewson et al., J. Exp. Biol 217, 261-273, 2014.

Presented by Yilan Zhang
(yilan.zhang@neura.edu.au).

INTERNAL MICROSTRUCTURAL DEFORMATION OF THE TIBIAL PLATEAU UNDER LOADING

Bennett, K.J.¹, Wearne, L.², Rapagna, S.², Martelli, S.³, Atkins, G.J.¹, Solomon, L.B.^{1,4}, Perilli, E.², Thewlis, D.^{1,4}

¹The University of Adelaide, Adelaide 5000, Australia; ²Flinders University, Tonsley 5042, Australia; ³Queensland University of Technology, Brisbane 4000, Australia; ⁴Royal Adelaide Hospital, Adelaide 5000, Australia.

INTRODUCTION

The mechanical response of trabecular bone structures in the knee due to external load can currently only be implied from external measurement. Using a combination of large specimen micro-CT imaging and digital volume correlation (DVC), this behavior can be examined. The aims of this study were to: (1) visualise the human proximal tibia bone microstructure while under an axial load using micro-CT imaging and, using these images, (2) calculate the strain distribution within the proximal tibia under load.

METHOD

Cadaveric knee specimens (n=3) were obtained. All soft tissues except for the articular cartilage and menisci were removed. The femur and tibia were mounted within a custom-made loading stage developed earlier [1]. The loading rig containing the specimen was positioned within a large-volume micro-CT scanner (Nikon XT H 225, Nikon Metrology, UK). Scans were performed at 46 μm isotropic pixel size in unloaded and then loaded conditions, with the proximal tibia and the distal femur contained in the field of view (86 x 86 mm, width x height). Axial loads equivalent to three bodyweights were applied to each specimen, based on the donor's mass at time of death. The angle of the femur was altered to obtain a 60:40 medial:lateral loading ratio. Loads were measured using a six degree-of-freedom load cell. Micro-CT cross-section images were reconstructed CTPro3D (Nikon Metrology). The loaded dataset was co-registered using DataViewer (Bruker) to the unloaded. Digital volume correlation (DVC) analysis was undertaken to calculate Von-Mises equivalent strains in four cylindrical volumes of interest (VOIs) (10x10 mm, diameter x length) located in regions of high and low loading [2] using DaVis (LaVision). The final subvolume size was 34 voxel subvolume length. The VOIs were: anteromedial (AM), anterolateral (AL), posteromedial (PM), and posterolateral (PL).

RESULTS

Within the four regions examined (Fig. 1), strains were within 1385-2170 $\mu\epsilon$. The highest strains were computed in the PM VOI (2170 \pm 640 $\mu\epsilon$ mean \pm SD).

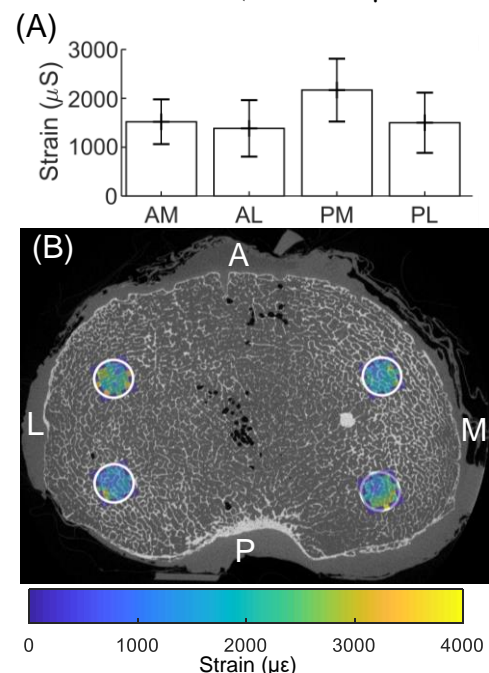


Fig. 1 (A) Mean and standard deviation (error bars) of strains within the four cylindrical VOIs. (B) Micro-CT cross-section of a human proximal tibia, with strains under load in the VOIs.

CONCLUSIONS

Micro-CT scans of three proximal human tibiae were obtained, in unloaded and loaded conditions. Using DVC, the internal strains were quantified. These were within the physiological range reported in the literature [3] and were highest in the posteromedial region. The study will continue, with the final aim to inform computational models of bone mechanics.

REFERENCES

- [1] Martelli S. J. *Mech Behav Biomed Mater.* 84: 267-272, 2015
- [2] Roberts B.C. *Osteoarthr. Cartil.* 25:1623-1632, 2017
- [3] Frost H.M. *Anat. Rec.* 1:1-9 (1987)

Presented by Kieran James Bennett
(Kieran.bennett@adelaide.edu.au).

DEEP LEARNING METHODS FOR AUTOMATED MEASUREMENT OF LOWER LEG MUSCLE VOLUMES FROM MRI SCANS OF CHILDREN WITH AND WITHOUT CEREBRAL PALSY

Zhu, J.^{1,2}; Bolsterlee, B.^{1,2,3}; Chow B.V.Y.^{1,2}; Cai, C.¹; Herbert, R.D.^{1,2}; Song, Y.¹; Meijering, E.¹

1) University of New South Wales, Randwick NSW, Australia; 2) Neuroscience Research Australia, Randwick NSW, Australia; 3) Queensland University of Technology, Brisbane QLD, Australia.

INTRODUCTION

Cerebral palsy is a condition that is known to affect muscle growth [1]. The most detailed investigations of muscle growth use magnetic resonance imaging (MRI). Measurement of muscle volumes from MRI scans currently requires manual segmentation of muscles, which is time-consuming and subjective. In this study, we test two deep learning models [2] for automated measurement of muscle volumes from MRI scans of children with and without cerebral palsy.

METHOD

Using a 3T MRI scanner (Philips Ingenia CX), T1-weighted MRI scans were obtained from the lower legs of 20 children, 6 of whom had cerebral palsy. Participants ranged in age from 5 to 15 years, weight from 17 to 77 kg and height from 108 to 172 cm. One researcher segmented 11 muscles and two bones (tibia and fibula) on all 20 scans. Some of the smaller muscles were grouped into muscle groups. Five scans were also segmented by another researcher to determine inter-rater performance.

2D UNet and H-DenseUnet networks were trained to automatically segment muscles and bones from the MRI scans. (H-DenseUnet is a hybrid network that combines 2D and 3D features [2].) Five-fold cross-validation was used to compare performance between models. Performance was evaluated by the **volume error**: the absolute difference in volume of automated and manual segmentations. The volume error of a scan is the median error of all labels in that scan.

RESULTS

The H-DenseUNet and the UNet gave plausible segmentations of most muscles on most scans. The median volume error across scans was 2.6 cm³ for both models, slightly lower than the median inter-rater volume error of 3.3 cm³. Performance varied between muscles (Table 1). Expressed as a percentage of mean muscle volume, median errors were 5.1% for the H-DenseUNet and 7.3% for the UNet.

Table 1 Mean muscle volume (from manual segmentations) and volume error of automated measurements from two deep learning models of selected muscles. Each cell shows the median error (1st quartile, 3rd quartile) of 20 scans. The last column shows inter-rater performance of 5 scans. LG=lateral gastrocnemius; MG=medial gastrocnemius; SOL=soleus; TA=tibialis anterior; TP=tibialis posterior.

	Volume (cm ³)	Error (cm ³)		
		UNet	H-Dense UNet	Inter-rater
LG	48.7	2.0 (1.4, 7.3)	2.6 (2.0, 9.6)	2.6 (1.2, 2.6)
MG	81.7	6.0 (2.2, 13.4)	5.6 (1.9, 9.9)	3.5 (0.7, 3.9)
SOL	166.1	8.1 (3.9, 22.6)	6.2 (2.4, 16.2)	10.4 (6.2, 13.3)
TA	51.3	2.3 (1.4, 5.8)	2.1 (1.3, 4.7)	3.3 (1.2, 3.6)
TP	52.9	1.9 (0.6, 5.3)	2.6 (1.8, 4.1)	3.4 (1.6, 4.2)

CONCLUSIONS

Deep learning can be used for automated measurement of muscle volumes from MRI scans of children's lower legs, with typical errors similar to those of manual segmentations. Further analyses (not presented here) show performance was similar between scans of typically developing children and children with cerebral palsy. These automated methods enable large-scale investigation of typical muscle growth and disordered muscle growth in children with cerebral palsy.

REFERENCES

- [1] D'Souza, A. Clin Biomech 68, 205-211, 2019.
- [2] Li, X. IEEE Trans Med Imag 37 (12), 2663-2674, 2018.

Presented by Bart Bolsterlee
(b.bolsterlee@neura.edu.au).

SHAPE DIFFERENCES IN THE SEMITENDINOSUS FOLLOWING TENDON HARVESTING FOR ANTERIOR CRUCIATE LIGAMENT RECONSTRUCTION

du Moulin, W¹; Bourne M¹; Diamond, L.E.¹; Konrath, J¹²; Vertullo, C¹³; Lloyd, D¹; Saxby, DJ¹.

¹Griffith Centre of Biomedical and Rehabilitation Engineering (GCORE), Menzies Health Institute Queensland, Griffith University, Gold Coast Campus, Gold Coast, Australia

²Principia Technology, Crawley, Western Australia, Australia

³Knee Research Australia, Gold Coast, Queensland, Australia.

INTRODUCTION

Anterior cruciate ligament reconstruction (ACLR) using a semitendinosus (ST) autograft, with or without gracilis (GR), results in donor muscle atrophy and retraction. Measures such as length, cross-sectional area, and volume may not fully describe the effects of tendon harvest on muscle morphology as these discrete measures lack spatial resolution and cannot characterize three-dimensional muscle shape. This study aimed to determine between-limb ST shape similarity and regional morphology in individuals with a unilateral history of ACLR using a ST-GR graft, and healthy controls.

METHOD

A secondary analysis of magnetic resonance imaging was undertaken from 18 individuals with unilateral history of ST-GR ACLR and 18 healthy controls. ST muscles were manually segmented, and shape similarity were assessed between limbs and groups using Jaccard index (0-1) and Hausdorff distance (mm). ST length (cm), peak cross-sectional area (CSA) (cm²), and volume (cm³) was compared between surgically reconstructed and uninjured contralateral limbs, and between the left and right limbs of control participants with no history of injury. For all comparisons Cohen's *d* was reported as a measure of effect size.

RESULTS

Compared to healthy controls, the ACLR group had significantly ($p < 0.001$, $d = -2.33$) lower bilateral ST shape similarity. Furthermore, the deviation in muscle shape was significantly ($p < 0.001$, $d = 2.12$) greater in the ACLR group. Within the ACLR group, maximum Hausdorff distance indicated ST from the ACLR limb deviated (23.1 ± 8.68 mm) from the shape of the healthy contralateral ST, this was observed particularly within the distal region of the muscle. Compared to the uninjured contralateral limb (Figure 1.) and healthy controls, deficits in peak cross-sectional area and volume in ACLR group were largest in proximal ($p < 0.001$, $d = -2.52$ to -1.28) and middle ($p < 0.001$, $d = -1.81$ to -1.04) regions.

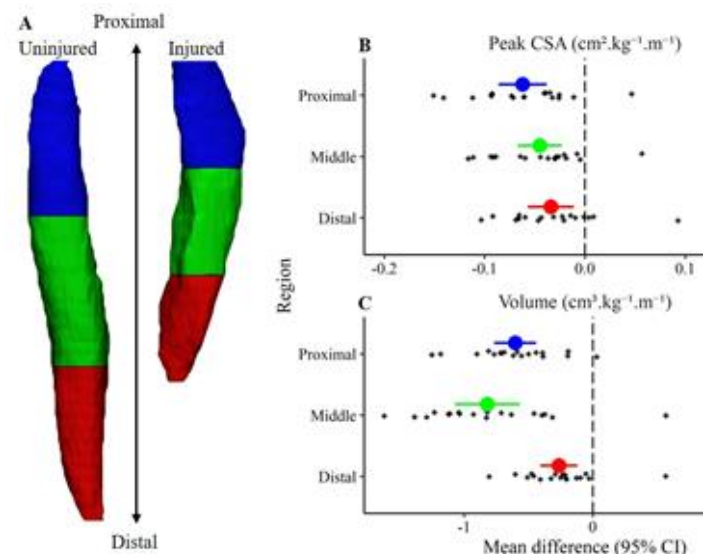


Figure 1. Mean difference of regional morphology in ACLR participant (injured - uninjured). **A)** A representative ACLR participant depicting ST muscle length in proximal (blue 100%-66%), middle (green 66%-33%), and distal (red 33%-0%) regions, **B)** normalised peak cross-sectional area (CSA), and **C)** normalised muscle volume across each region. 95% CI- 95% confidence interval of the mean difference.

CONCLUSIONS

Shape similarity analysis provided unique insight into regional adaptations in ST morphology post-ACLR. Findings highlight morphological features in distal ST not identified by traditional discrete morphology measures. ST shape was most different in the distal region of the muscle, despite deficits in CSA and volume being most pronounced in proximal and middle regions. ST shape following ACLR may affect force transmission and distribution within the hamstrings and contribute to persistent deficits in knee flexor and internal rotator strength. Future research should determine if ST shape change post-ACLR contributes to elevated risk secondary ACL injury.

Presented by William du Moulin
(will.dumoulin@griffithuni.edu.au)

EFFECT OF UPPER AIRWAY FAT ON TONGUE INSPIRATORY MOVEMENT IN AWAKE PEOPLE WITH OBSTRUCTIVE SLEEP APNEA

Jugé, L.^{1,2}; Olsza, I.¹; Knapman, F.L.^{1,2}; Burke, P.G.R.^{1,2,3}; Brown, E.C.^{1,4}; Stumbles, E.⁴; Bosquillon de Frescheville, A.F.¹; Gandevia, S.C.^{1,2}; Eckert, D.J.^{1,2,5}; Butler, J.E.^{1,2}; Bilston, L.E.^{1,2}

¹ Neuroscience Research Australia, Sydney, NSW, Australia; ² University of New South Wales, Sydney, NSW, Australia; ³ Macquarie University, Sydney, NSW, Australia; ⁴ Prince of Wales Hospital, Sydney, NSW, Australia; ⁵ Flinders University, Adelaide, SA, Australia.

INTRODUCTION

Obesity predisposes to, and increases the severity of, obstructive sleep apnea (OSA), a common breathing disorder, characterized by sleep fragmentation due to recurrent partial or complete airway collapses. However, how obesity contributes to OSA is only partially understood, undermining our understanding of the heterogeneity of OSA pathophysiology.

Tongue neuromuscular compensation likely plays a crucial role in maintaining airway patency during inspiration in obese people without OSA. Higher tongue fat content could be a mechanism by which tongue dilatory motion could be impaired in obese people with OSA. Thus, in this study we examined the effect of tongue fat content on inspiratory tongue motion. The aim was to describe the association of regional fat content of the tongue with tongue muscle dilatory movement during inspiration in OSA patients and healthy controls.

METHOD

63 participants without or with untreated OSA (48 men, age [20-73 years], body mass index (BMI) [21-38 kg/m²]) underwent a 3T magnetic resonance imaging (MRI) scan. Mid-sagittal inspiratory tongue movements were imaged using tagged MRI during wakefulness¹. Tissue percentages of fat were quantified using a mDIXON scan².

Four neuromuscular compartments of the genioglossus, the largest upper airway dilator muscle, were identified for regional analysis: 1- posterior horizontal, 2- anterior horizontal, 3- posterior oblique, and 4- anterior oblique.

Standard in-laboratory polysomnography was performed to determine OSA severity from the apnea-hypopnea index (AHI).

Using SPSS (v24, IBM, Armonk, NY, USA) relationships between fat percentage measurements and inspiratory movements were tested with Spearman correlations for all participants, while relationships between AHI and inspiratory tongue movement and fat percentage were assessed with partial Spearman correlations controlling for age, BMI and gender.

RESULTS

Data were obtained for 10 controls and 40 participants with OSA. Overall, the population had an average BMI of 27±5 kg/m² (11 obese participants).

Regional tongue movements during inspiration were not related to the local percentage of tongue fat (Horizontal posterior: P=0.99, Horizontal anterior: P=0.10, Oblique posterior: P=0.23, and Oblique anterior: P=0.43).

Increased OSA severity (higher AHI) was associated with a larger dilatory movement of the anterior horizontal compartment (partial Spearman, $r = -0.33$, $P = 0.023$). Other inspiratory tongue movements and all fat percentages were not associated with AHI.

CONCLUSIONS

Neuromuscular compensatory response in people with OSA was not influenced by higher tongue fat content. However, the study population is less overweight than the typical OSA population and whether this is also true in more obese patient populations requires further investigation.

REFERENCES

¹Jugé, L. J. Physiol. 598 (3): 581-597, 2020.

²Ma, J. J Magn Reson Imaging. 28 (3): 543-558, 2008.

Presented by Lynne Bilston (l.bilston@neura.edu.au).

GLUTEAL MUSCLE ATROPHY IN INDIVIDUALS WITH HIP OSTEOARTHRITIS AND ITS EFFECT ON ESTIMATIONS OF MAXIMUM ISOMETRIC MUSCLE FORCES

¹Mangi, M.D.; ¹Bahl, J.S.; ²Taylor, M.; ^{1,3}Solomon, L.B.; ^{1,3}Smitham, P.; ⁴Arnold, J.B.;
^{1,3}Thewlis, D.

1. Centre for Orthopaedic and Trauma Research, University of Adelaide, Adelaide, Australia; 2. Medical Devices Research Institute, Flinders University, Adelaide, Australia; 3. Department of Orthopaedics and Trauma, Royal Adelaide Hospital, Adelaide, Australia; 4. Allied Health & Human Performance Unit, University of South Australia, Adelaide, Australia.

INTRODUCTION

Estimations of muscle and joint forces are sensitive to musculotendon parameters, including the maximum isometric muscle force (MIMF).¹ Handsfield's equations allow MIMF to be calculated from an individual's height and mass.² However, these equations were based on healthy subjects, which may not reflect the muscle atrophy and fat infiltration seen in individuals with hip osteoarthritis (OA) or other musculoskeletal conditions. This study aimed to quantify muscle atrophy and fat infiltration in patients with end-stage hip OA, and compare MRI estimates of MIMF with height-mass scaling.

METHOD

Eight individuals with unilateral end-stage hip OA undergoing primary total hip arthroplasty were recruited. Patients underwent an MRI of the pelvis and thighs using a T2 turbo spin echo Dixon sequence (3.0 Tesla Siemens Skyra). The total muscle volume and fat content of the gluteus maximus, gluteus medius, and gluteus minimus of the OA and non-OA hips was segmented using Mimics (version 22.0, Materialise N.V., Belgium). A Boolean operation was performed to subtract the fat from the total muscle volume. Paired samples *t*-tests were used to test the difference between ipsilateral and contralateral total muscle volumes and between ipsilateral and contralateral muscle volumes with fat infiltration subtracted. Paired samples *t*-tests were used to compare estimates of MIMF from height-mass scaling to MRI.

RESULTS

Muscle volumes of the OA hip were significantly smaller than the non-OA hip for the gluteus maximus (-25%, $p<0.001$), medius (-15%, $p=0.006$), and minimus (-17%, $p=0.116$) (Table 1). Muscle volumes were further reduced when accounting for fat infiltration: gluteus maximus (-31%, $p<0.001$), medius (-18%, $p=0.004$), and minimus (-24%, $p=0.099$). The loss in gluteus maximus volume of the

OA hip (-3.6 cm³/kg) was comparable to the average of the entire volume of the gluteus medius. Height-mass scaling significantly overestimated MIMF for all three gluteal muscles of the OA hip (Figure 1).

Table 1. Average total and fat subtracted muscle volumes of the non-OA and OA hip (cm³/kg).

N=8	Non-OA	Non-OA fat-sub	OA	OA fat-sub
G.Max	10.83	10.45	8.09*	7.23*
G.Med	3.84	3.74	3.26*	3.08*
G.Min	1.22	1.15	1.01	0.87

* $P \leq 0.05$ compared to the non-OA muscle volume.

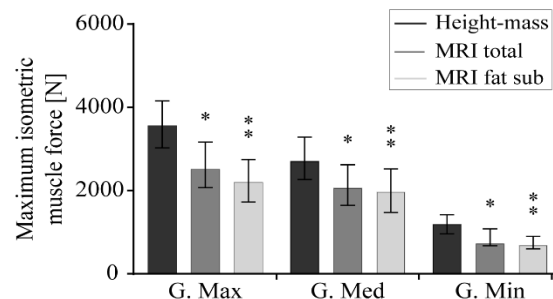


Figure 1. Comparison of MIMF estimates from height-mass scaling and MRI. * Significant difference to height-mass scaling. ** Significant difference to height-mass scaling. $P \leq 0.05$.

CONCLUSIONS

Individuals with end-stage hip OA have considerable atrophy and fat infiltration of the gluteal muscles of the OA hip. Consequently, the typical height-mass scaling of MIMF for biomechanical models is not appropriate for individuals with end-stage hip OA.

REFERENCES

1. Bosmans, L. J. Biomech 48, 2116-2123, 2015.
2. Handsfield, G. J. Biomech 47, 631-638, 2014.

Presented by Mohammad Mangi
(mohammad.mangi@adelaide.edu.au).



DAY 2

Podium 7

PATIENT REPORTED OUTCOMES AND GAIT FUNCTION IN PATIENTS FOLLOWING PRIMARY AND REVISION TOTAL HIP ARTHROPLASTY: A 1-YEAR FOLLOW-UP STUDY

¹Chai, H.; ¹Bahl, J.S.; ¹Grace, T.M.; ^{1,2}Smitham, P.; ^{1,2}Solomon, L.B.; ^{1,2}Thewlis, D.
1. Centre for Orthopaedic and Trauma Research, University of Adelaide, Adelaide, Australia; 2. Department of Orthopaedics and Trauma, Royal Adelaide Hospital, Adelaide, Australia

INTRODUCTION

Primary total hip arthroplasty (THA) is a highly successful procedure at relieving pain and improving functional outcomes. However, the replacement may fail, requiring a revision THA, which has technical challenges resulting in longer surgical times and increased costs.[1] Accordingly, the notion is that revision THA results in worse outcomes compared to primary THA, despite limited evidence to substantiate this.[2] This study aims to quantify self-reported outcomes and gait function in patients following primary and revision THA.

METHOD

Forty-three patients undergoing primary THA for osteoarthritis and 23 patients undergoing revision THA were recruited and followed longitudinally for their first 12 postoperative months. Reasons for revision were loosening (73%), dislocation (9%), and infection (18%). Patients completed the Hip dysfunction and Osteoarthritis Outcome Score (HOOS) [3], and underwent gait analysis preoperatively, and at 3 and 12 months postoperatively. A 10-camera motion analysis system (Vicon) recorded marker trajectories during walking at self-selected speeds. A generic lower-body musculoskeletal model (Gait 2392) was scaled using principal component analysis [4] and the inverse kinematics tool in Opensim 3.3 was used to compute joint angles. Independent samples *t*-test and statistical parametric mapping were used to compare patient reported outcomes and gait patterns, respectively between the primary and revision groups at each timepoint.

RESULTS

Preoperatively, patients undergoing primary THA reported significantly worse pain ($p<0.001$), symptoms ($p<0.001$), function ($p<0.001$), and quality of life ($p=0.004$) (Table 1). No differences were observed at 3 and 12 months postoperatively or in gait patterns between patients who had received a primary or revision THA. The only observed difference in gait pattern was that patients with a revision THA had reduced hip extension at 3 months (Figure 1).

Table 1. HOOS outcome scores for primary and revision groups; Mean (SD).

		Preop	3m	12m
Pain	Primary	36 (16)	84 (15)	85 (20)
	Revision	64 (26)*	82 (19)	82 (19)
Symptoms	Primary	39 (17)	82 (16)	85 (16)
	Revision	65 (21)*	82 (16)	83 (20)
ADL	Primary	37 (63)	78 (23)	82 (20)
	Revision	63 (23)*	80 (17)	75 (20)
QOL	Primary	19 (17)	70 (26)	72 (29)
	Revision	38 (27)*	64 (22)	67 (16)

* $P\leq 0.05$; ADL = activities of daily living. QOL = quality of life

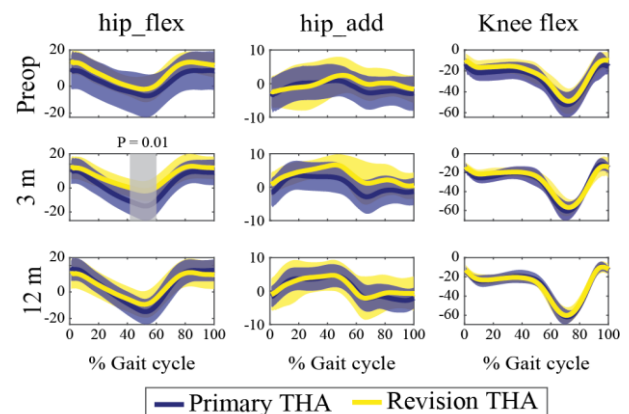


Figure 1. Hip and knee joint kinematics at each timepoint. Grey bar indicates significant difference between primary and revision THA groups from the SPM analysis.

CONCLUSIONS

Despite the notion that patients with a revision THA are likely to have worse outcomes, this study demonstrated no differences in patient-reported outcomes and gait patterns 12 months postoperatively.

REFERENCES

- [1] Vanhegan, I.S., J Bone & J Surg, 94, 5, 2012
- [2] Springer, B.D., J Clin Orthop, 467, 166-173, 2009
- [3] Nilsson A.K., J BMC 4, 10, 2003
- [4] Bahl J.S., J Biomech 85, 164-172, 2019.

Presented by Harvey Chai
haowei.chai@adelaide.edu.au

CHANGES IN POST-OPERATIVE LOWER LIMB BIOMECHANICS AFTER FEMORAL NAILING OF PROXIMAL FEMUR FRACTURES

Sivakumar, A.¹; Rickman, R.^{2,1}; Thewlis, D.^{1,2}

Centre for Orthopaedic & Trauma Research, The University of Adelaide, Adelaide SA, Australia; Department of Orthopaedics & Trauma, Royal Adelaide Hospital, Adelaide SA, Australia.

INTRODUCTION

Intertrochanteric (IT) hip fractures are highly prevalent in the elderly [1] with 40% to 60% of patients losing the ability to function independently and unable to return to preinjury ambulatory levels. [2] While a handful of authors have reported postoperative spatiotemporal gait parameters [3,4] there exists no published literature on gait biomechanics in geriatric IT fracture patients to date. This study aims to investigate if the joint kinematics and powers of the lower limbs changed between six weeks and six months in elderly IT patients after internal fracture fixation.

METHOD

Twenty eight patients (n=28) sustaining IT fractures and treated with a proximal femoral nail (PFN) were prospectively enrolled. Patients were followed up at six weeks and six months postoperative where three-dimensional gait analysis data were collected. Analyses were performed in OpenSim 3.3. The gait2392 model was scaled using an atlas based statistical shape modelling method (MAPClient). [5] For the joints of the lower limbs, angles and powers were calculated according to ISB recommendations. [6] Statistical parametric mapping was used to analyze changes in joint angles and powers between timepoints. Changes in gait speed between timepoints were assessed with a paired t-test.

RESULTS

There was a significant increase in gait speed of 0.2m/s between timepoints ($p < 0.001$). For joint angle at the hip, the SPM analysis showed improvements in peak extension during terminal stance (~35 to 55% gait cycle) ($p = 0.049$) and flexion during initial to mid swing (~65% to 80% gait cycle) ($p = 0.007$). Peak hip abduction also increased during mid to terminal stance (~25% to 40% gait cycle) ($p = 0.002$). Significant improvements in peak knee flexion ($p < 0.001$) as well as ankle plantarflexion and dorsiflexion ($p < 0.001$) were also shown across the gait cycle. The SPM analysis of joint powers showed an increase in hip power generation during the loading response to approximately midstance (~10 to 50% stance) and

during terminal stance and pre swing (~80% to 95% stance) ($p < 0.001$). At the knee, there were increased power absorption within the loading response ($p = 0.015$) and throughout terminal stance and pre swing (~85% to 95% stance) ($p < 0.001$). At the ankle joint, power absorption increased throughout single limb support phase of the ipsilateral foot, while power generation increased from approximately terminal stance (~80% stance) to toe off during pre-swing ($p < 0.001$).

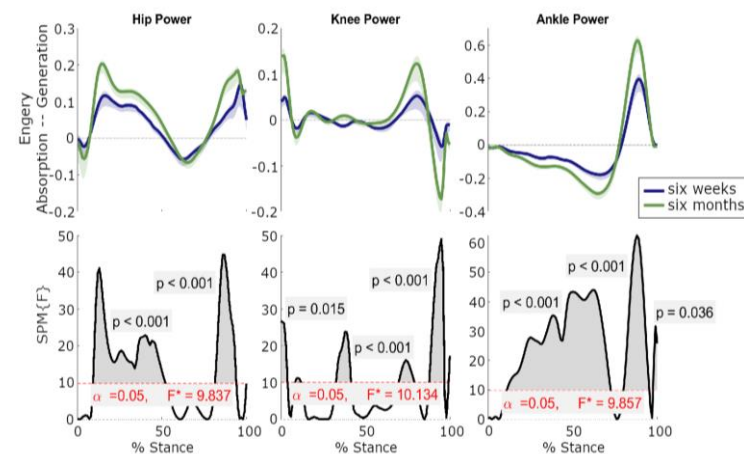


Figure 1. (A) Average joint powers at six weeks (blue) and six months (green) post-operative. (B) SPM(F) between six weeks and six months for hip, knee and ankle joint powers over stance.

CONCLUSIONS

The findings from this study are the first to highlight overall improvements in walking biomechanics after surgery from six weeks to six months.

REFERENCES

1. Sambrook, P. The Lancet 367, 2010-18, 2006.
2. Dyer, S.M. BMC Geriatrics 16, 158, 2016
3. Thingstad, P. BMC Geriatrics 15, 150, 2015
4. Gausden E.B. Journal of Orthopaedic Trauma 32, 554-8, 2018
5. Zhang. ISBMS 8789, 182-192, 2014
6. Wu G. J Biomech 35, 543-548, 2002

Presented by Arjun Sivakumar
(arjun.sivakumar@adelaide.edu.au).

ACCURACY AND FUNCTIONAL OUTCOMES OF VIRTUAL SURGICAL PLANNING AND SURGICAL GUIDES FOR JUVENILE PROXIMAL FEMORAL OSTEOTOMIES

Carty, C.^{1,2}; Bade, D.^{1,2}; Lloyd, D.²; Smith, D.^{2,3}; Barzan, M.²

¹Department of Orthopaedics, Children's Health Queensland Hospital and Health Service, Brisbane, AU; ²Griffith Centre of Biomedical and Rehabilitation Engineering, Griffith University, Gold Coast, AU; ³Advanced Design and Prototyping Technologies Institute, Griffith University, Gold Coast, AU.

INTRODUCTION

A proximal femoral osteotomy (PFO) is a commonly implemented surgical procedure used to address hip joint dysfunction in juvenile patients (e.g., Perthes' disease, slipped capital femoral epiphysis, cerebral palsy) [1]. Surgical planning and execution using standard two-dimensional medical imaging protocols (i.e., x-ray) requires a high degree of spatial intelligence and clinical experience, as most of these patients present with multiplanar femoral deformity and hip joint impingement.

In this medical device trial, we developed a novel platform for virtual surgical planning aimed at restoring hip joint anatomy and muscle function in juvenile patients with hip joint dysfunction. We also designed and manufactured patient-matched surgical guides using 3D printing to enable precise surgical execution. The aim of this investigation was to evaluate (a) the accuracy of PFO in juvenile patients when performed using 3D printed surgical guides, and (b) whether PFO led to improved gait function. We hypothesized that the surgical guides would enable accurate translation of the surgical plan in the operating theatre, and that PFO would lead to improved function nine months post-surgery.

METHOD

Twelve patients (age: 11.7 ± 2.6 years) with proximal femoral deformities were recruited at the Queensland Children's Hospital as part of a Phase I clinical trial. Preoperatively, all patients had medical images (CT scan of their affected hip, MRI scan of their pelvis and full-length femurs) taken. Three-dimensional bones and glutei muscles were reconstructed using Mimics 23.0 (Materialise, Leuven). Musculoskeletal models of each patient's hips were created in OpenSim and used to virtually plan the surgery. The most appropriate fixation implants were selected and virtually placed on the femurs. Adhering to quality control guidelines [2], surgical guides were designed in 3-matic (Materialise, Leuven), and 3D printed in biocompatible Nylon (Formiga P110, EOS, Germany) for use in surgery.

Using postoperative CT-data, 3D models of the femurs were reconstructed and superimposed with the planned correction to calculate 3D accuracy. Each patient had pre- and post-surgery 3D gait analysis and the data were processed using PlugInGait (Vicon, Oxford, UK). Movement Analysis Profiles (MAP) and Gait Profile Scores (GPS) were generated for each patient to compare pre- and post-surgery joint kinematics. The Minimal Clinically Important Difference (MCID) was defined as a change of 1.6° on the GPS [3].

RESULTS

On average, the use of patient-matched surgical guides produced rotational corrections similar (3D angle: $8.8 \pm 4.5^\circ$) to the planned corrections (Fig. 1). For patients who attended pre and post 3D gait analysis (8 patients, 10 surgeries) the overall GPS showed an overall mean improvement of 4.1° (>2 times the MCID) and a mean GPS improvement on the affected side of 5.3° (>3 times the MCID).

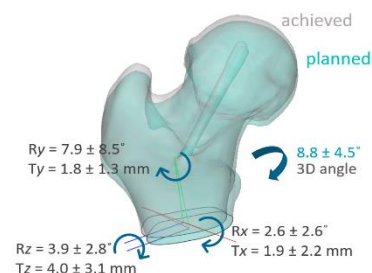


Figure 1. Planned versus achieved 3D accuracy assessment.

CONCLUSIONS

The use of virtual surgical planning and patient-matched surgical guides in PFO resulted in an accurate surgical correction that led to improved gait function nine months post-surgery.

REFERENCES

- [1] M'sabah, D., Orthop Traumatol Surg Res. 99, 171-186, 2013.
- [2] Martinez-Marquez, D., PloS one. 13(2), 2018.
- [4] Baker, R., Gait & Posture. 35, 612-530, 2012.

Presented by Chris Carty (c.carty@griffith.edu.au).

DIFFERENCES OF PASSIVE KNEE KINEMATICS BETWEEN MALES AND FEMALES

Bucci1, R; Taylor1, F.; Al-Dirini1, M.; Martelli12, S.

1. Flinders University, Bedford Park 5042, Australia; 2. QUT, Brisbane 4000, Australia.

INTRODUCTION

Women experience higher rates of knee ligament injuries than men [1], different anatomical features [2] and different knee kinematics during weight bearing activities [3]. However, kinematic differences between genders show mixed results [3]. Knee passive motion has been studied in large cohorts of male donors [4] and along selected axes of motion. The present study aims at studying gender differences of the knee passive kinematics over the six degrees of freedom in intact adult specimens.

METHOD

Twenty-nine healthy knee specimens (19 males and 9 females, between 43 and 82 years of age) were obtained from a body donation program with ethical approval (Science Care, Phoenix, USA); exclusion criteria included no reported history of knee surgery and osteoarthritis. Specimens were CT scanned (SOMATOM force, Siemens, Germany; in-plane voxel size: 0.33 mm). Femoral and tibial bone surfaces were segmented with ScanIP (Simpleware, Exeter, UK). Custom 3D printed potting cups were created for the tibia and the femur. Reflective markers (12) were placed on dedicated features on the femur and tibial potting cups, and the assembly was CT scanned to determine the relative position of the marker and the knee. Two trials of complete flexion-extension movements were performed respectively by manually applying a medial and lateral force to the femoral cup [6-8N], five repetitions each (Fig1). The marker trajectories were recorded using a 10-camera stereo-photogrammetric system (VICON, Oxford, UK). Anatomical bony landmarks were identified according to the ISB standards [5] using NMS Builder (IOR, Bologna, Italy). The anatomical joint coordinate system was created according to Gray et al. (2019) [6]. The knee kinematics for the six axes of motion was estimated using the Kinemat toolbox (MATLAB, MathWorks Inc., USA). Mean and standard deviation were calculated and compared between genders using two-tails t-test and statistical parametric mapping (SPM, Matlab toolbox, $\alpha = 0.05$).

RESULTS

Tibio-femoral kinematics were consistent with earlier reports. The largest difference between medial and

lateral force trials was 18° mean internal-external rotation (peak: 26°). Smaller differences were found for adduction-abduction (peak: 5°) and medio-lateral translation (peak: 3mm) (Fig1). Females presented greater adduction-abduction angles than males by applying a medial force (mean diff.: 2°, $p < 0.05$), whereas no gender-specific differences were found for the remaining axes of motion (Fig1).

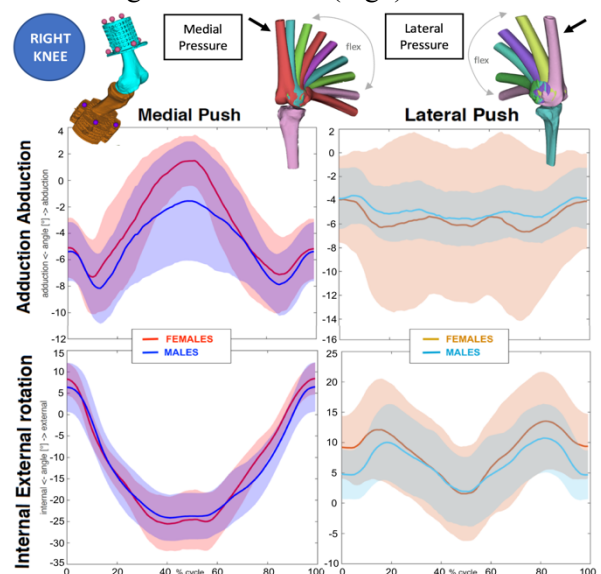


Figure 1. Knee gender passive kinematics differences.

CONCLUSIONS

Results demonstrate a gender-specific passive knee motion observed for the two medial and lateral extremes of the envelope of passive motion, obtained by applying medial and lateral force. Females display higher adduction-abduction and lower internal-external rotation than males, in partial agreement with literature [3]. These findings may complement current understanding of gender differences kinematics.

REFERENCES

- [1] Arendt et al., J.Athletic.Train,34:86-92,1999.
- [2] Conley et al, J.Am.Acad.Orthop.Surg.,15:S31-6,2007.
- [3] Roger James et al, Res.Q.Exerc.Sport,75(1):31-38, 2005.
- [4] Cyr et al. Proc.Inst.Mech.Eng.H., 228: 494-500, 2014.
- [5] Wu et al., J.Biomech.,35:543-548, 2002.
- [6] Gray et al., J.Biomech.Eng.,8:141, 2019.

Francesca Bucci (francesca.bucci@flinders.edu.au).

FINITE ELEMENT ANALYSIS OF A 3D-PRINTED SCAPHOLUNATE LIGAMENT UNDER PHYSIOLOGICAL CONDITIONS

¹Perevoshchikova N, ²Moerman KM, ³Akhbari B, ¹Bindra R, ¹Mahajar JN, ¹Diamond LE, ¹Lloyd DG, ⁵Gomez Cerezo M, ⁵Carr A, ⁵Vaquette C, ¹Saxby DJ
¹Griffith Centre of Biomedical and Rehabilitation Engineering, Griffith University, Australia; ²Biomechanics Research Centre, National University of Ireland, Ireland; ³Center for Biomedical Engineering, Brown University, USA; ⁵School of Dentistry, University of Queensland, Australia

INTRODUCTION

Scapholunate interosseous ligament (SLIL) rupture results in acute and long-term wrist dysfunction (e.g., osteoarthritis). Current treatments (e.g., tendon-based surgical reconstruction, screw fixation, etc) stabilize scaphoid and lunate, but do not regenerate ruptured SLIL or prevent degenerative sequelae. We propose a 3D-printed multiphasic bone-ligament-bone scaffold to affix scaphoid to lunate while promoting SLIL regeneration. Here, we use finite element analysis to determine if such scaffold withstands physiological wrist kinematics. We hypothesized scaffold will tolerate physiological wrist kinematics indicated by sub-critical stresses.

METHOD

Scaffold (Figure 1, left) was modified from [1], and made of medical grade polycaprolactone (PCL-12) (Corbion, Netherlands). Scaffold consisted of two bone plugs bridged by multi-layered parallel fibres.

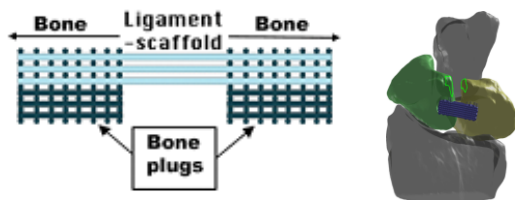


Figure 1. (Left) Scaffold schematic; and (right) finite element model embedded in wrist kinematic model.

Scaffold was 3D-printed using 3D-Bioplotter Developer Series 108 (EnvisionTEC GmbH, USA), and then subjected to uniaxial and cyclic tensile testing. Tensile testing data were used for inverse material fitting to describe scaffold's homogeneous, isotropic, hyperelastic, and viscoelastic behaviors, which were applied to scaffold finite element model (FEBio, v 2.8.5, University of Utah, USA). Mesh manipulations were performed in GIBBON toolbox [2] for Matlab (Mathworks, USA). A specialist orthopaedic wrist surgeon performed virtual surgery where surgical installation sites were identified and scaffold finite element model embedded (Figure 1, right). Scaphoid, lunate, and capitate kinematics were

derived from tri-planar videoradiography and applied to scaffold finite element model. Von Mises stresses (MPa) in scaffold ligament portion were assessed when wrist was in terminal flexion, neutral, ulnar deviation, and radial deviation.

RESULTS

Tensile testing of 3D-printed scaffold was consistent across repeated cycles and inverse fitting resulted in excellent approximation of experimental mechanics (not show here). Depending on scaffold geometry and surgical installation site (not show here), few (~10%) elements experienced supra-critical stresses (Figure 2).

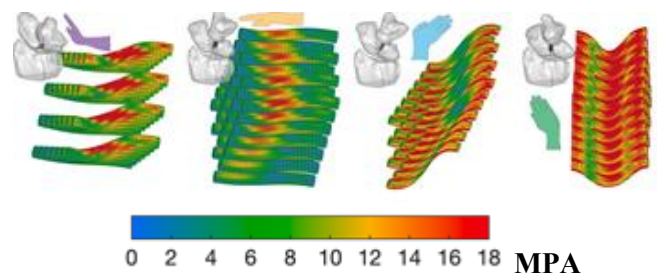


Figure 2. Von Mises stresses in scaffold ligament portion with wrist in (left) flexion, (middle left) neutral, and (middle right) ulnar deviation, and radial deviation (right). MPA – megapascals.

CONCLUSIONS

This is the first simulation of engineered ligament mechanics under continuous wrist motion. Results indicate careful selection of scaffold geometry and surgery are needed to ensure stresses remain sub-critical. Tri-planar videoradiography data acquired from different populations will help define typical physiological wrist motion, from which a design envelope can be defined to help this product satisfy regulatory requirements.

REFERENCES

1. Lui, H et al. Adv Healthcare Mater, 1900133: 1-15, 2019.
2. Moerman KM. J Open Source Softw, 3(22):506, 2018.

Presented by David John Saxby
d.saxby@griffith.edu.au.

SIMULATING THE EFFECT OF GLENOHUMERAL CAPSULORRHAPHY ON KINEMATICS AND MUSCLE FUNCTION

Fox, A.S.; Bonacci, J.; Gill, S.D.; Page, R.S.

Deakin University, Geelong, Australia; Barwon Health, Geelong, Australia.

INTRODUCTION

Surgical glenohumeral capsulorrhaphy is used to treat glenohumeral instability caused by damaged capsulo-ligamentous structures. Various techniques of selective plication to joint capsule sections are used (Gerber et al. 2003). Understanding the impact of glenohumeral capsulorrhaphy variations on movement and muscle function is relevant for targeted rehabilitation strategies. We used a predictive simulation framework to examine shoulder kinematics, muscle effort, and task performance during upper limb movements under various simulated selective capsulorrhaphy conditions.

METHOD

We used a seven-segment musculoskeletal model of the torso and right upper limb (Holzbaur et al. 2005; Wu et al. 2018). Muscle model parameters were set to those by De Groote et al. (2016), and tendon dynamics were ignored. A baseline model of no joint capsulorrhaphy was created (i.e. 'None' model), followed by eight models representing selective glenohumeral capsulorrhaphy procedures (i.e. anteroinferior, anterosuperior, posteroinferior, posterosuperior, total anterior, total inferior, total posterior, total superior). We included joint restraints in each model so that passive range of motion matched that observed in cadaveric experiments (Gerber et al. 2003). Each capsulorrhaphy model was used in predictive optimal control simulations (via OpenSim Moco 0.3) of movements replicating activities of daily living involving the shoulder (i.e. forward reach, upward reach, head touch). The simulations were generated via a series of task constraints and goals that contributed to an objective function value. We compared shoulder kinematics (mean absolute difference [MAD] in degrees), total and individual muscle cost (van der Krogt et al. 2012) (as a relative percentage change), and the time taken to complete the task (in seconds) for each capsulorrhaphy model against the 'None' model. All code used to generate the models and simulations, along with the resulting data are available at simtk.org/projects/gh-caps-sims/.

RESULTS

There were minimal differences in shoulder elevation (i.e. MAD < 2.0°) and elevation plane (i.e. MAD < 0.8°) angles between the capsulorrhaphy models and

the 'None' model across tasks. Shoulder axial rotation angles were consistent across the models in the forward reach (MAD < 0.4°); however, small differences (i.e. MAD ~1-5°) occurred for axial rotation in the head touch and upward reach tasks.

Total muscle cost typically increased under the selective capsulorrhaphy conditions relative the 'None' model – however the magnitude of change was task dependent. We observed the largest relative increases in total muscle cost (i.e. ~ +15-30%) during the simulated overhead movements (i.e. upward reach; head touch) with anteroinferior, and total anterior, inferior and posterior capsulorrhaphy. Only the total anterior capsulorrhaphy condition generated an increase in relative total muscle cost during the forward reach task.

Performance times remained consistent (i.e. within 0.05s) across the capsulorrhaphy conditions and tasks.

CONCLUSIONS

Selective capsulorrhaphy had a relatively minimal impact on movement (i.e. within 5°) and task performance time (i.e. within 0.05s). Despite the lack of kinematic changes, we saw an increase in total muscle cost. This was particularly evident in overhead movements with anteroinferior or total joint section capsulorrhaphy. The elevated muscle loading could present a risk to joint capsule repair in the early post-operative period. Appropriate rehabilitation following glenohumeral capsulorrhaphy is required to account for the elevated demands placed on muscles – particularly in individuals who commonly perform overhead movements.

REFERENCES

- De Groote, F. et al., *Ann Biomed Eng*, 44: 2922-2936, 2016.
- Gerber, C. et al. *J Bone Jt Surg Am*, 85, 48-55, 2003.
- Holzbaur, K. et al., *Ann Biomed Eng*, 33: 829-840, 2005
- van der Krogt, M., *Gait Posture*, 36: 113-119, 2012.
- Wu, W. et al., *J Biomech*, 49, 3626-3634, 2018.

Presented by Aaron Fox (aaron.f@deakin.edu.au).



DAY 2

Podium 8

PLANTAR APONEUROSIS STIFFNESS IS RELATED TO MORE THAN JUST THE SHAPE OF THE MEDIAL LONGITUDINAL ARCH

Schuster, R.W.; Cresswell, A.G.; Andrews, M.; Kelly, L.
The University of Queensland, Brisbane QLD, Australia

INTRODUCTION

The modern human foot's medial longitudinal arch has been identified as one of its defining features. Its importance emphasized by the fact that its shape has been linked to push-off efficiency when walking (DeSilva & Gill, 2013). As a component of the medial longitudinal arch, the plantar aponeurosis (PA) is thought to be intimately involved in the foot's ability to enhance push-off efficiency. Therefore, the question arises whether external foot shape, or how it deforms when loaded, is influenced by PA stiffness.

METHODS

Fifty-seven healthy participants' dominant foot was 3D scanned (FootIn3D, Elivnvision, Lithuania) while supporting 10% (mBW) and 100% (fBW) of their bodyweight. A statistical shape model was then created for each weightbearing condition using statistical shape analysis. These shape models consist of principal components (PC) and subject specific PC scores. The former describe the most prominent variations in shape within the sample, while the latter place each subject within the spectrum of foot shapes described by each PC.

Foot shape deformation between mBW and fBW was quantified in a similar manner. However, instead of using foot shapes as input into the statistical shape model, subject specific deformation vectors were used (Schuster et al., 2021). Thus, creating a statistical shape deformation model.

A custom-built device was used to passively extend the metatarsophalangeal joints (MTPj) from 0 to 45° while the foot was loaded to mBW and fBW. The toe extension device was driven by a manual winch and measured the degree of MTPj extension, as well as the MTPj moment. A string potentiometer, attached to the plantar aspect of the foot along the path of the central band of the PA was used to measure PA strain. From these three variables PA stiffness was calculated.

Whether foot shape, or foot shape deformation, can predict PA stiffness was examined using stepwise multiple linear regressions between PC scores and PA stiffness values.

RESULTS

No relationship was found between mBW scans and PA stiffness. Furthermore, only the third PC ($\approx 12\%$ of overall shape variation) of the fBW shape model was associated with fBW PA stiffness ($r = -0.265$, $p = 0.047$). This PC describes toe angle, hallux length and medial longitudinal arch height (Figure 1).

In contrast, PCs 4 to 6 of foot shape deformation between mBW and fBW were able to account for 24.7% of fBW PA stiffness variability ($r = 0.536$, $p < 0.001$). These PCs describe hallux extension and adduction, arch compression, as well as forefoot splay.

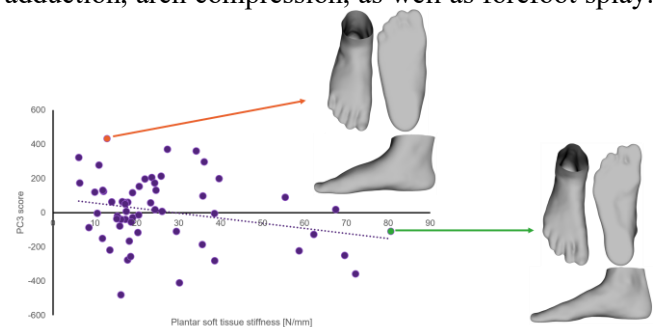


Figure 1. Relationship between fBW PC3 scores and PA stiffness.

CONCLUSIONS

While a relationship exists between foot shape and PA stiffness, this relationship is only weak to moderate and is not limited to the shape of the medial longitudinal arch, but also involves the shape and orientation of the toes. Furthermore, the shape changes a foot undergoes during loading are better at predicting a specific foot's PA stiffness. Similar to foot shape, the deformations related to PA stiffness are not limited to those involving the medial longitudinal arch. These results suggest that a foot's shape and mechanical properties result from the interactions between its many components and that a relationship between foot form and function is likely to be similarly complex.

REFERENCES

- DeSilva, J.M., Am. J. Phys. Anthropol. 115, 495-499, 2013.
- Schuster, R.W., J. Biomech. 115, 2021.

Presented by Robert Schuster (r.schuster@uq.net.au).

CHANGES IN LOWER LIMB BONE MEASUREMENTS WITH GROWTH INCLUDING SEX DIFFERENCES AND MEASUREMENT PREDICTIONS

Carman, L.; Besier, T.; Choisine, J.

Auckland Bioengineering Institute, The University of Auckland, Auckland, New Zealand

INTRODUCTION

How clinical bone measurements change with growth is not well understood and differences between the sexes has not been assessed on a large scale. Compounded with inconsistent methods of measurement, this leads to a gap in understanding of what values are typical for children [1]. The aim of this study is to understand changes in clinical bone measurements for a typically developed paediatric population and investigate the sex differences in these measurements.

METHOD

Post-mortem CT scans of 333 children (137 F, Age: 12 ± 5 Y, H: 148 ± 24 cm, M: 49 ± 22 kg) were obtained from the Victorian Institute of Forensic Medicine (VIFM, Melbourne, Australia). The lower limb bones were segmented, fitted, and aligned according to the ISB coordinate system [3]. A shape model was generated for the pelvis, femur, and tibia/fibula using principal component analysis [4]. 3D bone measurements were taken automatically from 1) reconstructed bone geometry and 2) predicted bone geometry from the shape model in a leave one out analysis. Measurements were taken for the pelvis: ASIS, PSIS width, and pelvis depth. For the femur: anteversion, neck shaft, bicondylar, and mechanical offset angle, epicondylar width, and femoral length. For the tibia/fibula: tibial torsion and tibial mechanical angle, condylar and malleolar width, and tibial length. Multiple linear regression was performed for each measurement using demographic (age, height, mass, sex) and linear bone measurements. Sex differences were investigated using two-way ANOVA.

RESULTS

Bone measurement prediction errors (Table 1) using multiple linear regression (MLR) and shape model prediction (SSM) show both methods have difficulty in predicting angle measurements from linear factors. Significant sex differences were found for the pelvis: ASIS, and PSIS width, and pelvis depth. For the femur: neck shaft, bicondylar, and mechanical offset angle, femoral head radius, and epicondylar width. For the tibia/fibula: tibial mechanical angle, condylar, and malleolar width, and tibial length. An interaction between age and sex (Figure 1) was found for the femur: anteversion, neck shaft, and mechanical offset angle,

femoral head radius, epicondylar width, and femoral length. For the tibia/fibula: tibial torsion, tibial mechanical angle, condylar, and malleolar width, and tibial length.

Table 1: Mean Absolute Error (MAE) \pm SD for bone measurements

	MAE MLR	MAE SSM
Anteversion Angle	$6.19^\circ \pm 5.00^\circ$	$7.16^\circ \pm 5.96^\circ$
Neck Shaft Angle	$6.09^\circ \pm 5.04^\circ$	$6.62^\circ \pm 5.76^\circ$
Fem. Head Radius	$0.06\text{cm} \pm 0.05\text{cm}$	$0.12\text{cm} \pm 0.15\text{cm}$
Tibial Torsion	$5.98^\circ \pm 4.72^\circ$	$6.60^\circ \pm 5.31^\circ$
Tib. Mech. Angle	$1.97^\circ \pm 1.65^\circ$	$2.25^\circ \pm 2.00^\circ$

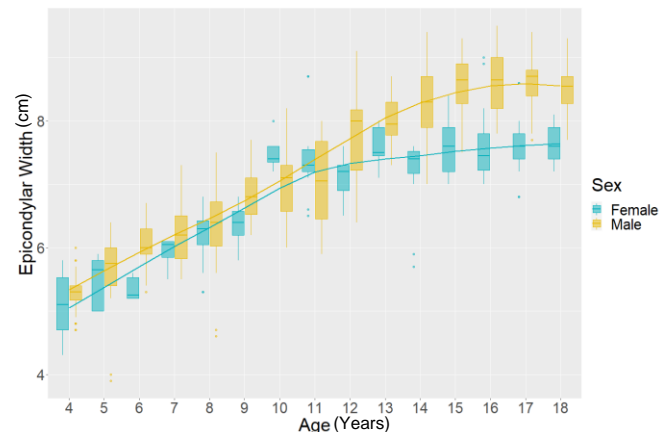


Figure 1: Absolute measurement of epicondylar width vs. age grouped by sex. Line of best fit created through the average measurement at each age.

CONCLUSIONS

A large range in bone measurements was found for children of the same age which can be predicted by a regression equation. The shape model was not more accurate at predicting angle measurements compared to the regression equations, this could be improved by use of an articulated shape model. Significant sex differences were found in many of the bone measurements with the age of deviation captured.

REFERENCES

- [1] Beutel et al. (2018). *J. Child. Ortho.*, **12**: 167-172
- [3] Wu G et al. (2002). *J. Biomech.*, **35**: 543-548
- [4] Zhang J et al. (2016). *Med. Eng. Phys.*, **38**: 450-457

Presented by Laura Carman (lcarr475@aucklanduni.ac.nz)

Acknowledgements: Data from VIFM made this research possible. Research was funded by UoA doctoral scholarship, HRC grant, and the Friedlander foundation.

IN SILICO EXPERIMENTS IDENTIFY THE NEUROMECHANICAL AETIOLOGY OF IDIOPATHIC TOE WALKING

Veerkamp, K.^{1,2}; van der Krogt, M.M.²; Waterval, N.F.J.²; Geijtenbeek, T.³; Walsh, H.P.J.⁴; Harlaar, J.³; Lloyd, D.G.¹; Carty, C.P.^{1,4}

¹Griffith University, Gold Coast, Australia

²Amsterdam UMC, Amsterdam, Netherlands

³Delft University of Technology, Delft, Netherlands

⁴Queensland Children's Hospital, Brisbane, Australia

INTRODUCTION

Idiopathic toe walking (ITW) is diagnosed in the absence of clear causes for equinus gait. To unravel the cause-and-effect mechanisms of ITW, predictive neuromusculoskeletal gait simulations may be used. Hence, this study evaluated 1) whether musculotendon contracture of the triceps surae in isolation can explain ITW, or 2) if neural spinal control (i.e., hyperreflexia or an increased supraspinal drive), or 3) higher-level control (i.e., prevention of high normalised fibre lengths) are additionally involved in ITW.

METHOD

Gait data from seventeen children diagnosed with ITW were used as comparative experimental data (i.e., ground reaction forces, joint angles, moments, and powers). A previously developed forward-dynamic neuromusculoskeletal model that showed good agreement with healthy gait was employed [1]. This consisted of a generic musculoskeletal model controlled by reflexes and supraspinal drive, the latter governed by a weighted cost function that minimised cost of transport, foot-ground impact, head accelerations, muscle fatigue, and knee hyperextension [1]. Three *in silico* experiments were performed to predict ITW. First, Achilles tendon contracture was implemented, matching the level of contracture from ITW children. Second, either hyperreflexia or increased supraspinal drive during the whole gait cycle was imposed on the contracted model. Third, the contracted model was forced to function on the ascending limb and plateau region of the muscle force-length curve for the plantar flexors. In each *in silico* experiment, the match of modeled gait with the experimental ITW data was quantified by root mean square errors (RMSE).

RESULTS

Isolated tendon contracture did not lead to toe walking and had an RMSE of 2.24 SD (Fig. 1). A better match with experimental data (RMSE=1.84) occurred when imposing hyperreflexia or increased supraspinal drive. Adding the high fibre length penalty to the contracted model, the predicted gait best approached ITW

(RMSE=1.37; Fig. 1). This best ITW simulation used a control strategy with higher velocity- and length-based reflex gains and supraspinal drive in stance and late swing compared to healthy heel-toe gait simulations.

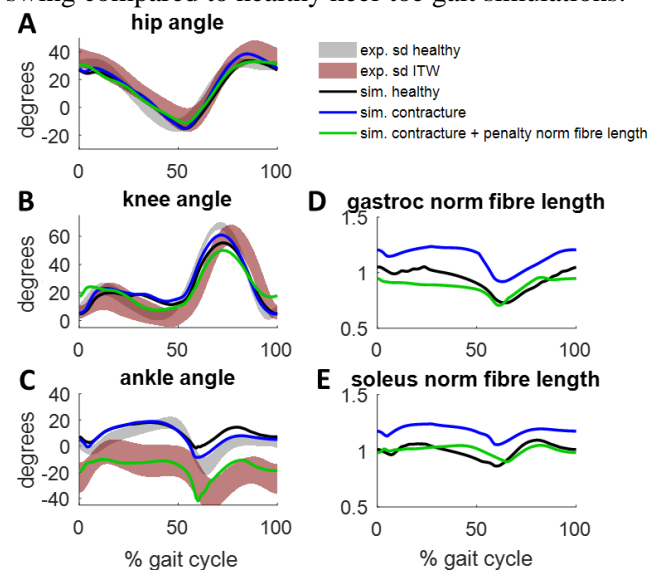


Figure 1. Predicted kinematics (A-C) and fibre lengths, normalised by optimal fibre length (D-E), by the healthy model, contracted model, and the contracted model with penalty on high fibre lengths. The predicted gait by the healthy model (black line) and the contracted model (blue line) are compared against experimental data for healthy gait (gray area; +/- one standard deviation from the mean) and ITW gait (red area). Predicted fibre lengths for the (D) gastrocnemius and (E) soleus muscles are normalised by the optimal fibre length.

CONCLUSIONS

Aligned with previous research [2], implementing contracture alone resulted in the plantar flexors working on the descending limb of the force-length curve, which may not be a physiologically feasible solution [3]. Our *in silico* experiments provided mechanistic insights into how a contracture with an altered neural control strategy could contribute to ITW. Thus, these results suggest that targeting the altered control strategy could be a therapeutic rationale to train typical heel-toe gait, thereby delaying, or even preventing surgical intervention.

REFERENCES

- [1] Veerkamp, K. J. Biomech 123, 110530, 2021.
- [2] Ong, C.F. PLoS Comput.Biol., 15, e1006993, 2019.
- [3] Rubenson, J. J. Exp. Biol., 215, 3539-3551, 2012.

Presented by Kirsten Veerkamp
(kirsten.veerkamp@griffithuni.edu.au)

DEEP HIP MUSCLES CAN CHANGE THE DIRECTION OF HIP LOADING

Evvy Meinders¹, Claudio Pizzolato¹, Basilio AM Goncalves¹, David G Lloyd¹, David J Saxby¹,
Laura E Diamond¹

¹Griffith Centre of Biomedical and Rehabilitation Engineering, Griffith University, Gold Coast, Australia

INTRODUCTION

A better understanding of deep hip muscle function is needed to guide targeted rehabilitation programs for people with hip pathology. The deep hip muscles have limited ability to contribute to hip motion or rotational stability [1] because of their limited force generation capacity and small moment arms relative to other hip muscles [2]. However, the deep hip muscles may be able to change the orientation of hip loading in the acetabulum, which may be important to distribute the load across the acetabular surface and prevent edge loading. The aim of this study was to evaluate whether the deep hip muscles could change the orientation of hip loading towards the centre of the acetabulum.

METHOD

Three-dimensional marker trajectories and ground reaction forces, together with electromyography (EMG) from 12 superficial and 4 deep (gluteus medius, piriformis, obturator internus, and quadratus femoris) muscles of the lower limb, were recorded during walking in 12 participants with no history of hip pain (age 24±4 yrs). Inverse kinematics, inverse dynamics, and muscle analysis were performed in OpenSim using a linearly scaled generic model [3]. Muscle-tendon parameters were calibrated to the individual using CEINMS [4]. The calibrated neuromusculoskeletal model was used to calculate muscle forces via an EMG-informed approach using three model configurations: (i) deep hip muscles (gemelli, obturator externus and internus, piriformis, quadratus femoris) informed by EMG measurements (*assisted activation*), and (ii) zero (*zero activation*) and (iii) maximal activation (*maximal activation*) imposed onto the deep hip muscles, respectively. Muscle forces were used within the joint reaction toolbox in OpenSim to calculate hip contact forces (HCF).

The orientation of hip loading in the acetabulum was defined as the angle between the HCF and the vector from the centre of the femoral head to the centre of the acetabulum (HCF angle); a smaller HCF angle equated to hip loading towards the centre of the acetabulum. The HCF angle was compared over the gait cycle between models using a within-subject analysis of

variance with statistical parametric mapping (SPM) methods ($p < 0.05$).

RESULTS

Over the gait cycle, HCF angle differed significantly between models. Post-hoc analysis revealed HCF angle was smaller for *maximal activation* compared to both *assisted* and *zero activation* models over the full gait cycle (Figure 1). HCF angle was larger for *zero activation* compared to *assisted activation* during the loading response, late stance, and most swing phases.

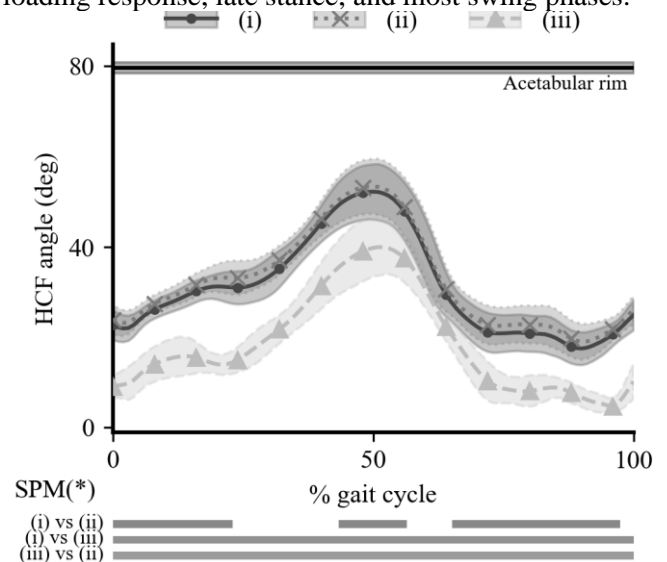


Figure 1. Ensemble average (\pm standard deviation, top) and phases of statistical significance (bottom) for HCF angle over the gait cycle for (i) *assisted*, (ii) *zero*, and (iii) *maximal* activation models. HCF angle equating to edge loading is shown in black (~ 80 deg).

CONCLUSIONS

The deep hip muscles can shift the orientation of hip loading towards the centre of the acetabulum. Targeted training of these muscles may be relevant for people with hip pathology who present with unfavorable regional/edge loading.

REFERENCES

- [1] Meinders et al. Submitted for review, 2021
 - [2] Parvaresh et al. BMC Musculoskel Disord 20, 611, 2019
 - [3] Rajagopal et al. IEEE Trans Biomed Eng 63, 2068-79, 2016
 - [4] Pizzolato et al. J Biomech 48, 3929-36, 2015
- Presented by Evvy Meinders (evvy.meinders@griffithuni.edu.au)

STATISTICAL SIMULATION OF SHOULDER KINEMATICS: A MONTE-CARLO APPROACH

Lavaill M^{1,2,3}; Martelli S^{1,2,3}; Kerr G^{2,3,4}; Pivonka P^{1,2,3}

1. School of MMPE, QUT, Brisbane, Australia; 2. ARC ITTC for Joint Biomechanics, Brisbane, Australia; 3. Queensland Unit for Advanced Shoulder Research, Brisbane, Australia; 4. School of Exercise & Nutrition Sciences, QUT, Brisbane, Australia

INTRODUCTION

Shoulder kinematics provide critical clinical and performance information for a wide range of occupational, rehabilitation and sports contexts. Inverse kinematics (IK) is the main tool in assessing joint angles based on the assumption of a general underlying anatomy and is commonly used for musculoskeletal (MSK) modelling applications. However, lower limb studies have shown that the outcomes of IK are very sensitive to the assumptions made on the MSK model parameters and the reliability of the experimental inputs [1,2]. Marker-based motion capture setups are particularly affected by operator-dependent placement errors. However, the effect of errors in marker positioning on IK is unclear for the upper-limbs. The current study therefore aims to quantify the effect of marker position errors on IK calculation of shoulder motion using a Monte Carlo statistical approach.

METHOD

The skeletal geometry of the right upper-limb (sternum, clavicle, scapula and humerus) was segmented using MR images (*Ingenia*, Koninklijke Philips N.V., The Netherlands, T1 Dixon sequence, resolution $0.4 \times 0.4 \times 0.8\text{mm}$), from a healthy volunteer (female, 29 yo, 57.2 kg, 159.5 cm). The model included 4 rigid segments and 8 degrees-of-freedom. Virtual markers were then placed on shoulder bony landmarks recommended by the ISB. [3]. The virtual marker trajectories describing three different shoulder planar motions (i.e. abduction-adduction, AA; flexion-extension, FE; internal-external rotation, IER) were inferred based on experimental motion data performed by the subject. Note that each task consisted of 1) arm moving, 2) stationary phase, 3) arm returning to initial pose. Computed marker trajectories were considered as ground-truth and were utilized to avoid bias from marker-based errors.

Marker placement error was simulated by prescribing a perturbation from the ground-truth landmark in its local coordinate system. The offset was dependent on the marker and was randomly chosen to follow a normal distribution ($0 \pm \text{SD mm}$) which accounts for common inter-operator variability reported in [4].

Finally, for each sample of the Monte-Carlo analysis, each of the 12 marker trajectories used in the MSK model was perturbed as described previously, with respect to the ground-truth. The new markers trajectory file was then used for IK to compute the perturbed shoulder joint angles.

RESULTS

1000 samples were determined to be sufficient in order to reach convergence for the values of the 5-95% confidence bounds in resulting joint angles. As seen in Fig. 1, the impact of marker placement uncertainty resulted in mean bounds of 2.7° , 3.9° and 5.9° for the main glenohumeral angle responsible for AA, FE and IER respectively. Maximum error bounds were found during the stationary phase of each task, i.e. 3.0° , 5.0° , 6.7° for the AA, FE and IER respectively.

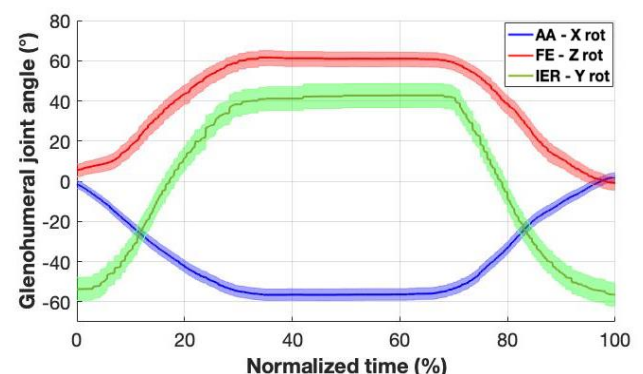


Figure 1. Main glenohumeral joint angle and its confidence bounds for three different shoulder motion.

CONCLUSIONS

Shoulder joint angles computed via IK vary greatly due to marker position errors. We believe that the current study will highlight the limitations and uncertainties of marker-based computed kinematics for the upper-limbs. Influence of marker-based errors will be studied further by including skin motion artifacts in the Monte-Carlo analysis.

REFERENCES

1. Myers CA, et al, BMES. 43(5):1098-1111, 2015.
2. Valente G, et al., PLOS one, 9(11) :e112625, 2014.
3. Wu G, et al, J. Biomech. 38(5):981-992, 2005.
4. De Groot JH, Clin. Biomech. 12(7-8):461-472, 1997.

Presented by Maxence Lavaill (lavaillm@qut.edu.au).

UNDERSTANDING GEOMETRIC VARIATION OF THE HUMAN TIBIA: A PUBLIC DATASET OF TIBIAL SURFACE MESHES AND STATISTICAL SHAPE MODEL

Keast, M.; Bonacci, J.; Fox, A.
Deakin University, Waurin Ponds, Victoria, Australia.

INTRODUCTION

Variation in skeletal geometry is a risk factor for tibial stress fractures (Crossley et al., 1999; Popp et al., 2020). Quantifying skeletal anatomy provides an opportunity to evaluate and understand injury risk. Geometric variability in bones is often quantified using statistical shape modelling (SSM) (Zhang et al., 2016). SSM has been used to identify variability in other long bones, but there is limited research examining tibial geometries and its variability in healthy adults. This study investigated geometrical variation of the tibia to provide an open access SSM and database of tibial models.

METHOD

Lower limb computed tomography (CT) scans from the right tibia of 30 cadavers (male $n = 20$, female $n = 10$) were obtained from the New Mexico Decedent Image Database (Edgar et al., 2020). The images included were from individuals who had impact-based physical activities reported during life. Images were excluded if there was any noticeable damage to the right tibia or the inclusion of medical devices (plates, rods, or screws). The tibias were segmented and reconstructed from the CT images using Mimics (Materialise, Leuven, Belgium). Thresholding with manual corrections were used to segment tibial geometry. The tibias were segmented into both cortical and trabecular bone. Remeshing, smoothing and landmark registration was performed using 3-matic (Materialise, Leuven, Belgium).

Gias2 (Zhang et al., 2016) was used in Python 3.7 to develop the SSM. Initially, surfaces were re-meshed to have matching point numbers ($n=10,000$). The points were then non-rigidly registered to a target surface using radial basis functions. The surface points were then rigidly (i.e. translation and rotation; unscaled) registered to a target surface. Principal component analysis (PCA) was applied to quantify the geometric variation of the tibias. The principal components (PCs) that explained greater than 97% of variance were retained. PCs were interpreted by comparing the mean tibial surface against surfaces reconstructed as ± 3 standard deviations of each PC. Heatmaps of these reconstructed surfaces were developed to assist with

interpretation, where colour variation indicated a greater versus lesser change in position of the surface nodes compared to the mean.

RESULTS

The first three PCs accounted for 97.34% of the geometric variation across the tibial surfaces. PC1 was indicative of size variation (i.e., length and width) and accounted for 94.5% of variation. Higher versus lower PC1 scores reflected shorter and narrower versus longer and wider tibiae, respectively. PC2 accounted for 1.85% of variation and was indicative of anterior-posterior shaft curvature, with variation in malleoli prominence. Increased shaft curvature resulted in a decreased prominence of the malleoli and vice versa. PC3 accounted for 0.99% of variation and represented changes in distal third shaft thickness. Increased PC3 scores resulted in a thicker tibia at the distal third.

CONCLUSIONS

The major source of geometric variation in the human tibia was overall size variation (length and width). Anterior-posterior shaft curvature, lateral malleoli prominence, and distal third shaft thickness were also found to be a source of geometric variation. Length and width of the tibia, particularly at the distal third, may play a role in tibial stress injury risk (Popp et al., 2020). Future work using this publicly available dataset and shape model may help understand the potential mechanistic relationship between geometrical risk factors and tibial stress injury risk. The developed tibial surface models and statistical shape model will be made publicly available for use at: https://simtk.org/projects/ssm_tibia.

REFERENCES

Crossley KM, Med Sci Sport Exerc. 31,1088–1093, 1999

Zhang J, Med Eng Phys, 38, 450-457, 2016.

Edgar, HJH, New Mexico Decedent Image Database. 2020

Popp KL. J Sci Med Sport. 23(2), 145-150, 2020.

Presented by Meghan Keast (mfkeast@deakin.edu.au).



DAY 2

Podium 9

AUGMENTED RESPIRATORY MECHANICS DURING ENHANCED FORCE PRODUCTION IN TRAINED MARTIAL ARTS PRACTITIONERS.

Walters, S.J.¹; Hoffman, B.^{1,2}; MacAskill, W.¹; Johnson, M.A.³; Sharpe, G.R.³; Mills, D.E.¹

¹School of Health and Wellbeing and Centre for Health Research, Institute for Resilient Regions, University of Southern Queensland, Ipswich, Australia; ²School of Human Movement and Nutrition Sciences, The University of Queensland, Brisbane, Australia;

³Exercise and Health Research Group, Sport, Health and Performance Enhancement (SHAPE) Research Centre, School of Science and Technology, Nottingham Trent University, Nottingham, United Kingdom.

INTRODUCTION

Traditional martial arts include highly refined techniques developed to improve performance in combat. Trained martial arts practitioners (MA) produce higher impact forces than individuals not trained in martial arts (Non-MA) [1]. While improved technique, muscular strength and endurance as a result of physical training play a role, the mechanisms that explain the ability of MA to produce and resist greater forces than Non-MA to aid combat performance are not fully understood. Due to specialised forms of breath control training found in many traditional martial arts systems, it is speculated that enhanced force production may be associated with an enhanced control of respiratory pressures [2] and neuromuscular activation of the respiratory, abdominal, and pelvic floor musculature. However, the comparison of respiratory pressures and associated musculature activation between MA and Non-MA has yet to be examined and thus was the aim of the present study.

METHOD

Nine MA and nine healthy Non-MA controls performed two tasks to measure force production: Standing Isometric Unilateral Chest Press (Task 1) and Standing Posture Control (Task 2). During each task, EMG of the sternocleidomastoid (EMG_{scm}), rectus abdominis (EMG_{ra}), and the group formed by the transverse abdominal and internal oblique muscles (EMG_{tra/io}) was measured. Gastric (P_g : a surrogate measure of intra-abdominal pressure), esophageal (P_e), and transdiaphragmatic (P_{di}) pressures and EMG of the crural diaphragm (EMG_{di}) were obtained using a multipair esophageal EMG electrode catheter. Between-group data were analysed using independent t-tests.

RESULTS

The trained group produced higher forces normalised to body mass^{2/3} (0.033 ± 0.01 vs. 0.025 ± 0.007 N/kg^{2/3} mean force in Task 1 (Figure 1)), lower P_e , and higher P_{di} in both tasks. Additionally, they produced higher

P_g (73 ± 42 vs. 49 ± 19 cmH₂O mean P_g) and EMG_{tra/io} in Task 1 and higher EMG_{di} in Task 2. The onset of P_g with respect to the onset of force production was earlier, and the relative contribution of P_g/P_e (Figure 1) and P_{di}/P_e were higher in MA in both tasks.

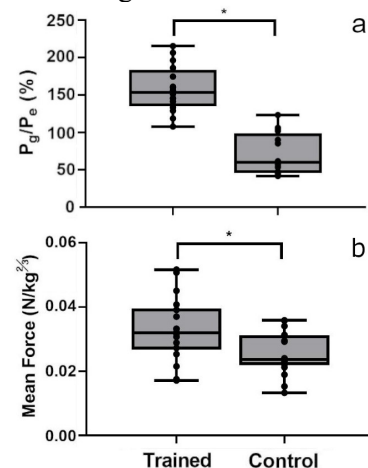


Figure 1. Relative contribution of gastric/oesophageal pressure (P_g/P_e ; a) and mean force (b) normalised for body mass^{2/3} applied during Task 1. *Sig. different from Non-MA, $P < 0.05$

CONCLUSIONS

MA produced and resisted higher forces compared to Non-MA. MA achieved this while utilising a greater contribution of abdominal and diaphragm musculature to chest wall recruitment and higher P_g with respect to P_e . These findings indicate that MA may utilize augmented respiratory mechanics to enhance force production. Future studies are required to investigate the role of martial arts breath control training in enhancing force production in active and inactive populations.

REFERENCES

1. Neto, O. P. Percept Mot Skills. 106, 188-196, 2008.
2. Kawabata, M. Eur J Appl Physiol. 109, 279-286, 2010.

Presented by Sherrilyn Walters
(sherrilyn.walters@usq.edu.au).

PHASE OFFSET BETWEEN ARTERIAL PULSATIONS AND SUBARACHNOID SPACE PRESSURE FLUCTUATIONS ARE UNLIKELY TO DRIVE PERIARTERIAL CEREBROSPINAL FLUID FLOW

Martinac, A.M.; Fletcher, D.F.; Bilston, L.E.

Neuroscience Research Australia and Prince of Wales Clinical School, UNSW, Kensington, Australia; School of Chemical and Biomolecular Engineering, The University of Sydney, Camperdown, Australia.

INTRODUCTION

The glymphatic system is hypothesised to play a key role in waste removal of solutes from the brain, including amyloid beta. Consequently, reduced function of the glymphatic pathway may be involved in the pathophysiology of Alzheimer's disease. The driving force for the bulk flow of cerebrospinal fluid (CSF) through the proposed glymphatic pathway is unknown. The computational approaches used in this project aim to address such controversies within the field by determining which conditions are required for CSF and solutes/tracers to flow through perivascular spaces (PVS) and the parenchyma. Previous computational fluid dynamics (CFD) modelling of flow in the spinal cord suggests that timing offsets between arterial and spinal subarachnoid space (SAS) pressure pulses can give rise to a net inflow (Bilston et al., 2010). This study investigates whether such a mismatch of cardiac and intracranial pressure (ICP) pulse timing, causing a varied resistance to perivascular flow, can facilitate movement of tracer particles along the arterial perivascular space and into the brain parenchyma.

METHOD

The perivascular space geometry was adapted from studies by Bilston et al. (2010) who used a 10° radial 'slice' through the PVS and SAS of an idealised spinal cord artery. In this study, a similar slice model of 2° was developed, with both surfaces of constant angle being treated as symmetry planes to provide a 2D representation of the domain, which approximated a slice of the brain SAS, arterial PVS (300 µm in length), an astrocyte end-foot layer (1 µm wide), and the adjacent brain parenchyma.

We simulated the movement of the commonly used CSF tracer, Dextran 70 kDa (Asgari et al., 2016). The tracer was modelled as both discrete particles only affected by bulk flow and as a diffusive continuum. The discrete particles were 3 nm in diameter and were injected at the centre of the SAS-PVS boundary.

RESULTS

The temporal offset between the arterial pressure pulse and ICP influences the direction and net mass flow rate per cardiac cycle in the model perivascular space. The offsets plotted are from 0-100% in 10% increments. The maximum positive flow rate occurred at a 30% offset (5.2 µg/cycle). The maximum negative flow rate occurred at a 90% offset (-6.1 µg/cycle).

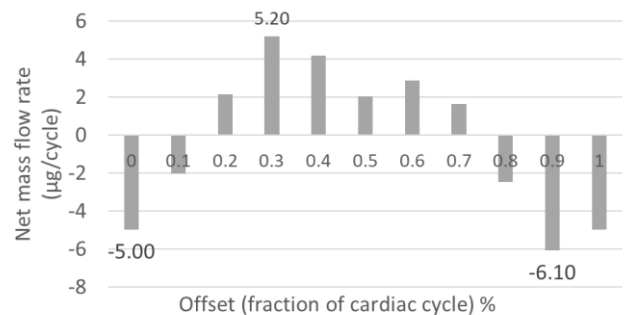


Fig 1. Arterial Pulse – ICP offset.

CONCLUSIONS

In this microscale parametric analysis, it has been shown that a pulse offset mechanism between arterial and ICP pulses can enable net fluid and tracer transport through the PVS in the brain in the absence of a net pressure difference between the SAS and parenchyma. However, the temporal offset required appears to be unphysiologically large. The role of arterial pulsation is still unclear. If the pulse offset mechanism is not physiological, then ICP, not arterial pulsation, may be a driving force for fluid movement in the PVS. However, arterial pulsations may also play a role in enhancing diffusion in the PVS and parenchyma.

REFERENCES

Bilston, L.E. J Neurosurg 112, 808-813, 2010

Asgari, M. Sci Rep 6, 38635, 2016

Presented by Adam Martinac

(a.martinac@neura.edu.au).

A COUPLED BIOMECHANICAL-SPH MODEL TO INVESTIGATE EMPTYING OF SOLID-LIQUID CONTENT FROM THE STOMACH

Ghosh, S.G.; Sinnott, M.D.; Cleary, P.W.; Harrison, S.M.
CSIRO Data61, Clayton South, VIC, Australia 3169;

INTRODUCTION

Our stomach plays a critical role in the digestion of food. Its functions include mixing, shearing, grinding, chemical breakdown and transport of the resulting liquid-particulate mixture to the duodenum. The rate of stomach emptying regulates satiety which is important for issues such as obesity and diabetes. However, the mechanisms controlling emptying rates of solid-liquid contents are not well understood.

In this study we use a coupled biomechanical-Smoothed Particle Hydrodynamics (B-SPH) model to study gastric mixing and emptying. The simulations are evaluated in comparison to *in-vivo* experiments by Marciani et al. (2001), in which multiple volunteers ingested solid agar beads in a liquid meal. The resulting model will enable us to investigate the role of different phenomenon such as peristaltic antral contraction waves (ACWs) and opening/closing of pyloric sphincter (Figure 1A) in emptying of solid-liquid digesta.

METHOD

The simulations are performed using SPH, a mesh-free particle-based method which can be used to solve partial differential equations (Harrison et al. 2018). The stomach wall is represented by a deforming surface mesh, and the liquid digesta is considered as a Newtonian fluid. The agar beads are represented as dynamic spherical objects with six degrees of freedom. Stomach contractions are modelled as kinematically prescribed deformations to the stomach mesh. The amplitude, frequency and speeds of the contractions vary along the length of the stomach using high-resolution electrophysiological activity data (Berry et al. 2016) as a basis for these parameters.

Following the protocol in Marciani et al. (2001), 500 mL of liquid and 15 agar beads were positioned within the stomach mesh and to settle under gravity loading with no contraction waves present. Next, digesta flow was simulated for 100 s and spatiotemporal velocities of the fluid and agar beads were calculated.

RESULTS

Figure 1A shows a visualisation of the model after 100 seconds of simulated gastric mixing. None of the 15 agar gel beads were emptied after this period. Figure 1B

shows the centre of mass (COM) of the agar beads in the X and Y directions. The COM fluctuated with the peristaltic contractions; however these motions were not sufficient in magnitude for passage through the pyloric sphincter when open. Figure 1C shows mean and maximum (Max) speed of the liquid digesta, which varies in proportion to the position of the peristaltic waves. Unlike the agar beads, the liquid content emptied from the stomach in a steady rate in the periods when the pyloric sphincter was open (Figure 1D).

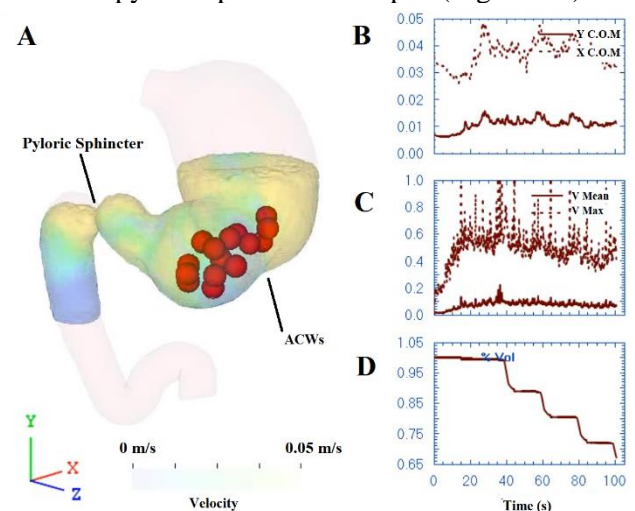


Figure 1. (A) Contents of the stomach after 100 sec, (B) Centre of Mass (COM) of the solid beads in X & Y direction, (C) Maximum (Max) and mean velocity of liquid digesta, (D) Percentage volume of digesta in stomach as a function of time.

CONCLUSIONS

Results from the B-SPH model are consistent with experimental studies that show there is often a substantial emptying of liquid digesta with little or no emptying of solid particles. Future work will involve simulating larger timeframes of digestion, incorporating slow tonic contraction of the upper stomach, and chemical and mechanical breakdown of food.

REFERENCES

- Harrison S M, Food Funct., 2018, 9, 3202.
 - Marciani L, Am J Physiol Gastrointest Liver Physiol. 280, G844 G849, 2001.
 - Berry R, Am J Physiol Gastrointest Liver Physiol. 311, G895 G902, 2016.
- Presented by Shouryadipta Ghosh (Shouryadipta.ghosh@data61.csiro.au).

PATIENT-SPECIFIC RADIOCEPHALIC ARTERIOVENOUS FISTULA MODELS FOR SURGICAL TRAINING AND FLOW VISUALISATION

Vijayaratnam, P.R.S; Kim, Y.C.; Barber, T.J.,
UNSW Sydney, Sydney NSW 2052, Australia

INTRODUCTION

A radiocephalic arteriovenous fistula (AVF) is a surgical connection which is created between the radial artery and the cephalic vein in the wrist and is the preferred form of vascular access for kidney disease patients undergoing dialysis. This connection allows blood to bypass the resistance of peripheral capillary beds and, after a maturation period of 4-6 weeks [3] can allow the venous flow rate to increase to high enough levels for effective dialysis. Nonetheless around two-thirds of radiocephalic AVFs fail to mature into usable vascular access points due to stenosis [4].

Obtusely angled 'smooth loop' AVF geometries have been found to minimise flow disturbances which cause stenosis [1]. This has recently resulted in the off-label use of kink-resistant Supera™ peripheral stents to achieve these 'smooth loop' geometries within patients [4]. The initial results with this technique have been promising, with low reintervention rates and no AVFs lost after a 12-month mean follow-up period; however, this procedure is still in its infancy. The development of a realistic stent deployment trainer, along with data showing the haemodynamic improvements which result from using this technique, could help it to achieve widespread adoption.

METHOD

Silicone AVF stent deployment trainers were made by casting polydimethylsiloxane (SYLGARD™ 184 Silicone Elastomer) within casting boxes containing 3D-prints of the patient-specific AVF geometries, which were subsequently dissolved/melted away. These geometries were previously obtained from patients using an in-house 3D ultrasound system, which consisted of an ultrasound machine, (Mindray, TE7) and a linear ultrasonic transducer (Mindray, L14-6NS, 14MHz, 38mm FOV) [2]. This ultrasound system did not have sufficient resolution to obtain the stent geometry within the patient, however.

To achieve scans of the stent geometry, the stent deployment procedure [4] was repeated within the silicone trainers and micro-CT scans (MILabs, U-CT) were performed.

RESULTS

Deployment of a Supera™ peripheral stent into the silicone trainers was achieved by an experienced vascular surgeon, as may be seen in Figure 1. Micro-CT scans of these stented silicone trainers then allowed computational fluid dynamics simulations to be performed, as also shown in this figure.

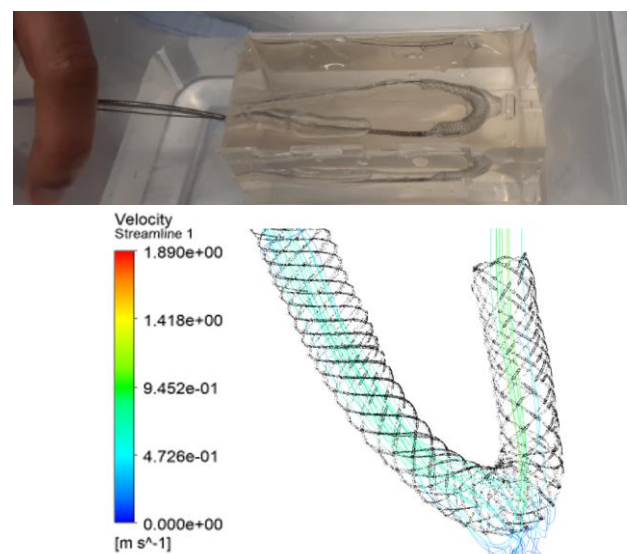


Figure 1. Stent deployment within the silicone trainer (top) and flow analysis (bottom).

CONCLUSIONS

Silicone surgical trainers were developed to allow vascular surgeons to be trained in the deployment of kink-resistant Supera™ peripheral stents into patient-specific AVF geometries. Micro-CT scans then allowed fluid dynamics simulations to be performed, so that the haemodynamics of these obtusely angled 'smooth loop' AVF geometries could be compared against standard geometries.

REFERENCES

1. Carroll, J. Nephrology 24, 245-251, 2019.
2. Colley, E. IEEE Transactions on Biomedical Engineering 65, 1885-1891, 2018.
3. Gameiro, J. J. Vascular Access 21, 134-147, 2020.
4. Thomas, S. J. Endovascular Therapy 26, 394-401, 2019.

Presented by Pujith Vijayaratnam
(p.vijayaratnam@unsw.edu.au)



DAY 1

Posters

A FLEXIBLE FRAMEWORK FOR REAL-TIME CONTROL OF NEUROMECHANICAL PROSTHESES

Sousa, A.; Quinn, A.; Mulholland, K.; Mannan, M.; Crossley, C.; Lloyd, D.; Pizzolato, C.
Griffith Centre of Biomedical and Rehabilitation Engineering, Griffith University, Gold Coast, Australia

INTRODUCTION

Neuromechanical prostheses comprise a network of sensors, actuators, and control systems to interface electrical and mechanical devices with humans to replace or augment motor and sensory functions [1]. Combining two or more acquisition devices is common when using instruments specifically developed for the research laboratory, such as integrated data acquisition software (e.g., Vicon Nexus). However, developing a reliable network of devices that continuously acquire data and controls in real-time, motorised (e.g., exoskeletons) and electrical stimulation of devices rapidly becomes an engineering challenge. Additionally, how can we ensure the scalability of this network to facilitate the future inclusion of additional devices? Unfortunately, most approaches still involve developing homemade integration solutions that do not follow a sustainable and scalable software structure. This situation hinders research and translation to market.

The *Robot Operating System* (ROS) [2] is a middleware developed by the robotic research community. ROS enables the communication between two or more applications or application components in a distributed network. While a powerful tool, the uptake of ROS for applications in biomechanics and rehabilitation is still minimal. Here, we present a modular ROS design that combines brain-computer interface (BCI), electrical stimulation, and ergometer crank control for rehabilitation after spinal cord injury.

METHOD

We structured control based on the 2nd ROS version (ROS2), allowing data acquisition control and storage in real-time [2]. Within ROS2, we created *nodes* in C++ and python, stand-alone executables capable of receiving, computing, and transmitting data. Nodes *publish* messages on a *topic* and/or *subscribe* to a *topic* to receive information. This design preserves data integrity and avoids multiple threads to write on the exact memory location at once [3]. Then, we designed a real-time control system for electrical stimulation cycling triggered by a BCI, represented in Figure 1. First, the *electroencephalogram* (EEG) node acquires raw EEG data for the *BCI classification* to interpret the

target speed. Next, the *Neuromechanical control*, which implements a real-time neuromusculoskeletal model, calculates the required functional electrical stimulation parameters and target crank torque for the ergometer.

RESULTS

We may quickly add, remove, or change sensors, mechanical components, and computational methods fitting to flexible rehabilitation setups. For example, we developed nodes for different ergometer and EEG devices that we can choose before starting the session.

This framework follows a scalability structure, in which we may quickly add, remove, or change i.e. sensors, mechanical components, and computation methods, fitting to flexible rehabilitation setups.

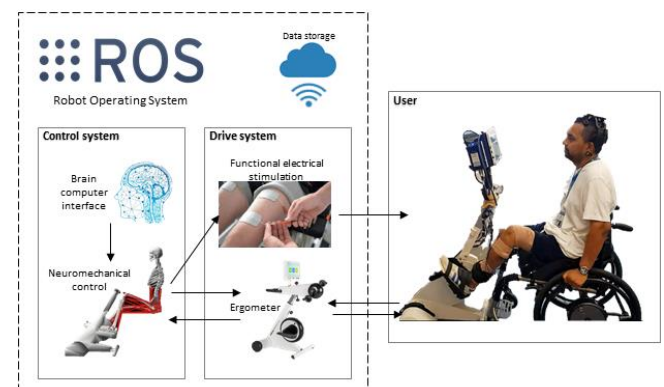


Figure 1. Control diagram of the real-time control.

CONCLUSIONS

ROS2 facilitated communication, enabling high-performance, real-time, scalable data exchanges using a publish-subscribe pattern. This solution integrates sensory and driver equipment in a flexible and scalable development environment for biomechanics and rehabilitation.

REFERENCES

- [1] Pizzolato et al., Front. Neurorobot., 97, 2019
 - [2] Maruyama et al., Proc. EMSOFT, 0-9, 2016
 - [3] Pizzolato, Comput Methods Biomech Biomed Eng., 20, 4, 2017
- Presented by Ana de Sousa (a.cardosodesousa@griffith.edu.au).

ASSESSMENT OF TRABECULAR BONE ADAPTATION IN ADOLESCENT IDIOPATHIC SCOLIOSIS DUE TO ALTERED JOINT LOADING

E. Pickering,^{1,2} J Wang,¹ L. Stickel,^{1,2} M. Martin,¹ C. Miller,^{1,2} J.P. Little,^{1,2} M.T. Izatt,^{1,2} R. D.

Labrom,² G. N. Askin,² Davide Fontanarosa,¹ P. Pivonka¹

¹ Queensland University of Technology, Brisbane, Australia

² Queensland Children's Hospital, Brisbane, Queensland

³ Université Paris-Est, Paris, France

INTRODUCTION

Adolescent Idiopathic Scoliosis (AIS) is the most common deformity of the spine, affecting 2–4% of the population. Previous studies have shown that the vertebrae in scoliotic spines undergo abnormal morphological changes. In particular, the rapid progression of vertebral wedging in AIS during the adolescent growth spurt is caused by asymmetrical growth. The latter has been attributed to the Hueter-Volkman law of mechanically modulated endochondral growth [1].

One aspect of deformity progression that is less well known is whether vertebral body adaptation based on Wolff's law also contributes to deformity progression [2]. While animal studies have shown that vertebral bone adaptation takes place, this finding hasn't been fully confirmed in humans. The study of Adam and Askin [3] showed a marked convex/concave asymmetry in bone mineral density (BMD) for vertebral levels at or near the apex of the scoliotic curve. However, due to lack of in vivo CT image resolution no information regarding trabecular architecture was provided. The purpose of the current study was to test the hypothesis whether altered mechanical loading conditions may lead to adaptation of the trabecular bone microstructure in accordance of Wolff's law.

Bone cores (diameter: 5 mm; length: 10-20 mm) were taken at the mid-vertebral height. After extraction, the bone cores were PMMA embedded. Microarchitecture was assessed via microCT (Scanco Medical 50, 6.8 μm resolution), mineralization was assessed via quantitative backscatter electron imaging (qBEI) (Tescan TIMA, 20 kV), and mechanical properties were assessed via nanoindentation (Hysitron TI950).

RESULTS

Based on microCT analysis the average trabecular thickness was between 125-160 μm which is within the values reported for mean horizontal trabecular bone thickness in the healthy adult population. The trabecular orientation was contained between 30 and 60 degrees relative to the vertical direction which may be linked to the altered loading directions of the vertebrae in AIS patients. Bone value fraction (BV/TV) was increased at the concave side compared to convex side of the deformity which would confirm findings from the earlier in vivo CT study [3]. Bone mineralization was uncovered through qBEI, trends along the length of the vertebral body, and relationship to deformity were elucidated. Further, nanoindentation unveiled relationship with deformity and bone mechanical properties.

CONCLUSIONS

We developed an experimental method to extract (undisturbed) bone samples from apical vertebrae in AIS patients. Bone core microarchitecture, mineralization, and mechanical properties were studied. Relationships were elucidated with respect to deformity. These results were used to assess how asymmetric loading in AIS impacts asymmetric vertebral growth.

REFERENCES

- [1] I.A. Stokes et al. Spine, 21:1162, 1996.
- [2] P.L. Mente et al. Spine, 22:1292, 1997.
- [3] C.J. Adam and G.N. Askin. Bone, 45:799, 2009.

Presented by Edmund Pickering
(ei.pickering@qut.edu.au)

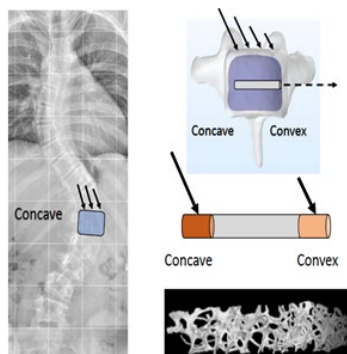


Figure 1: Schematic representation of apex vertebral bone core extraction from AIS patients and microCT analysis. Furthermore, the expected mechanical loading conditions at the concave and convex side are shown.

METHOD

Vertebral levels at or near the apex of the scoliotic curve were identified in AIS patients undergoing anterior scoliosis correction surgery (see Figure 1).

KNEELING TASKS WITH AND WITHOUT KNEE PADS: REPEATABILITY AND LOADING VISUALISATION

Thwaites, S.¹; Rickman, M.^{1,2}; Thewlis, D.^{1,2}.

¹Centre for Orthopaedic and Trauma Research, The University of Adelaide, Adelaide, SA, Australia;

²Department of Orthopaedics and Trauma, Royal Adelaide Hospital, Adelaide, SA, Australia

INTRODUCTION

Kneeling is an important activity of daily living. Trauma, degenerative conditions such as osteoarthritis, or the after-effects of local surgery may all lead to difficulty or the inability to kneel [1]. Anatomical structures contacting the ground change with varying kneeling postures [2]. Previous work [3] instrumented specific anatomical landmarks of the knee throughout kneeling tasks and presented the overall magnitude of applied loads. The aims of this work were to: (1) calculate the repeatability of left/right knee weight distribution; and (2) describe the loading distribution around the knee throughout various kneeling tasks. All kneeling tasks were performed with and without kneepads.

METHOD

Eight 12.7 mm diameter force sensitive resistors (FSRs) (Delsys, USA, 2000 Hz) were placed about the right knee (Figure 1) of 14 healthy participants (M/F: 7/7, age: 26.4 ± 2.5 years, height: 171.8 ± 4.9 cm, mass: 68.5 ± 12.8 kg). Vertical ground reaction force (F_z) data were captured using two in-ground force platforms (AMTI Optima, USA, 2000 Hz). Participants performed three trials of upright kneeling (60 secs) and reaching tasks: forward, back, left, and right (5 secs), with and without kneepads. Testing was repeated after a minimum three-day break. Matlab 2019b (MathWorks, USA) and R 4.0.3 (R Core Team, Austria) were used for data analysis. All participants provided written informed consent.

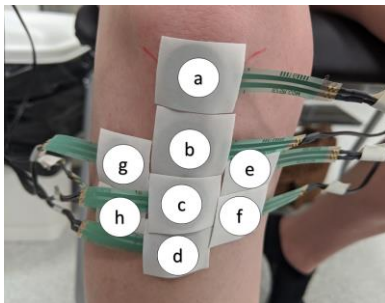


Figure 1: Four FSRs were placed in a line from (a) the inferior pole of the patella (IPP) to (d) the tibial tuberosity (TT); two FSRs were placed medially (e, f) and laterally (g, h) to this line, respectively.

RESULTS

The intra-class correlation coefficient (ICC(2,1)) of normalised F_z (BW) showed good (ICC = 0.6 – 0.74) to excellent (ICC = 0.75 – 1.0) [4] intersession

repeatability between left/right knees for all kneeling tasks except for no pad upright kneeling on the left knee (ICC = 0.33), padded upright kneeling on the right knee (ICC = 0.38), padded right reaching on the left knee (ICC = 0.51). Bland-Altman analysis showed mean differences (BW) in left/right knees for all conditions between sessions lying within the 95% confidence intervals of the upper and lower limits of agreement.

Kneeling load distribution for all conditions are presented in Figure 2. The distal patella tendon (Figure 1c) was active for all kneeling conditions.

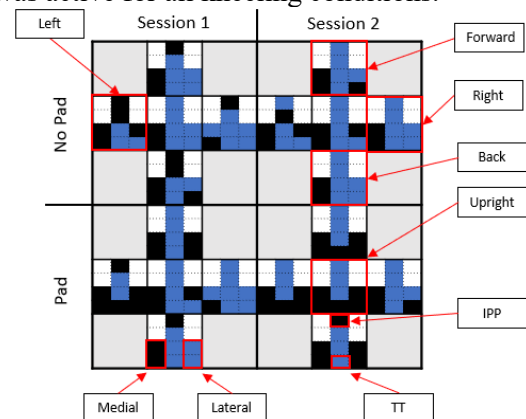


Figure 2: Heatmap representation of average FSR activation of the right knee during kneeling tasks as viewed from above. Black = no activation, blue = activation, white = no FSR placed.

CONCLUSIONS

We have demonstrated the repeatability of left/right knee weight distribution throughout various kneeling tasks and described the loading distribution of the right knee. Left/right knee weight distribution has shown to be reasonably reliable between sessions. Individual FSR activation of specific anatomical landmarks has shown to be an effective tool for visualising which structures are contacting the ground during kneeling. F_z data coupled with FSR activation provides valuable insights into both the magnitude and locations of applied loads throughout kneeling.

REFERENCES

- [1] Weiss et al. (2002) Clin Orthop Relat Res, 404:172–188.
 - [2] Palmer et al. (2002) J Bone Joint Surg Br, 84(2): 220-2.
 - [3] Xu et al. (2017) Appl. Ergon, 58: 308-13.
 - [4] Cicchetti (1994) Psychol. Assess, 6(4): 284–290.
- Presented by Simon Thwaites (simon.thwaites@adelaide.edu.au).

EFFECT OF DIFFERENT TREADMILL-INDUCED PERTURBATIONS ON AGONIST AND ANTAGONIST MUSCLE FORCES IN COMPENSATORY STEP

Namayeshi, T.¹; Haddara, R.²; Lee V.S. P.¹

¹The University of Melbourne, Parkville, Australia; ²Western University, London, Canada.

INTRODUCTION

Falls in older adults are a major problem and can lead to head injuries, hip fractures and even death. In order to better understand falls and successful recovery strategies, identifying kinematics, kinetics and muscle forces patterns during recovery from loss of balance is crucial. To obtain reactive gait patterns, participants must be subjected to unexpected perturbations such as trips and slips. Previous researchers have reported kinematics and kinetics recovery data following trips and slips [1]; however, the muscle force recovery patterns remain unknown. To better target exercises to reduce the risk of falls, we must first understand which muscles, their magnitude, and their coordination patterns, play a role in a successful recovery from a trip and a slip.

METHOD

A total of 20 healthy adults in their twenties with similar athletic backgrounds were perturbed on a split-belt treadmill using Computer-Assisted Rehabilitation Environment (CAREN, Motkforce Link) at a preset speed of 1.1 m/s. Two kinds of perturbations were administered: slip and trip. Slips were simulated by accelerating one belt, whereas trips were simulated by decelerating one belt. Both perturbations had similar intensity and only differed in the direction. Static Optimization was employed in OpenSim 4.1 (open source, Simbios) to obtain lower-limb muscle forces during the stance phase of the compensatory step. Statistical Parametric Mapping paired t-test was used to compare differences in recovery strategies between slip and trip perturbations through magnitude and patterns of muscle forces.

RESULTS

Results showed that trips required larger gluteus maximus (GMAX) (at 15% to 19%; 5.452 ± 5.989 vs 2.282 ± 2.505 N/kg, $p=0.029$ and at 28% to 34%; 3.385 ± 4.292 vs 1.773 ± 2.4607 N/kg, $p=0.019$, critical threshold 3.354), hamstrings (HAM) (at

6% to 8.5%; 7.871 ± 6.594 vs 3.372 ± 6.0689 N/kg, $p=0.046$, critical threshold 3.491) and gastrocnemius (GAS) (at 0 to 8%; 1.956 ± 1.514 vs 0.7525 ± 1.458 N/kg, $p=0.003$, critical threshold 3.53) than slips, respectively. However, muscle force patterns are not significantly different than on the recovery steps after both perturbations.

CONCLUSIONS

These findings suggest that greater GMAX, HAM and GAS muscle forces are vital in post-trip recovery. Future studies can examine the effects of strengthening these muscles on reducing trip fall risk.

REFERENCES

- [1] D. Yoo, K. H. Gait Posture, vol. 71, pp. 98–104, 2019.

Tayebeh Namayeshi
(tnamayeshi@student.unimelb.edu.au)

VALIDATION OF THE CALF RAISE APPLICATION

Hébert-Losier¹, K; Fernandez¹, M.R.; Athens², J; Kubo³, M; Balsalobre-Fernández⁴, C.

¹University of Waikato, Adams Centre for High Performance, Tauranga, New Zealand;

²University of Otago, Dunedin, New Zealand; ³Niigata University of Health and Welfare,

Niigata, Japan; ⁴Universidad Autónoma de Madrid, Spain.

INTRODUCTION

Researchers and clinicians in rehabilitation and sports medicine use the calf raise test (CRT) to evaluate calf muscle function. For testing, individuals stand on one leg and go up on their toes and back down as many times as possible. The newly developed Calf Raise application uses computer-vision algorithms that enables image-processing features to track the 2D path of selected objects in the video footage. These features facilitate automatic and more objective tracking of CRT outcomes. This study aimed to validate the Calf Raise application and examined the concurrent validity and level of agreement of its outcomes against laboratory-based equipment measures.

METHOD

CRT outcomes (i.e., repetitions, fatigue index, total height, peak height, peak positive power, peak negative power, positive work, and negative work) were assessed in forty-three healthy individuals (23 men, 20 women; age: 30 ± 10 y) using the Calf Raise application and laboratory-based equipment (3D motion capture and force plate) simultaneously. Data were extracted from two reflective markers: one placed on the heel (posterior view, $n = 222$) and another below the lateral malleolus (lateral view, $n = 239$). Concurrent validity and agreement for the number of repetitions, fatigue index, total height, peak height, peak positive power, peak negative power, positive work, and negative work were determined using intraclass correlation coefficient (ICC_{3,k}), typical error expressed as a coefficient of variation (CV), and Bland-Altman limits of agreement statistical measures. Additionally, three independent raters performed analysis using the Calf Raise app on 106 videos on three different days to determine inter-rater and intra-rater reliability of app use

RESULTS

ICC showed excellent agreement between the Calf Raise app and laboratory-based equipment for all outcomes on both markers (ICC \geq 0.925). Typical error values ranged from 0% to 10.2%, and was the poorest for the fatigue index. Additionally, the Bland-Altman analysis showed that the agreement between the two systems was good for all outcomes. Inter-rater

(ICC \geq 0.950) and intra-rater (ICC \geq 0.983) reliability were excellent. Typical errors values ranged from 0.4 to 5.6% and 0 to 3.5% across measures for inter-rater and intra-rater, respectively.

CONCLUSIONS

These results demonstrate that the Calf Raise application is valid and reliable for measuring CRT outcomes in healthy adults. Thus, the Calf Raise application is a step towards improving clinical data quality, management, accessibility, efficiency, and accuracy compared to standard clinical practice where only the number of repetitions is used as key outcome measure. The application can now be used to establish empirically based normative values across populations and in clinical research. This application is in line with recent advances in mobile technology to enhance patient care and use of evidence-based objective outcomes. The Calf Raise application shows good to excellent concurrent validity against laboratory-based systems, excellent reliability between and within raters, and can be used with confidence by clinicians and researchers. Given that fewer trials were captured from the posterior marker due to out-of-plane motion, positioning the marker on the lateral side of the foot below the malleolus is recommended for tracking.

REFERENCES

- Atkinson, G. Sports Medicine, 26, 217-238. 1998.
- Byrne, C. J Electromyogr Kinesiol, 36, 34-39. 2017
- Hébert-Losier, K. Calf raise mobile application software. 2020. <https://doi.org/10.17605/OSF.IO/N9SG7>
- Balsalobre-Fernández. J Sports Sci, 38(6), 710-716. 2020

Presented by Kim Hébert-Losier (kim.hebert-losier@waikato.ac.nz).

EFFECT OF INCREMENTAL INCREASES IN LOAD ON LOWER-LIMB COORDINATION VARIABILITY DURING LOAD CARRIAGE

Hoolihan, B.^{1*}; Wheat, J.²; Dascombe, B.¹; Vickery-Howe, D.³; Middleton K.³

¹University of Newcastle, Ourimbah, Australia; ²Sheffield Hallam University, Sheffield, UK; ³La Trobe University, Bundoora, Australia.

INTRODUCTION

Load carriage related injuries directly impact military personnel's availability for service, with 34% of soldiers having sustained one in their career (Orr et al., 2017). Such injuries have been linked to lower-limb coordination variability (CV), where both higher and lower CV has been demonstrated in injured individuals when compared to healthy controls (Davis et al., 2019). While the addition of external load may impact CV and lower-limb injury susceptibility, the effects of external loads on lower-limb CV is unknown.

METHOD

Twenty-six participants (13 female, 13 male) with no prior heavy load carriage experience completed three treadmill-based walking trials at a self-selected walking speed wearing body-borne external loads of 0%, 20% and 40% of body weight [BW]. A Vicon motion capture system tracked marker trajectories with a lower-body direct-kinematic model calculating sagittal-plane segment kinematics of the thigh, shank, and foot. The standard deviations of Continuous Relative Phase quantified the lower-limb CV across 19 strides for the Thigh-Shank, Shank-Foot, and Thigh-Foot couplings. The effect of incremental load on lower-limb CV was assessed using statistical parametric mapping repeated measures ANOVAs and paired t-tests (Pataky et al., 2013).

RESULTS

Significant main effects were observed for all couplings (Figure 1). In the Thigh-Shank coupling, the 40%BW condition demonstrated significantly greater lower-limb CV than the 0%BW condition between 40-47% of the gait cycle. In both the Shank-Foot and Thigh-Foot couplings, there was significantly greater CV in the 40%BW condition than both the 0% and 20%BW conditions. For the Shank-Foot, the 40%BW was significant greater across intermittent stages of the gait cycle than the 0% (0-2%, 3-8%, 41-51%, 66-100%) and 20% BW (5-9%, 14-25%, 42-54%, 70-72%, 80-91%) conditions. Similarly, the Thigh-Foot coupling in the 40% BW condition was significantly greater than the 0% BW (20-40%, 80-92%) and 20% BW (80-92%) conditions.

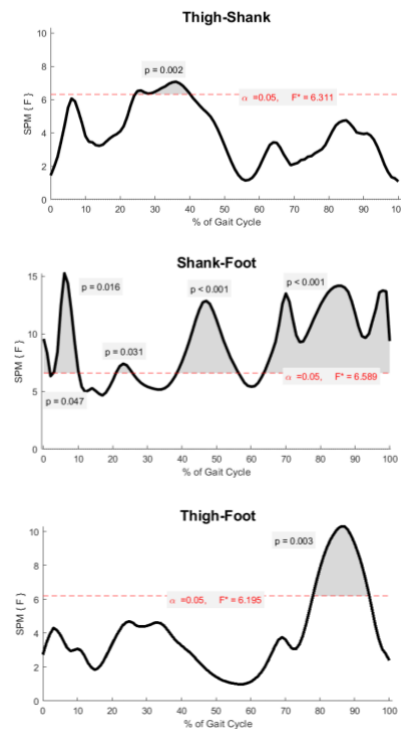


Figure 1. SPM ANOVA F-statistic for each coupling. Shaded region represents a significant main effect of load on CV on the portion of gait cycle.

CONCLUSIONS

The greater CV displayed in the 40%BW condition likely reflects the greater external load acting as a perturbation on the neuromuscular system and the lack of heavy load carriage experience of the participants, resulting in unstable coordination patterns. Given the links between load carriage and injury, loads of 40%BW may present a greater risk of lower-limb injury compared with lighter loads. Further prospective studies are needed to support this.

REFERENCES

- Davis, K. *Gait & Posture* 67, 154-159, 2019.
- Orr, R. M. *Int. J. Inj. Contr. Saf. Promot.* 24, 189-197, 2017.
- Pataky, T. C. J. *Biomech.* 46, 2394-2401, 2013.

Presented by Brooke Hoolihan
(brooke.hoolihan@uon.edu.au)

CHANGES TO KINEMATICS AND KINETICS OF TYPICALLY DEVELOPING CHILDREN USING THE PYCGM2 MODEL

Anderson, D.C.¹; Passmore, E.^{1,2,3}

¹ Hugh Williamson Gait Analysis Laboratory, The Royal Children's Hospital, VIC, Australia.

² Gait Lab & Orthopaedics, Murdoch Children's Research Institute, VIC, Australia.

³ Faculty of Engineering & Information Technology, University of Melbourne, VIC, Australia.

INTRODUCTION

Kinematics and kinetics obtained from 3D gait analysis (3DGA) are dependent on the underlying biomechanical model, marker-set and data processing choices. The Conventional Gait Model (CGM), implemented in Vicon Nexus as Plug-in-Gait (PiG) is still widely used in clinical centres, despite its known limitations and weaknesses.

Leboeuf and colleagues proposed a series of changes to the CGM, pyCGM2 project¹, to improve prediction of joint centre and axes locations and implement inverse kinematics. Inverse kinematics is important to enable compatibility with musculoskeletal modelling packages, which is lacking in the clinical setting. However, the proposed changes on model outputs have not been fully evaluated, particularly in a paediatric setting. The aim of this study was to evaluate the effect of CGM2 changes on kinematics and kinetics of typically developing children.

METHOD

We analysed motion capture data from 32 typically developing children and adolescents, mean age 12 years (range: 5-18yrs)². All participants had both the CGM1.0(PiG) marker-set and the cluster-based marker-set of CGM2.3 applied. For each participant the kinematics and kinetics were calculated for each step of the CGM2 project from CGM1.0 to CGM2.3. Briefly, these changes include CGM1.0(PiG clone) in python, CGM1.1 includes minor changes related to bug fixes and the order in which pelvic angles are decomposed. CGM2.1 introduces new hip joint centre regression equations, CGM2.2 implements inverse kinematics and CGM2.3 implements thigh and shank marker clusters.

The Root mean square difference (RMSD) between CGM1.0 and each version of CGM2 were calculated for the entire gait cycle. For comparison of CGM1.1 to CGM2.1 where regression equations for hip joint centre location were changed, the difference between joint centre location was also calculated.

RESULTS

The RMSD between versions of the model are presented in Figure 1. For the sagittal plane RMSD were < 3°, coronal plane < 5° and transverse plane < 7°. The largest differences can be seen for the hip and knee kinematics in the transverse plane for version CGM2.2 and 2.3. On average the hip joint centre between CGM1.1 and 2.1 was more lateral, posterior and proximal, absolute difference 13mm ± 8.

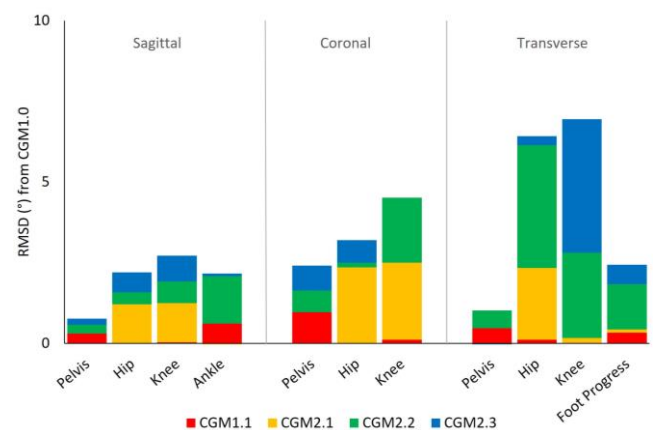


Figure 1. Zero represents the kinematics from version CGM1.0 (Plug-in Gait clone). Each stacked bar represents the RMSD from CGM1.0 to the corresponding version.

CONCLUSIONS

Implementing the different versions of the CGM2 model produced significant changes in kinematic and kinetic outputs compared to the original CGM1.0 (PiG clone). The largest changes were seen for the hip and knee in the transverse plane for model CGM2.2 and 2.3 as these implemented inverse kinematics and marker-clusters for the thigh and shank. Further evaluation on the effect on clinical datasets is warranted before clinical implementation.

REFERENCES

1. Leboeuf, F et al. Gait & posture 69, 235–241, 2019.
2. Tirosh O et al. J Electromyogr Kinesiol, 23, 1451-1459, 2013.

Presented by Dan Anderson (dan.anderson@rch.org.au).

THE EFFECTS OF SEX AND AGE ON HUMAN TENDON BIOMECHANICS

Ashton D.M¹; Blaker C.L¹; Hefferan S.A¹; Hartnell N.J²; Little C.B¹; Clarke E.C¹.

¹ Kolling Institute, Sydney, Australia; ² Bowral and District Hospital, Bowral, Australia

INTRODUCTION

Tendinopathy disproportionately affects the older population, yet biomechanical studies of ageing human tendons are rare. Age-related tendon changes are most commonly investigated in small animal models (e.g. rat/rabbit) or *in vivo* human studies that do not report data on failure properties. A small number of *in vitro* studies have investigated the effects of ageing or sex on human tendon biomechanics, but these are generally single tendon types, small sample sizes, and narrow range of ages.

The present study aimed to determine the effects of aging and sex on human tendon biomechanical properties across a range of lower limb tendons in an advanced age cohort.

METHOD

31 (19 male, 12 female) human cadaveric lower legs (tibial plateau to toe-tip) were sourced fresh-frozen. Donor ages ranged from 68 to 99 years old, with a mean±SD age of 82±8 (males 81±7; females 84±8). Nine tendons from each lower leg were retrieved by a trained surgeon (NH) including: Achilles Tendon (AT), Tibialis Posterior (TP), Tibialis Anterior (TA), Fibularis Longus (FL), Fibularis Brevis (FB), Flexor Hallucis Longus (FHL), Extensor Hallucis Longus (EHL), Plantaris (Plt) and Flexor Digitorum Longus (FDL). 10-20mm portions were cut from both proximal- and distal-ends for histological assessment with the remaining central length allocated to biomechanical testing.

Biomechanical evaluation was performed by uniaxial tensile testing to failure at 5% strain/s. Cross-sectional area (CSA), force and displacement data was used to calculate maximum load at failure, ultimate tensile strength (UTS), strain at failure and elastic modulus. Tendons damaged during dissection (n=20) and those which slipped during testing (n=6) were excluded. Results for 253 samples were analysed using mixed model regression controlling for age, sex and tendon, with pairwise comparisons between groups, adjusting for multiple comparisons using the Benjamini Hochberg procedure with false discovery rate of 0.05. Matched biochemical samples were also collected from the rupture site after testing for future analysis.

RESULTS

Differences were observed between various tendon types for all 5 outcomes measured. For example, the maximum load at failure for each tendon was significantly different to every other tendon except: TP vs TA, FB vs FHL; FB vs FDL; FHL vs FDL (Fig. 1A). Males had significantly higher CSA ($\beta=5.71\text{mm}^2$; $p<0.001$), maximum load ($\beta=279.63\text{N}$; $p=0.003$, Fig.1A) and strain at failure ($\beta=0.02$; $p=0.002$) and lower stiffness ($\beta=-42.67\text{MPa}$; $p=0.015$) compared to females. However, there was no effect of age on these outcomes. Conversely, there was no effect of sex on UTS ($p=0.170$), but tendons slightly decreased in strength with age ($\beta=-0.40\text{MPa}$; $p=0.002$; Fig. 1B).

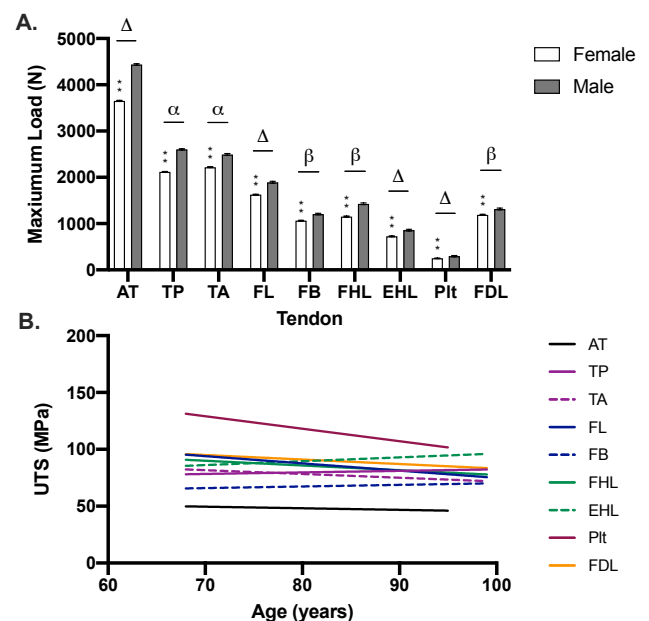


Figure 1. Biomechanical Data of Advanced Age Lower Limb Tendons. (A) Effect of sex and tendon type on max load. Significant differences identifiable by (i) between sexes ** ($p<0.01$), (ii) between tendons: Δ different all; α different to all except TP and TA; β different to all except FB, FHL and FDL ($p<0.05$). (B) Effect of age and tendon type on UTS.

CONCLUSIONS

This is the first study to investigate the effects of age and sex across a large range of advantaged age human tendons. All outcomes were affected by sex, but not age, except for UTS. Strength was unaffected by sex but decreased with age. However, this effect size was small.

Presented by Dylan Ashton
(dylan.ashton@sydney.edu.au)

LINKING MUSCLE MECHANICS TO THE METABOLIC COST OF CONSTRAINED HOPPING

Jessup, L.N.; Lichtwark, G.A.; Kelly, L.A.; Cresswell, A.G.
The University of Queensland, Brisbane, QLD, Australia

INTRODUCTION

Various theories exist for how metabolic energy consumption can be predicted by mechanical parameters during steady-state human locomotion. Derivatives of mechanical work and force have received the most compelling rationale and support as proxies of muscle ATP utilisation. However, these frameworks appear only effective over a small fraction of the movement conditions that humans can perform.

This study aimed to determine how changing hopping requirements (e.g., height, frequency) influenced key muscle outputs that may contribute to energy consumption, so that we can better predict how changing mechanics influences energy consumption.

METHOD

Data is presented from $n = 5$ (4 males, 1 female; age 26.4 ± 1.3 (mean \pm SD); height 173.3 ± 9.5 cm; mass 69.4 ± 13.1 kg). We aim to collect data from $n = 15$.

Each participant performed 19 x 4 min trials: 7 partly constrained (hop frequency (f) or height (h) specified), 8 fully constrained (both f and h specified), and 4 unconstrained (neither f nor h specified).

Steady-state metabolic energy expenditure was elicited prior to, and measured during, the final 2 min of each trial. Kinematics and kinetics were measured simultaneously at 3 min (11-camera motion analysis system and 2 x force plates). Electromyography (EMG) data presented here, was collected from lateral gastrocnemius (LG), soleus (SOL), and vastus lateralis (VL). EMG of other leg muscles was also measured, but not reported here. Ultrasound imaging was used to measure muscle fascicle length changes from the same muscles.

4 subsets of data are used for comparison – low frequency and high hop height (**HH**; 1.8 ± 0.06 Hz, 19.9 ± 1.3 cm); low frequency and low hop height (**LH**; 1.87 ± 0.06 Hz, 10.0 ± 2.8 cm); high frequency and low hop height (**HF**; 3.01 ± 0.01 Hz, 7.08 ± 2.1 cm); and self-selected (**SS**; 2.54 ± 0.07 Hz, 9.53 ± 0.4 cm). With low participant numbers, here we describe trends between metabolic power output and muscle parameters. A more detailed statistical approach (e.g.,

principal component analysis) is planned as more participants are examined.

RESULTS

Metabolic power (Fig. 1A) was greatest for the HH condition, followed by LH. Similar power was found for SS and HF, although SS tended to be higher. Thus, hopping to higher heights and/or lower frequencies showed increases in metabolic power. Fascicle shortening of the calf muscles (LG: Fig 1B, SOL: Fig 1C) resembled the metabolic power, however this was not the case for VL (Fig 1D). The opposite was the case for integrated EMG. Thus, it seems a combination of work and force requirements of different muscles contributes to the overall metabolic cost.

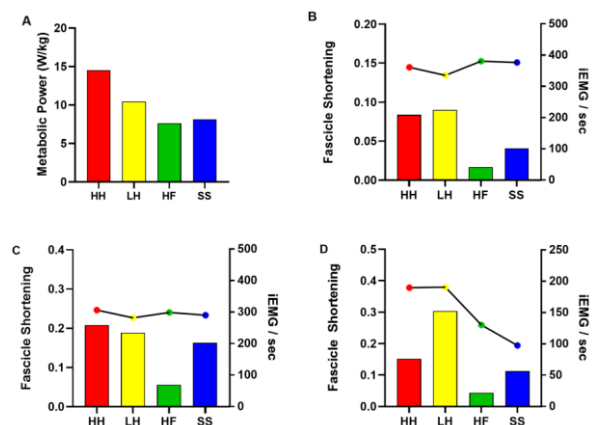


Figure 1: The metabolic power (W/kg; Fig. 1A), and normalised LG (Fig. 1B), SOL (Fig. 1C), and VL (Fig. 1D) fascicle shortening (bars) and integrated EMG (iEMG) per second (dots) between HH, LH, HF and SS conditions.

CONCLUSIONS

There were no clear trends across muscles which explain metabolic cost. Therefore, a more detailed approach to determining muscle force, work and efficiency is required to explain the metabolic cost of hopping under different conditions. Data from 10 more participants should lessen the variability in our results and enable better predictive capacity for specific mechanical parameters.

REFERENCES

- Beck, O. N. Proc. R. Soc. B. 287, 2020.
- Gutmann, A. K. Exp. Physiol. 98, 1178-1189, 2013.
- Gutmann, A. K. J. Exp. Biol. 220, 1654-1662, 2017.

Presented by Luke Jessup (luke.jessup@uq.edu.au)

PROBING MUSCLE ADAPTATION FOLLOWING LOCALISED AND WIDESPREAD DAMAGE USING A MECHANOBIOLOGICAL MODEL

S. Khuu^a, J. Fernandez^{a,b}, and G. Handsfield^a

^aAuckland Bioengineering Institute; ^bDept of Engineering Science, The University of Auckland.

INTRODUCTION

Skeletal muscle is an adaptable tissue with the potential to repair in response to injury. Mechanical stimuli such as active lengthening of muscles causes focal, segmental or large-scale damage to cell membranes and trigger an acute immune response [1]. Surrounding cells migrate towards the damage site and begin the repair process that usually results in repaired tissue that is well-organised. This model has been used to investigate the changes in muscle recovery in response to localised muscle damage similar to active lengthening, and widespread random damage such as that seen in inflammatory muscle pathologies [2].

Agent-based modelling (ABM) is a technique where autonomous agents (in our case, cells) are situated in an environment (skeletal muscle) with changeable relationships. In ABM, dynamic interactions reflect the complex and non-linear nature of physiological systems, and often lead to emergent phenomena. To guide cell behaviour in a physiological manner, we have created a 3D finite element model (FEM) of a muscle fibre bundle with active contraction using FEBio software (<https://febio.org/>). We used these models to simulate the difference in clearance and recovery time of damaged tissue with and without mechanically localised damage.

METHOD

The ABM of human skeletal muscle regeneration was created in Repast Symphony, a Java-based modelling platform. The ABM was seeded using experimental studies on muscle regeneration and injury. Cellular populations in the ABM include inflammatory cells (macrophages, neutrophils, and cytokines), SCs, fibroblasts, and other ECM components. The simulation represented muscle regeneration over 28 days following 5% damage. Damage was implemented in one of two ways: 1) ‘Localised damage’ seeded by using strain values from the FEM, or 2) ‘widespread damage’ by labelling a percentage of the original fibre count throughout the cross-section of the muscle as damaged. Necrosis was implemented following the initial damage to simulate realistic conditions of clearing neighbouring damaged tissue.

A 3D finite element model of a muscle fibre bundle (20 fibres) with active contraction was created using FEBio.

This model was used to simulate 30% active muscle lengthening and used to seed locations of high strain in the localised simulations.

RESULTS

Fibril recovery was optimal following localised 5% damage with final fibril counts exceeding initial values (Fig 1). Damaged fibres in localised simulations were cleared earlier compared to the widespread damage, and extensive necrosis occurred on surrounding fibres in the widespread damage simulation. Fibril recovery was also adequate following widespread damage, however, not did not show as much growth.

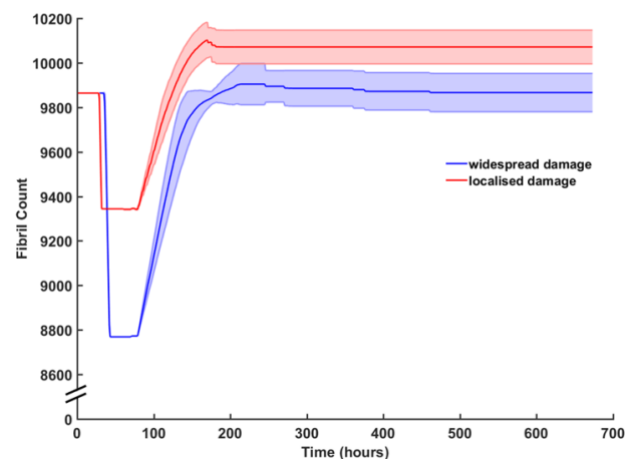


Figure 1. Fibril recovery (mean \pm SD) over 28 days following localised or widespread damage of 5%.

CONCLUSIONS

The inclusion of mechanical inputs that localize damage and regeneration have the effect of altering the behaviour of cells in unexpected ways. This simulation is reflective of a comparison between mechanical damage (e.g. caused by exercise) and inflammatory damage which would affect the muscle tissue in a more spatially random way. This indicates that skeletal muscle may be adapted for regeneration after mechanical damage and may incur longer term muscle fibre adaptation from inflammatory damage.

REFERENCES

1. Smith et al., Sport. Med. 38, 947–969, 2008.
2. Cavazzana et al., Clin. Rev. Allergy Immunol, 52:88–98 2016

DESIGN AND EVALUATION OF A NOVEL EXPANDABLE HELMET FOR BICYCLISTS

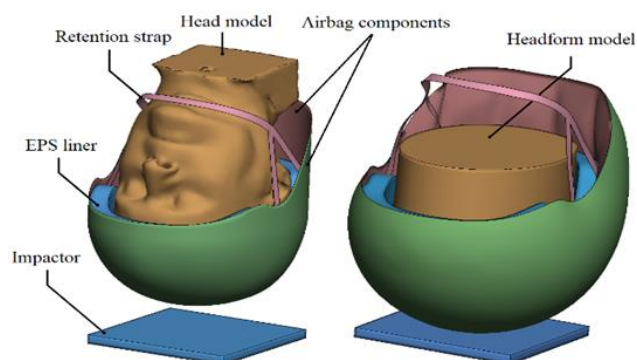
Tse, K.M.; Holder, D.
Swinburne University of Technology, Australia

INTRODUCTION

Most of the current bicycle helmets, which are ultimately designed to prevent blunt trauma, e.g., skull fracture, comprised of a soft foam comfort liner, a polymeric foam absorption liner, encased in a thin plastic outer shell with a chin strap for retention in impact. However, in severe cases, the energy absorbing capability of traditional the conventional liners is insufficient to negate serious brain injury or death. In this study, the authors explore the synergetic features of an expandable airbag and a standard commuter type EPS helmet in their expandable helmet design. Since most instances of serious harm and death in cyclists are attributed to injuries pertaining to the head and neck, the authors conceptualised that the novel expandable helmet, comprising of the conventional EPS helmet and an airbag that will being deployed prior to impact, will protect the vital regions vulnerable to fatal head and neck injuries.

METHOD

In the present study, a series of dynamic impact simulations were carried out on the helmeted head with two configurations (conventional EPS bicycle helmet and our novel design of “airbag” helmet), using Ansys Workbench LS-DYNA. The impact simulations were designed to replicate the impact testing with a flat anvil, as described in Australian Standard AS/NZS 2512. The entire inflation of the expandable airbag was included in the dynamic simulation, with the fluid in the airbag modelled as air with an atmospheric density, pressure, and molar gas constants, following Kurt et al. [1].



RESULTS

A significant decrease in linear acceleration at the CG of the head model is shown in Figures 6 and 7. The duration of the impulsive acceleration is significantly longer, hence reducing the reported HIC36 value from 1170 to 536. This resulted in a decrease in probability of AIS level 3 injury from 64% to 17% based on injury curves developed by Mertz et al. [2].

The case of the EPS helmet showed the average MPS was 0.08-0.10 with a centroid sectional peak of 0.40 located in the interface of the white matter and gray matter in the central cerebrum, outlined in the Fig.7. For the case of the Airbag helmet, the average MPS was 0.02-0.04 with centroid sectional peaks of around 0.26 in the same location in the brain.

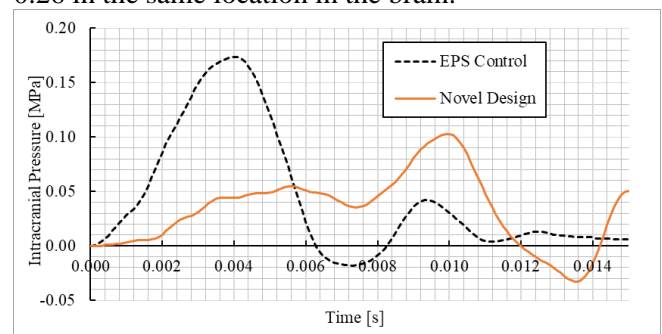


Figure 1. Ensure figure is clear and text is readable.

CONCLUSIONS

To conclude, current EPS helmet designs provide adequate protection but there is potential for technological optimization to further reduce the risk of head injury and TBI. A novel expandable helmet design performed admirably when compared to a control EPS design, showing improvements in kinematic and biometric injury risk factors.

REFERENCES

- [1] Kurt, M., et al. Ann Biomed Eng 45 , 1148-1160, 2017.
- [2] Mertz, H.J. SAE. 33, 1996.

Presented by K.M. Tse (ktse@swin.edu.au).

JOINT CONTACT FORCES DURING POSTERIORLY SEATED CYCLING

Crossley C¹; de Sousa A¹; Saxby DJ¹; Diamond LE¹; Fornusek C²; Lloyd DG¹; Pizzolato C¹.

¹Griffith Centre of Biomedical and Rehabilitation Engineering, Griffith University, Australia;

²Faculty of Medicine and Health, The University of Sydney, Australia.

INTRODUCTION

Following spinal cord injury (SCI), bone mineral density decreases, leading to osteoporosis and increased likelihood of bone fracture. Functional electrical stimulation (FES) cycling uses precisely timed contractions of paralysed muscles to produce cycling exercise. In contrast to traditional upright position cycling, SCI patients are seated in a recumbent position in their own wheelchair. FES cycling can generate joint contact forces sufficient to fracture bone in the lower limbs [1]. However, appropriate joint contact forces might be protective against bone demineralisation [2]. Thus, understanding the internal biomechanics of posteriorly seated cycling might help improve the safety and efficacy of FES rehabilitation for SCI individuals.

This study used an electromyography (EMG)-informed neuromusculoskeletal model to estimate hip, knee, and ankle contact forces [3] in one able-bodied individual. We present preliminary data, a first step towards safer FES cycling approaches for individuals with SCI.

METHOD

Motion capture (Vicon, Oxford, UK), surface EMG (Myon Aktos, Switzerland) of 8 muscles of a single leg, and bilateral radial and tangential crank reaction forces (Swift Performance, Brisbane, Australia) were time synchronised and recorded for one healthy participant cycling on a clinical ergometer (RT300, Restorative Therapies, Baltimore, MD, USA). The participant performed cycling at 40 (50W), 60 (75W) and 80 (100W) revolutions per minute while maintaining approximately 12 Nm crank torque. Inverse kinematics and dynamics were performed in OpenSim [4] using a linearly scaled model coupled to a model of the cycle ergometer. Muscle-tendon parameters were calibrated to the individual using the calibrated EMG-informed neuromusculoskeletal modelling toolbox (CEINMS) [5]. Joint contact forces for hip, knee, and ankle were calculated in CEINMS using an EMG-assisted approach. Output joint contact forces were amplitude-normalised to bodyweight (BW), and reported as a function of crank angle, where 0° corresponded to bottom dead-centre. Peak and location of knee contact forces for 10 cycles per condition were analysed.

RESULTS

The peak total knee contact forces reached a mean \pm standard deviation of $86 \pm 5.9\%$, $103 \pm 5.6\%$, and $110 \pm 5.7\%$ of BW for the 40, 60, and 80 revolutions per minute conditions, respectively (Figure 1). Increase in speed did not change average peak total knee contact force location, which remained, on average at $270 \pm 3.6^\circ$.

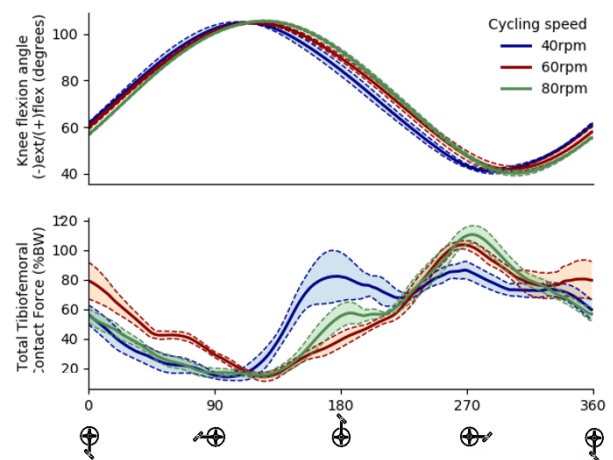


Figure 1. Knee flexion and total knee contact forces for cycling at consistent torque output (11.6 ± 0.6 Nm) for 40, 60, and 80 revolution per minute (rpm) cadences (mean \pm standard deviation).

CONCLUSIONS

Preliminary results show increased cycling speed resulted in increased peak total tibiofemoral contact forces. Generating lower limb joint contact and muscle forces for a cohort of healthy individuals is underway, which will act as normative data for interpreting the same metrics from SCI individuals. The joint contact and muscles forces may be also used as boundary conditions for bone finite element models to assess if bone stresses exceed strength limits. All these data will inform and improve protocols for FES rehabilitation for individuals with SCI.

REFERENCES

- [1] J. C. Franco et al., *Rehabil Res Dev*, 36, 207-16, 1999.
- [2] F. Biering-Sorensen et al., *Eur J Clin Invest*, 20, 330-5, 1990.
- [3] D. J. Saxby et al., *Gait Posture*, 49, 78-85, 2016.
- [4] S. L. Delp et al., *IEEE Trans Biomed Eng*, 54, 1940-50, 2007.
- [5] C. Pizzolato et al., *J Biomech*, 48, 3929-36, 2015.

Claire Crossley, claire.crossley@griffithuni.edu.au

PREDICTING THE 3D GROUND REACTION FORCE OF RUNNING USING LSTM BASED ON KINEMATIC PARAMETERS

F. Ferryanto; Alvin; Mahyuddin, Andi Isra

Mechanical Design Research Group, Faculty of Mechanical and Aerospace Engineering,
Institut Teknologi Bandung, Jawa Barat, Indonesia

INTRODUCTION

Measuring the Ground Reaction Forces (GRF) of running on a treadmill usually needs a force plate that had been instrumented into a treadmill. However, due to the high-priced of the instrumented treadmill, a virtual 3D force plate that was able to predict the 3D GRF based on the kinematics parameter alone was developed. Thus, the measurement could be conducted while maintaining the variability of speed to a bare minimum with relatively low-cost equipment. The prediction itself was doable by implementing the Long Short Term Memory (LSTM), a neural network that was specially created for time series data prediction. This virtual force plate will be integrated with a 3D markerless motion capture system to create a robust running motion analysis system in the future.

METHOD

The dataset used to train the model was provided by Fukuchi et al [1]. This dataset consists of 28 subjects' markers and forces data that were recorded while running in three variations of speed, 2.5 m/s, 3.5 m/s, and 4.5 m/s. These raw markers and forces data then were preprocessed to a time series 3D matrix that was suitable to train our model. The preprocessing included interpolating zero values, filtering noises using 4th order Butterworth filter, differentiation to obtain velocity and acceleration data, and lastly transforming and normalizing the shape of the matrix.

Before the dataset was fed to train the model, the input data was first scaled using a min-max scaler to ensure the sensitivity of the activation functions inside the LSTM model. Then five layers of LSTM were deployed and trained while we observed the performance through a historical plot. This was done to prevent an overfitting phenomenon. The hyperparameters used were also tuned by considering the result performance and the duration of training.

An 80-20 train-test split method was done so that we can evaluate the prediction using the data that was not fed to train the model. Then the mean RMSE and correlation coefficient were also calculated to quantify the performance of the prediction. In addition to that, a

mean significance statistical test was also conducted to give us an idea of whether the performance is equally good in predicting the GRF in all variations of speed.

RESULTS

The mean RMSE and correlation coefficient shown in **Table 1**, were obtained by comparing the predicted GRF was compared to the original dataset. These results were also good in all variations of running speed as only one statistical test failed. The statistical test used a 95% confidence level and the critical value, Z-critical, equals 1.96. The statistical test result was presented in Table 2 where failed testing, Z-value higher than Z-critical, was bold. This was because GRFz has small value thus it was dominated by noise.

Table 1. Mean RMSE and mean correlation coefficient

GRF	Mean RMSE (\pm S.D.) 10^{-2}	Correlation Coefficient
Anteroposterior	1.91 \pm 0.63	0.993
Vertical	4.45 \pm 2.60	0.999
Mediolateral	0.75 \pm 0.32	0.985

Table 2. Statistical testing result

Speed	Z-value		
	GRFx	GRFy	GRFz
2.5 to 3.5 m/s	0.69	0.85	1.40
3.5 to 4.5 m/s	0.15	0.44	1.42
2.5 to 4.5 m/s	0.89	1.19	4.16

CONCLUSIONS

The models generated had successfully predicted all 3D GRF in all variations of running speed with considerably small mean RMSE and high mean correlation coefficient. The prediction was also equally good in all variations of running speed except the 2.5 to 4.5 m/s in GRFz.

REFERENCES

Fukuchi, et al., "A public dataset of running biomechanics and the effects of running speed on lower extremity kinematics and kinetics," *PeerJ*, vol. 5, p. e3298, 2017.

Presented by F. Ferryanto (ferryanto@ftmd.itb.ac.id)

BEYOND MUSCLE ARCHITECTURE: PREDICTING ANKLE MECHANICS FROM 3D TRICEPS SURAE MUSCLE FASCICLE INFORMATION

¹Kazemi, M.; ²Mirjalili, A.; ³Agur, A.; ¹Fernandez, J.; ¹Besier, T.; ¹Handsfield, G.

¹Auckland Bioengineering Institute, The University of Auckland, Auckland, NZ

²Faculty of Medicine and Health Sciences, The University of Auckland, Auckland, NZ

³Department of Surgery, Faculty of Medicine, University of Toronto, Canada

INTRODUCTION

Does loading change the muscle architecture as infants transition to walking, or does a change in architecture precede the shift to walking? The answer to this may be probed with computational modelling of muscle architecture in a young paediatric population. Developing musculoskeletal models from standard medical images may not create reliable and high-fidelity results especially for very young populations. This occurs because children under 6 years old may not remain still during sequential image acquisitions. Cadaveric studies, on the other hand, provide detailed architectural descriptions, often for educational purposes, but generating finite element models from this data has not been reported yet. This research aims to turn a qualitative 3D digitized architectural description of Triceps Surae (TS) muscles into a finite element (FE) model and simulate the role of weight-bearing conditions on muscle architectural changes.

METHOD

Muscle fiber fascicles (FFs) and connective tissues were digitized in a 6-month-old female cadaver (UT, HSREB, #32679, and UoA, HPEC, #016164). Fascicles were outlined from their proximal to their distal attachment sites and digitized using a MicroScribe™ G2X Digitizer (0.05 mm accuracy; Immersion Corporation, San Jose, CA). The digitized fascicles of each muscle (Soleus, Lateral and Medial Gastrocnemius) were wrapped by 2D convex skin grids and then converted into volumetric tetrahedral meshes. Information from fiber fascicles was used to define the fiber orientation as inputs for a Transversely Isotropic Mooney Rivlin material property in a FE model. Figure (1) demonstrated the model features as set in FEBio (Salt Lake City, UT, USA). FE model parameters were tuned to reproduce passive range of motion of *in vivo* and cadaveric experiments [2,3]. Lagrange strain was computed from incremental applied load at the calcaneus bone to mimic antagonist loading.

RESULTS

Maximum strains were observed at the myotendinous junctions of the muscles (Figure 2) and non-uniformity

of stress and strain patterns were observed, suggesting that there are local inhomogeneities of mechanical strains and biological remodeling of these tissues.

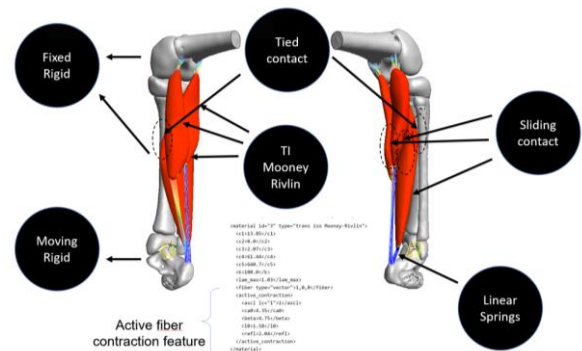


Fig 1. Finite element features as modelled in FEBio. Muscles and connective tissues were modelled as Transversely Isotropic Mooney Rivlin and linear springs, respectively.

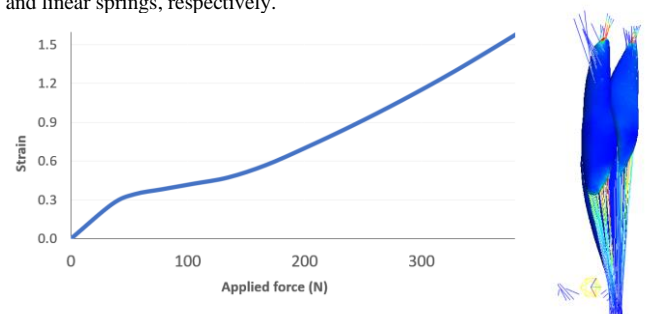


Fig 2. Effective Lagrange strain in the tendons caused by a range of loads applied to the calcaneus bone

CONCLUSIONS

We developed a robust computational modelling to estimate ankle joint mechanics using high-fidelity architectural data. Our model reproduced experimental data and estimated effective strain in muscle and soft tissue of TS muscles. Future work will continue to probe the question of how loading impacts muscle architectural development in infant humans [3].

REFERENCES

- [1] Orishimo, K.F. The J.foot and ankle surgery 47.1, 34-39, 2008.
- [2] Wong S., Australian J. of Physiotherapy 44(1),57-60, 1998.
- [3] Bradshaw, L.R., Eur. J. Anat 24.6,491-499, 2020.

Presented by Mousa Kazemi
(mkaz010@aucklanduni.ac.nz).



DAY 2

Posters

EXPLORING THE RELATIONSHIP BETWEEN SIZE AND SHAPE OF THE HUMAN TARSAL BONES

Treherne, P.; Welte, L.; Rainbow, M.; Kelly, L.

University of Queensland, Saint Lucia 4067, Australia; Queens University, Kingston K7L 3N6, Canada.

INTRODUCTION

The human foot retains substantial variability in shape and size despite being quite unique to our species¹. The square-cube law states that as a shape (bone) isometrically grows, its surface area grows at a slower rate (volume^{2/3}). Deviations either side of this function are termed allometric scaling. Across terrestrial species, some skeletal structures scale allometrically as animals get larger, to cope with the increased loading associated with increasing body weight. Despite the wide variation in the size and shape of humans and their feet, less is known about how our feet change shape with increasing size. This may have important consequences for how we contend with our bodyweight and the large muscle forces that are applied to the ground, via our feet. The calcaneus and talus are the largest bones in the foot, are subject to high loading forces and are distinctly different from the corresponding bones in non-human primates. We wondered if these two bones and their joint surfaces may scale via allometry, changing shape across the spectrum of bone size. Therefore, this study aimed to explore if bone and joint scaling and shape can be explained by size differences.

METHOD

3D bone models of the talus and calcaneus were generated from computed tomography scans of the right foot in 36 individuals (mass: 73.4 ± 13.9 kg; height: 171.2 ± 8.1 cm; 21M, 15F) using Mimics. Bone models were centred and aligned based on their inertial axes. An iterative closest point approach was applied to improve alignment, based on a selected reference bone. Initial mesh correspondence to the reference bone was obtained using a non-rigid coherent point drift (CPD) algorithm². Bones were scaled to centroid size using a Procrustes analysis. A final mesh correspondence was obtained using non-rigid CPD to align each bone to the mean bone calculated from the sample. This process was undertaken for the calcaneus, talus and the surface of the talus that articulates with the tibia (talar dome). To evaluate allometry, log-log plots were calculated for the volume and surface area of the talus and calcaneus, as well as the volume of the talus and surface area of the talar dome. A principal component (PC) analysis of shape of the calcaneus, talus, and talar dome was performed. The determine the relationship between

bone size and shape, the PC scores for each mode of variation were plotted against bone centroid size.

RESULTS

Preliminary analysis indicates a negative allometric relationship exists for the calcaneus (slope = 0.62, $p < 0.05$), with the surface area growing slower than volume. The talus appears to scale isometrically (slope = 0.67, $p < 0.05$), with the talar dome showing a positive allometric relationship, with the joint surface area growing faster than the entire bone volume (slope = 0.69, $p < 0.05$). The first PC of calcaneus shape variation (20.2% of variation, $p < 0.05$) has a relationship with bone size, with the tuberosity getting larger and the bone appearing to grow taller (relative to length), as the bone gets larger (Figure 1 top, +3SD). No PCs for the talus showed any relationship with size. For the talar dome, PC5 (5.4% of variation, $p < 0.05$) changed with increasing bone size, with the medial malleolar facet becoming more rotated (Figure 1 bottom, +3SD).

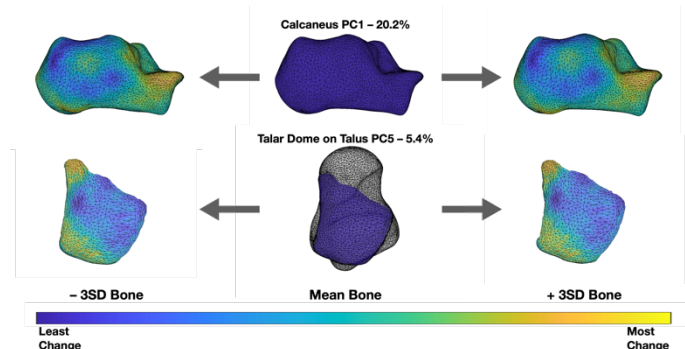


Figure 1. Anatomical shape changes at $\pm 3SD$ from mean shape (centre) of calcaneus PC1 and talar dome PC5 modes of variation. Heatmap shows where on the bone the most change is occurring.

CONCLUSIONS

We have shown the presence of distinct patterns of shape and scaling variance in the two largest bones of the feet. Interestingly, these patterns of variation are different between the two bones, with the calcaneus scaling allometrically and the talus scaling isometrically. Further analysis is required to determine if these scaling and shape variances are related to function.

REFERENCES

1. McNutt, E. J. *Evol. Anthropol.* 27, 197-217, 2018.
2. Myronenko, A. *IEEE. TPAMI.* 32, 2262-2275, 2010.

Presented by Paige Treherne (p.treherne@uq.edu.au).

THE INFLUENCE OF SPINE CAGE POSITION ON THE MECHANICAL RESPONSE OF SUPERIOR LUMBAR ENDPLATE: A FINITE ELEMENT MODELLING STUDY

Yu, Y¹.; Robinson, D. L¹.; Ackland, D. C¹.; Yang, Y¹.; Bert, E².; Lee, P. V. S¹.

¹The University of Melbourne, Parkville VIC 3010, Australia.

²3DMediTech, Port Melbourne VIC 3207, Australia.

INTRODUCTION

Lumbar interbody fusion (LIF) with interbody cages is an established treatment for lumbar degenerative disc disease. However, the use of interbody cages can lead to well established complications such as cage migration and subsidence. Previous studies around surgical outcomes of LIF have shown that interbody cage positioning can affect rates of post-operative complications (Abbushi et al., 2009). The aim of this study is to assess the influence of cage positioning on the mechanical response of superior lumbar endplate using a spine finite element (FE) model.

METHOD

A FE model of the L5 vertebra was established based on computed tomographic (CT) scans of a healthy male subject (18 years old). The 3D geometry of the vertebra was reconstructed in Mimics 21.0 software, and the 3D model was meshed with tetrahedral elements (HyperMesh 2017). The meshed model was imported into a FE modelling software package (Abaqus CAE 2017) and the material properties of the vertebra were assigned based on the Hounsfield units (HU) of the CT scans (Morgan et al., 2003). The interbody cage in the model was based on a kidney-shaped Polyether-ether-ketone (PEEK) cage. The cage was meshed in tetrahedral elements and assigned material properties of PEEK. The cage was placed in four different positions on the superior endplate of L5 (Figure 1a). Surface-to-surface contact was assigned to the interface between the cage and endplate (Calvo-Echenique et al., 2019). A 1000N axial compression load was applied on top of the cage while the lower surface of L5 was clamped.

RESULTS

The resultant stresses and strains of the endplate were computed (Table 1) along with the stress contour on the endplate for middle position (Figure 1b). Lower minimum (Min) principal strains (7.9%-27.27%) and higher von Mises stresses (21.40%-26.39%, except posterior position) were observed for models with the cage located on the peripheral region of the endplate compared to the medial region.

Table 1. Main mechanical responses of the endplate with different cage positions.

Cage position	Peak value	
	Von Mises stress (MPa)	Min principal strain ($\mu\epsilon$)
Anterior	72.17	46500
Middle	57.10	50600
Posterior	47.79	46600
Lateral	69.32	36800

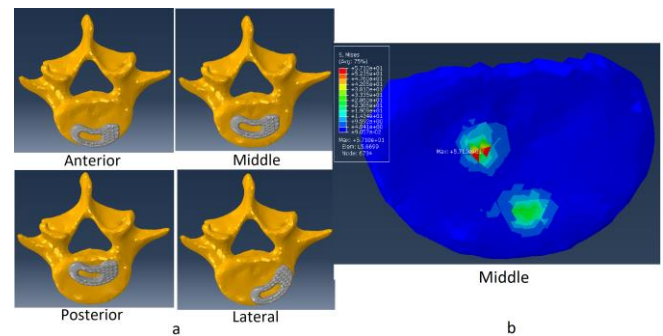


Figure 1. (a) Four cage positions on L5 superior endplate, (b) Stress contour on the endplate for middle position.

CONCLUSIONS

Models with cage located on peripheral positions had lower Min principal strain on the endplate which relates to lower compressive deflection. This was consistent with previous surgical outcomes that cages located on the medial region of the endplate had higher migration and subsidence rates. To reduce post-operative complication rates, Min principal strain on the endplate can be used as a guide during cage design. Experimental validation of the model will be examined in the future.

REFERENCES

- Abbushi, A. Eur. Spine J. 18(11), 1621, 2009.
- Calvo-Echenique, A. Biomed. Eng. Online. 18(1), 1-17, 2019.
- Morgan, E.F. J. Biomech. 36(7), 897-904, 2003.

Presented by Yihang Yu
(yihangy@student.unimelb.edu.au).

TITANIUM PRESS-FIT TRAY IMPLANTED IN HUMAN TIBIA: A ZERO-STRAIN MICRO-CT AND DIGITAL VOLUME CORRELATION ANALYSIS

Wearne, L.S.¹; Rapagna, S.¹; Taylor, M.¹; Perilli, E.¹.

¹ Medical Device Research Institute, Flinders University, Adelaide, Australia.

INTRODUCTION

Primary stability of press-fit tibial trays is achieved by introducing an interference fit between bone and implant. The internal strains generated during such a process are currently unknown. Large-gantry micro-CT (μ CT) systems combined with digital volume correlation (DVC) offer the potential to quantify such strains. This pilot study aims to assess the DVC zero-strain errors of four plausible μ CT scanning configurations for a human tibia implanted with a titanium press-fit tray.

METHOD

μ CT Imaging: One cadaveric human tibia was resected, implanted with a titanium tibial tray (Depuy Synthesis) and μ CT scanned at four plausible configurations (Nikon XT H225 ST, $42\mu\text{m}/\text{voxel}$ size: Tab.1). Configurations varied in rotation step and hence resulting scanning time (106min vs 66min), presence or not of a 2mm-thick aluminum cylinder (Al Tb) required for mechanical loading while scanning¹, and X-ray tube voltage (150kVp and 215kVp). Repeated scans were taken at each configuration, with specimen repositioning inbetween. The resulting μ CT datasets were rigidly 3D co-registered (DataViewer).

Masking of μ CT Images: Regions external to the tibial cortex were masked (CT Analyser). A custom MATLAB script was written to mask soft tissue or marrow not consistently present in the paired μ CT datasets. From each dataset, nine cubic volumes of interest (VOIs) were selected (13.4mm side length): five containing only trabecular bone (A-E, Fig.1:I) and four centered on implant pegs (7mm \varnothing) containing also the surrounding bone (F-I, Fig. 1:I).

DVC Analysis: DVC analysis (DaVis 8.3.1, LaVision) was performed on each VOI. Direct correlation with a 3-step multipass sequence (final subvolume: 28 voxels side) was applied. The strain mean error (MAER) and standard deviation of error (SDER) were calculated as indicators of accuracy and precision, respectively².

Statistical Analysis: After assessing data for normality (Shapiro-Wilk) and performing a repeated measures ANOVA, Bonferroni-adjusted paired t-tests for MAER and SDER in the 9 VOIs between the first scan in air and subsequent configurations were performed.

RESULTS

Across the four scanning configurations, MAER ranged between $223\text{--}540\mu\epsilon$ and SDER between $88\text{--}261\mu\epsilon$ (Fig. 1:II). In air, a shorter scan time did not increase errors. The Al Tb induced small, statistically significantly increased errors than scans in air, at both voltages.

Table 1. μ CT Scanning Configurations

1. Air, 150kVp, 34W, 0.11° rst, 106m scan time
2. Air, 150kVp, 34W, 0.18° rst, 66m scan time
3. Al Tb, 150kVp, 42W, 0.18° rst, 66m scan time
4. Al Tb, 215kVp, 42W, 0.18° rst, 66m scan time

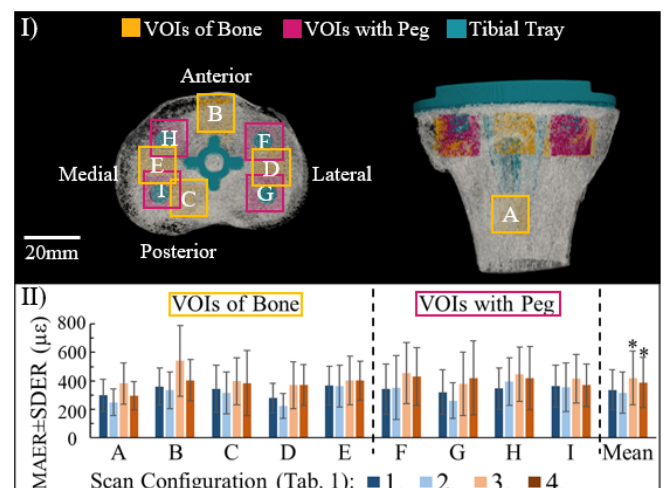


Figure 1. I) 3D μ CT rendering of tibia with titanium implant, showing 9 VOIs. II) DVC error analysis of VOIs and mean, * $p < 0.05$ to scan configuration 1.

CONCLUSION

Strain errors across the four scanning configurations were sufficiently low for assessing bone within its elastic region ($<10\%$ yield strength, $7000\mu\epsilon$)³. A shorter scanning time with specimen placed within the aluminium testing rig, is deemed suitable to assess the internal strain field of a human cadaveric tibia implanted with a titanium tibial tray. This study will continue, performing time-lapsed mechanical loading.

REFERENCES

1. Martelli, S. J Mech Behav Biomed, 84:265-272, 2018.
2. Tozzi, G. J Mech Behav Biomed, 67:117-126, 2017.
3. Liu, L. J Biomech, 40:3516-3520, 2007

Presented by Lauren Wearne
(lauren.wearne@flinders.edu.au).

BIOMECHANICAL ANALYSIS OF NOVEL WRIST IMPLANT

Quinn A, Pizzolato C, Bindra R, Lloyd DG, Saxby DJ.

Griffith Center of Biomedical and Rehabilitation Engineering, Griffith University, Australia

INTRODUCTION

There is currently no commercially available clinically successful treatment for scapholunate interosseous ligament rupture, the consequence of which is development of hand-wrist osteoarthritis. We have created a novel biodegradable implant which fixed the dissociated scaphoid and lunate bones and encourages regeneration of the ruptured native ligament. Here, we aimed to determine if scaphoid and lunate kinematics in cadaveric specimens were maintained, relative to the intact native case, when the implant was installed and specimens robotically manipulated.

METHOD

Ten cadaveric experiments were performed with identical conditions except for implant geometry which varied due to anatomical differences between cadaveric specimens. Each arm was mounted upright in a six degrees of freedom robot using k-wires drilled through the radius, ulna, and metacarpals (Figure 1). Ulna and radius were fixed such the hand was in neutral pronation-supination. Two weights (each 0.5 kg) compressed the radio-carpal joint. Infrared markers were attached to scaphoid, lunate, radius, and 3rd metacarpal. Cadaveric specimens were robotically manipulated through flexion-extension and ulnar-radial deviation by $\pm 40^\circ$ and $\pm 30^\circ$, respectively.

Scaphoid and lunate kinematics were examined under configurations: 1) intact native ligament, 2) severed ligament, 3) and installed implant. Each configuration had two repeated recordings for each motion direction using motion profile consisting of three sinusoidal cycles performed over 100 seconds.

Using biomechanics software (OpenSim 4.2), motion data were filtered and aligned to digital models of each specimen along with implant orientation and location [1]. Digital wrist models were generated from computed tomography scans and aligned to motion capture data using anatomical landmarks. Inverse kinematics of each trial was used to estimate bone motion and implant installation location. Implant insertion points in both scaphoid and lunate were tracked dynamically throughout robotically applied motion. Root mean squared distance (RMSD) was compared among severed, and implant conditions, relative to intact.

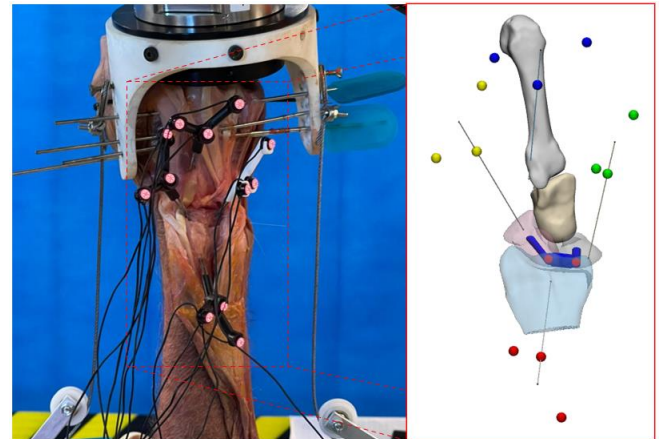


Figure 1. Left: cadaver experiment. Right: digital model with markers, implant, and implant insertions.

RESULTS

Preliminary data (five cadaveric specimens) indicate implant reduced distance between scaphoid and lunate compared to severed configuration for all but three trials (Figure 2).

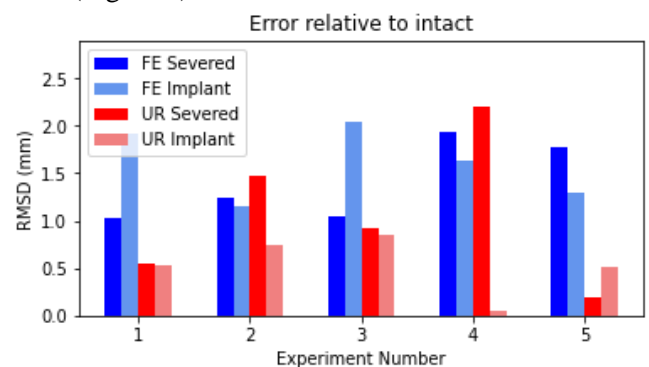


Figure 2. RMSD between implant insertion points relative to intact. FE: Flexion-extension. UR: ulnar-radial deviation.

CONCLUSIONS

Preliminary results indicate our novel implant reduced scapho-lunate gap caused by ligament transection. Future analysis will reveal if the implant can achieve wrist kinematics similar to the native intact wrist.

REFERENCES

[1] S. Delp, Biomed Eng, IEEE Trans 54. 1940-1950, 2007.

Presented by Alastair Quinn (alastair.quinn@griffith.edu.au)

FRONTAL CRASH PERFORMANCE OF LARGE HARNESSSED CHILD RESTRAINTS FOR OLDER CHILDREN

Kent, N.; Whyte, T.; Mills, E.; Bilston, L.
Neuroscience Research Australia, Randwick, NSW, Australia;
The University of New South Wales, Kensington, NSW, Australia.

INTRODUCTION

Optimal restraint of child passengers in cars requires specialized child restraint systems due to in-vehicle restraints (seat belts, airbags etc.) being designed for adult occupants. For older children, booster seats aim to align the seat belt with the anatomy of the child, better positioning the restraint across the shoulder and bony pelvis. Australian regulations require children aged 4 to 7 years use an approved forward facing harnesssed child restraint system or a booster seat and the majority in this age range use booster seats (Royal Children's Hospital, 2019). However, previous research has suggested booster seats may place child occupants at increased risk of abdominal injury compared to in-built harnesssed systems (EEVC, 2008).

Forward-facing harnesssed child restraint systems are highly effective at protecting children in crashes, with the majority of studies showing this benefit for younger children that are too large for rearward facing restraints. In an attempt to extend the benefits of harnesssed restraints to older children, a new type of child restraint system (Type G) was introduced in the 2013 version of the Australian/New Zealand standard (AS/NZS 1754:2013). Type G restraints are harnesssed systems designed to accommodate children aged up to 8 years.

The crash performance of Type G restraints has not been extensively studied. A single crash test has suggested Type G restraints may be less safe than booster seats due to a larger observed head excursion (Suratno, 2018). Since the leading cause of serious injury to children in crashes is head, neck and face injury due to contact with the vehicle interior, limiting forward head excursion is critical. The aim of this study was to compare the forward head excursion of Type G restraints to common booster seats.

METHOD

A collection of four Type G restraints and six Type E booster seats were tested in simulated frontal crash tests at 49 km/h on a deceleration sled. The restraint or booster seat was placed on the test bench, equipped with an emergency locking retractor three-point seat

belt, according to manufacturer instructions. A Q6 anthropometric test device (ATD), representative of a six-year-old child, was secured within the restraint system. Each test was visually recorded using two high speed cameras, viewing the crash from the side and above. The peak forward head excursion of the ATD from the seat bight of the test bench was calculated using ProAnalyst motion tracking software.

RESULTS

The peak forward head excursion of the restraints is pictured in Figure 1. The Type G restraints all showed larger average peak head excursions than all the Type E booster seats.

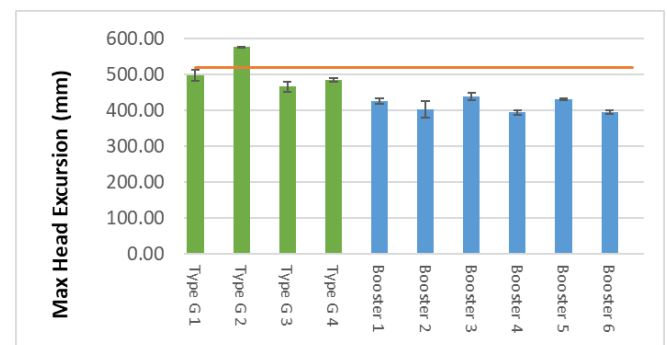


Figure 1. Peak head excursion of the Type G restraints (green bars) and Type E booster seats (blue bars).

CONCLUSIONS

Current commercial Type G restraint designs exhibit larger peak forward head excursions than booster seats, potentially increasing the risk of injury to a restrained child in a frontal crash. The benefits of in-built harnesssed restraints are negated for older children due to the large size of these restraints unless changes to current designs can be made.

REFERENCES

- The Royal Children's Hospital National Child Health Poll, Poll Number 14, 2019
- EEVC, Q10 Dummy Report, 2008.
- Suratno, B. Australasian Road Safety Conference, 2018.
- Presented by Nick Kent (n.kent@neura.edu.au)

NECK INJURY RISK FROM HEAD-FIRST DIVES INTO TRAMPOLINE DISMOUNT FOAM PITS

Whyte T.^{1,2,3}, Richards A.⁴, Lind E.⁴, Eager D.⁵, Brown J.^{1,2,3}, Bilston L.^{1,2,3}

1. Neuroscience Research Australia, Randwick, Australia. 2. University of NSW, Kensington, Australia. 3. The George Institute for Global Health, Newtown, Australia. 4. Mr Trampoline Pty Ltd, Carnegie, VIC, Australia. 5. University of Technology Sydney, Ultimo, Australia

INTRODUCTION

Trampoline parks first emerged in Australia in 2011 and increased to over 1000 globally by 2017. Trampoline parks typically consist of connected trampolines, angled trampolines, vertical wall surfaces and dismount devices such as foam pits and airbags.

Despite the aim of cushioning a fall, injuries occur during falls into foam pits, including serious cervical bilateral facet dislocations with spinal cord injuries reported in the literature and media reports (Lee, 2019). The primary mechanism of this type of injury is compression and compressive buckling of the spine (Nightingale, 2019). In a head-first impact this occurs when the neck fails to manage the energy of the following torso. The behavior of the spine in a head-first impact into loose foam pieces such as in a foam pit has not been studied.

Notwithstanding this lack of knowledge, specifications for different designs of foam pits and fail safety systems can be found in standards and guidelines used by trampoline park operators. The ability of foam pits designed to these specifications in mitigating neck injury risk remains unknown. The aim of this study was to quantify neck forces in head-first entries into a range of foam pit designs to examine the potential neck injury risk.

METHOD

Neck forces in head-first falls into foam pits were measured using a Hybrid III 50th percentile male anthropometric test device (ATD), dropped head-first into different foam pit designs. A 6-axis upper neck load cell recorded neck forces sampled at 20 kHz.

The foam pit design specifications were varied using a custom foam pit enclosure measuring 2.6 m long, 2.6 m wide and 1.9 m high from the base, constructed from steel supports with Perspex side panels. The pit was filled with foam cubes sourced from a local trampoline park foam pit having an average size of 0.2 m cubed and density of 23.7 kg/m³. Three design conditions were tested, which are specified by two commonly used foam pit guidelines or standards

(ASTM F2970-20, ATPA Code of Practice), as follows:

- Pit A: 0.4 m thick foam slab at the base, 1.4 m deep foam cubes, total depth 1.8 m.
- Pit B1: 0.2 m thick foam slab at the base, trampoline bed mounted 0.6 m from base, 0.9 m deep foam cubes above trampoline bed, total depth 1.5 m.
- Pit B2: 0.2 m thick foam slab at the base, netting bed mounted 0.6 m from base, 0.9 m deep foam cubes above netting bed, total depth 1.5 m.

ATD drop height was progressively increased, aiming to achieve drops from 1.5 m above the level of the foam cubes. Measured neck loads were compared to published injury assessment reference values for neck compression force (F_z), Neck Injury Criterion (N_{ij}) and a time dependent criterion for a tolerable duration of compressive force above prescribed load levels.

RESULTS

A summary of results showing injury assessment reference values for each pit condition is provided in Table 1.

Table 1 Average neck loads in each foam pit test condition (values in bold exceed published injury assessment reference values)

Pit Type	ATD drop height (m)	F_z (kN)	N_{ij}	Duration $F_z < -1.1$ kN (ms)
A	1.15	-1.79	0.44	94.6
B1	1.5	-1.41	0.68	43.4
B2	1.5	-1.36	0.42	39.7

CONCLUSIONS

At least one injury assessment reference value was exceeded in drops into all pit types. The risk of cervical spine injury may not be sufficiently reduced by the current guidelines and standards globally.

REFERENCES

Lee, J.E. Medicine 98, 48, 2019.
Nightingale, R. Clin. Biomech. 64, 90-97, 2019.

Presented by Tom Whyte (t.whyte@neura.edu.au).

ESTIMATING CARTILAGE CONTACT MECHANICS AND 3D JOINT SPACE FROM RADIOGRAPHS INFORMED BY STATISTICAL SHAPE MODELS

Kazemi, M.; Zhang, J.; Monk, P.; Besier, T.

Auckland Bioengineering Institute, The University of Auckland, Auckland, New Zealand.

INTRODUCTION

Clinicians currently rely on weight bearing anterior-posterior (AP) radiographs to assess joint narrowing caused by cartilage degeneration. Measurement of cartilage morphology requires MR imaging, which is useful, but not weight-bearing. Coupled bone and cartilage morphology can be accurately represented using statistical shape models derived from a population and can be used to predict anatomical variation from sparse data [1]. We present a 3D measurement of joint space narrowing using two weight-bearing radiographs and a shape model that captures variation in bone and cartilage morphology.

METHOD

A case study was performed on a 48-year-old male football player, who presented with mild medial knee pain. The participant consented to take part in this study, which was approved by the Auckland Hospitals Research and Ethics Committee (AHREC 000086). Two standing leg x-rays were taken (AP and lateral) and silhouettes of the femur, tibia and fibula bones were automatically segmented using OpenCV Gaussian and K-mean masks and Canny edge detection filters [1]. An MRI of the knee was acquired to assess cartilage damage and was manually segmented to define the cartilage morphology. A statistical shape model of the femur and tibia was used to reconstruct bone morphology, using the participant's height, mass, and silhouettes obtained from x-ray images. Cartilage was then locally fit to the articulating surface segmentations from MRI. The 3D bone models were registered to the 2D x-ray silhouettes using a custom python script. Cartilage contact was defined as regions of overclosure between femoral and tibial cartilage surfaces. A normal vector on the tibia sub-cartilage mesh was used to find a corresponding tibia and femur mesh point and calculate a joint space distance. By performing these projections across the tibial cartilage bone, we defined the 3D joint space.

RESULTS

The bone-cartilage geometries from our model were predicted within ~1 mm root mean square error of the MRI segmentation. Cartilage contact area on the medial and lateral compartments were 550 and 357

mm², respectively. The minimum joint space occurred on the medial compartment.

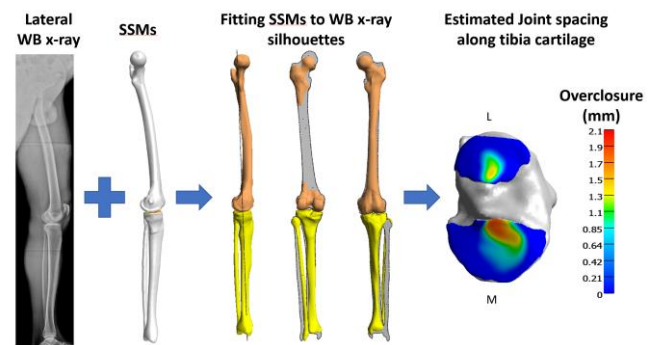


Figure 1. Steps in workflow to estimate contact overclosure and 3D joint space from weight-bearing radiographs.

CONCLUSIONS

We developed a method to combine weight-bearing x-ray with supine MRI to estimate cartilage contact and 3D joint space. Improvements in our shape model can potentially predict cartilage morphology from x-ray, thus reducing the need to obtain costly MR images. The 3D joint space measurement extends previous work [2], which estimates a 2D estimate of joint space and has application for diagnosing and monitoring patients with knee osteoarthritis. Scaled cartilage contact areas were close to experiment [3]. The shape models used in this research were generated from a sample of only 21 knees, so further work is ongoing to increase this sample size, which will improve registration and fitting errors. This workflow has useful application, not just for monitoring 3D joint space, but developing accurate musculoskeletal and FE models for pre-operative planning and gait analysis.

REFERENCES

- [1] Kazemi, M., PhD thesis, the University of Auckland, NZ, 2018.
- [2] Swiecicki, A. Computer-Aided Diagnosis. Vol. 11314. International Society for Optics and Photonics, 2020.
- [3] Shin, C.S. J. of MRI, 34.6: 1405-1413, 2011.

Presented by

Mousa Kazemi (mkaz010@aucklanduni.ac.nz).

EFFECTS OF IMPLANT-BONE CONTOURING AND SCREW CONFIGURATIONS ON STRESS DISTRIBUTION IN TEMPOROMANDIBULAR IMPLANT

Tse, K.M. & Mao, C.
Swinburne University of Technology, Melbourne, Australia

INTRODUCTION

Approximately 25% of the population is experiencing certain forms of temporomandibular joint (TMJ) issues [1]. These problems are resulted from the displacement of the articular disk from the condyle head and limit the range of motion to perform activities as well as inflict pain. The prosthetics for TMJ have been proven to play a vital role in alleviating the discomfort that patients suffer from temporomandibular disorders (TMD) as depicted in various studies. There are many research and studies that have been conducted, however, to best of our knowledge, there is no study comparing between flat and anatomic designs of the Biomet stock prosthetic regarding screw configurations. This study aims to investigate the effects of the implant and screw head design towards the stress distribution in the screws, and condylar using finite element analysis (FEA).

METHOD

Two implant designs – (i) a commercial Zimmer Biomet implant and (ii) anatomic fitted implant, were developed in SolidWorks, implemented with a 3D subject-specific skull model and analysed using a finite element package – Abaqus. These two types of implant designs were with a flat, standard condylar component and paired with button screws (SBS) as well as countersunk screws (SCS). With the aim of differing in the geometry, a second design was modelled that followed the anatomical curvature (raised middle part of the condylar body) of the mandible together with countersunk screws (ASCS). For each implant design, we have 8 types of screw configurations (Fig.1).

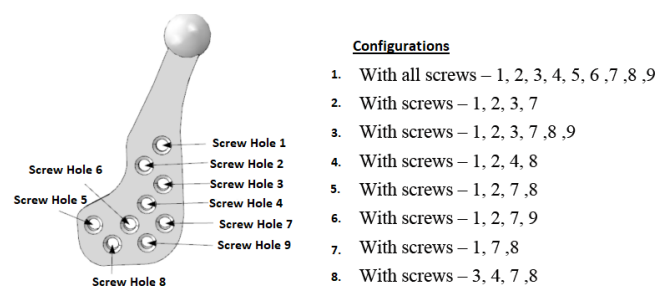


Figure 1: Various TMJ implant screw configurations.

RESULTS

It is shown in Figure 2 that ASCS had the optimal maximum load (123.5 MPa) on screws, followed by SBS (143.1 MPa) and lastly (154.5 MPa). Conversely, SBS has the highest average screw stress of 106.4 MPa, followed by ASCS (84.2 MPa) and SCS (70.23 MPa). However, SCS had the highest standard deviation of 53.73 while SBS and ASCS achieved similar results (33.17 and 33.03, respectively). Overall, the ASCS delivered more desirable outcomes on all three shown categories.

Regarding screw configurations, the configuration with screws 3, 4, 7, 8 provided the lowest amount of stress on all screws. Hence, we looked at how stress was distributed on screw 3, 4, 7, 8 throughout all three implant modifications (SBS, SCS, ASCS). Both SBS and ASCS had quite equal stress distribution amongst given screws. On the other hand, SCS showed a significant gap of that between screws. The maximum screw stress in ASCS was the lowest out of three implant configurations. Lastly, SCS held the highest standard deviation while others resulted similarly.

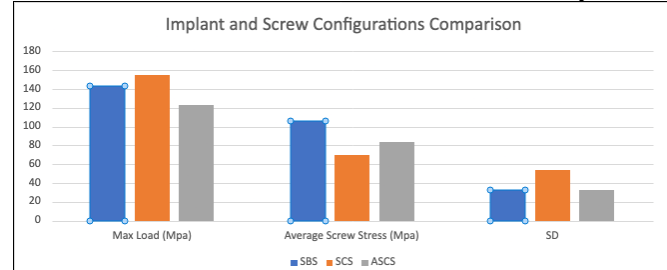


Figure 2: Implant and screw configuration comparison between SBS, SCS, and ASCS.

CONCLUSIONS

This study demonstrates that the better design of the implant resembling the anatomic curvature of the mandible, the more sufficient stress distributed amongst screws. In most cases, screws that are closer to the TMJ bear the most stresses and strains, whilst those in middle of the condylar component exhibit very low stress, especially when using all screws.

REFERENCES

[1] Barkin, S. and Weinberg, S. J Canadian Dental Assoc 66, 2000.

Presented by K.M. Tse (ktse@swin.edu.au).

THE EFFECT OF SPEED ON GAIT STABILITY DURING LOAD CARRIAGE

Cofré Lizama, L.E.^a; Middleton, K.^a; Slattery P.^a; Wheat, J.^b

^a School of Allied Health, Human Services and Sport, La Trobe University, Melbourne, Australia; ^b College of Health, Wellbeing and Life Sciences, Sheffield Hallam University, Sheffield, United Kingdom.

INTRODUCTION

Load carriage is required during many occupational tasks, which may lead to an increased risk of injuries and reduced performance during walking [1]. Speed strongly affects many walking variables, so it is likely to influence walking during load carriage. Since one of the main aims during walking is to maintain stability, increasing speed during load carriage may lead to a more unstable gait, potentially increasing the risk of injuries.

The aim of this study was to determine the effects of speed during load carriage on gait stability measures at the sacrum and trunk. We hypothesised that instability measured at both locations would be greater at faster walking speeds.

METHOD

Fourteen Australian Army recruits with no history of recent musculoskeletal injuries were recruited (4f/11m, height 178 ± 9 cm, mass 83 ± 15 kg, age 25 ± 6 years). Participants walked on a treadmill at a self-selected speed (SS; 5.0 ± 0.2 km/h), 3.5 km/h, 5.5 km/h and 6.5 km/h for 12 minutes while carrying a 23 kg weighted vest. A 10-minute rest was given in between trials.

Stability was assessed with the short-term local divergence exponent (Lyapunov λ ; LDE) using 3D accelerations recorded with a 4-APDM (Portland, USA) IMU system (128 Hz) placed at the feet, sacrum and sternum (manubrium). Feet sensors were used to determine heel contacts and extract data for 200 consecutive strides.

To calculate the LDE (LDE_{sacrum} and LDE_{trunk}), data were first normalised to 100 data points x 200 strides. The 9D state space was constructed using 3 x 3D delayed copies (10 samples delay) using Rosenstein's algorithm [2] and divergence rate was calculated in the 0-0.5 stride interval. In brief, the LDE measures the ability of a person to deal with small perturbations, where higher LDE values indicate lower stability. All calculations were performed in Matlab 2020b (Natick, USA). IBM-SPSS 27 was used to conduct a RMANOVA (4 speeds x 2 locations).

RESULTS

A significant effect of speed, location and their interaction ($p < .01$) was found. Pairwise comparisons showed LDE_{trunk} was significantly higher than LDE_{sacrum} , but only at 3.5 km/h. LDE_{trunk} at 3.5 km/h was significantly higher than the three faster conditions (Figure 1).

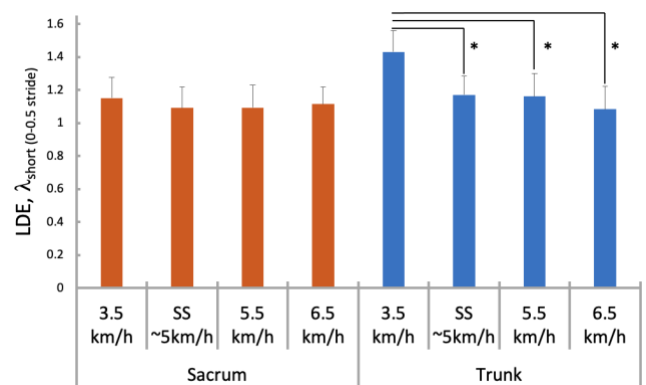


Figure 1. Mean \pm SD LDE values (0-0.5 stride) at each speed for the sacrum and trunk sensor. *Denotes significant differences ($\alpha = .05$).

CONCLUSIONS

Contrary to our hypothesis, speed did not affect stability measured at the sacrum. Furthermore, decreased speed increased LDE (less stable) at the trunk. These results indicate that when dealing with potentially more perturbing conditions (i.e. slow walking speeds; 3.5 km/h), individuals may be more stability-challenged than walking at speeds closer to, or above, self-selected speed when carrying a load.

In conclusion, stability at the trunk decreased when walking at 3.5 km/h compared with faster speeds. However, stability at the sacrum was not affected by speed.

REFERENCES

- [1] Drain, J. et al. Dsto-Tr-2765, 1–69, 2012.
- [2] Bruijn, S.M. et al J. R. Soc. Interface 10:20120999, 2013.

Presented by L. Eduardo Cofré Lizama (e.cofrelizama@latrobe.edu.au).

DETERMINANTS OF THROWING SPEED IN ELITE MALTE CRICKETERS

Djanis, P; Dempsey, A.R
Murdoch University, Murdoch, WA, Australia

INTRODUCTION

Despite the importance to performance, there is limited research on the determinates of throwing speed in cricket. While studies have investigated biomechanical¹ and strength² contributors to throwing speed in cricket, there is yet to be a study that has combined both. Therefore the aim of this study was to investigate how both strength and biomechanical factors influence throwing speed

METHOD

The sample included 14 elite males (12 right hand dominant/2 left hand dominant) who were either a contracted player by Cricket Australia, a contracted player for the Western Australia Cricket Association, or a part of the senior development academy at the Western Australia Cricket Association (age, 22.6 ± 3.0 years; height, 188.7 ± 8.2 cm; weight, 85.21 ± 8.82 kg).

Participant strength was assessed via the following assessments: one repetition maximum bench press, isometric mid-thigh pull, isometric shoulder internal rotation strength, lateral to medial jump, medicine ball rotation throw and overhead scoop toss. All strength variables had previously been associated with increased overhead throwing velocity.

Participants were required to undertake two throws – maximal velocity throw targeting the stumps and a throw for maximal distance. Participants were required to undertake six throws for each condition. During the throwing task, full three dimensional biomechanics were recorded using a 12 Camera Qualisys Motion Capture system capturing at 200Hz with ground reaction force captured from two Kistler 9287C force plates capturing at 2000Hz. Participants wore a custom marker set.

Following trajectory filtering at 15Hz, joint angles were calculated using Visual3D using standard joint coordinate systems with dynamic functional methods utilized to calculate knee and elbow flexion extension axis and hip joint centres. Data was analysed from back foot contact through to 500 ms post ball release.

Correlations and multiple forward linear regression were undertaken to identify strength and biomechanical factors that were related to ball release

speed in both the targeted throw, and throw for maximal distance. All statistics were undertaken in SPSS.

RESULTS

In the maximal distance throw, throwing speed was associated with trunk flexion at ball release ($r = 0.23$ and $p = .035$), lateral trunk flexion ($r = -.25$ and $p = .023$), one repetition max bench press, $r = .73$ and $p = <.001$), overhead scoop toss ($r = .34$ and $p = .006$), medicine ball rotation throw ($r = .52$ and $p = <.001$) and shoulder internal rotation strength ($r = .55$ and $p = <.001$). When combined in a multiple regression, 1-repetition maximum bench press, shoulder internal rotation angular velocity relative to ball release, Isometric mid-thigh pull, maximal shoulder external rotation, lateral to medial jump, and shoulder internal rotation strength, explained 72% of the variance.

For the targeted throw, propulsive ground reaction force ($r = .31$ and $p = .011$), lateral trunk flexion ($r = -.54$ and $p = .001$), trunk flexion at ball release ($r = .26$ and $p = .018$) 1-repetition maximum bench press ($r = .55$ and $p = <.001$), overhead scoop toss ($r = .3$ and $p = .018$), medicine ball rotation throw ($r = .59$ and $p = <.001$) and shoulder internal rotation strength ($r = .4$ and $p = .001$) correlated to maximal velocity. In the linear regression, stride length, braking ground reaction force, trunk flexion at ball release and 1-repetition maximum bench press, explained 68% of the variance.

CONCLUSIONS

Different variables were associated with increased velocity for the two different throws, however bench press and trunk position were consistent. This study's findings and previous research in cricket and other sports may be task-dependent thus making it difficult to draw comparisons and provide guidance across or within other sports.

REFERENCES

- Cook DP., J. J Sports Sci.18(12):965-73, 2000.
Freeston JL. J Strength Cond Res. 30(6):1646-51,2016.

Presented by Alasdair Dempsey
(alasdair.dempsey@murdoch.edu.au).

SPRINT ACCELERATION FORCE-VELOCITY PROFILES IN TRACK AND FIELD ATHLETES WITH AND WITHOUT HAMSTRING INJURY

Wolski, L.¹; Halaki, M.¹; Hiller, C.¹; Pappas, E.²; Fong Yan, A.¹.

¹The University of Sydney, Sydney, Australia

²University of Wollongong, Wollongong, Australia.

INTRODUCTION

Hamstring strain injury (HSI) poses a significant problem for sports involving high speed running, particularly those involving rapid acceleration. Age and previous HSI are the most evidence-based risk factors for HSI, but various modifiable risk factors have also been identified (1).

The hamstrings' role in high-speed running is well researched (2), however the relationship between running kinetics and HSI is less understood. Sprint force-velocity profiling (FVP) is a novel method of characterising kinetics of acceleration (3), which has been utilised in only one published study to date investigating HSI. This case control study reported horizontal force deficits in soccer players with a history of HSI when compared to controls (4).

The current research project aimed to retrospectively and prospectively analyse the relationship between FVP of track and field athletes, and HSI.

METHOD

Athletes aged 17-50, who participate in a sport involving sprinting and do not have a current medical condition or injury that affects their ability to sprint pain-free, were invited to participate in the study. Twenty-three track and field athletes (10 female, 13 male) were tested at baseline. Thirteen had a history of HSI (Mean age 31±11.9years; height 1.73±0.1m; weight 70±12.7kg), 10 did not (Mean age 19±2.7years; height 1.78±0.1m; weight 74±5.9kg). Following a warm up, testing consisted of one 30 m maximum sprint from a 3-point start. FVP was determined via a computation method utilising vertical markers and video analysis on the 'MySprint' iPhone application for split times. Participants subsequently were followed for a one-year injury surveillance period, involving weekly SMS reporting. Analysis of covariance (ANCOVA) assessed group differences at baseline, while controlling for age and sex.

RESULTS

Baseline cross-sectional analysis revealed no significant differences in FVP between participants with and without history of HSI. Age and sex

covariates, however, influenced the FVP data as indicated in Table 1.

	<i>History of HSI</i> Mean (SD)	<i>Controls</i> Mean (SD)	<i>P value</i>
Vmax (m/s)	7.48 (0.81)	8.01 (0.59)	0.660 [^]
F0 (N/kg)	8.98 (1.28)	8.90 (0.48)	0.489 [^]
V0 (m/s)	7.77 (0.93)	8.45 (0.70)	0.663 [^]
Pmax (W/kg)	17.39 (2.97)	18.80 (1.63)	0.312* [^]
FV Slope	-1.75 (0.24)	-1.06 (0.12)	0.753
RFmax (%)	44.55 (2.98)	46.56 (1.75)	0.582* [^]
Drf (%)	-11 (2)	-10 (1)	0.782

*Significant difference in age covariant between groups

[^]Significant difference in sex covariant between groups

Vmax: Maximum velocity

F0: Theoretical maximum horizontal force at null velocity

V0: Theoretical maximum velocity under zero load

Pmax: Maximal mechanical power output

FV Slope: Linear F-V relationship slope, negative indicates more force oriented, positive indicates more velocity oriented

RFmax: Ratio of horizontal component of ground reaction force (RF) maximum value

Drf: Rate of decrease in RF

Table 1: Baseline between-subject differences in FVP variables

Small sample size (as a result of restrictions imposed with COVID-19) precluded formal prospective statistical analysis. Nineteen participants completed the full injury surveillance period. Of these, two males sustained a HSI (Age HSI1: 24; HSI2: 18). Both participants had a history of HSI and were in the higher percentiles for maximum velocity (m/s) for both the entire cohort (HSI1: 89th percentile, HSI2: 83rd percentile) and the cohort with a history of HSI (HSI1: 91st percentile, HSI2: 82nd percentile).

CONCLUSIONS

The small sample size limits practical interpretation of results. Further research is needed with larger sample sizes to control for FVP differences with age and sex.

REFERENCES

- (1) Green, B. Br J Sports Med, 54, 1081-1088, 2020.
- (2) Danielsson, A. BMC Musculoskelet Disord, 21, 1-21, 2020.
- (3) Samozino, P. Scand J Med Sci Spor, 26, 648-658, 2016.
- (4) Mendiguchia, J. Int J Sports Med, 35, 690-695, 2014.

Presented by Lisa Wolski (lisawolski@hotmail.com).

OBJECTIVE ASSESSMENT OF FAST BOWLING DELIVERY INTENSITY IN AMATEUR MALE CRICKETERS

Epifano, D.J.; Ryan, S; Clarke, A.C.; Middleton, K.J.
La Trobe University, Melbourne, Australia

INTRODUCTION

An individualised approach to training is essential in cricket, as athletes of different positional roles can have considerably different physical demands (Petersen et al., 2010) and susceptibility to injury. This is particularly relevant to fast bowlers, who are most at-risk to injury of all cricketers (Orchard et al., 2015). Wearable microtechnology is effective in detecting fast bowling deliveries in cricket (Jowitt et al., 2020), however research into the quantification of delivery intensity remains limited. This study aimed to investigate the utility of metrics derived from both trunk- and tibia-mounted wearable sensors in quantifying subjective fast bowling intensity.

METHOD

Fifteen sub-elite male fast bowlers (mean \pm SD; age 21.0 ± 3.8 years; height 1.8 ± 0.1 m; mass 80.1 ± 8.6 kg) conducted a prescribed protocol of short, good, and full-length deliveries at warm-up, match, and maximal intensities. Ball speed was measured using a Stalker Sport 2 sports radar gun. PlayerLoad™ was measured via a Catapult GPS unit (10 Hz) whereas peak tibial accelerations at back foot impact, front foot impact, front foot re-impact, and back foot re-impact were measured via Vicon Blue Trident IMUs (1600 Hz). Data were converted to relative peak measures (%) based on individual maximum results. One-way repeated measures ANOVAs and post hoc paired t

tests were conducted to assess the effect of subjective delivery intensity on the dependent variables.

RESULTS

There were significant main effects of intensity with large effect sizes for all variables (Table 1, $p \leq .005$, $\eta_p^2 > 0.14$). Post-hoc pairwise comparisons showed that the magnitude of all variables in the match and maximal conditions were significantly larger compared with the warm-up condition ($p \leq .005$). No differences were observed between the match and maximal conditions ($p > .05$).

CONCLUSIONS

Acceleration-based data from trunk and tibia-mounted IMUs can accurately distinguish between a subjective warm-up bowling intensity and both subjective match and maximal bowling intensities. These devices provide a unique, time-efficient approach to cricket fast bowling intensity quantification.

REFERENCES

- Petersen, C. J. J. Sports Sci. 28, 45-52, 2010.
Orchard, J.W. Brit. J. Sports Med. 49, 1064-1068, 2015.
Jowitt, H.K. J. Sports Sci. 38, 1-6, 2020.

Presented by Daniel Epifano
(d.epifano@latrobe.edu.au).

Table 1. Relative microtechnology and performance outputs (mean \pm SD) across bowling intensities. Results presented as percentage of individual maximum. *significantly different to warm-up intensity ($p \leq .005$).

Variable (%)	Intensity (mean \pm SD)			<i>p</i> value	Effect size (η_p^2)
	Warm-up	Match	Maximal		
Ball speed	86.0 \pm 7.2	96.5 \pm 1.2*	97.0 \pm 1.6*	< .001	0.685
PlayerLoad™	67.8 \pm 14.0	88.4 \pm 7.4*	90.1 \pm 4.8*	< .001	0.922
Tibial acceleration					
@ back foot impact	39.2 \pm 18.7	53.3 \pm 17.6*	57.2 \pm 22.4*	< .001	0.466
@ front foot impact	45.5 \pm 17.1	59.0 \pm 15.4*	62.8 \pm 14.9*	< .001	0.551
@ back foot re-impact	46.6 \pm 15.4	63.5 \pm 12.2*	63.8 \pm 17.2*	.005	0.438
@ front foot re-impact	36.3 \pm 16.2	53.6 \pm 12.3*	59.7 \pm 16.0*	< .001	0.628

IMPACT OF FOOT-STRETCHER HEIGHT ON ROWING PERFORMANCE: A NONLINEAR ANALYSIS

Barratt¹, G.K.; Bellenger¹, C.; Robertson², E.Y. Lane², J.; Crowther¹, R.G.

¹University of South Australia, Adelaide, Australia; ²South Australian Sports Institute, Adelaide, Australia.

INTRODUCTION

The rowing stroke is a coordinated, cyclic movement involving complex relationships between the rower and the rowing boat (Sanderson, 1986). The foot-stretcher is where the rower's feet are placed in the boat and can be adjusted vertically to change foot-stretcher height (Soper, 2004). The position of the foot-stretcher can impact rowing technique and movement efficiency in rowing (Kleshnev, 2016).

Although rowing is a cyclic movement, it is typical that the rowing mechanics are examined in parts (i.e., a single rowing stroke or a group of strokes and not as a series of cyclic movements linked together). Non-linear analysis (Lyapunov Exponent [LyE]) is a useful method to examine the variability of a dynamic system (Mehdizadeh, 2018). Research has used the LyE to examine walking gait and there has been some use in running gait, however, this method has rarely been applied to other cyclic movements such as rowing.

Therefore, the aim of this project is to determine the effect of the foot-stretcher height (low [17 cm], high [12.5 cm] and current [measured from participants own boat]) on force at the oarlock and force at the foot-stretcher during a 1250 m rowing trial. It is hypothesised that there will be a higher variability in the force at the oarlock and force at the foot stretcher when the participant is placed in a higher foot-stretcher position.

METHOD

Twelve rowers from South Australian State Rowing Team and South Australian Sports Institute were recruited. Participants completed three 1250 m trials with each trial at a different foot stretcher position.

LyE (dim = 5; lag = 10) was calculated for the full trial of data using custom MATLAB script. Repeated measure analysis was performed with an $\alpha < 0.05$.

RESULTS

Mean and standard deviations at current, low and high foot-stretcher heights are presented in Table 1. There were no significant differences presented in the data.

Table 1. Mean and standard deviations of Lyapunov Exponent for force variables at current, low and high foot-stretcher heights.

		Mean (SD)			Sig.
		C	L	H	
Oarlock Force X	Port	0.78 (0.11)	0.74 (0.15)	0.77 (0.11)	0.28
	Starboard	0.70 (0.11)	0.71 (0.12)	0.70 (0.12)	0.94
Oarlock Force Y	Port	0.27 (0.19)	0.28 (0.13)	0.24 (0.13)	0.29
	Starboard	0.42 (0.23)	0.42 (0.23)	0.39 (0.27)	0.68
Foot Stretcher Force	Left	1.66 (0.22)	1.65 (0.17)	1.55 (0.16)	0.17
	Right	1.68 (0.14)	1.77 (0.19)	1.71 (0.21)	0.33
	Total	1.67 (0.22)	1.77 (0.24)	1.71 (0.30)	0.56

C = current, L = low, H = high, X = x-component, Y = y-component.

CONCLUSIONS

The use of the LyE demonstrated no significant difference between low, high and current foot-stretcher heights. This outcome is supports unpublished work by the authors where analysis of the difference in rowing performance across these three foot-stretcher heights using 10 strokes also found no significant changes for the same variables. The study used a heterogenous group which may have impacted the mean, therefore when assessing changes in foot-stretcher height in on-water rowing, individual analyses should be considered. Additionally, this analysis is typically performed on gait and to our knowledge has not been performed on kinetic variables during other cyclic movements. As such, the results should be considered with caution.

REFERENCES

- Soper, C. Sports Medicine. 13, 825-848, 2004
- Kleshnev, V. Biomechanics of Rowing. 2016
- Mehdizadeh, S. Gait & Posture. 60, 241-250, 2018
- Sanderson, C. Medicine & Science in Sports & Exercise. 18, 454-486, 1986

Presented by Georgina Barratt
(georgina.barratt@mymail.unisa.edu.au).

THE EFFECT OF DIFFERENT SOCCER SHOE STUD ON TRACTION RATIO AND RUNNING SPEED IN TURNING MOVEMENT

F. Ferryanto; Iroth, Kevin T.P.; Wicaksono, Satrio; Mahyuddin, Andi Isra
Mechanical Design Research Group, Faculty of Mechanical and Aerospace Engineering,
Institut Teknologi Bandung, Jawa Barat, Indonesia

INTRODUCTION

Currently, football is the most popular sport in the world. The high interest in the sport of football causes the performance of players to be an important thing. As a result, an analysis of soccer shoes, greatly support the improvement of player performance. The interaction between the soccer shoe and the field surface occurs in the stud part of the shoe. Although the use of soccer shoe studs on soccer fields has been identified, the effect of soccer shoe studs in terms of user biomechanics is not fully understood. Therefore, the purpose of this study was to analyze the effect of different soccer shoe studs on synthetic turf on the biomechanical parameters, such as shoe traction and running speed. In the present work, the turning movement was chosen as the target since it is the basic movement if the soccer.

METHOD

The shoe traction was measured by force plate. Then, the traction ratio, i.e., the ratio between the ground reaction force in horizontal and vertical direction. Besides, the running speed before the turning movement was also measured. The position of force plate could be seen in the experimental setup presented in Figure 1. In addition, running time perception (RTP) and traction suitability perception (TSP) were also carried out to subjectively assess soccer shoes [1]. The RTP was scored from one (very good) to four (very poor). The TSP was scaled from one (very good) to nine (very poor).

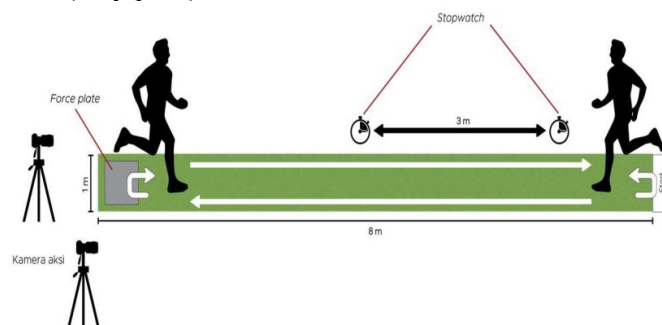


Figure 1. Experimental setup

There were two types of studs that were investigated in this work, i.e., artificial grass (AG) and firm ground

(FG). In the data acquisition, ten recreational soccer players with 21.33 ± 1.24 years old participated in this research. All participants had normal BMI and there was no abnormal posture.

RESULTS

The result of the present study was summarized in Table 1. The mean of AG and FG was compared by *t*-test with significance level $\alpha = 5\%$. It is obtained that the mean of traction ratio and TSP between AG and FG shoes was different significantly. Conversely, the *t*-test for running speed and RTP implies that there was no different between AG and FG shoes.

Table 1 The average and standard deviation of traction ratio, TSP, running speed, and RTP

Parameter	AG	FG
Traction ratio	0.60 ± 0.07	0.50 ± 0.04
TSP	4.90 ± 1.81	6.10 ± 1.75
Running speed (m/s)	16.97 ± 2.74	15.83 ± 1.72
RTP	2.00 ± 0.77	2.30 ± 1.18

The mean value of the traction ratio in Table 1 shows that AG shoes are less prone to slipping when performing turning movements on artificial trump. This finding is also supported by the average TSP value. However, the type of stud on soccer shoes does not affect the running speed of the participant. The effect of stud on kinematics parameters of turning movement is still under research.

CONCLUSIONS

In the turning movement on the artificial turf, the AG stud of soccer shoe give higher traction ratio compared to FG stud. On the other hand, there is no different running speed of participant when using both studs.

REFERENCES

- [1] Sterzing et al., Footwear Science, 2(1), 37-49, 2010.

Presented by F. Ferryanto (ferryanto@ftmd.itb.ac.id)

12th Australasian Biomechanics Conference (ABC12)

06 - 07 December 2021

List of Registered Delegates (at the time of printing, surname ordered alphabetically)

Title	First Name	Surname	Institution	E-mail
Mr	Alvin	-	Institut Teknologi Bandung, Indonesia	23121017@mahasiswa.itb.ac.id
Dr	Hamid	Abbasi	The University of Auckland, New Zealand	h.abbasi@auckland.ac.nz
A/Prof	David	Ackland	The University of Melbourne, Australia	dackland@unimelb.edu.au
Mr	Hossein	Ahmadi	NeuRA, Australia	f.knapman@neura.edu.au
Dr	Massoud	Alipour	Auckland Bioengineering Institute, Australia	mali569@aucklanduni.ac.nz
Mr	Dan	Anderson	The Royal Children's Hospital Melbourne, Australia	dan.anderson@rch.org.au
Mr	Dylan	Ashton	Kolling Institute / University of Sydney, Australia	dylan.ashton@sydney.edu.au
Miss	Georgina	Barratt	University of South Australia, Australia	georgie.barratt95@gmail.com
Mr	Kieran	Bennett	The University of Adelaide, Australia	kieran.bennett@adelaide.edu.au
Prof	Thor	Besier	Auckland Bioengineering Institute, New Zealand	t.besier@auckland.ac.nz
Prof	Lynne	Bilston	The University of New South Wales, NeuRA	l.bilston@neura.edu.au
Prof	Silvia	Blemker	University of Virginia, USA	ssblemker@virginia.edu
Dr	Bart	Bolsterlee	Neuroscience Research Australia, Australia	b.bolsterlee@neura.edu.au
Prof	Steven	Boyd	University of Calgary, Canada	skboyd@ucalgary.ca
Mr	Marco	Branni	Queensland University of Technology, Australia	marco.branni@qut.edu.au
Ms	Francesca	Bucci	Flinders University, Australia	francesca.bucci@flinders.edu.au
Dr	Ana Carolina	Cardoso De Sousa	Griffith University, Australia	a.cardosodesousa@griffith.edu.au
Miss	Laura	Carmen	Auckland Bioengineering Institute, New Zealand	lcarr475@aucklanduni.ac.nz
A/Prof	Christopher	Carty	Griffith University, Australia	c.carty@griffith.edu.au
Mr	Harvey	Chai	The University of Adelaide, Australia	chaihaowei123@hotmail.com
Dr	Julie	Choisne	Auckland Bioengineering Institute, New Zealand	j.choisne@auckland.ac.nz
Mr	Brian	Chow	Neuroscience Research Australia, Australia	b.chow@neura.edu.au
Dr	L Eduardo	Cofre Lizama	La Trobe University, Australia	e.cofrelizama@latrobe.edu.au
Mr	Tyler	Collings	Griffith University, Australia	tyler.collings@griffithuni.edu.au
Dr	Celeste	Coltman	University of Canberra, Australia	celeste.coltman@canberra.edu.au
Mr	Bradley	Cornish	Griffith University, Australia	bradley.cornish@griffithuni.edu.au
Dr	Daniel	Cottam	Australian Institute of Sport, Australia	daniel.cottam@ausport.gov.au
Ms	Claire	Crossley	Griffith University, Australia	claire.crossley@griffithuni.edu.au
Dr	Alasdair	Dempsey	Murdoch University, Australia	alasdair.dempsey@murdoch.edu.au
Mr	Daniel	Devaprakash	Griffith University, Australia	d.devaprakash@griffith.edu.au
Dr	Laura	Diamond	Griffith University, Australia	l.diamond@griffith.edu.au
Dr	Taylor	Dick	The University of Queensland, Australia	t.dick@uq.edu.au
Mr	Eoin	Doyle	Macquarie University, Australia	eoin.doyle@mq.edu.au

Mr	William	Du Moulin	Griffith University, Australia	will.dumoulin@griffithuni.edu.au
Mr	Kayne	Duncanson	The University of Adelaide, Australia	kayne.duncanson@adelaide.edu.au
Mr	Daniel	Epifano	La Trobe University, Australia	d.epifano@latrobe.edu.au
Ms.	Maura	Eveld	Vanderbilt University, United States	eveldm@gmail.com
Mr	Xiaolong	Fan	Queensland University of Technology, Australia	x7.fan@hdr.qut.edu.au
Mr.	Ferryanto	Ferryanto	Institut Teknologi Bandung, Indonesia	ferryanto@ftmd.itb.ac.id
Dr	Aaron	Fox	Deakin University, Australia	aaron.f@deakin.edu.au
Dr	Nikita	Ghosh	The University of Auckland, New Zealand	ngho752@aucklanduni.ac.nz
Dr	Shouryadipta	Ghosh	CSIRO, Australia	shouryadipta.ghosh@data61.csiro.au
Mr	Basilio	Goncalves	Griffith University, Australia	l.diamond@griffith.edu.au
Ms	Tamara	Grant	Griffith University, Australia	tamara.grant@griffithuni.edu.au
Dr	Hans	Gray	The University of Melbourne, Australia	hans.gray@unimelb.edu.au
Dr	Geoffrey	Hansfield	The University of Auckland, New Zealand	g.hansfield@auckland.ac.nz
Dr	Kim	Hebert-Losier	The University of Waikato, New Zealand	kim.hebert-losier@waikato.ac.nz
Miss	Salindi	Herath	Flinders University, Australia	salindi.herath@flinders.edu.au
Prof	Rob	Herbert	NeuRA, Australia	r.herbert@neura.edu.au
Dr	Hoa	Hoang	Queensland University of Technology, Australia	hoa.hoang@qut.edu.au
Dr	Ben	Hoffman	University of Southern Queensland, Australia	ben.hoffman@usq.edu.au
Miss	Brooke	Hoolihan	University of Newcastle, Australia	brooke.hoolihan@uon.edu.au
Mr	Dan	Hopkins	The University of Melbourne, Australia	dchopkins@student.unimelb.edu.au
Mr	Yichen	Huang	The University of Melbourne, Australia	yichenh2@student.unimelb.edu.au
Ms.	Laura	Hutchinson	The University of Queensland, Australia	laura.hutchinson@uq.edu.au
Mr	Luke	Jessup	The University of Queensland, Australia	l.jessup@uqconnect.edu.au
Mr	Arun	Jolly	Queensland University of Technology, Australia	arun.jolly@hdr.qut.edu.au
Ms	Nicole	Jones	The University of Southern Queensland, Australia	d9817473@uemail.usq.edu.au
Dr	Lauriane	Juge	NeuRA, Australia	f.knapman@neura.edu.au
Dr	Mousa	Kazemi	The University of Auckland, New Zealand	mkaz010@aucklanduni.ac.nz
Miss	Meghan	Keast	Deakin university, Australia	mf.keast@gmail.com
Mr	Nicholas	Kent	NeuRA, Australia	f.knapman@neura.edu.au
Dr	Luke	Kelly	The University of Queensland, Australia	l.kelly@uq.edu.au
Prof	Graham	Kerr	Queensland University of Technology, Australia	g.kerr@qut.edu.au
Miss	Stephanie	Khuu	Auckland Bioengineering Institute, New Zealand	skhu770@aucklanduni.ac.nz
Mr	Adam	Kositsky	Griffith University, Australia	adam.kositsky@griffithuni.edu.au
Mr	Praveen	Krishna	The University of Melbourne, Australia	pkkris@student.unimelb.edu.au
Mr	Maxence	Lavaill	Queensland University of Technology, Australia	maxencecyprienjules.lavaill@hdr.qut.edu.au
Mr	Michael	Lennon	Queensland University of Technology, Australia	m3.lennon@hdr.qut.edu.au
Ms	Xin	Li	The University of Melbourne, Australia	lix13@student.unimelb.edu.au
Prof	Glen	Lichtwark	The University of Queensland, Australia	g.lichtwark@uq.edu.au
Miss	India	Lindemann	The University of Queensland, Australia	i.lindemann@uq.net.au
Miss	Mingyue	Liu	The University of Adelaide, Australia	mingyue.liu@adelaide.edu.au
Dr	Rob	Lloyd	NeuRA, Australia	f.knapman@neura.edu.au
Dr	Joe	Lynch	Trauma and Orthopaedic Research Unit, Australia	joe.lynch@act.gov.au
Mr.	Nathan	Lyons	Griffith University, Australia	nathan.lyons@griffithuni.edu.au
Prof.	Andi	Mahyuddin	Institut Teknologi Bandung, Indonesia	aim@ftmd.itb.ac.id
Mr	Mohammad	Mangi	The University of Adelaide, Australia	mdmangi@gmail.com

Dr	Malik Muhammad Naeem	Mannan	Griffith University, Australia	m.mannan@griffith.edu.au
A/Prof	Saulo	Martelli	Queensland University of Technology, Australia	saulo.martelli@qut.edu.au
Mr	Adam	Martinac	NeuRA, Australia	f.knapman@neura.edu.au
Mr	Christian	Matthey	The University of Queensland, Australia	habs.finance@uq.edu.au
Ms	Grace	Mcconnochie	The University of Adelaide, Australia	grace.mcconnochie@adelaide.edu.au
Dr	Kirsty	Mcdonald	The University of New South Wales, Australia	kirsty.mcdonald@unsw.edu.au
Ms.	Maddie	McIntyre	Queensland University of Technology, Australia	maddie.mcintyre@qut.edu.au
Ms	Evy	Meinders	Griffith University, Australia	evy.meinders@griffithuni.edu.au
Dr	Karen	Mickle	La Trobe University, Australia	k.mickle@latrobe.edu.au
Dr	Kane	Middleton	La Trobe University, Australia	k.middleton@latrobe.edu.au
Mr	Corey	Miller	Queensland University of Technology, Australia	corey.miller@hdr.qut.edu.au
Miss	Daniela	Mini	Flinders University, Australia	mini0017@flinders.edu.au
Mrs	Sarah	Mollet	The University of Auckland, New Zealand	sarah.mollet@auckland.ac.nz
Mr	Mukherjee	Satanik	KU Leuven, Belgium	satanik.mukherjee@kuleuven.be
Ms	Tayebah	Namayeshi	The University of Melbourne, Australia	tnamayeshi@student.unimelb.edu.au
Dr	Azadeh	Nasseri	Griffith University, Australia	a.nasseri@griffith.edu.au
Dr	Dermot	O'Rourke	Flinders University, Australia	dermot.orourke@flinders.edu.au
Mr	Branson	Palmer	University of South Australia, Australia	branson.palmer@mymail.unisa.edu.au
Dr	Elyse	Passmore	Murdoch Children's Research Institute, Australia	elyse.passmore@rch.org.au
Dr	Jing	Peng	Queensland University of Technology, Australia	ling.peng@qut.edu.au
A/Prof	Egon	Perilli	Flinders University, Australia	egon.perilli@flinders.edu.au
Dr	Edmund	Pickering	Queensland University of Technology, Australia	ei.pickering@qut.edu.au
Dr	Patricio	Pincheira	The University of Queensland, Australia	uqppinch@uq.edu.au
Prof	Peter	Pivonka	Queensland University of Technology, Australia	peter.pivonka@qut.edu.au
Dr	Claudio	Pizzolato	Griffith University, Australia	c.pizzolato@griffith.edu.au
Miss	Jemima	Po	The University of Queensland, Australia	j.po@uq.net.au
Dr	Ryan	Quarrington	The University of Adelaide, Australia	ryan.quarrington@adelaide.edu.au
Mr	Alastair	Quinn	Griffith University, Australia	alastair.quinn@griffith.edu.au
Mr	Mohammad Fazle	Rabbi	Griffith University, Australia	fazle.rabbi@griffithuni.edu.au
Ms	Sophie	Rapagna	Flinders University, Australia	sophie.rapagna@flinders.edu.au
Dr.	Rodrigo	Rico Bini	La Trobe University, Australia	r.bini@latrobe.edu.au
Dr	Dale	Robinson	The University of Melbourne, Australia	drobinson@unimelb.edu.au
Miss	Nynke	Rooks	Auckland Bioengineering Institute, New Zealand	nroo469@aucklanduni.ac.nz
Ms	Monica	Russell	Materialise	monica.russell@materialise.com.au
Mr	Michael	Russo	Flinders University, Australia	michael.russo@flinders.edu.au
Ms	Sarah	Safavi	The University of Melbourne, Australia	ssafavi@student.unimelb.edu.au
Dr	David John	Saxby	Griffith University, Australia	d.saxby@griffith.edu.au
Mr	Robert	Schuster	The University of Queensland, Australia	r.schuster@uq.net.au
Mr	Kyle	Shapland	Materialise	kyle.shapland@materialise.com.au
Mr	Beichen	Shi	Griffith University, Australia	beichen.shi@griffithuni.edu.au
Mr	Arjun	Sivakumar	The University of Adelaide, Australia	arjun.sivakumar@adelaide.edu.au
Mr	Scott	Starkey	The University of Melbourne, Australia	ssstarkey@student.unimelb.edu.au
Prof	Mark	Taylor	Flinders University, Australia	mark.taylor@flinders.edu.au
A/Prof	Dominic	Thewlis	University of Adelaide, Australia	dominic.thewlis@adelaide.edu.au
Mr	Darcy	Thompson-Bagshaw	The University of Adelaide, Australia	darcy.thompson-bagshaw@adelaide.edu.au

Mr	Simon	Thwaites	The University of Adelaide, Australia	simon.thwaites@adelaide.edu.au
Mr	E Hong	Tiew	The University of Melbourne, Australia	etiew@student.unimelb.edu.au
Miss	Paige	Treherne	The University of Queensland, Australia	p.treherne@uqconenct.edu.au
Dr	Kwong Ming (KM)	Tse	Swinburne University of Technology, Australia	ktse@swin.edu.au
Ms	Natali	Uribe Acosta	Queensland University of Technology, Australia	natali.uribeacosta@hdr.qut.edu.au
Dr	Wolbert	Van Den Hoorn	Queensland University of Technology, Australia	w.vandenhooorn@qut.edu.au
Ms	Kirsten	Veerkamp	Griffith University & Amsterdam UMC, Netherlands	kirsten.veerkamp@griffithuni.edu.au
Dr	Pujith	Vijayaratnam	The University of New South Wales, Australia	p.vijayaratnam@unsw.edu.au
Mrs	Sherrilyn	Walters	University of Southern QLD, Australia	finance-researchoffice@usq.edu.au
Ms	Lauren	Wearne	Flinders University, Australia	lauren.wearne@flinders.edu.au
Mr	Denny	Wells	Logemas	denny@logemas.com
Mr	Christopher	Whalley	The University of Adelaide, Australia	a1704979@adelaide.edu.au
Dr	Tom	Whyte	NeuRA, Australia	f.knapman@neura.edu.au
Dr.	Satrio	Wicaksono	Institut Teknologi Bandung, Indonesia	satriowicaksono@ftmd.itb.ac.id
Mr	James	Williamson	The University of Queensland, Australia	james.williamson@uq.net.au
Mr	Lachlan	Winter	University of South Australia, Australia	lachlan.winter@mymail.unisa.edu.au
Dr	Elizabeth	Wojciehowski	The Children's Hospital at Westmead, Australia	elizabethwoj@hotmail.com
Miss	Lisa	Wolski	The University of Sydney, Australia	lisawolski@hotmail.com
Ms	Sarah	Woodford	The University of Melbourne, Australia	swood1@student.unimelb.edu.au
Mr	Matthew	Worsey	Griffith University, Australia	matthewworsey08@gmail.com
Mr	Zhengliang	Xia	Griffith University, Australia	zhengliang.xia@griffithuni.edu.au
Mr	Yihang	Yu	The University of Melbourne, Australia	yihangy@student.unimelb.edu.au
Mr	Homayoon	Zarshenas	Auckland Bioengineering Institute, New Zealand	hzar638@aucklanduni.ac.nz
Miss	Yilan	Zhang	The University of New South Wales, NeuRA	yilan.zhang@neura.edu.au
